SAKARYA ÜNİVERSİTESİ

FEN BİLİMLERİ ENSTİTÜSÜ
DERGİSİ

Sakarya University Journal of Science (SAUJS)

SAKARYA
ÜNİVERSİTESİ

e-issn: 2147-835X

SAÜ Fen Bil Der/SAUJS

Cilt/Volume: 26

Sayı/Issue: 5

Ekim/October 2022

Sakarya Üniversitesi Fen Bilimleri Enstitüsü Dergisi
(Sakarya University Journal of Science)
Cilt/Volume: 26 No/ Issue:5 Ekim/October 2022

Editör Kurulu/Editorial Boards

Owner

Hamza Al, Sakarya University (Turkey)

Publishing Manager

Halit Yaşar, Mechanical Engineering, Sakarya University (Turkey)

Editor-in-Chief

Davut Avcı, Pyhsics, Sakarya University (Turkey)

Associate Editors

Ihsan Hakan Selvi, Information Systems Engineering, Sakarya University (Turkey)

Ömer Tamer, Physics, Sakarya University (Turkey)

Editors

Abderrahmane Benbrik, M'Hamed Bougara University at Boumerdes (Algeria)

Abdullah Oğuz Kızılçay, Computer Engineering, Zonguldak Bülent Ecevit University (Turkey)

Ali Cemal Benim, Faculty of Mechanical and Process Engineering, Duesseldorf University of Applied Sciences (Germany)

Ali Demir, Mathematics, Kocaeli University (Turkey)

Aligholi Niaei, Chemistry, Tabriz University (İran)

Aslı Uçar, Faculty of Health Sciences, Nutrition and dietetics, Ankara University (Turkey)

Asude Ateş, Environmental Engineering, Sakarya University (Turkey)

Bahadır Saygı, Physic, Ege University (Turkey)

Barış Yüce, Engineering Management, Exeter University, UK

Belma Zengin Kurt, Chemistry, Bezmiâlem Vakıf University (Turkey)

Benjamin Durakovic, Department of Industrial Engineering, Bosnia International University of Sarajevo (Bosnia and Herzegovina)

Berrin Denizhan, Industrial Engineering, Sakarya University (Turkey)

Can Serkan Keskin, Chemistry, Sakarya University (Turkey)

Caner Erden, International Trade and Finance, Sakarya University of Applied Sciences (Turkey)

Ceren Tayran, Physic, Gazi University (Turkey)

Cansu Akbulut, Biology, Sakarya University (Turkey)

Ece Ümmü Deveci, Environmental Engineering, Niğde Ömer Halisdemir University (Turkey)

Edgar Perez-Esteve, Food Technology, Polytechnic University of Valencia (Spain)
Elif Ağcakoca, Civil Engineering, Sakary Apllied Science University (Turkey)
Elif Eker Kahveci, Mechanical Engineering, Sakarya University (Turkey)
Fahrettin Horasan, Computer Engineering, Kırıkkale University (Turkey)
Faruk Fırat Çalım, Civil Engineering, Alparslan Türkeş University (Turkey)
Feyza Gurbuz, Industrial Engineering, Erciyes University (Turkey)
Francesco de Paulis, Electrical and Electronics Enginering, University of L'Aquila (Italy)
Gökhan Dok, Civil Engineering, Sakary Apllied Science University (Turkey)
Grazyna S Martynkova, Nanotechnology Centre, VŠB-Technical University of Ostrava · Nanotechnology Centre (Czech Republic)
Grzegorz Jaworski, Physics, Heavy Ion Laboratory, University of Warsaw (Poland)
H. F. Nied, Department of Mechanical Engineering and Mechanics, Lehigh University (U.S.A.)
Hakan Alp, Geophysical Engineering, Cerrahpaşa University (Turkey)
Hatice Esen, Industrial Engineering, Kocaeli University (Turkey)
Hüseyin Aksoy, Biology, Sakarya University (Turkey)
Issa Al-Harty, Civil and Architectural Engineering, Sultan Qaboos University (Oman)
İbrahim Bahadır Başyiğit, Electrical and Electronics Engineering, Isparta Apllied Science University (Turkey)
İsmail Hakkı Demir, Architecture, Sakarya University (Turkey)
Kamaruzzaman Sopian, Renewable Energy, Universiti Kebangsaan Malaysia (Malaysia)
Khalifa Al-Jabri, Civil and Architectural Engineering, Sultan Qaboos University (Oman)
Luan Thach Hoang, Mathematics, Texas Tech University (U.S.A.)
Luis A. Materon, Biology, The University of Texas Rio Grande Valley (USA)
M. Hilmi Nişancı, Electrical and Electronics Engineering, Sakarya University (Turkey)
Mahmud Tokur, Metallurgical and Materials Engineering, Sakarya University (Turkey)
Mehmet Emin Aydın, Industrial Engineering, University of Bedfordshire (UK)
Mehmet Uysal, Metallurgical and Materials Engineering, Sakarya University (Turkey)
Mesut Baran, Electrical and Computer Engineering, FREEDM Systems Center, North Carolina State University (U.S.A.)
Miraç Alaf, Metallurgical and Materials Engineering, Bilecik Şeyh Edebali University (Turkey)
Mohammad Sukri bin Mustapa, Faculty of Mechanical & Manufacturing Engineering, Universiti Tun Hussein Onn Malaysia (Malaysia)
Muhammed Fatih Adak, Computer Engineering, Sakarya University (Turkey)
Muhammed Maruf Öztürk, Computer Engineering, Süleyman Demirel University (Turkey)
Murat Güzeltepe, Mathematics, Sakarya University (Turkey)
Murat Sarduvan, Mathematics, Sakarya University (Turkey)
Murat Tuna, Chemistry, Sakarya University (Turkey)

Mustafa Akpınar, Software Engineering, Sakarya University (Turkey)

Mustafa Gülfen, Chemistry, Sakarya University (Turkey)

Nahit Gencer, Chemistry, Balıkesir University (Turkey)

Nazan Deniz Yön Ertuğ, Biology, Sakarya University (Turkey)

Necati Olgun, Mathematics, Gaziantep University (Turkey)

Nihan Akıncı Kenanoğlu, Biology, Çanakkale Onsekiz Mart University (Turkey)

Oğuz Kurt, Biology, Manisa Celal Bayar University (Turkey)

Ozan Erdinç, Electrical and Electronics Engineering, Yıldız Technical University (Turkey)

Raja Mazuir Raja Ahsan Shah, Aerospace and Automotive Engineering, Coventry University (United Kingdom)

Rıfkı Terzioğlu, Electrical and Electronics Engineering, Bolu Abant İzzet Baysal University (Turkey)

S.C. Yao, Mechanical Engineering, Carnegie Mellon University, PA (U.S.A.)

Sadık Kakaç, Mechanical Engineering, TOBB ETU (Turkey)

Selma Özçağ, Mathematics, Hacettepe University (Turkey)

Seong Jin Park, Department of Mechanical Engineering, Pohang University of Science and Technology (Korea)

Serap Coşansu Akdemir, Food Engineering, Sakarya University (Turkey)

Syed Nasar Abbas, Food Engineering, Curtin University (Australia)

Şenay Çetin Doğruparmak, Environmental Engineering, Kocaeli University (Turkey)

Tahsin Turğay, Architecture, Sakarya University (Turkey)

Tauseef Aized, Mechanical Engineering, University of Engineering and Technology (Pakistan)

Tuba Tatar, Civil Engineering, Sakarya University (Turkey)

Tuğrul Çetinkaya, Metallurgical and Materials Engineering, Sakarya University (Turkey)

Ufuk Durmaz, Mechanical Engineering, Sakarya University (Turkey)

Urvir Singh, Electrical and Electronics Enginering, Schweitzer Engineering Laboratories: SEL Inc. (U.S.A.)

Guest Editor

Ertan Bol, Civil Engineering, Sakarya University (Turkey)

Murat Utkucu, Geophysics Engineering, Sakarya University (Turkey)

Erman Aslan, Mechanical Engineering, Kocaeli University (Turkey)

English Language Editor

Ömer Tamer, Physics, Sakarya University (Turkey)

Editorial Assistant

Ahmet Erhan Tanyeri, Sakarya University (Turkey)

Evrim Yüksel, Sakarya University (Turkey)

SAKARYA ÜNİVERSİTESİ FEN BİLİMLERİ ENSTİTÜSÜ DERGİSİ
(SAKARYA UNIVERSITY JOURNAL OF SCIENCE)
İÇİNDEKİLER/CONTENTS

Cilt/Volume: 26 – No/Issue5: (EKİM/OCTOBER-2022)

RESEARCH ARTICLES

SAKARYA ÜNİVERSİTESİ
FEN BİLİMLERİ ENSTİTÜSÜ
DERGİSİ

Sakarya University Journal of Science
SAUJS

ISSN 1301-4048 | e-ISSN 2147-835X | Period Bimonthly | Founded: 1997 | Publisher Sakarya University |
http://www.saujs.sakarya.edu.tr/

Title: An Experimental Study of a Pico Hydro Turbine

Authors: Ümit BEYAZGÜL, Ufuk DURMAZ, Orhan YALÇINKAYA, Mehmet Berkant ÖZEL, Ümit PEKPARLAK

Recieved: 2022-05-30 00:00:00

Accepted: 2022-07-04 00:00:00

Article Type: Research Article

Volume: 25
Issue: 5
Month: October
Year: 2022
Pages: 850-857

How to cite
Ümit BEYAZGÜL, Ufuk DURMAZ, Orhan YALÇINKAYA, Mehmet Berkant ÖZEL, Ümit PEKPARLAK; (2022), An Experimental Study of a Pico Hydro Turbine. Sakarya University Journal of Science, 25(5), 850-857, DOI: 10.16984/saufenbilder.1123406
Access link
http://www.saujs.sakarya.edu.tr/en/pub/issue/73051/1123406

Sakarya University Journal of Science 25(5), 850-857, 2022

An Experimental Study of a Pico Hydro Turbine

Ümit BEYAZGÜL[1], Ufuk DURMAZ*[1], Orhan YALÇINKAYA[1],
Mehmet Berkant ÖZEL[1], Ümit PEKPARLAK[2]

Abstract

Today, the storage and transporting of electricity from one place to another is still an unsolved problem. Besides, it is not economical to install power lines everywhere for low-voltage electronic circuits such as valves which are used to reduce leakage in water lines. When water demand is lower, it is a practical solution to use the pico hydro turbines to supply the required electrical energy for the electronic circuits of the valves used to reduce the losses in the water discharge lines. For this purpose, it is experimentally investigated electricity production in a pico hydro turbine and validated with experimental data that a pico hydro turbine (PHT) generates 1 W electricity under a water flow velocity of 0.53 m/s. It is concluded that the higher resistances were used in the test rig, the less turbine power produced. As the voltage increased, the current obtained decreased, and the turbine power reached its maximum at a resistance of 130 Ω.

Keywords: Pico hydro turbine, hydropower, banki turbine, energy efficiency, experimental setup

1. INTRODUCTION

Pico hydro turbines are frequently used for opening and closing valves, which regulate the flow rate in water distribution pipelines. Also, it is an energy harvesting device that uses the energy of a water pressure drop. This energy is captured by the pico hydro turbine and converted into electricity.

Most studies have been conducted on numerical investigation of cross-flow water turbines as opposed to this current study [1, 2].

Borkowski et al. [3] tested and validated the single-equation Spalart-Allmaras (SA) model, as well as the k-ε and k-ω shear-stress transport (SST) turbulence models, in an experimental hydroelectric power plant with a power of 75 kW. The calculation results

---

* Corresponding author: udurmaz@sakarya.edu.tr
[1] Sakarya University
E-mail: umitbyzgl1@hotmail.com, orhanyalcinkaya@sakarya.edu.tr, mozel@sakarya.edu.tr
ORCID: https://orcid.org/0000-0001-5534-8117, https://orcid.org/0000-0002-1471-793X, https://orcid.org/0000-0003-2380-1727, https://orcid.org/0000-0002-2439-1494
[2] TBM Industry
E-mail: u.pekparlak@porte.com.tr
ORCID: https://orcid.org/0000-0002-5554-6989

according to the turbulence models differed significantly. As a result of the comparisons, the Spalart-Allmaras model provided the best experimental results. Verma et al. [4] analyzed runner speed and efficiency variation with different attack angles, nozzle tip height, and nozzle tip distance from the runner. The runner consists of 12 blades symmetrically arranged between the two circular end plates around the plate. They prepared the installation for places with relatively moderate or low head consideration. While the inlet angle β_1 of the vane was kept between about 26° and 28°, and the outlet angle β_2 was 90°. Namely, the outlet was radial. Critical parameters such as nozzle inlet angle, nozzle tip height, and horizontal distance from the center of the runner shaft were changed for different heads under different field configurations. Sinagra et al. [5] designed and tested a 10 kW prototype of a new compact in-line turbine called the Power Recovery System (PRS) in the University of Palermo hydraulic laboratory. They proposed a Banki-type microturbine with positive outlet pressure and a mobile regulating vane for hydraulic control of the characteristic curve. They aimed to control the pressure or discharge in a water transport or distribution network by producing energy up to 76% of the efficiency value of the device. Using two pressure gauges located just before and after the turbine made it possible to control the net head in inactive mode at the given discharge point or to control the discharge by regulating the net head in active mode. Sammartano et al. [6] carried out a numerical and experimental study to validate a previously proposed design criterion for a cross-flow turbine and a new semi-empirical formula that relates the inlet velocity to the inlet pressure. An experimental test stand was designed to perform a series of experiments and measure the efficiency of the turbine designed according to the proposed criteria. Experimental efficiency was compared with numerical simulations using a Reynolds-Averaged Navier-Stokes (RANS) turbulence model. The proposed semi-empirical velocity formula was also validated with numerical solutions for cross-flow turbines with different geometries and boundary conditions. They verified the previous hydrodynamic analysis with obtained results. Therefore, they found that it can be used to design cross-flow turbines to reduce the cost of simulations required while optimizing the turbine geometry. Elbatron et al. [7] proposed a new system configuration to extract as much kinetic energy as possible from the water stream. This system, known as a bidirectional diffuser augmented (BDA) channel, works by using bidirectional nozzles in the flow. The proper angle is essential to direct its flow so that it touches the wings vertically to capture as much torque and power as possible. Therefore, experimental and numerical studies were carried out and verified with each other to examine the performance characteristics of the cross-flow turbine (CFT) configuration applied to the BDA system and to investigate the effects of the inlet and outlet angles of the blades on the internal flow properties and efficiency of the CFT runners. Dragomirescu et al. [8] presented the results of the experimental and numerical study of a Banki turbine with a horizontal nozzle operating at 5% and 30% below nominal values and discharges. In line with the experimental results, they predicted that a maximum efficiency of over 55% could be reached even if there were sharp decreases in the values of the working parameters. Numerical simulations were performed to get an idea of the flow through the turbine. It has been determined that the obtained numerical results were compatible with the experimental results. Sammartano et al. [9] tested the performance of a cross-flow water turbine, which provides high efficiency in a wide water discharge range, by experimentally working on cross-flow micro-turbines and verified a new approximate formula that relates the inlet pressure to the main inlet velocity. They found that the experimental tests and CFD analysis results were in agreement with each other, and both experimental studies and CFD computations provided a consistent reduction in machine efficiency due to increased internal energy losses of the internal shaft. Giosio et al. [10] investigated a comprehensive range of micro hydro turbine units recently. They presented an affordable micro-hydro turbine unit with an improved operating range. As a result, utilizing a pump impeller as a runner provided an efficiency of 79% and near-peak efficiency at off-design conditions. Moreover, this micro-hydro turbine unit had the ability to power supply remote areas.

The availability of a continuous energy source enables optimal pressure management that is continuously maintained at a lower value to reduce water leaks, improve network efficiency, and extend pipeline lifetime. The main objective of the present study is to experimentally investigate the performance of PHT and its characteristics through varying the resistance (Ω) and voltage (*V*). In this study, the electrical power produced by a pico hydro turbine (PHT) was experimentally tested by measuring the average volumetric flow (Q), voltage, and current under real conditions with an experimental setup.

2. MATERIALS AND METHODS

The hydraulic power of a PHT depends upon the flow rate (Q) and the water head (*H*), which are the significant parameters that affect the turbine performance exposed on the turbine shaft. While impulse turbines are adapted for sites with high heads and low flow conditions, reaction turbines such as cross-flow and Banki turbines perform best at low heads and high flow rates. These main parameters determine the runner diameter (*D*), angular velocity (*w*), turbine power output (*P*), and output torque (*T*) in a water turbine. Several equations were considered to have accurate measurements for hydroelectric power while using different amounts of resistances during the experiment in this study. By assuming no friction through the pipe and the turbine, available hydraulic power (P_H) generated by water can be measured as a function of the amount of volume flow rate (Q) and water head (*H)* at incompressible flow conditions. Since there is no available water head for the PHT in this study, P_H can also be measured based on voltage (*V*) and current (*I*) in line with resistance (R), whose equations represented by Eq. (1) are as follows:

$$P_H = \rho Q g H = VI \qquad (1)$$

Where P_H is available hydraulic power, ρ is the water density, presented by a value of 997 $\mathrm{kg/m^3}$ at ambient temperature, g is the acceleration of gravity, with a value of 9.81 $\mathrm{m/s^2}$, Q is the volume flow rate passing through the turbine ($\mathrm{m^3/s}$), H is the available water head at the turbine. It is equal to the power provided by voltage and current generated by the turbine shaft by using a wide range of resistances in this study.

Furthermore, P_M is the mechanical power output of the PHT turbine and is defined as the product between angular velocity (ω) and torque (*T*) on the turbine shaft by Eq.(2).

$$P_M = T\omega \qquad (2)$$

As a result of Eq.(1) and Eq.(2), experimental turbine efficiency (η) is as follows

$$\eta = {}^{VI}\!/_{T\omega} \qquad (3)$$

2.1. Experimental Setup and Design Parameters

A cross-flow turbine at a pico scale was investigated to examine the effects of several geometric factors involved in the design, including turbine diameter (*D*), the number of blades (*z*), and volume flow rate (Q) on maximum turbine performance. The tested turbine shown in Figure 1 is comprised of a runner with 32 mm of inner diameter and 40 mm of outer diameter. The total number of turbine blades is 24. The PHT turbine is made up of plastic material in the turbine body and blade. The hydraulic test bench consists of a system of pipes connecting an inlet and outlet of the turbine whereby the water was recirculated.

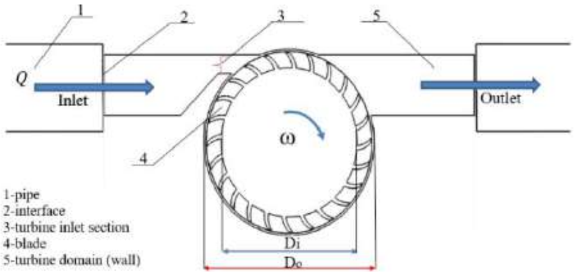

Figure 1 Schematic of 2-D tested turbine model flow surface section

Experiments have been carried out in the hydraulic research laboratory (HRL) of the faculty of Mechanical Engineering of Sakarya University (Turkey). The test stand comprises a PHT turbine coupled with resistances, flowmeter, pipe, multimeter, and probes on a test bench, as shown in Figure 2. Flowmeter has been used to measure the volume flow rate of the water through the pipe. The water volume flow rate has been set to be the maximum flow rate after several attempts and varied from 0.25 L/s to 0.167 L/s at the inlet and outlet of the turbine. The velocity (v) at the turbine outlet can be calculated by using the continuity equation as follows:

$$v = {}^{Q}/_{A} \tag{4}$$

A represents the cross-sectional area of the runner. The velocity of PHT was obtained with a value of 0.53 m/s under the volume flow rate of 0.167 L/s.

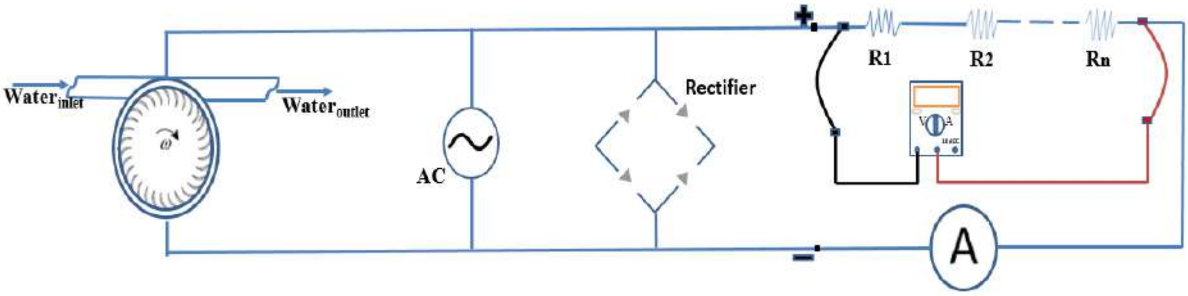

Figure 2 The test-rig model schematic diagram established in HRL

There is also one calibrated multimeter used to measure each voltage to determine the maximum hydraulic power by using three amounts of resistances in the test rig. It has been respectively used 10 Ω, 15 Ω, and 100 Ω, which correspond to 2050 Ω resistances totally during the experiment.

2.2. Experimental Procedure and Uncertainty Analysis

The actual water volume flow rate and the voltage generated by the turbine have been recorded by flowmeter and multimeter, respectively, to calculate input power. The runner velocity has been calculated by using a flowmeter to reach maximum velocity in PHT. Also, voltage coupled with resistance has been measured using a multimeter to reach maximum power. Therefore, it has been prioritized for two parameters to analyze maximum uncertainties. Parameter accuracy and maximum uncertainties for power and volume flow rate have been determined by several tests with forty-eight voltage value point that equal 4%. Moreover, multimeter uncertainty has been determined by Mc-Clintock equation, and it has been found to be 0.5%. Also, the uncertainty of the flowmeter used to measure water volume flow rate is 0.09%.

Using Mc-Clintock, the maximum uncertainties of P and Q are represented in Eqs. (5) and (6), respectively:

$$W_P = \pm\left[\left(\frac{\partial P}{\partial V}W_V\right)^2 + \left(\frac{\partial P}{\partial I}W_I\right)^2\right]^{1/2} \tag{5}$$

$$W_Q = \pm\left[\left(\frac{\partial Q}{\partial V}W_V\right)^2 + \left(\frac{\partial Q}{\partial A}W_A\right)^2\right]^{1/2} \tag{6}$$

3. RESULTS AND DISCUSSIONS

Response surface methodology (RSM) has been conducted to establish relationships among selected parameters referring to a set of mathematical and statistical techniques to create a regression model characterizing affecting parameters of turbine performance. For this purpose, it has been calculated power increase by means of coupled different amounts of resistance in the electric circuit among several trials. It has been split into three categories starting from the first 10 Ω resistance intervals between 10 Ω and 200 Ω (R_1), 15 Ω between 200 Ω and 350 Ω (R_2), and 100 Ω between 350 Ω and 2050 Ω (R_3). The experimental study matrix and regression models are obtained on ANOVA by combining the considered factors and levels, which are R-square/adjusted (R^2/adj.), p-value, sum of squares (SS), degrees of freedom (df), mean square (MS) and F-ratio, etc. for each treatment according to RSM. In this regard, several regression models representing the turbine power performance have been created, including linear and polynomial models, as shown in Table 1.

Table 1 ANOVA for fitted polynomial and lineal regression model using RSM for PHT

Resistance model	**R^2**	**R^2_{adj}**	**MS**	**SS**	**F-ratio**	**df**	**p-value**	**Regression model**
R_1	0.99	0.99	0.73	1.46	1254.12	18	0.06	Polynomial
R_2	0.99	0.99	0.05	0.10	6448.83	8	1.61	Polynomial
R_3	0.96	0.95	0.08	0.16	182.10	15	0.558	Polynomial
R_1	0.54	0.51	0.79	0.79	22.35	19	0.40	Lineal

The PHT model significance and adequacy have been analyzed by the p-value of the regression model and the R^2 and R^2_{adj}, respectively. The results analysis shows the fact that the polynomial regression model had a p-value of more than 0.05 (0.06), and the highest R^2_{adj} (99.20%) unlike the linear regression model. Furthermore, the value corresponding to R^2 for the linear regression model revealed that a minimum 40% of the deviation of the obtained experimental data for the resistance model-R_1 is shown in Figure 3 and Table1. Therefore, the polynomial regression model was selected because this model gives a higher significance and an adequate regression model which fits the best for PHT. The equation referred to polynomial equation model defining the maximum turbine power is given by Eq. (7).

$$y = 0.061 + 0.014x - 5.442\text{x}10^{-5}x^2 \quad (7)$$

Where y is ascribed to the maximum turbine power and x are the defined levels for the turbine voltage values. As a result of the experimental study between related voltages, it has been obtained that the PHT generates approximately 1 W against 130 Ω, which is a value similar to that one predicted by the polynomial model.

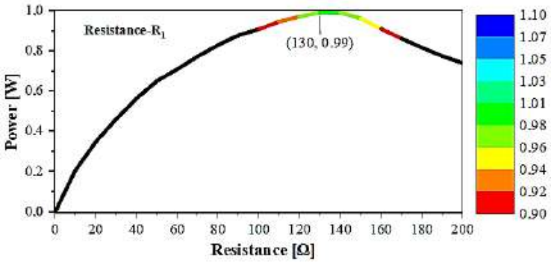

Figure 3 Power-R_1 until 200 Ω

The polynomial model has also been applied to the resistance-R_2 and R_3 models shown in Figure 4 and Figure 5, respectively. Figure 4 represents the experimental voltage data versus power for the optimal conditions found at 200 Ω. This value has turned out to be at 350 Ω in Figure 5.

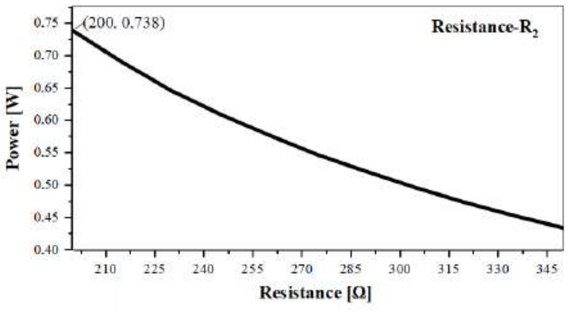

Figure 4 Power-R_2 until 350 Ω

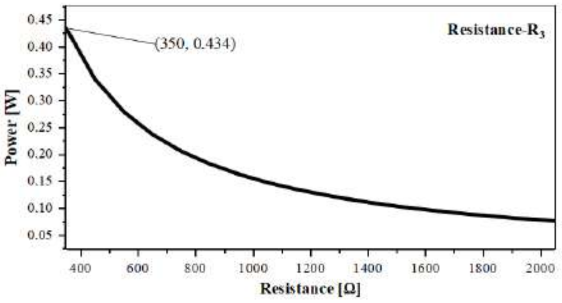

Figure 5 Power-R_3 until 2050 Ω

While the maximum power is 0.73 W for the resistance-R_2 model, it is obtained that the power is a maximum of 0.43 W for resistance-R_3. As a result of this study, it is important to note that the kinetic energy is generated from the water-energy by means of a pipe. When the flow rate is gradually declining towards the turbine outlet, it is observed that even though the amount of resistance is increasing, the power generation is decreasing depending on the current.

4. CONCLUSION

This study involves the experimental study to demonstrate turbine performance with a set of voltages evaluated with the RSM procedure under the regression model. In the current work, the turbine experimental study is conducted to obtain maximum electrical power value using a resistance of 2050 Ω in a test rig through a multimeter and flowmeter. It was concluded that PHT generates 1 W output power at 130 Ω under the water velocity of 0.53 m/s at operating flow conditions. It is also observed that as the resistance amount increases, the turbine generates less power. In this regard, minimum power is measured at the last resistance point, 2050 Ω. RSM is an efficient tool to provide a prediction model demonstrating turbine performance. In this context, the polynomial regression model predicted maximum power turbine efficiency is approximately 1 W when R^2 is equal to 0.99. The experimental results obtained in this study are essential in terms of validating the numerical models to be made in the future.

Acknowledgments
The authors would like to acknowledge the reviewers and editors of Sakarya University Journal of Science.

Funding
The authors has no received any financial support for the research, authorship or publication of this study.

Authors' Contribution
The authors contributed equally to the study.

The Declaration of Conflict of Interest/ Common Interest
No conflict of interest or common interest has been declared by the authors.

The Declaration of Ethics Committee Approval
This study does not require ethics committee permission or any special permission.

The Declaration of Research and Publication Ethics
The authors of the paper declare that they comply with the scientific, ethical and quotation rules of SAUJS in all processes of the paper and that they do not make any falsification on the data collected. In addition, they declare that Sakarya University Journal of Science and its

editorial board have no responsibility for any ethical violations that may be encountered, and that this study has not been evaluated in any academic publication environment other than Sakarya University Journal of Science.

NOMENCLATURE

β_1	Inlet angle [°]
β_2	Outlet angle [°]
ω	Angular velocity [rad/s]
η	Turbine efficiency [-]
A	Cross-sectional area [m^2]
BDA	Bidirectional diffuser augmented [-]
CFT	Cross-flow turbine [-]
D	Turbine diameter [mm]
g	Gravity [m/s^2]
df	Degrees of freedom [-]
H	Head [m]
HRL	Hydraulic research laboratory [-]
I	Current [A]
MS	Mean square [-]
P	Power [W]
PHT	Power hydro turbine [-]
PRS	Power recovery system
P_H	Hydraulic power [W]
P_M	Mechanical power [W]
Q	Volume flow rate [m^3/s]
R	Resistance [Ω]
RANS	Reynolds-Averaged Navier-Stokes [-]
RSM	Response surface methodology [-]
R^2	R-square [-]
R^2_{adj}	R-square adjusted [-]
SS	Sum of squares [-]
SA	Spalart-Allmaras [-]
SST	Shear-stress transport [-]
T	Torque [N.m]
V	Voltage [V]
v	Velocity [m/s]
z	Number of blades [-]

REFERENCES

[1] A. P. Prakoso, Warjito, A. I. Siswantara, Budiarso, D. Adanta, “Comparison between 6-DOF UDF and moving mesh approaches in CFD methods for predicting cross-flow pico-hydro turbine performance,”

CFD Letters, vol. 11, no. 6, pp. 86–96, 2019.

[2] Warjito, A. P. Prakoso, Budiarso, D. Adanta, “CFD simulation methodology of cross-flow turbine with six degree of freedom feature,” AIP Conference Proceedings, vol. 2255, no. September, 2020.

[3] D. Borkowski, M. Węgiel, P. Ocłoń, T. Węgiel, “CFD model and experimental verification of water turbine integrated with electrical generator,” Energy, vol. 185, pp. 875–883, 2019.

[4] V. Verma, V. K. Gaba, S. Bhowmick, “An Experimental Investigation of the Performance of Cross-flow Hydro Turbines,” Energy Procedia, vol. 141, pp. 630–634, 2017.

[5] M. Sinagra, C. Aricò, T. Tucciarelli, G. Morreale, “Experimental and numerical analysis of a backpressure Banki in-line turbine for pressure regulation and energy production,” Renewable Energy, vol. 149, pp. 980–986, 2020.

[6] V. Sammartano, G. Morreale, M. Sinagra, T. Tucciarelli, “Numerical and experimental investigation of a cross-flow water turbine,” Journal of Hydraulic Research, vol. 54, no. 3, pp. 321–331, 2016.

[7] A. H. Elbatran, O. B. Yaakob, Y. M. Ahmed, A. S. Shehata, “Numerical and experimental investigations on efficient design and performance of hydrokinetic Banki cross flow turbine for rural areas,” Ocean Engineering, vol. 159, no. March, pp. 437–456, 2018.

[8] A. Dragomirescu M. Schiaua, “Experimental and Numerical Investigation of a Bánki Turbine Operating far away from Design Point,” Energy Procedia, vol. 112, no. October 2016, pp. 43–50, 2017.

[9] V. Sammartano, G. Morreale, M. Sinagra, A. Collura, T. Tucciarelli, “Experimental study of Cross-Flow micro-turbines for aqueduct energy recovery,” Procedia Engineering, vol. 89, no. December, pp. 540–547, 2014.

[10] D. R. Giosio, A. D. Henderson, J. M. Walker, P. A. Brandner, J. E. Sargison, P. Gautam, “Design and performance evaluation of a pump-as-turbine micro-hydro test facility with incorporated inlet flow control,” Renewable Energy, vol. 78, pp. 1–6, 2015.

SAKARYA ÜNİVERSİTESİ

FEN BİLİMLERİ ENSTİTÜSÜ
DERGİSİ

Sakarya University Journal of Science
SAUJS

ISSN 1301-4048 | e-ISSN 2147-835X | Period Bimonthly | Founded: 1997 | Publisher Sakarya University |
http://www.saujs.sakarya.edu.tr/

Title: Electrochemical Performances of NMC811 Lithium-Ion Pouch Cells under Dynamic Conditions

Authors: Mahmud TOKUR

Recieved: 2022-06-08 00:00:00

Accepted: 2022-07-08 00:00:00

Article Type: Research Article

Volume: 25
Issue: 5
Month: October
Year: 2022
Pages: 858-866

How to cite
Mahmud TOKUR; (2022), Electrochemical Performances of NMC811 Lithium-Ion Pouch Cells under Dynamic Conditions. Sakarya University Journal of Science, 25(5), 858-866, DOI: 10.16984/saufenbilder.1128132
Access link
http://www.saujs.sakarya.edu.tr/en/pub/issue/73051/1128132

Sakarya University Journal of Science 25(5), 858-866, 2022

Electrochemical Performances of NMC811 Lithium-Ion Pouch Cells under Dynamic Conditions

Mahmud TOKUR*[1]

Abstract

Lithium-ion batteries have a wide range of usage areas, from transportation to the defense industry, from daily usage to space applications. The widespread use of consumer electronics day by day also increases the need for this critical strategic technology, which allows us to live at almost every point of our lives without binding factors such as cables. But this technology also has many limitations, which dominate our lives so much that it needs to be overcome. Low cycle life due to poor electrochemical efficiency of electrode materials is one of these limitations. At the same time, energy density constraints are also an obstacle to many technological developments. Therefore, finding new materials with higher capacity and higher cycle life has become inevitable to meet the demands. Moreover, developing novel production techniques suitable for the materials used in the battery is also critical. Cylindrical cells are mostly used commercially in the market due to their easy and fast production technics and relatively safe components. However, the energy density and capacity limit of this architecture pushes the market to use alternative cell designs. There are different cell structures in the lithium-ion battery industry apart from cylindrical cells, such as button type, pouch type, and prismatic type. Among them, pouch cells have rising star geometry due to their unique properties and flexible production style. But many parameters still need to be overcome in pouch cells. In this study, the NMC811 cathode has been selected to investigate some critical parameters in lithium-ion pouch cells. The effects of dynamic conditions such as electrode film thickness, variable temperatures, and current rates on electrochemical performance were analyzed. Finally, a cycle life test was performed on the cell with optimum parameters.

Keywords: Energy storage, lithium-ion battery, pouch cell, NMC cathode

1. INTRODUCTION

The quality of life of living things is becoming poor due to unprecedented ecological degradation depending on many factors such as global warming and pollution. One of the most important reasons for this is the irresistible increase in the use of fossil fuels [1]. Therefore, it has become inevitable to find clean and renewable alternatives to these extremely attractive and harmful energy sources [2]. Over the last two decades, scientists have extensively researched

---

* Corresponding author: mtokur@sakarya.edu.tr
[1] Sakarya University,
ORCID: https://orcid.org/0000-0003-3612-5350

batteries as an alternative to fossil fuels. And at this point, the first quarter of this century has been the beginning of an important transition period [3]. In recent years, lithium-ion batteries have been widely used in portable, mobile, and stationary applications, and their designs are being broadened [4, 5]. With the acceleration of technological developments so fast, the demand for electrochemical energy storage systems grew day by day [6]. Increasing energy density, reducing cost, and improving the electrochemical performance of the existing battery technologies are some of the most important efforts to meet the energy needs of commercial electric vehicles [7, 8]. The energy density of the current lithium-ion batteries is changed between 100–265 Wh/kg depending on the cell chemistry, cell type, and cell shape, which are all factors that were chosen for the specific application areas. This performance is still significantly less than that of gasoline. While cell chemistry is responsible for the efficiency of electrochemical reactions, the structure of the cell determines the weight and usage area. Thus, improving both cell chemistry and design is critical to increasing the energy densities of lithium-ion batteries. The elements mentioned above also significantly affect the cost of the cell. The energy sector is trying to reduce the battery costs from $200/kWh to $125/kWh and then $100/kWh, respectively. However, the unfortunate developments, such as the pandemic and Ukraine war between 2020 and 2022, that affect the world negatively, have brought along the increase in raw material prices and production costs, and logistics problems. Therefore, in the shadow of these unexpected developments, battery prices do not look to appear to decrease for a long time. In addition, the unpredictable rapid growth of the electric vehicle industry, and the consequent high demand for batteries, made supply difficult and intensified competition in the market. For all these reasons, it has become a necessity to better understand the current battery technology and to approach the aspects that need improvement more modestly.

In this study, parametric research on the electrochemical performance of commercially available NMC811 cathode in pouch cells has been carried out to understand the key parameters to building better energy storage systems. The most important reason for choosing this pouch type system among geometries such as cylindrical and prismatic is the attractive passion for high energy density. Because pouch cells are lighter than cylindrical and prismatic cells. It is also more likely and possible that they will be adapted to next generation battery operations. This is the first study to compare the electrode thickness, working temperature, and current rates of non-commercial pouch cell prototypes under real conditions. It is believed that this study, which simulates our daily life, will make positive contributions to the literature and the mobility industry.

2. EXPERIMENTAL STUDIES

This study consists of a detailed examination of four main parameters in pouch cells.

(i) Comparison of electrochemical results of the electrodes in different thicknesses in pouch cells, (ii) Investigation of electrochemical performance of pouch cells at different temperatures, (iii) Investigation of the electrochemical performance of the pouch cells at different current rates, (iv) Investigation of electrochemical cycling performance of pouch cells.

A battery consists of some active materials such as an anode, a cathode, and an ion conducting electrolyte. In this paper, the electrolyte is used commercially available 1M lithium hexafluorophosphate ($LiPF_6$) in ethylene carbonate, diethyl carbonate, and dimethyl carbonate (EC:DEC:DMC) (1:1:1) mixed solution. The anode and cathode electrodes were prepared by the conventional mixing methods using commercial NMC811 and Artificial Graphite (AG) powders.

For the anode preparation process, 94% active material (artificial graphite), 4% binder (Carboxymethylcellulose sodium (Na-

CMC)), and 2% conductive carbon (carbon black (Super-P)) composition was used. To prepare the homogeneous slurry, the CMC binder was first dissolved in deionized water with 4 wt. % concentration in a vacuum mixer and then a selected amount of powders were dry mixed mechanically. Finally, the mixed powders were added into the binder solution and mixed for an additional 2 hours. The obtained slurry was then cast onto 9 μm thick copper foil and coated using a doctor blade (tape casting method). The coating process was applied to both sides of the copper foil. After leaving it for 10 min. in an ambient atmosphere, the drying process was carried out in a tape casting device at 70 °C for 10 h to remove the remaining solvent.

The cathode preparation method is also similar to the anode preparation method. The main difference between the two electrodes is the used materials. For the cathode preparation process, 90% active material (NMC811), 4% binder (Poly(vinylidene fluoride) (PVDF)) and 6% conductive carbon (carbon black (Super-P)) composition was used. To prepare the homogeneous slurry, the PVDF binder was first dissolved in n-methyl-2-pyrrolidone (NMP) with 4 wt. % concentration in a vacuum mixer and then selected amount of powders were dry mixed mechanically. Finally, the mixed powders were added into the binder solution and mixed for an additional 2 hours. The obtained slurry was then cast onto 15 μm thick aluminum foil and coated using a doctor blade (tape casting method). The coating process was applied to both sides of the aluminum foil. After leaving it for 1 h in an ambient atmosphere, the drying process was carried out in a tape casting device at 120 °C for 10 h to remove the remaining solvent. In order to see the differences in electrochemical performances of the cells depending on the cathode thickness, the electrodes were coated as 50 μm, 100 μm, 150 μm, and 200 μm.

The pouch cells were manufactured with the electrodes prepared in the same conditions. The stages of the pouch cell manufacturing process after the electrode preparation step are (i) calendaring to electrodes to decreasing of the porosity, (ii) die cutting of the calendared electrodes in 4,5x5,5 cm dimensions, (iii) vacuum drying of the electrodes to completely remove the remained solvents and humidity, (iv) stacking of the electrodes to separate the anodes and cathodes with an electronic isolator and ion conductive separator (polypropylene (PP)) to prevent physical contact between the anodes and cathodes. They were stacked repetitively in a cycle of anode-separator-cathode-separator-anode with a semi-automatic stacking tool, (v) tab welding using an ultrasonic welding process. Before packaging the pouch cells, copper and aluminum current collectors were contacted with nickel and aluminum cell tabs, (vi) case forming of aluminum laminated film to put stacked electrodes in it, (vii) sealing of the three sides of the aluminum laminated film and electrolyte filling in an argon filled glove box, (vii) vacuum sealing of the electrolyte filled cell to make formation test, (ix) preconditioning and degassing of the cell to teach them the specific electrochemical characteristic. After vacuum sealing, the pouch cells were charged and discharged according to defined current and voltages. Defined charge-discharge potentials are between 2.8V - 4.2V and the current densities are C/20, C/10, and C/5 respectively. The solid electrolyte interface (SEI) layers and gas evaluations form during the first charging and discharging process. The pouch cells were put again in the glove box. The gas was removed from the pouch cells, (x) final sealing, and (xi) aging. For the aging process, the pouch cells were stored at room temperature for up to 3 days before utilizing the battery performance. Digital images of the prepared pouch cells are given in Figure 1. Galvanostatic charging and discharging processes were performed for the parametric electrochemical tests under different conditions of assembled pouch cells.

Figure 1 Digital images of pouch cells

3. RESULTS AND DISCUSSIONS

Undoubtedly, electrode thickness is a very important parameter in determining the amount of active material per unit area. While this parameter directly affects the capacity of the cell, it also indirectly affects the energy density. In other words, as the amount of inactive materials used in the cell increases, the energy density of the cell decreases [9]. Depending on this information, the cathode active materials were cast on both surface areas of the aluminum foil with 50 µm, 100 µm, 150 µm, and 200 µm thicknesses to compare the electrochemical performances by mass loading in approximately 500 mAh capacity pouch cells. These cells were subjected to electrochemical tests under the same conditions and examined from different perspectives.

The electrodes are cast on foils of four different thicknesses. The parameters were analyzed for the cathode (NMC811) parts. The anodes in all the pouch cells used exactly the same conditions. However, the anode side should also be studied, and determined the optimum anode/cathode ratio to get maximum electrochemical efficiency. All the pouch cells are compared in almost equal capacities, that is, approximately 500 mAh. Naturally, some pouch cells had to have more or fewer electrodes. For example, when high-thickness electrodes are used in the cell, the amount of material per unit area increases, and the desired values can be achieved with fewer electrodes. Since this will reduce the amount of inactive materials (current collectors and separators) used, the weight of the cell will decrease and its energy density will increase [10]. Therefore, it is very important to determine the critical coating thickness, especially in applications where weight is very important (such as the aerospace industry).

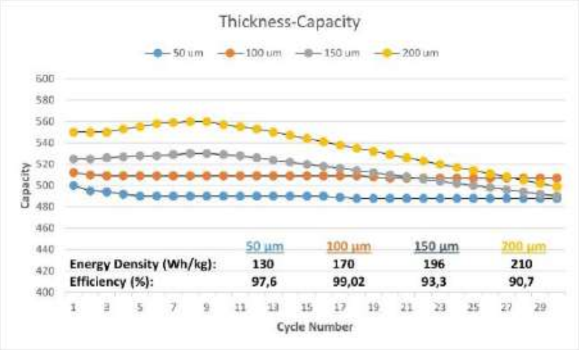

Figure 2 Electrochemical performances of the pouch cells assembled with the electrodes in different thickness

Charge-discharge tests of the pouch cells are performed at C/10 current rate and the capacity efficiencies and energy densities are compared. As shown in Figure 2, the cells were subjected to the charge-discharge test for 30 cycles. The 50 µm electrode exhibited a very stable behavior and showed an efficiency of 97.6%. However, besides this efficiency, the energy density is quite low at 130 Wh/kg. The cell assembled with the 100 µm electrode also showed good stability. At the end of 30 cycles, the cell showed a stable performance of close to 100%, which means almost no capacity loss. The energy density value is at a promising level with 170 Wh/kg. The electrochemical stability of the cell with a thickness of 150 µm electrode decreased when compared to the others. However, the energy density is higher. The 200 µm electrode was performed at the lowest efficiency with approximately 90% stability. However, due to the high coating thickness, the energy density is at the highest level. In fact, the energy densities of the cells were calculated according to their initial capacities.

In other words, the energy density calculation that has been carried out according to the first cycle can be misleading. Therefore, it is even more important to calculate and compare the energy densities of the cells at the end of 30 cycles. In other words, the energy densities of all pouch cells were calculated by multiplying their initial discharge capacity by their nominal voltage, dividing by the total weight of the cell, and compared with the calculated values using the discharge capacities after the 30th cycle. The calculated energy densities of the cells at the end of the 30 cycles are 126.88 Wh/kg, 168.334 Wh/kg, 182.868 Wh/kg, and 190.47 Wh/kg, respectively. According to these calculated values, the electrochemical performance of the cells seems to increase as the coating thickness increases. However, as can be seen from the electrochemical results curves, the gradual decrease in the capacity of the 150 µm and 200 µm electrodes means that it can turn into a disadvantage at high cycle numbers. Therefore, in this study, the optimum coating thickness was found as 100 µm and subsequent analyzes were carried out accordingly. Important note that the key parameter for increasing the energy density of a cell is increasing the ratio of capacity to volume or weight. For this, either a higher capacity should be obtained from a cell of the same volume or weight, or the volume or weight of the cell with the same capacity should be reduced. When it comes to volume and weight, in addition to active materials, the importance of inactive materials that do not contribute to the capacity emerges. Because each component used changes these values. Therefore, in addition to the correct choice of active materials in determining the energy density, the inactive separator, current collector, assembling geometry of the cell, and packaging materials also play an important role.

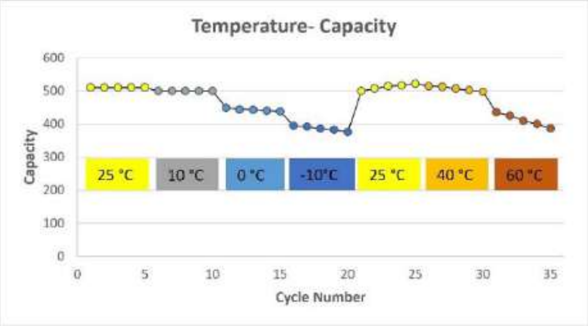

Figure 3 Electrochemical performance of pouch cells at different temperatures

The dynamic conditions mentioned above are also studied in this section. The electrochemical performance differences of the pouch cells in variable seasonal conditions were determined by air-conditioning tests. The electrochemical performances of the pouch cells assembled for this aim were performed at -10 °C, 0 °C, 10 °C, 25 °C, 40 °C, and 60 °C temperatures, assuming room temperature as 25 °C. In fact, the biggest improvements that should be realized in this parameter are on the electrolyte side. Because the main factor affecting the temperature-dependent performance of a cell is the stability of the electrolyte [11]. Nonetheless, the climate tests of the pouch cells are still an important step to see the electrochemical character of the batteries at selected temperatures even if used the same aqueous electrolyte. Because most electronic devices have standard aqueous lithium-ion batteries, they are used in dynamic weather conditions. Figure 3 shows the electrochemical performance results of the pouch cell versus the dynamically changing temperature parameter. The cell assembled with a capacity of approximately 500 mAh/g was subjected to the charge-discharge test at room temperature at a current rate of C/10. Testing intervals vary between -10 and 40 °C depending on the temperature values that are likely to be encountered around the world. However, in some cases, the temperature of the cells may rise abnormally due to the sudden increase in the current rate. Therefore, an additional 60 °C temperature value was added to the electrochemical tests. As expected, when temperatures begin to decrease or increase from standard conditions, variations in the cell's capacity can be seen. However, depending on the obtained results, it managed to preserve approximately 75% of the cell capacity even under the most adverse conditions, which is a very promising result for safety. However, polymer gel electrolytes or solid electrolytes that can remain more stable at variable temperatures can be developed in order to minimize capacity losses [12].

Another parameter affected by electrolytes is the current density. As it is known, since electronic devices are multifunctional, the power needed from the system changes with the activation of each function. Human beings lead a very dynamic life, which is more attractive and sustainable rather than staying in fixed environments. Similarly, battery-powered electronics are also mostly used dynamically. Therefore, the current rate of the cells plays a very important factor to keep the energy stable in need. For example, when a mobile phone is in standby mode, the current need is minimal, and the battery produces low energy. However, when more than one function is used together in this phone, much more current requirements will occur, and the battery must produce a high amount of energy. Even this situation causes the phone to overheat from time to time as a result of producing high energy by the battery. This issue prevents the standard performance of the battery life and can pull the lifeline down [13]. In order to determine the performance behavior of the cells used in such dynamic conditions, electrochemical tests were analyzed at different current densities in this study. The tests were carried out in variability starting from C/10 current rates and then performed at C/5, C/2, C, 2C, and 5C, respectively. The C value corresponds to the capacity value consumed in 1 hour. In other words, the 1C value in a 1 Ah cell is the 1A current rate. Eventually, the cell will be charged and discharged within 1 hour.

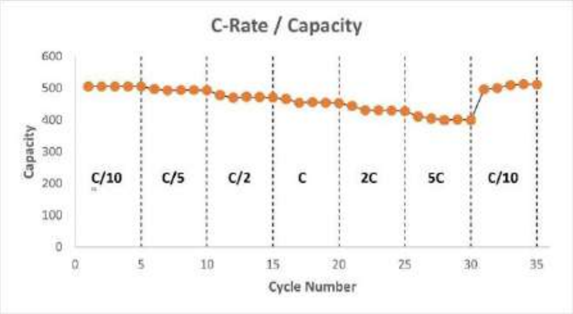

Figure 4 Rate capability of the pouch cell

It is very important to know how the cell behaves at different current densities. Because, depending on the desired features, it would be possible to increase or decrease the capacity that arises. For example, when a 10Ah battery is used for a drone that requires a 10A current, it is a possibility that the drone will stay in the air for approximately 1 hour. However, the activation of the wind during use, frequent maneuvering, or the use of extra features such as a camera will increase the amount of current needed. This time, higher current densities will need to get from the battery. Considering such conditions, current density tests are important in order to estimate how long the battery can be used in different conditions. The electrochemical performance values of a cell cycled at different current densities can be seen in Figure 4.

A cell prepared with a capacity of approximately 500 mAh was subjected to the charge-discharge test at C/10 current rate. For five cycles, the cell showed a stable capacity of 500 mAh. Afterward, the current rate was doubled to C/5 and the test was continued for five more cycles. Despite the doubling of the current rate, there was no significant decrease in the cell's capacity. Subsequently, in the cell, which was subjected to five cycles of charge-discharge tests at C/2, C, 2C, and 5C current rate, respectively, decreases in capacity were observed with the increase in the current rate, as expected naturally, but this decrease is not such a serious degree. In other words, the cell was able to protect 80% of its capacity even at the maximum current rate (5C). Afterward, by reducing the current rate to C/10 again, the capacity of the cell reached back to about 500 mAh as it was at the beginning.

There is a direct relationship between current density and ionic conductivity in a cell. The higher ionic conductivity in the electrochemical cell leads to able to have a higher current density in the cell. Liquid electrolytes have relatively low ionic conductivity when compared to gel or solid electrolytes. In addition, liquid electrolytes may face some risks such as decomposition and fired in the cases of temperature increases at high current densities. Therefore, polymer or solid electrolytes are generally suggested to use when a high current density is desired. Although polymer electrolytes have been used commercially, the applications of solid electrolytes have not been widely encountered yet. Moreover, the discharge capacity of the cell drops at the higher C-rate. With more passivation of the electrode surfaces at high C-rates the resistance of the cell increases which leads to reaching the discharge cut-off voltage limit earlier, and because of that, the available discharge capacity is lower.

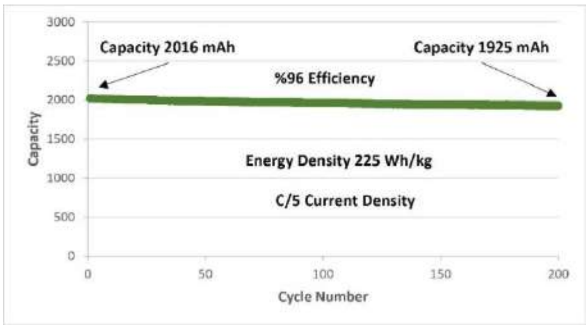

Figure 5 Cycle performance of a pouch cell at C/5 current density for 200 cycles

Considering the parameters optimized so far, 100 μm electrodes were prepared and a pouch cell of approximately 2000 mAh was assembled for a life cycle test. In order to see the capacity loss depending on the number of cycles, charge-discharge tests were carried out at an ambient temperature of 25 °C at a current density of C/5, that is, 400 mA, for 200 cycles. The electrochemical performance values of the cell can be seen in Figure 5. The initial capacity of the pouch cell was determined as 2016 mAh. In addition, the energy density of the pouch cell based on the initial capacity was calculated as 225 Wh/kg, which is quite promising for state of the art lithium ion batteries. A serious decrease in the cell's capacity was not observed depending on the number of cycles. Finally, the cell showed an efficiency of 96% after 200 cycles and was able to maintain its 1925 mAh capacity.

4. CONCLUSIONS

The electrochemical performance of pouch-type cells, which is widely used today and is a suitable geometry for next-generation batteries, was investigated parametrically in this study. The NMC811 cathode, which is described as the most efficient in terms of capacity and energy density, was chosen as a variable parameter in the cell. The analyzes performed were reflected in the study according to the variability of daily life. Indeed, a systematic guide has arisen from intracellular factors, such as comparing the electrodes of different thicknesses, to extracellular factors, such as using the cells at different current rates and different temperatures. It is believed that this study will contribute to the battery optimization of current and future electric vehicle technologies.

Acknowledgments
The author thanks the TUBITAK TEYDEB-BIGG-1512 program for their financial support under contract number 2190317.

The Declaration of Conflict of Interest/ Common Interest
The author has declared no conflict of interest or common interest.

Authors' Contribution
The author contributed fully to the study.

The Declaration of Ethics Committee Approval
This study does not require ethics committee permission or any special permission.

The Declaration of Research and Publication Ethics

The author of the paper declare that he comply with the scientific, ethical and quotation rules of SAUJS in all processes of the paper and that he does not make any falsification on the data collected. In addition, he declares that Sakarya University Journal of Science and its editorial board have no responsibility for any ethical violations that may be encountered, and that this study has not been evaluated in any academic publication environment other than Sakarya University Journal of Science.

REFERENCES

[1] M. S. Patil, J. H. Seo, S. Panchal, M. Y. Lee, “Numerical study on sensitivity analysis of factors influencing liquid cooling with double cold-plate for lithium-ion pouch cell,” International Journal of Energy Research, vol. 45, no. 2, pp. 2533-2559, 2021.

[2] E. Schuster, Z. Carlos, M. Andreas, R. Magnus, J. S. Hans, "Thermal behavior and electrochemical heat generation in a commercial 40 Ah lithium ion pouch cell," Journal of Power Sources, vol. 286, pp. 580-589, 2015.

[3] M. Tokur, A. Aydin, T. Cetinkaya, H. Akbulut, “Shoring up the lithium ion batteries with multi-component silicon yolk-shell anodes for grid-scale storage systems: experimental and computational mechanical studies,” Journal of The Electrochemical Society, vol. 164, no. 9, pp. A2238-A2251, 2017.

[4] Y. Chen, Y. Hu, Z. Shen, R. Chen, X. He, X. Zhang, Y. Li, K. Wu, “Hollow core–shell structured silicon@ carbon nanoparticles embed in carbon nanofibers as binder-free anodes for lithium-ion batteries,” Journal of Power Sources, vol. 342, pp. 467-475, 2017.

[5] T. Çetinkaya, "Synthesis, characterization and electrochemical performance of core/shell structured carbon coated silicon powders for lithium ion battery negative electrodes," Sakarya University Journal of Science, vol. 21, no. 3 pp. 489-495, 2017.

[6] F. Hall, J. Touzri, S. Wußler, H. Buqa, W.G. Bessler, “Experimental investigation of the thermal and cycling behavior of a lithium titanate-based lithium-ion pouch cell,” Journal of Energy Storage, vol. 17, pp. 109-117, 2018.

[7] J. Deng, C. Bae, A. Denlinger, T. Miller, “Electric vehicles batteries: requirements and challenges,” Joule, vol. 4, no. 3, pp. 511-515, 2020.

[8] H. Köse, "Production and morphological characterization of tin dioxide nano thin films," Sakarya University Journal of Science, vol. 21, no. 6 pp. 1613-1619, 2017.

[9] M. Tokur, M.Y. Jin, B.W. Sheldon, H. Akbulut, “Stress bearing mechanism of reduced graphene oxide in silicon-based composite anodes for lithium ion batteries,” ACS Applied Materials & Interfaces, vol. 12, no. 30, pp. 33855-33869, 2020.

[10] H. Zheng, J. Li, X. Song, G. Liu, V.S. Battaglia, “A comprehensive understanding of electrode thickness effects on the electrochemical performances of Li-ion battery cathodes,” Electrochimica Acta, vol. 71, pp. 258-265, 2012.

[11] J. Landesfeind, H.A. Gasteiger, “Temperature and concentration dependence of the ionic transport properties of lithium-ion battery electrolytes,” Journal of The Electrochemical Society, vol. 166, no. 14, pp. A3079, 2019.

[12] R. He, T. Kyu, “Effect of plasticization on ionic conductivity enhancement in relation to glass transition temperature

of crosslinked polymer electrolyte membranes,” Macromolecules, vol. 49, no. 15, pp. 5637-5648, 2016.

[13] V. G. Choudhari, A.S. Dhoble, T.M. Sathe, “A review on effect of heat generation and various thermal management systems for lithium ion battery used for electric vehicle,” Journal of Energy Storage, vol. 32, pp.101729, 2020.

SAKARYA ÜNİVERSİTESİ
FEN BİLİMLERİ ENSTİTÜSÜ
DERGİSİ

Sakarya University Journal of Science
SAUJS

ISSN 1301-4048 | e-ISSN 2147-835X | Period Bimonthly | Founded: 1997 | Publisher Sakarya University |
http://www.saujs.sakarya.edu.tr/

Title: A Case Study on the Relationship between Water Quality Parameters: Bursa

Authors: Ergun GUMUS

Recieved: 2022-03-05 00:00:00

Accepted: 2022-07-22 00:00:00

Article Type: Research Article

Volume: 25
Issue: 5
Month: October
Year: 2022
Pages: 867-878

How to cite
Ergun GUMUS; (2022), A Case Study on the Relationship between Water Quality Parameters: Bursa. Sakarya University Journal of Science, 25(5), 867-878, DOI: 10.16984/saufenbilder.1083427
Access link
http://www.saujs.sakarya.edu.tr/en/pub/issue/73051/1083427

Sakarya University Journal of Science 25(5), 867-878, 2022

A Case Study on the Relationship between Water Quality Parameters: Bursa

Ergun GUMUS*[1]

Abstract

Monitoring the quality of mains water in residential areas where industrialization is intense is of vital importance in terms of human health. For this purpose, quality parameters expressing the physical, chemical and biological properties of water are periodically observed through laboratory tests. During the evaluation of water quality, these parameters can be assessed individually or as a group by considering their interrelations. In this context, by using water quality reports of Bursa province which is an industrial city, answers to two questions were sought. The first of these questions is, getting evaluated on a group basis, which groups of water quality parameters are found to be highly correlated. The second question is whether the correlation between these interrelated parameter groups can be maintained in different measurement periods. For these purposes, analyzes were made using an approach which utilizes canonical correlation analysis, exhaustive scanning, and sliding window methods. As a result of these analyzes, it was observed that used approach gave successful results in terms of determining interrelated parameter groups and the differences in terms of interrelations between the measurement periods over these groups.

Keywords: Water quality parameters, canonical correlation analysis, exhaustive search, sliding window

1. INTRODUCTION

Water is the basic building block and indispensable element of all living organisms, from the smallest one to the largest. In terms of mass, 73% of our brain and heart, 79% of our skeletal muscles and kidneys, and 83% of our lungs are composed of water [1]. Water plays an important role in balancing our body temperature, digesting and transporting nutrients, excretion, working of our joints, protecting our brain and spinal cord against impacts, and many more. When all these aspects are taken into account, it becomes clear that human beings' access to water is of vital importance.

Water is essential not only for biological life, but also for agriculture, textile and industrial production. Water used in production is polluted with various chemicals and unfortunately is

---

* Corresponding author: ergun.gumus@btu.edu.tr
[1] Bursa Technical University,
ORCID: https://orcid.org/0000-0002-1327-6845

sometimes left back to the water cycle without being filtered. This situation especially affects drinking water quality of people living in cities that are intertwined with industry. For this reason, local governments frequently test the quality of the mains water in terms of physical, chemical and biological aspects. In these tests, (i) physical properties of water such as color, smell, taste, turbidity, (ii) chemical properties such as hardness, electrical conductivity, dissolved gases and elements in it, (iii) biological properties such as presence/number of viral pathogens and other microorganisms are examined. If the parameter values are within the standard ranges, the water source is considered to be suitable for use/drinking.

To date, many academic studies have been conducted on water quality parameters. In general, these studies focus on three main topics: Analysis of the relationship between quality parameters [2- 5], Depending on the analyzed relationship, estimation of a certain quality parameter [6- 9], and Estimation of total water quality using quality parameters [10- 14].

Among the studies on analysis of relationships between quality parameters, Noori et al. [2] examined physical and chemical parameters obtained from the Karoon River using Canonical Correlation Analysis. As a result of the research, it was reported that parameters of electrical conductivity, total dissolved solids, total amount of ions and water hardness have a high weight in explaining the canonical diversity. In a similar study [3], measurements taken from Macau main storage reservoir for ten years were used. Principal Component Analysis, a dimension reduction tool, was applied on two different groups of physical and chemical parameters. The canonical relations between remaining parameters were examined and it was seen that electrical conductivity from the physical parameters group and amount of chloride from the chemical parameters group had the highest canonical weight in their own group. In another study, Parmar et al. [4] divided water quality measurements into sub-levels using Discrete Wavelet Transform method instead of using them directly like in current studies. They obtained measurement-signal vectors of these levels. Afterwards, they showed that the chemical oxygen demand parameter was highly correlated with other three chemical parameters. On the other hand, Sallam et al. [5], established regression models for estimation of parameters such as pH, dissolved oxygen, electrical conductivity, and total dissolved solids using air temperature, relative humidity, and quantitative/qualitative properties of the water released into the water source. They stated that there is a strong correlation between these parameters.

This study focused on the relationship between water quality parameters. In this context, six-years-long water quality measurements of Bursa province were used and two separate subjects were examined. First subject is to identify two subgroups of quality parameters that provide a high canonical correlation. For this purpose, Exhaustive Search (ES) method was used. The second subject of the study is to determine whether there is a significant correlation between two different measurement periods or not. At this point, a sliding window approach along with Canonical Correlation Analysis (CCA) was applied on the data which is in form of time series.

Rest of the study is organized as follows: In the second part, the dataset and approaches used are introduced. In the third part, experimental results are given. The fourth and final part is devoted to conclusions.

2. MATERIAL AND METHODS

2.1. The Dataset

In the study, quality of drinking water reports published weekly by Bursa Water and Sewerage Administration were used (www.buski.gov.tr/SuAnalizRaporu/Detay/). There are 257 measurement reports in total for the period between June 15th, 2014 and May 6th, 2020 (70 months). Distribution of these reports by months and years can be seen in Table 1.

Table 1 Number of measurements on the basis of Months&Years

	Month												
Year	**1**	**2**	**3**	**4**	**5**	**6**	**7**	**8**	**9**	**10**	**11**	**12**	**Total**
2014						1	1	1	1	1	2	1	8
2015	1	1	1	1	1	1	5	4	4	4	4	5	32
2016	2	4	5	4	2	5	3	5	3	4	5	4	46
2017	4	3	5	4	5	4	4	4	4	4	5	4	50
2018	5	4	4	4	5	4	4	4	4	5	4	4	51
2019	5	4	4	4	5	3	5	4	4	5	4	4	51
2020	5	4	4	5	1								19

In the aforementioned reports, there are a total of 54 parameters regarding the physical, chemical and biological properties of drinking water. For some of these parameters, data before a specific date is not available. At the same time, for some parameters, number ranges are used instead of exact values. There are also parameters that have the same value for each measurement or that can be neglected because their standard deviation is very low. For these reasons, 18 parameters which are shown in Table 2 were selected to be used in the study.

Table 2 Water quality parameters used in the study

Par#	**Name of the parameter**	**[Min - Max]**	**Mean**	**Standard Deviation**
1	pH	[7.36 – 8.41]	7.889	0.260
2	Blurriness	[0.02 – 0.91]	0.264	0.131
3	Total Hardness	[137.8 – 250.9]	177.463	26.331
4	Total Iron	[0 - 64]	21.659	10.490
5	Manganese	[1 - 30]	12.284	4.147
6	Chloride	[3.8 – 20.37]	8.662	2.666
7	Sulfate	[7 - 51]	19.548	11.283
8	Nitrate	[0 – 5.3]	0.991	0.702
9	Conductivity	[277 - 432]	356.813	36.961
10	Permanganate Index	[0.12 – 4.06]	0.996	0.406
11	Sodium	[3.94 – 13.255]	7.787	1.880
12	Aluminum	[0 - 163]	32.458	29.314
13	Fluoride	[0 – 0.17]	0.065	0.021
14	Free Chlorine	[0.42 – 0.78]	0.648	0.062
15	Arsenic	[0.017 – 5.914]	2.637	1.271
16	Copper	[0 – 6.57]	0.710	0.725
17	Nickel	[0.25 – 9.22]	3.201	1.256
18	Trihalomethane (THM)	[0.42 - 64]	30.117	8.981

There is a missing data problem for some of the selected parameters. To overcome this problem, the "window average" approach was used, and each missing data area was filled with the average of the other data in its 14 neighborhood. In the last step, all parameters were normalized to the range [0,1] since they take values from different number ranges.

Measurement reports were fetched from website of Bursa Water and Sewerage Administration using Python library “Beautiful Soup”. All analyzes were carried on PC platform using MATLAB.

2.2. Canonical Correlation Analysis

Canonical Correlation Analysis (CCA) method is a statistical analysis tool which is used to find canonical projection vectors that transfer samples of two different observation sets (views) belonging to the same entity to ideal data spaces in order to maximize their correlation (Pearson's correlation) between [15]. The method is used in many research areas like feature selection in classification processes [16, 17], biomedical applications [18- 20], bioinformatics [21, 22], and so on.

CCA can be briefly stated as follows:

Suppose that we have two zero-mean views $S_X = [x_1, x_2, \ldots, x_N]$, and $S_Y = [y_1, y_2, \ldots, y_N]$ in *D*-dimensional space for *N* samples. We can project these samples into a one-dimensional space using two basis vectors w_X and w_Y, and write the correlation coefficient *r* between these projections as seen in Eq. 1.

$$r = \frac{w_X{}^T S_X S_Y{}^T w_Y}{\sqrt{(w_X{}^T S_X S_X{}^T w_X)(w_Y{}^T S_Y S_Y{}^T w_Y)}} = \frac{w_X{}^T C_{XY} w_Y}{\sqrt{(w_X{}^T C_{XX} w_X)(w_Y{}^T C_{YY} w_Y)}} \tag{1}$$

Here, C_{XX} and C_{YY} are within-class covariance matrices and $C_{XY} = C_{YX}{}^T$ are between-class covariance matrices. Our goal is to find the ideal canonical projection vectors w_X and w_Y that will maximize coefficient *r*. For this, we can create the optimization problem seen in Eq. 2 by specifying a set of constraints and using the Lagrangian relaxation method.

$$L(\lambda, w_X, w_Y) = w_X{}^T C_{XY} w_Y - \frac{\lambda}{2}(w_X{}^T C_{XX} w_X - 1) - \frac{\lambda}{2}(w_Y{}^T C_{YY} w_Y - 1) \tag{2}$$

By solving our optimization problem, the equality seen in Eq. 3 and the eigenproblem seen in Eq. 4 are obtained. The coefficient λ is the Lagrange multiplier from our optimization problem and is also the square root of the eigenvalue of our eigenproblem.

$$w_Y = \frac{C_{YY}{}^{-1} C_{YX} w_X}{\lambda} \tag{3}$$

$$C_{XX}{}^{-1} C_{XY} C_{YY}{}^{-1} C_{YX} w_X = \lambda^2 w_X \tag{4}$$

With the solution of our eigenproblem, the canonical projection vector w_X (eigenvector) and the coefficient λ (eigenvalue) are obtained. By substituting both of them in Eq. 3, the canonical projection vector w_Y is obtained.

2.3. Exhaustive Search

In the first stage of the study, it was aimed to find subgroups of water quality parameters that have a significant relationship. Some of previous studies [2, 3] used CCA method to examine the relationship between physical and chemical quality parameters for this purpose. Unlike their work, instead of using views of two logical classes, relationships between mixed subsets (views) of all parameters given in Table 2 were examined in this study. In literature, there are iterative [23] and adaptive [24] techniques for composing CCA views. However, since the number of parameters subject to the study is appropriate, Exhaustive Search (ES) approach, in which all possible subsets of parameters are used, was applied. The algorithm regarding to application of the approach together with CCA can be seen in Figure 1.

Like many machine learning methods, CCA can be affected by the way training and test sets are formed, and it can be under the influence of bias effect. For this reason, the algorithm was run using 5×2 cross validation, and 10 different test scenarios were obtained.

```
$N \leftarrow$ number of samples
$D \leftarrow$ number of parameters
$Par \leftarrow \{1, 2, \ldots, D\}$
$Data \leftarrow N \times D$ dimensional data matrix
$train \leftarrow$ indices of training samples
$test \leftarrow$ indices of test samples

for $i \leftarrow 1$ to $2^D - 1$ do
    $f \leftarrow i^{th}$ subset of $Par$                                  / Except null set
    if number_of_elements($f$) > 1 then
        $half \leftarrow \lfloor$ number_of_elements($f$) / 2$\rfloor$
        for $k \leftarrow 1$ to $half$ do
            $x \leftarrow$ a $k$-element combination of $f$
            $y \leftarrow f - x$
            $train\_view1 \leftarrow Data(train, x)$
            $train\_view2 \leftarrow Data(train, y)$
            $test\_view1 \leftarrow Data(test, x)$
            $test\_view2 \leftarrow Data(test, y)$
            $[w_x, w_y] \leftarrow$ CCA($train\_view1, train\_view2$)                / CCA training
            $r \leftarrow$ pearson_correlation( $test\_view1 \times w_x^T$ , $test\_view2 \times w_y^T$ )  / CCA test
        end for
    end if
end for
```

Figure 1 Implementation of CCA using ES

2.4. Sliding Window Approach

Another subject of study is to find out whether there is a significant correlation between water quality parameters in different measurement periods when measurements are ordered from oldest to newest according to their dates. For this purpose, the sliding window approach seen in Figure 2 was used. Accordingly, two observation periods (Period1 and Period2), which contain equal number of observations (W) but do not overlap with each other were created. Then, canonical projection vectors which maximize CCA training correlation of two views in Period1 were calculated. Lastly, using same canonical projection vectors, samples in both views of Period2 were projected to a new data space and test correlation of projected views, which resolves a possible relationship between two observation periods, was obtained. In each iteration of the approach, one of the observation periods (Period1) remained constant while the other (Period2) was shifted by one sample forward. In case where Period2 could not be shifted any further, the approach was repeated from the beginning by shifting Period1 one sample further. Whole process is maintained until the case where two periods overlap.

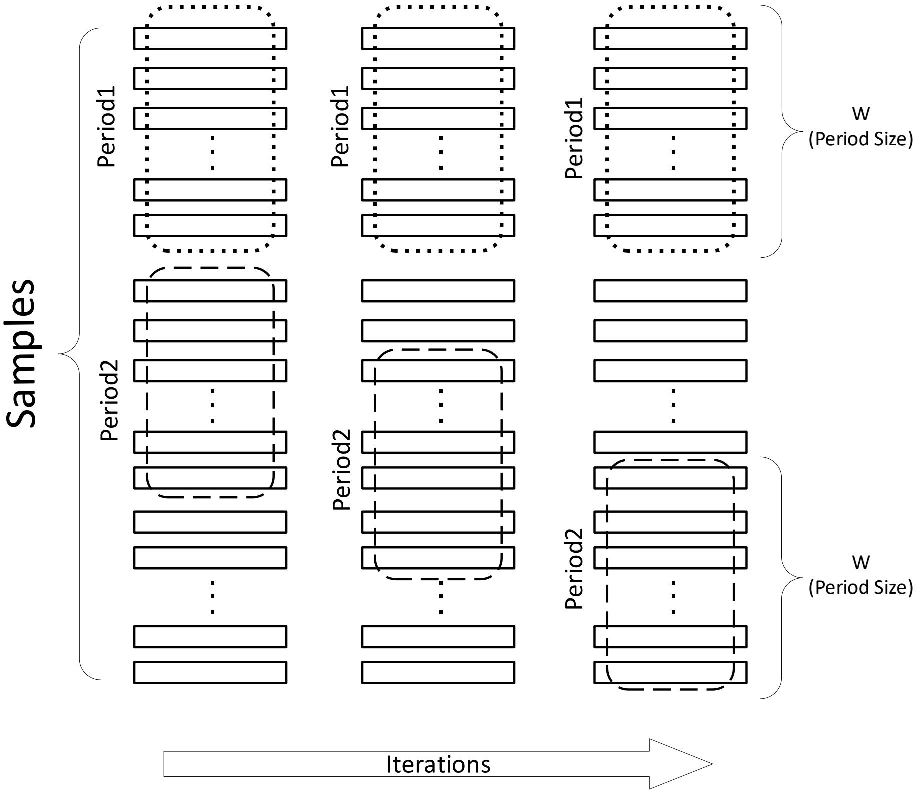

Figure 2 Sliding window approach for detecting periodic relationships

3. RESULTS

3.1. Group-Based Relationships among Water Quality Parameters

In order to find an answer to the question of whether there is a significant relationship between water quality parameters on a group basis, the algorithm mentioned in Figure 1 was applied to whole dataset, with a 5×2 cross-validation approach. In this way, 10 different test scenarios were created, each containing $2^{18} - 19$ test correlations. The 5-number summary obtained after eliminating extreme values for each of these scenarios is shown in Table 3.

Table 3 5-number summary of test scenarios

Test #	Minimum	Lower Quartile	Median	Upper Quartile	Maximum
1	0.3938	0.6966	0.8064	0.8985	0.9510
2	0.3056	0.6520	0.7935	0.8829	0.9282
3	0.3987	0.6982	0.8386	0.8978	0.9592
4	0.3081	0.6543	0.7815	0.8852	0.9340
5	0.4205	0.7041	0.7991	0.8931	0.9409
6	0.3202	0.6596	0.7969	0.8859	0.9540
7	0.3419	0.6678	0.8037	0.8852	0.9322
8	0.3549	0.6791	0.7849	0.8952	0.9557
9	0.3644	0.6720	0.8145	0.8772	0.9404
10	0.3114	0.6637	0.8024	0.8985	0.9424

When Table 3 is examined, it is seen that there is not a big difference between upper quartile values of the test scenarios. The same is also true for maximum values. At this point, top 100 test correlations for each scenario and corresponding water quality parameter groups (View1 parameters and View2 parameters) were detected. Afterwards, among these 100×10 cases, the most common parameter group in View1 was scanned. As a condition for this scan, selection of parameter groups in View1 which took place in at least half of cases was taken as a basis. Result of this scan is given in Table 4.

Table 4 Most frequently encountered parameter groups in selected test scenarios (View1)

Parameter Group	Observation Rate (%)
{Total Hardness, Chloride}	86.2
{Total Hardness, Chloride, Permanganate Index}	70.4
{Total Hardness, Chloride, Arsenic}	55.6

For View1, it was observed that high test correlations had been obtained by using three parameter groups formed by quality parameters #3 (Total Hardness), #6 (Chloride), #10 (Permanganate Index), and #15 (Arsenic).

Most frequently observed parameter group for View1 is the group consisting of “Total Hardness” and “Chloride” pair. This group took place in a total of 862 cases. Among all cases, most frequently observed parameter groups for View2 were scanned with a similar approach, where selection of parameter groups in View2 which took place in at least half of cases was taken as a basis. Result of this scan is given in Table 5.

Table 5 Most frequently encountered parameter groups in selected test scenarios (View2)

Parameter Group	Observation Rate (%)
{Conductivity, Sodium}	100
{Nitrate, Conductivity, Sodium}	96.9
{Nitrate, Conductivity, Sodium, Fluoride}	77.8
{Sulphate, Nitrate, Conductivity, Sodium}	77.3
{Nitrate, Conductivity, Sodium, THM}	62

For View2, it was observed that high test correlations had been obtained by using five parameter groups formed by quality parameters #7 (Sulphate), #8 (Nitrate), #9 (Conductivity), #11 (Sodium), #13 (Fluoride), and #18 (THM). “Conductivity” and “Sodium” parameters were encountered in all of these five groups.

After application of cross-validation approach, CCA test correlations ranging from 0.9021 to 0.9434 were obtained between View1 created with “Total Hardness” and “Chloride” parameters and View2 created with “Conductivity” and “Sodium” parameters.

Considering average test correlations obtained from 10 test scenarios which were formed by 5×2 cross-validation approach, the highest average test correlation was 0.9402. This value was obtained by using {Blurriness, Total Hardness, Chloride, Permanganate Index} parameters for View1, and {Manganese, Nitrate, Conductivity, Sodium, Fluoride, THM} parameters for View2.

3.2. Relationship between Observation Periods

For the secondary purpose of the study, observations, which were ordered from oldest to newest according to measurement dates, were converted into periods covering 12 months. After that, couples of periods were analyzed using the sliding window approach mentioned in Section 2.4 in order to check for existence of a similarity/difference between them. In this context, as seen in Table 1, observations covering 6 years were divided into consecutive 12-months-long periods with a one-month progress, and a total of 61 periods were obtained. While forming these periods, if there were more than one observation belonging to some specific month, only one of these observations was randomly selected. Since this selection is a stochastic process, each pair of non-overlapping periods (Period1 and Period2) whose relationship will be questioned were created 1000 times and averages of training and test correlations were used in analysis. While calculating both training and test correlations, {Blurriness, Total Hardness, Chloride, Permanganate Index} parameters for View1 and {Manganese, Nitrate, Conductivity, Sodium, Fluoride, THM} parameters for View2 were used in each period. The reason for this choice is that the highest possible test correlation was obtained with the relationship between these parameter groups.

In trials using the sliding window approach, first 49 of 61 periods were used to calculate i) training correlations between views of these periods, and ii) canonical projection vectors that maximize these correlations. Out of 1000 trials, training (Period1) correlations obtained using these periods are shown in Figure 3 together with outliers in box graphic form.

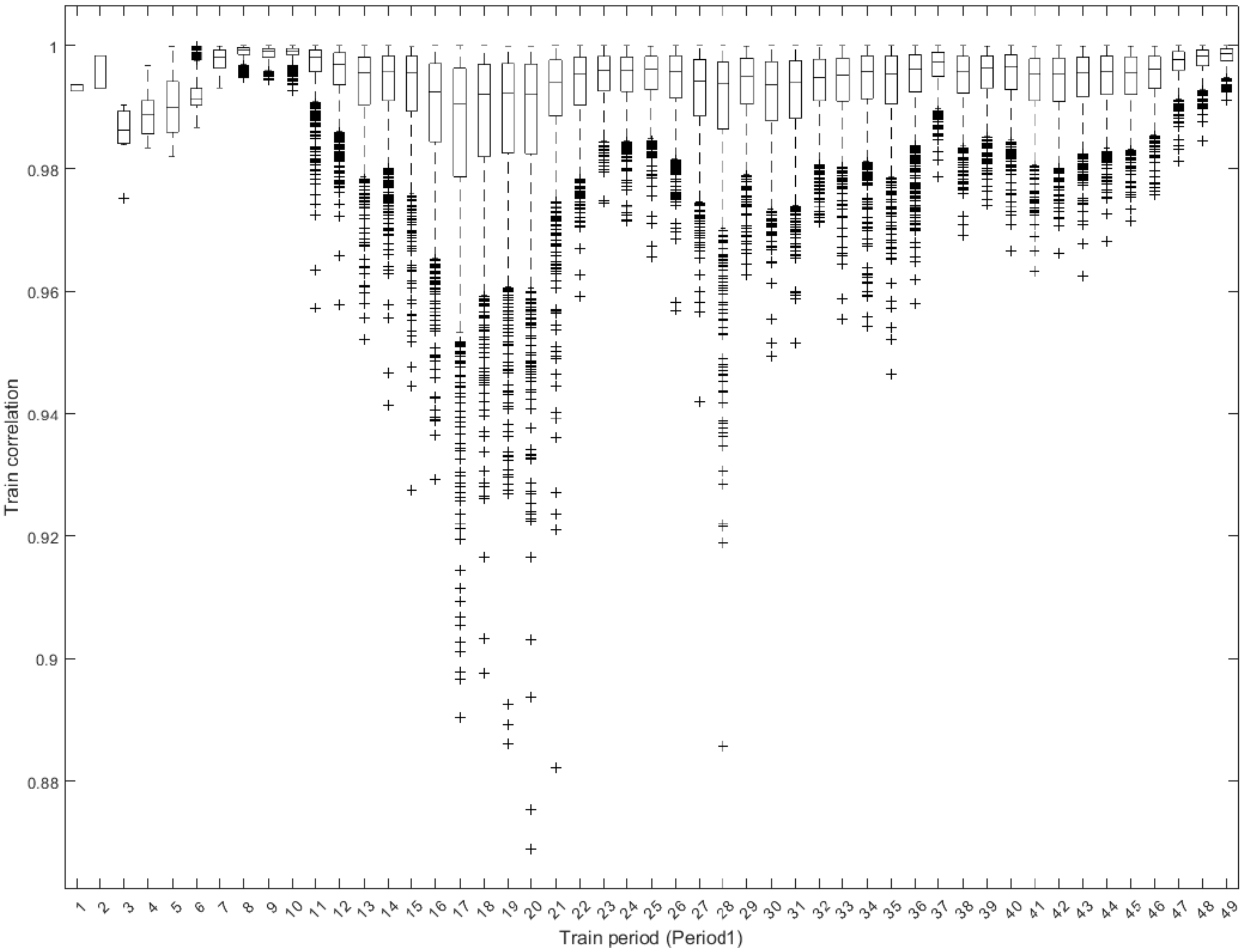

Figure 3 Training correlations obtained during various train periods

When Figure 3 is examined, it is seen that high training correlations ranging from 0.87 to 0.99 can be obtained in each of the different train periods, as would be expected from CCA approach. It is also seen that correlation values obtained at the end of multiple trials per period do not show much variation for train periods including initial months with few observations. Lowest outliers (+ symbol) in training correlation are seen in train periods #17, #18, #19, #20, #21, and #28 (5 consecutive 12-months-long periods covering October 2015 – January 2017 interval, and a single 12-months-long period covering September 2016 – August 2017 interval).

In accordance with the sliding window approach seen in Figure 2, test correlation between views of Period2 (test period) were obtained by applying canonical projection vectors which maximize the training correlation between views of Period1 (train period). Accordingly, *i*. period was accepted as Period1 and each of the following periods in the interval [i + 12, 61] was considered as Period2 one by one. In this way, the relationship of each Period1 with each subsequent Period2 was evaluated through the test correlation obtained. The boxplot created using test correlations obtained over 1000 trials is shown in Figure 4.

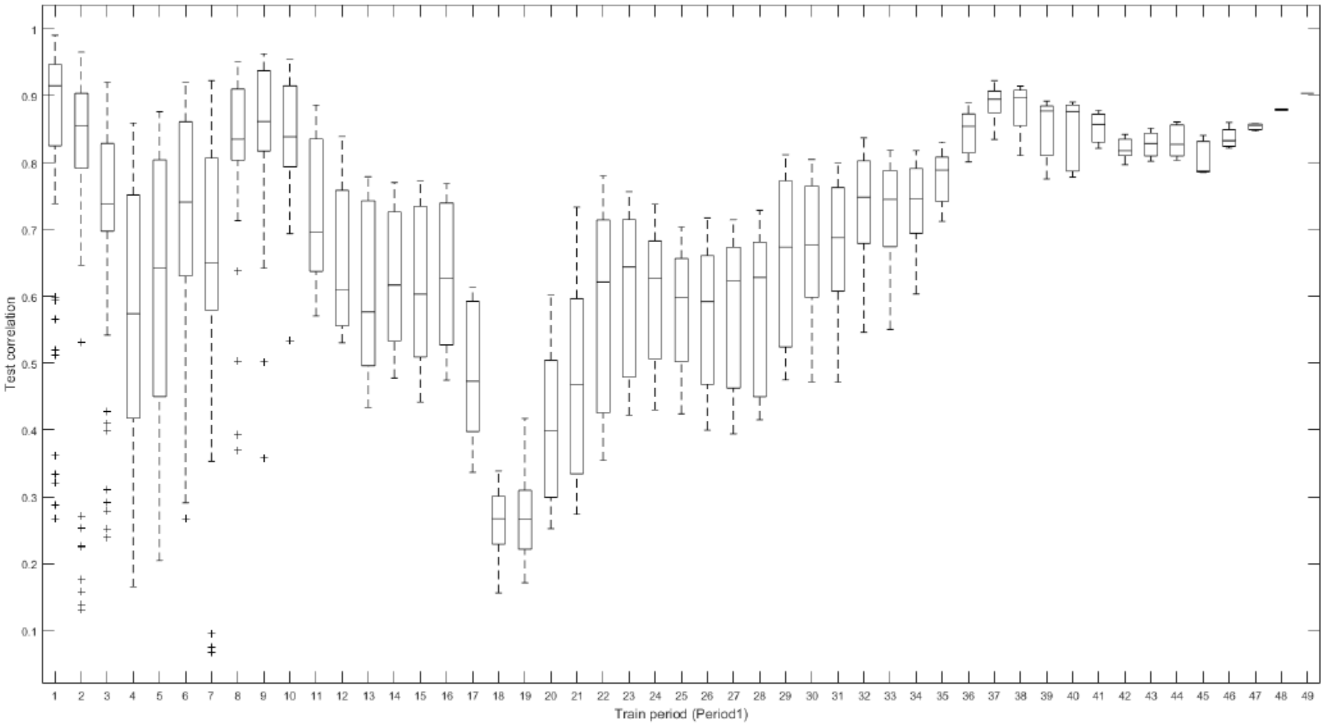

Figure 4 Test correlations obtained by applying canonical vectors of training period (Period1) to views of test period (Period2)

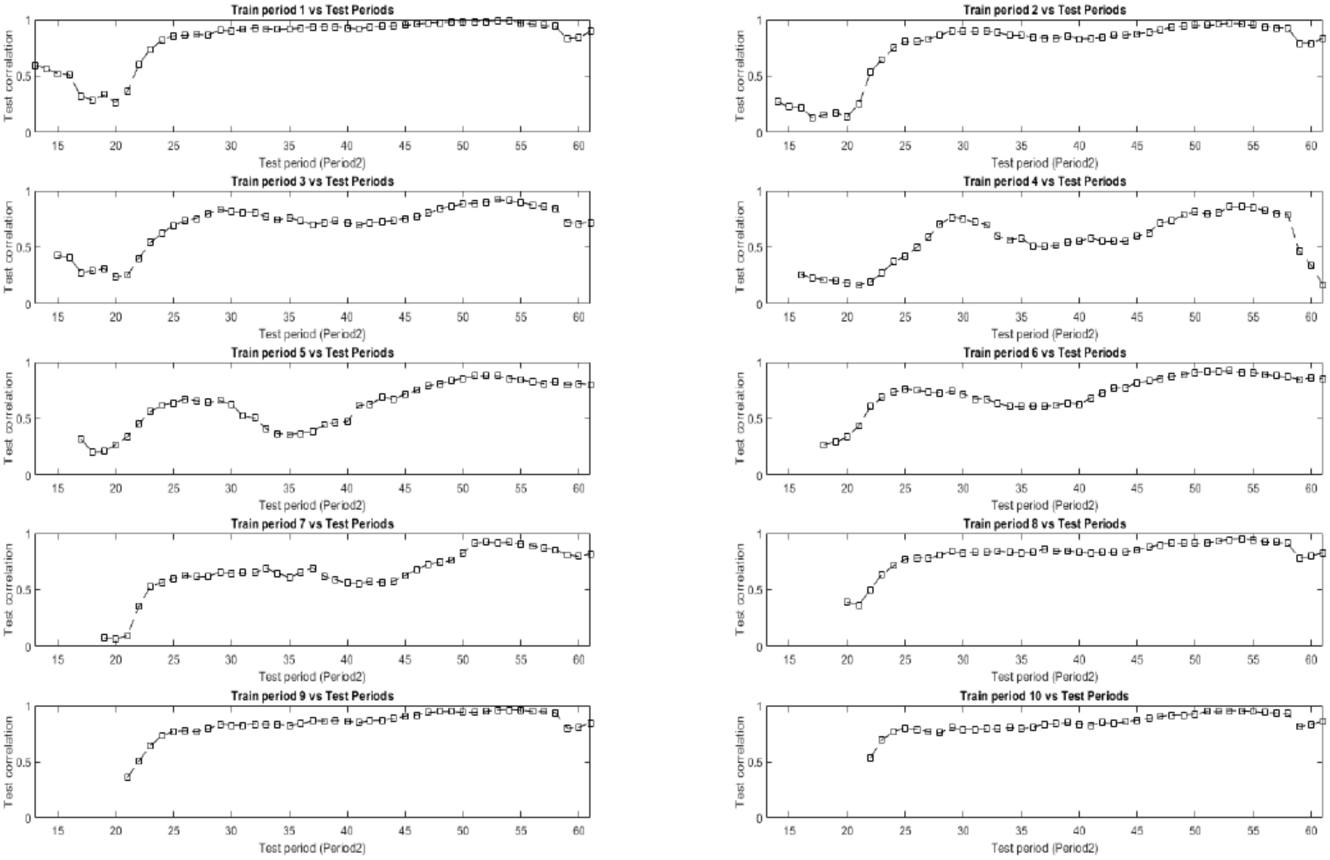

Figure 5 Variation of mean test correlations obtained using first 10 training periods

As can be seen in Figure 4, median values of test correlations obtained by applying canonical vectors of training period (Period1) to views of test period (Period2) remained low (at the level of 0.2665) especially for 18th and 19th training periods (two consecutive periods of 12 months each, covering the range of November 2015 - November 2016). For 18th training period, mean and standard deviation of test correlations were as low as 0.2603 and 0.0507, respectively. Similarly, for 19th training period, mean and standard deviation of test correlations were as low as 0.2722 and 0.0666, respectively. Median training correlations obtained for these two periods were similar, about 0.99. Other than this, test correlations which can be defined as outliers (+ symbols) were observed using first 10 training periods. Variation of mean test correlations for these periods is shown in Figure 5.

Examining Figure 5, it is clear that mean test correlation values remain low until 20th test period. Only after that, a rise is possible. One might suspect that, the reason is lack of diversity in observations for leading periods (check number of measurements for leading months in Table 1). However, although observation diversity is low for first 10 periods, it is seen that canonical vectors obtained in training phases of these periods provide high mean test correlations after 20th test period. Moreover, checking Table 1, we can see that lack of diversity in observations comes to an end after 13th period.

4. CONCLUSIONS

In this study, a case analysis was conducted i) to determine the relationship between water quality parameter groups, and ii) to determine whether there exists a periodic relationship between measurements taken at different times or not. In this context, exhaustive search and sliding window approaches are employed along with canonical correlation analysis. When the relationship of quality parameters on a group basis is evaluated, it is seen that the relation between the group consisting of {Blurriness, Total Hardness, Chloride, Permanganate Index} parameters and the group consisting of {Manganese, Nitrate, Conductivity, Sodium, Fluoride, THM} parameters is maximized using the sets of observations in accordance with 5×2 cross-validation. In addition, by using detected groups of quality parameters, the relationship between distinct 12-months-long periods was also questioned. As a result of this inquiry, it was seen that the relationship established between these two parameter groups was valid in most of the observation periods covering 70 months. However, especially for the periods covering November 2015 - November 2016 interval, low-level test correlations such as 0.2603 and 0.2722 were observed, which means the relationship established between detected parameter groups in this interval does not hold in other observation periods. This gives us an idea about benefit of applied methodology in order to detect seasonal variability of the relationship between water quality parameters.

Acknowledgments
The author would like to thank reviewers and editors for their valuable time.

Funding
The author has not received any financial support for the research, authorship or publication of this study.

The Declaration of Conflict of Interest/ Common Interest
No conflict of interest or common interest has been declared by the author.

Authors' Contribution
The author contributed 100% to the study.

The Declaration of Ethics Committee Approval
This study does not require ethics committee permission or any special permission.

The Declaration of Research and Publication Ethics
The author of the paper declare that he complies with the scientific, ethical and quotation rules of SAUJS in all processes of the paper and that he

does not make any falsification on the data collected. In addition, he declares that Sakarya University Journal of Science and its editorial board have no responsibility for any ethical violations that may be encountered, and that this study has not been evaluated in any academic publication environment other than Sakarya University Journal of Science.

REFERENCES

[1] H. H. Mitchell, T. S. Hamilton, F. R. Steggerda, H. W. Bean, “The chemical composition of the adult human body and its bearing on the biochemistry of growth,” in The Journal of Biological Chemistry, 158, pp. 625-637, 1945.

[2] R. Noori, M. S. Sabahi, A. R. Karbassi, A. Baghvand, H. Taati Zadeh, “Multivariate statistical analysis of surface water quality based on correlations and variations in the data set,” in Desalination, 260, pp. 129-136, 2010.

[3] M. C. Chan, I. Lou, W. K. Ung, K. M. Mok, “Integrating principle component analysis and canonical correlation analysis for monitoring water quality in storage reservoir,” in Applied Mechanics and Materials, 284-287, pp. 1458-1462, 2013.

[4] K. S. Parmar, R. Bhardwaj, “Wavelet and statistical analysis of river water quality parameters,” in Applied Mathematics and Computation, 219, pp. 10172-10182, 2013.

[5] G. A. H. Sallam, E. A. Elsayed, “Estimating relations between temperature, relative humidity as independent variables and selected water quality parameters in Lake Manzala, Egypt,” in Ain Shams Engineering Journal, 9, pp. 1-14, 2018.

[6] E. Dogan, B. Sengorur, R. Koklu, “Modeling biological oxygen demand of the Melen River in Turkey using an artificial neural network technique,” in Journal of Environmental Management, 90, pp. 1229-1235, 2009.

[7] M. J. Alizadeh, M. R. Kavianpour, “Development of wavelet-ANN models to predict water quality parameters in Hilo Bay, Pacific Ocean,” in Marine Pollution Bulletin, 98, pp. 171-178, 2015.

[8] I. Seo, S. H. Yun, S. Y. Choi, “Forecasting water quality parameters by ANN model using preprocessing technique at the downstream of Cheongpyeong dam,” in Procedia Engineering, 154, pp. 1110-1115, 2016.

[9] S. Mazhar, A. Ditta, L. Bulgariu, I. Ahmad, M. Ahmed, A. A. Nadiri, “Sequential treatment of paper and pulp industrial wastewater: Prediction of water quality parameters by Mamdani fuzzy logic model and phytotoxicity assessment,” in Chemosphere, 227, pp. 256-268, 2019.

[10] G. A. Cordoba, L. Tuhovcak, M. Taus, “Using artificial neural network models to assess water quality in water distribution networks,” in Procedia Engineering, 70, pp. 399-408, 2014.

[11] A. D. Sutadian, N. Muttil, A. G. Yilmaz, B. J. C. Perera, “Using the analytic hierarchy process to identify parameter weights for developing a water quality index,” in Ecological Indicators, 75, pp. 220-233, 2017.

[12] G. Sotomayor, H. Hampel, R. F. Vazquez, “Water quality assessment with emphasis in parameter optimisation using pattern recognition methods and genetic algorithm,” in Water Research, 130, pp. 353-362, 2018.

[13] A. N. Ahmed, F. B. Othman, H. A. Afan, R. K. Ibrahim, C. M. Fai, M. S. Hossain, M. Ehteram, A. Elshafie, “Machine learning methods for better water quality prediction,” in Journal of Hydrology, 578, 124084, 2019.

[14] M. Tripathi, S .K. Singal, “Use of principal component analysis for parameter selection for development of a novel water quality index: A case study of river Ganga India,” in Ecological Indicators, 96, pp. 430-436, 2019.

[15] D. R. Hardoon, S. Szedmak, J. S. Taylor, “Canonical Correlation Analysis: An overview with application to learning methods,” in Neural Computation, 16(12), pp. 2639-2664, 2004.

[16] C. O. Sakar, O. Kursun, F. Gurgen, “A feature selection method based on kernel canonical correlation analysis and the minimum Redundancy-Maximum Relevance filter method,” in Expert Systems with Applications, 39(3), pp. 3432-3437, 2012.

[17] W. Yan, C. Shuang, Y. Hongnian, “Mutual information inspired feature selection using kernel canonical correlation analysis,” in Expert Systems with Applications: X, 4, 100014, 2019.

[18] D. Lin, V. D. Calhoun, Y. Wang, “Correspondence between fMRI and SNP data by group sparse canonical correlation analysis,” in Medical Image Analysis, 18(6), pp. 891-902, 2014.

[19] W. Xingjie, Z. Ling-Li, S. Hui, L. Ming, H. Yun-an, H. Dewen, “Blind source separation of functional MRI scans of the human brain based on canonical correlation analysis,” in Neurocomputing, 269, pp. 220-225, 2017.

[20] A. S. Janani, T. S. Grummett, T. W. Lewis, S. P. Fitzgibbon, E. M. Whitham, D. DelosAngeles, H. Bakhshayesh, J. O. Willoughby, K. J. Pope, “Improved artefact removal from EEG using Canonical Correlation Analysis and spectral slope,” in Journal of Neuroscience Methods, 298, pp. 1-15, 2018.

[21] M. G. Naylor, X. Lin, S. T. Weiss, B. A. Raby, C. Lange, “Using canonical correlation analysis to discover genetic regulatory variants,” in PLoS ONE, 5(5), e10395, 2010.

[22] Y. Zhang, J. Zhang, Z. Liu, Y. Liu, S. Tuo, “A network-based approach to identify disease-associated gene modules through integrating DNA methylation and gene expression,” in Biochemical and Biophysical Research Communications, 465(3), pp. 437-442, 2015.

[23] L. Liu, Q. Wang, E. Adeli, L. Zhang, H. Zhang, D. Shen, “Feature selection based on iterative canonical correlation analysis for automatic diagnosis of Parkinson’s disease,” in International Conference on Medical Image Computing and Computer-Assisted Intervention, 9901, pp. 1-8, 2016.

[24] W. Hu, D. Lin, S. Cao, J. Liu, J. Chen, V.D. Calhoun, Y. Wang, “Adaptive sparse multiple canonical correlation analysis with application to imaging (epi)genomics study of schizophrenia,” in IEEE Transactions on Biomedical Engineering, 65(2), pp. 390-399, 2019.

SAKARYA ÜNİVERSİTESİ

FEN BİLİMLERİ ENSTİTÜSÜ
DERGİSİ

Sakarya University Journal of Science
SAUJS

ISSN 1301-4048 | e-ISSN 2147-835X | Period Bimonthly | Founded: 1997 | Publisher Sakarya University |
http://www.saujs.sakarya.edu.tr/

Title: Spectroscopic Characterization and DFT Calculations on
1H-benzimidazole-2-carboxylic acid monohydrate Molecule

Authors: Emine BABUR ŞAŞ, Songül ÇİFÇİ, Mustafa KURT

Recieved: 2022-04-08 00:00:00

Accepted: 2022-08-09 00:00:00

Article Type: Research Article

Volume: 25
Issue: 5
Month: October
Year: 2022
Pages: 879-891

How to cite
Emine BABUR ŞAŞ, Songül ÇİFÇİ, Mustafa KURT; (2022), Spectroscopic
Characterization and DFT Calculations on 1H-benzimidazole-2-carboxylic acid
monohydrate Molecule. Sakarya University Journal of Science, 25(5), 879-891,
DOI: 10.16984/saufenbilder.1100391

Sakarya University Journal of Science 25(5), 879-891, 2022

Spectroscopic Characterization and DFT Calculations on 1H-benzimidazole-2-carboxylic acid monohydrate Molecule

Emine BABUR ŞAŞ*[1], Songül ÇİFÇİ[1], Mustafa KURT[1]

Abstract

After first determining the optimized geometry of the 1H-benzimidazole-2-carboxylic acid monohydrate (1HBCM) molecule using the B3LYP/6-311+ + G (d, p) basis set, we investigated the spectroscopic properties, electronic properties and optical band gap of the molecule. We presented the fitted values of the vibrational frequencies of the molecule both as a table and as a spectrum and compared them with the experimental data. While the band gap energy (ΔE) values of the molecule were calculated using HOMO and LUMO energies, the optical band gap (Eg) values of the molecule were obtained from the Tauc equation. We have given the Eg values of the molecule calculated for direct and indirect transmission by comparing them with the experimental data. In the article, we have also calculated and presented the data of the 1HBCM molecule such as MEP, Mulliken, and DOS.

Keywords: FT-Raman, FT–IR, optical band gap DFT, MEP.

1. INTRODUCTION

The biological activities of benzimidazole and benzimidazole derivatives, such as anticancer, antiviral, anthelmintic, antimalarial, anti-ulcer, antihistaminic, antioxidant, and antifungal, have been widely reported in the literature [1-3]. Benzimidazole derivatives are also widely used in industrial processes as corrosion inhibitors for metal and alloy surfaces. In this molecule, it is difficult to assign the vibrational modes that occur with respect to the different chemical bonds. Despite these problems, there are always attempts to assign vibrational modes of such molecules [4].

The fact that benzimidazole and its derivatives are used in many fields such as medicine, chemistry, and industry has attracted many researchers. In previous studies, benzimidazoles have also been used in organic semiconductor materials [5] and solar cells [6]. When electron acceptor and electron donor molecules come together, charge transfer complexes are formed [7]. The donor-receptor interactions are determined by the HOMO-LUMO energy difference of the

---

* Corresponding author: ebsas@ahievran.edu.tr

[1] Kırşehir Ahi Evran University

E-mail: sngl_cifci_cfc@hotmail.com, mkurt@ahievran.edu.tr

ORCID: https://orcid.org/0000-0002-9547-5951, https://orcid.org/0000-0003-3009-3490, https://orcid.org/0000-0001-6040-1189

molecules [8]. In this study, we investigated the electronic, spectroscopic, and optical properties of the 1HBCM molecule using the DFT method. In addition to the HOMO-LUMO energy difference, we used DOS spectra for the interactions between neighboring orbitals. Based on the properties of the semiconductor material, we have investigated the optical band gap values experimentally and theoretically using the Tauc equation [9-10].

2. EXPERIMENTAL

The FT-IR and dispersive Raman spectra of the molecule 1H-benzimidazole-2-carboxylic acid monohydrate (1HBCM) were recorded at room temperature using a Bruker IFS 66/S spectrometer in the range 400–4000 cm^{-1} and a 532 nm laser in the range 3200–100 cm^{-1} using Renishaw/Invia. Since the molecule is an organic molecule, the UV spectrum was recorded with Thermoscientific Evulation 60 s in the range of 200–600 nm in ethanol solution.

3. COMPUTATIONAL DETAILS

The molecular structure of 1HBCM was visualized by the DFT /B3LYP/6 311++G(d,p) method, where the optimized parameter values were determined and compared with X-ray data [11]. Vibrational spectra of the molecule were obtained by this method and the spectra were recorded and compared with experimental FT-IR and dispersive Raman spectra. The thermodynamic properties were studied by the same method and correlation plots were obtained. UV-Vis spectra, MEP, frontier molecular orbital energies were calculated in DMSO, ethanol and vacuum. Optical band gap values were determined using the experimental and theoretical UV spectra and presented with figures.

4. RESULT AND DISCUSSIONS

4.1. Molecular Structure

Having found the minimum energy level of the 1HBCM molecule, the shape and geometrical parameters of the molecule in this state are given in Figure 1 and Table 1. As shown in Table 1, these values were compared with X-ray data [11]. According to the X-ray data, the C1-C2 bond length, which was reported to be 1.393, was calculated to be 1.42 in the 1HBCM molecule and was found to be larger than the other C-C bond lengths. This bond length was calculated to be 1.41 in similar molecules [12, 13]. The C4-C5 bond length, calculated as 1.415, is the largest C-C bond length observed in the X-ray data [11].

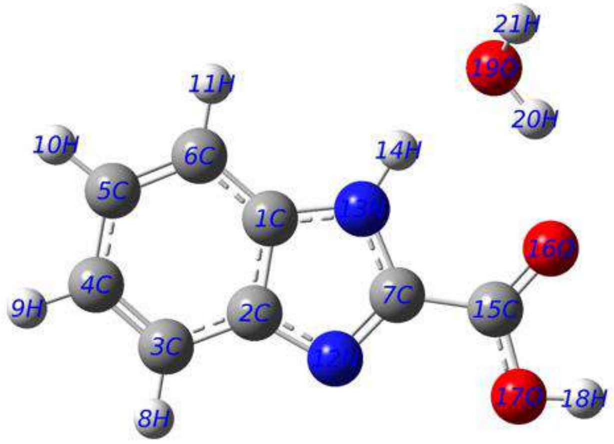

Figure 1 The geometric structure of the 1HBCM

The internal bond angles of the benzene ring in the title molecule are greater or less than the bond angle of a hexagon. For example, the C2-C1-C6 and C1-C6-C5 bond angles were calculated and recorded as 122.2^{o} and 116.3^{o} in 1HBCM and X-ray data, respectively [11]. This difference in bond angles may be due to the imidazole group. This is because the same bond angles are different compared to similar molecules. [12, 13]. The O19-H20 and O19-H21 bond lengths of 1HBCM were calculated to be 0.973 and 0.961 Å, respectively. This bond length was reported to be 0.85 Å in the X-ray data [11].

4.2. Vibrational spectral analysis

The 1HBCM molecule has C1 symmetry and 57 fundamental modes. The fundamental vibration bands of the molecule calculated using the method DFT were fitted with the scaling factors reported in the literature to match the experimental data. A value of 0.958 was used for large frequencies and 0.983 for frequencies below 1700 cm^{-1} [14].

Table 1 Geometrical parameters of 1HBCM and X-Ray data

Bond Lengths (Å)	X-ray	B3LYP/6-311++G(d,p)	Bond angles (°)	X-ray	B3LYP/6-311++G(d,p)
C1-C2	1.393	1.420	C2-C1-C6	122.2	122.2
C1-C6	1.397	1.400	C2-C1-N13	106.9	105.2
C1-N13	1.386	1.371	C6-C1-N13	130.8	132.6
C2-C3	1.393	1.404	C1-C2-C3	121.6	120.1
C2-N12	1.384	1.374	C1-C2-N12	106.0	110.1
C3-C4	1.379	1.383	C3-C2-N12	132.4	129.8
C3-H8	0.936	1.083	C2-C3-C4	116.5	117.8
C4-C5	1.424	1.415	C2-C3-H8	120.0	120.3
C4-H9	1.087	1.084	C4-C3-H8	123.0	121.9
C5-C6	1.367	1.386	C3-C4-C5	121.5	121.5
C5-H10	1.069	1.084	C3-C4-H9	120.0	119.7
C6-H11	0.966	1.083	C5-C4-H9	117.0	118.9
C7-N12	1.335	1.317	C4-C5-C6	121.9	121.9
C7-N13	1.341	1.377	C4-C5-H10	113.0	118.9
C7-C15	1.501	1.472	C6-C5-H10	124.0	119.2
N13-H14	0.900	1.023	C1-C6-C5	116.3	116.6
H14-O19	-	1.873	C1-C6-H11	120.0	121.8
C15-O16	1.254	1.221	C5-C6-H11	124.0	121.5
C15-O17	1.247	1.337	N12-C7-N13	108.9	113.6
O16-H20	-	1.931	N12-C7-C15	125.9	125.9
O17-H18	-	0.969	N13-C7-C15	125.1	120.6
O19-H20	0.850	0.973	C2-N12-C7	109.5	104.7
O19-H21	0.850	0.961	C1-N13-C7	108.6	106.3
			C1-N13-H14	121.0	127.7
			C7-N13-H14	130.0	126.0
			N13-H14-O19	-	162.2
			C7-C15-O16	114.8	124.1
			C7-C15-O17	116.2	113.4
			O16-C15-O17	128.9	122.5
			C15-O16-H20	-	130.7
			C15-O17-H18	-	107.0
			H14-O19-H20	-	88.1
			H14-O19-H21	-	133.2
			H20-O19-H21	107.0	106.9
			O16-H20-O19	-	148.1

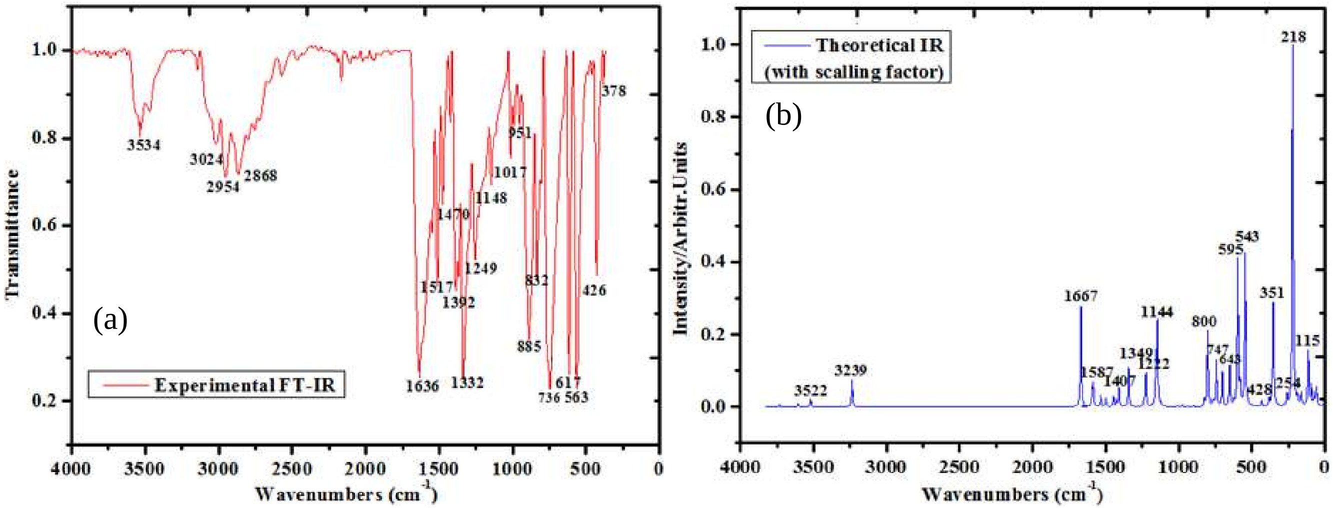

Figure 2 (a) The experimental and (b) the theoretical IR spectra of 1HBCM

The difference between the experimental and theoretical wavenumbers is that the experimental spectra were recorded in the solid phase and the theoretical spectra calculations were performed in the gas phase. The theoretical and experimental spectra are shown in Figure 2 and 3, the values are listed in Table 2.

In molecules an imidazole ring structure, the N-H stretching vibration is generally observed in the range 3500–3000 cm^{-1} [15].

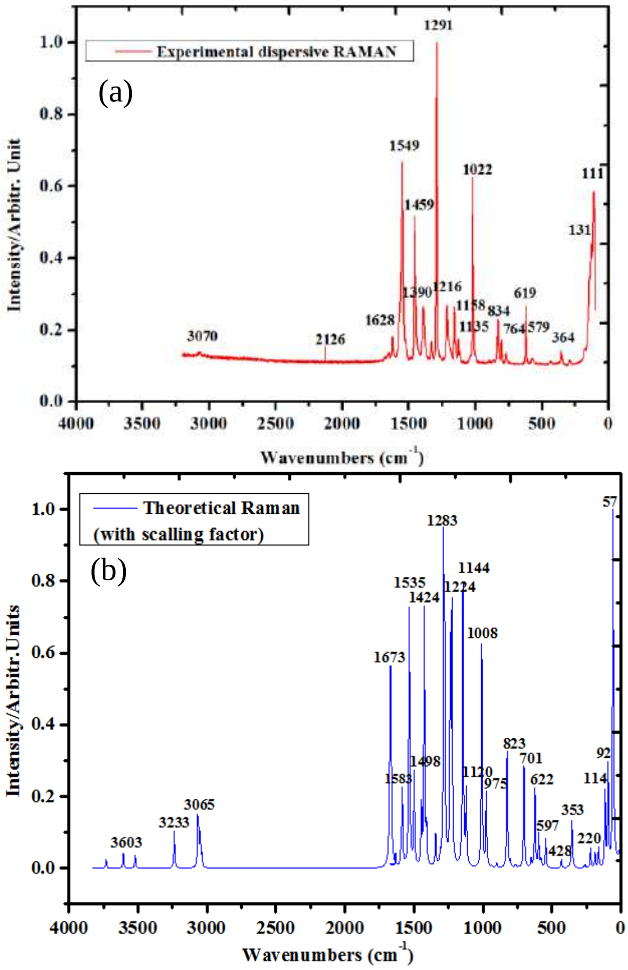

Figure 3 (a) The experimental and (b) the theoretical Raman spectra of 1HBCM

In some similar molecules (2Br1HB, 2-arylaminomethyl-1H-benzimidazole, 2-chloromethyl-1H-benzimidazole hydrochloride, and 2-(4-bromophenyl)-1H-benzimidazole), this vibration is measured above 3500 cm^{-1} at 3546, 3513, 3509, and 3502 cm^{-1}, respectively, and in the 5-benzimidazole carboxylic acid molecule it was measured as 3237 cm^{-1} [12, 16- 19]. This band was calculated as 3236 cm^{-1} in our study and proved to be a pure band according to TED.

In the 1HBCM molecule, C-H vibrations were calculated in the range 3065–3036 cm^{-1} and recorded in the experimental spectrum at the values 3070 cm^{-1} and 3024 cm^{-1}. In aromatic rings, C-H vibrations are observed in the range of 3100–3000 cm^{-1}, in-plane bending vibrations in the range of 1000–1300 cm^{-1} and out-of-plane bending vibrations in the range of 800–950 cm^{-1} [15,20- 22]. These vibrations in the study molecule were calculated in the desired range and presented in detail in Table 2. The correlation graph of the experimental and theoretical wavenumbers given in Table 2 is shown in Figure 4. According to the correlation graph, the R^2 value being 0.99 indicates that the experimental and theoretical data are in agreement.

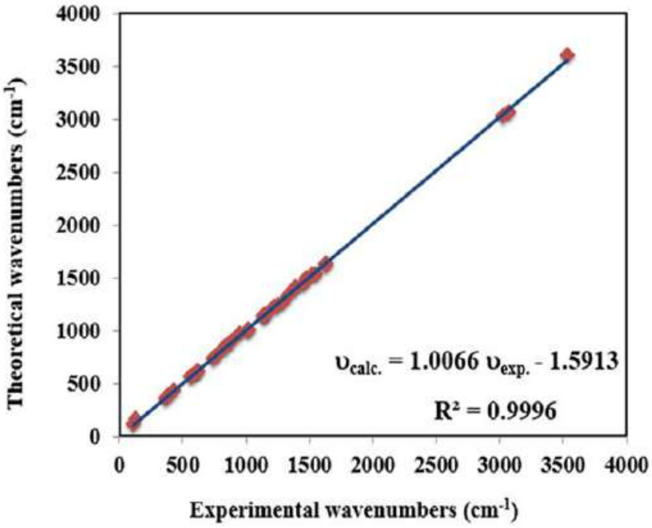

Figure 4 Correlation graphic of calculated and experimental (total) wavenumbers of 1HBCM

C-C, C-N, and C=N vibrations are generally observed to be intermixed. In the literature, these bands are reported to be found in the range of 1480–1650 cm^{-1}, 1338 cm^{-1}, and 1617 cm^{-1}, respectively [23- 25]. For the title molecule, the C-C vibrations were calculated to occur at 1633–1499, 1446–1343, 1281–1224, 1120–975 cm^{-1}, and the C-N and C=N vibrations at 1534–1446, 1408, 1308–1224, 975 cm^{-1}. The highest contribution was calculated as 55% for C-C vibrations at 1633 cm^{-1} and 45% for C-N and C=N vibrations at 1446 cm^{-1}. C-C vibrations were observed experimentally in dis-Raman and FT-IR in 1628, 1549, 1390, 1291, 1216, 1022 cm^{-1}, and 1636, 1517, 1470, 1392, 1332, 1249 1017 cm^{-1}, respectively. C-N and C=N stretching vibrations were also obtained in 1459, 1390, 1291, 1216 cm^{-1} in dis-Raman and 1517, 1470, 1392, 1249 cm^{-1} in FT-IR.

Table 2 The wavenumbers of 1H-Benzimidazole-2-Carboxylic Acid Monohydrate molecule.

	Theoretical wavenumber				Experimental wavenumber		Assignments TED[a] (≥10%)
No	Scaled	I_{IR}	S_{Ra}	I_{Ra}	IR	Raman	
4	114	10.1	1.4	12.19		111	υOH(13)+δNOH(58)+ δCNH(12)
5	161	3.5	0.5	2.67		131	δOH[δNOH(11)]+ υOH(83)
11	356	34.1	2.6	3.49		364	ɣOH[τCNOH(42)]+ ɣHOH(11)+υCC(13)
16	571	2.0	0.2	0.14	560		τCCCC(40)+τCCCN(16)+τCCCH(15)
17	579	21.8	0.9	0.57		579	δCCC(34)+ δCOO(11)
19	623	6.3	10.9	6.39	616	619	υCC(21)+δCCN(34)+ δCCC(21)
22	741	71.6	0.1	0.03	746		ɣCH[τCCCH(60)+ τCNCH(15)]
24	766	8.6	0.5	0.20		764	τCNCO(39)+τCOOH(19)+τNOHH(15)
26	824	13.9	24.1	9.42	829	834	υCC(55)+ υCN(12)
28	900	2.9	1.3	0.43	889		υCN(14)+δCCC(47)+ δCCH(17)
30	968	0.0	0.2	0.07	956		ɣCH[τCHCH(65)+τCCCH(18)]
32	1008	4.2	64.9	18.79	1011	1022	υCC(54)+δCCH(19)
34	1144	245.4	101.9	24.26	1149	1135	υCO(23)+δCCH(39)+ δCOH(13)
35	1156	145.6	4.3	1.01		1158	υCO(28)+δCCH(22)+ δCOH(15)
36	1224	111.5	102.1	21.84	-	1216	υCN(28)+ υCC(12)+ δCOH(18)
37	1236	20.4	87.0	18.29	1252		υCN(22)+ υCC(14)+ δCCH(29)
38	1281	2.1	246.0	48.87		1291	υCN(42)+ υCC(19)+ δCCH(18)
40	1343	149.9	15.8	2.90	1334		υCC(53)+ δCOH(15)
41	1408	79.2	18.6	3.15	1386	1390	υCO(10)+υCN(17)+ υCC(20)+ δCNH(12)
43	1446	44.9	33.8	5.47	1469	1459	υCN(45)+ δCCH(15)
45	1534	56.5	201.7	29.44	1547	1549	υCC(20)+ υCN(16)+ δCNH(19)
48	1633	1.2	10.0	1.30	1634	1628	υCC(55)
50	3036	1.5	51.8	1.63	3021		υCH(100)
53	3065	10.8	255.1	7.83		3070	υCH(99)
54	3236	726.3	210.5	5.48			υNH(101)
56	3606	139.8	136.3	2.49	3536		υOH(100)

[a] υ: stretching. δ: bending.δ:in plane bending.γ: out of plane bending.Γ: torsion

4.3. UV-Vis Analysis and Optical Band Gap

UV spectrum analysis of the 1HBCM molecule was performed in 2 different solvents (DMSO and ethanol) and in the gas phase. The spectrum obtained experimentally in ethanol is compared theoretically with the spectrum obtained in ethanol and these spectra are shown in Figure 5.

According to Fig. 5, the experimental values were observed at 314, 298, and 291 nm and the theoretical values observed as a shoulder of 1 peak were observed as two peaks at 312 and 293 nm. Although the theoretical absorption peak is calculated at 256 nm in the spectrum, the intensity of this transition is feeble. The theoretical and experimental absorption peak values are very close to each other. The wavelengths of the absorption bands determined experimentally and theoretically are given in Table 3 with the corresponding energies for this transition.

UV spectra are commonly used to investigate a molecule's optical band structure (direct and indirect band gap). Using the Tauc model, we investigated the optical band gap (Eg) of the 1HBCM molecule. Figures 6 show the optical band gaps of the molecule, both theoretically and experimentally. The slope of the graph was used to calculate the Eg values using the Tauc equation. The theoretical and experimental values for the direct optical band gap were 4.12 and 3.68 eV, respectively, as shown in Figure 6, while the indirect band gap was 4.09 and 3.57 eV. The values obtained experimentally show that the material has semiconductor.

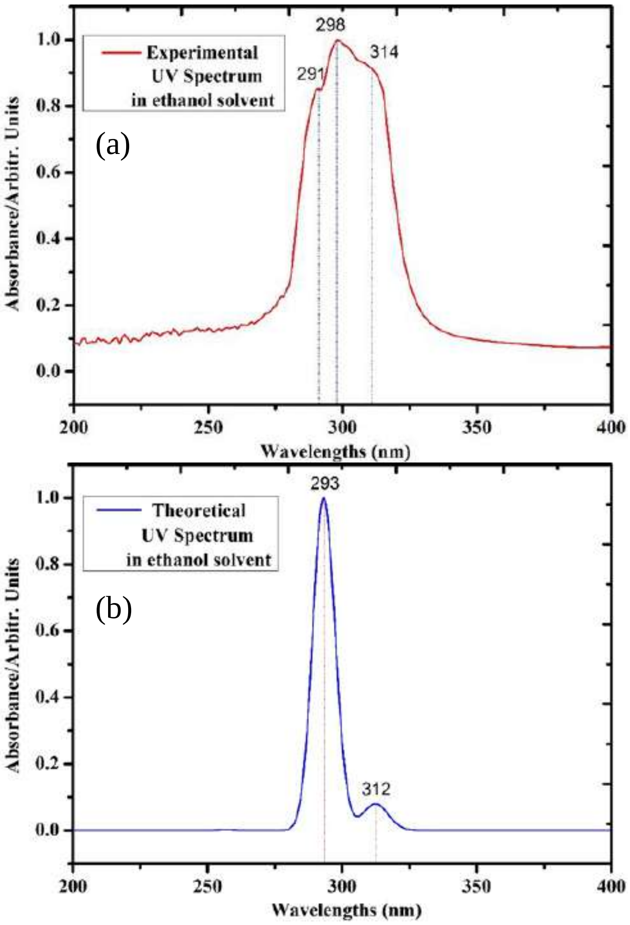

Figure 5 (a) The experimental and (b) the theoretical UV-Vis spectra of 1HBCM

4.4. Frontier Molecular Orbitals and Total, Partial and Population Density of States (DOS, PDOS and OPDOS)

The energy band gap in semiconductor materials is of great importance for electrical and optical studies [26]. The theoretical band gaps of 1HBCM are obtained by using the HOMO and LUMO energies. For electronic properties, the energy band was calculated using the TD-DFT method and determined which atoms are concentrated on it. The valence band (HOMO) was localized throughout the molecule except for the carboxylic acid and the monohydrate group, while the conductance band (LUMO) was localized throughout the molecule except for the monohydrate group.

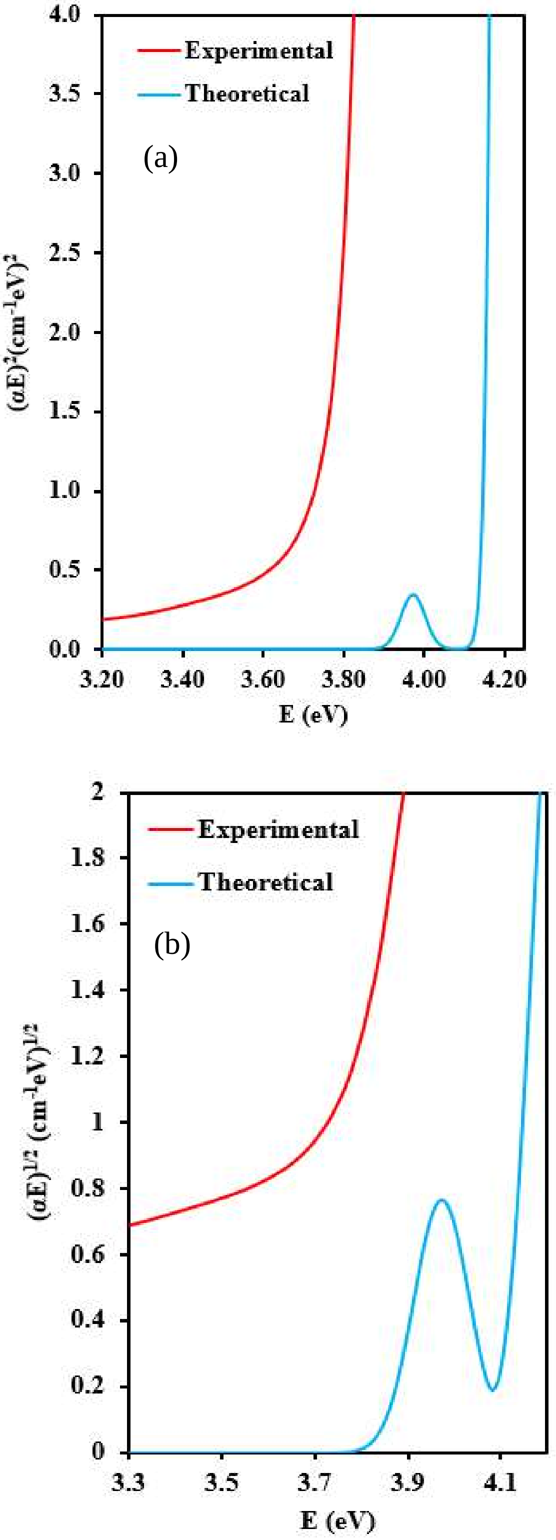

Figure 6 (a) Direct ($(\alpha E)^2(cm^{-1}eV)^2$ vs photon energy) and (b) indirect ($(\alpha E)^{1/2}(cm^{-1}eV)^{1/2}$ vs photon energy) band gap of 1HBCM

Table 3 Electronic values of the 1HBCM molecule.

DMSO			**Theoretical Gas**			**Ethanol**			**Experimental (Ethanol)**	
λ(nm)	**E(eV)**	**f**	**λ(nm)**	**E(eV)**	**f**	**λ(nm)**	**E(eV)**	**f**	**λ(nm)**	**E(eV)**
312.44 (46→48) (47→48) $\pi \rightarrow \pi^*$	3.9683	0.0433	312.22 (46→48) (47→48) $\pi \rightarrow \pi^*$	3.9710	0.0305	312.22 (46→48) (47→48) $\pi \rightarrow \pi^*$	3.9697	0.0417	314	3.9566
293.77 (46→48) $\pi \rightarrow \pi^*$	4.2205	0.5324	288.09 (46→48) $\pi \rightarrow \pi^*$	4.3036	0.4298	293.13 (46→48) $\pi \rightarrow \pi^*$	4.2296	0.5209	298	4.1605
256.38 (45→48) $\pi \rightarrow \pi^*$	4.8360	0.0010	267.11 (45→48) $\pi \rightarrow \pi^*$	4.6418	0.0010	256.69 (44→48) (45→48) $\pi \rightarrow \pi^*$	4.8302	0.0010	291	4.2693

Table 4 The calculated energy values and the energy gaps of 1HBCM)

Parameters	**Gas**	**Ethanol**	**DMSO**
E_{total} (Hartree)	-645.08	-645.091	-645.09
E_{HOMO} (eV)	-6.64	-6.79	-6.77
E_{LUMO} (eV)	-2.16	-2.29	-2.25
E_{HOMO-1} (eV)	-6.76	-7.03	-6.89
E_{LUMO+1} (eV)	-0.56	-0.42	-0.42
$E_{HOMO-LUMO\ gap}$ (eV)	**4.48**	**4.50**	**4.52**
$E_{HOMO-1-LUMO+1\ gap}$ (eV)	**6.20**	**6.61**	**6.47**
Chemical hardness (h)	2.24	2.25	2.26
Electronegativity (χ)	4.40	4.54	4.51
Chemical potential (μ)	-4.40	-4.54	-4.51
Electrophilicity index (ω)	4.32	4.57	4.50

Figure 7 also shows this localization. Using this figure, the energy band interval is calculated to be 4.48 eV and the detailed values are given in Table 4. Also, the values of chemical hardness, chemical potential, electrophilicity index and electronegativity are given in the table.

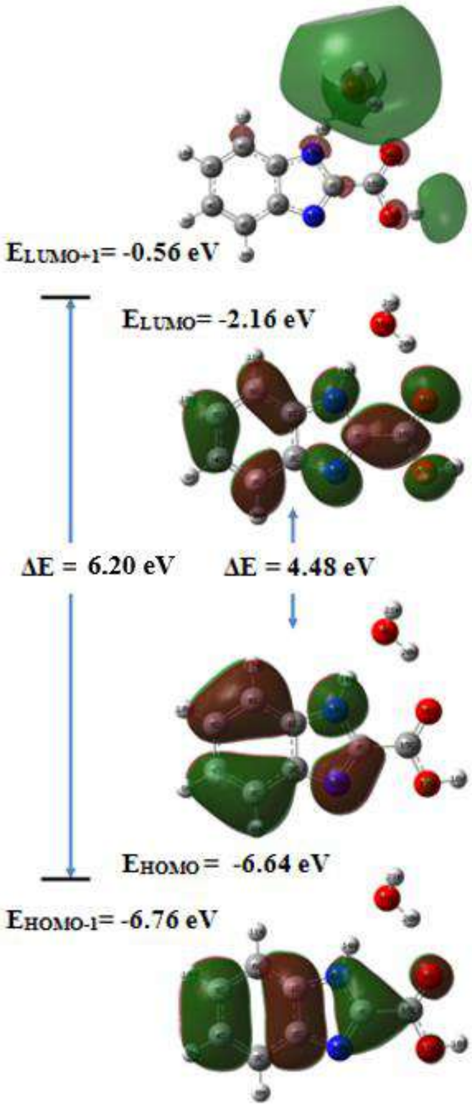

Figure 7 The frontier molecular orbitals of the 1HBCM for vacuum

The energy range of the molecule, i.e., the distance between the energy levels of the highest filled molecular orbital (HOMO) and the lowest empty molecular orbital (LUMO), and the total electronic density of states (TDOS or DOS) to show the interaction between the bonding, antibonding, and nonbonding orbitals, the density of states (PDOS), and the overlap population density of states (OPDOS or COOP) were calculated and generated using the GaussSum 2.2 program [27- 31].

The total electronic density of states (TDOS) displays the density spectrum of the molecule on the orbitals and is shown in Figure 8.

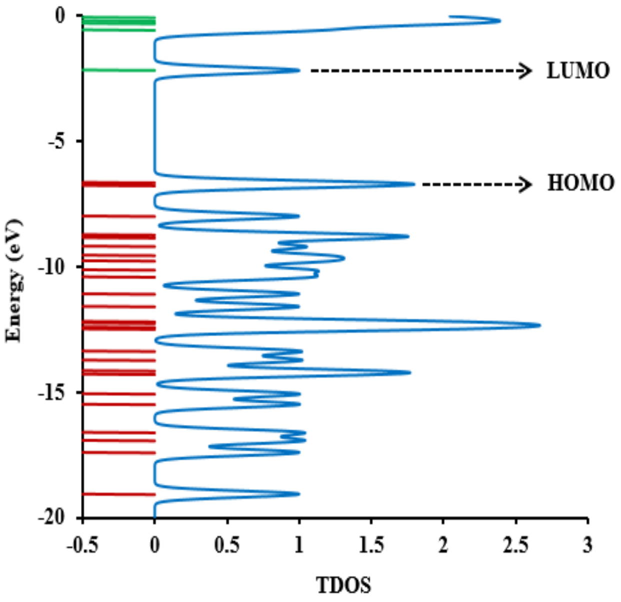

Figure 8 TDOS diagram of the 1HBCM in gas phase

In this spectrum, it can be seen which orbital has a higher electron density and HOMO-LUMO energy range can be calculated. For the molecule studied, the HOMO energy was calculated as -6.64 eV, the LUMO energy as -2.16 eV, and the energy range as 4.48 eV. In the TDOS spectrum, the red lines indicate the HOMO orbitals and the blue lines indicate the LUMO orbitals. The energy range chosen for these spectra is 0–20 eV.

The molecule studied was divided into 3 groups (benzimidazole, water, and carboxyl groups) and shown in Figure 9. The contribution of these groups to the HOMO-LUMO orbitals is shown in the figure.

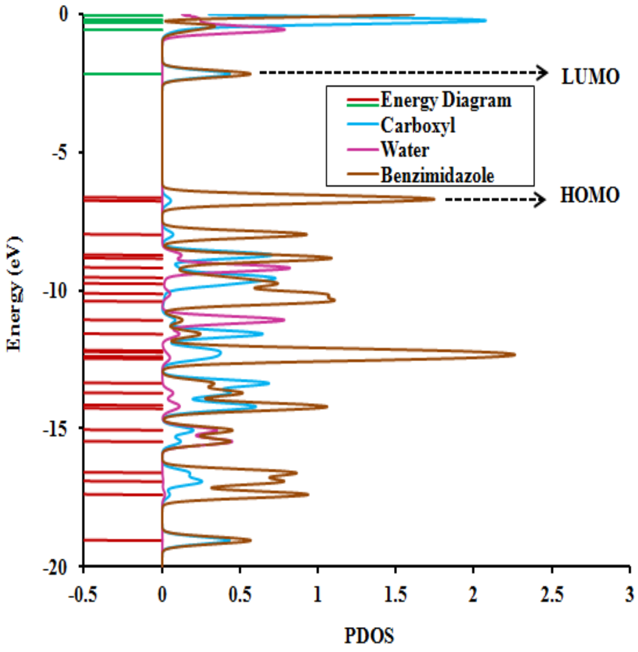

Figure 9 PDOS diagram of 1HBCM in gas phase

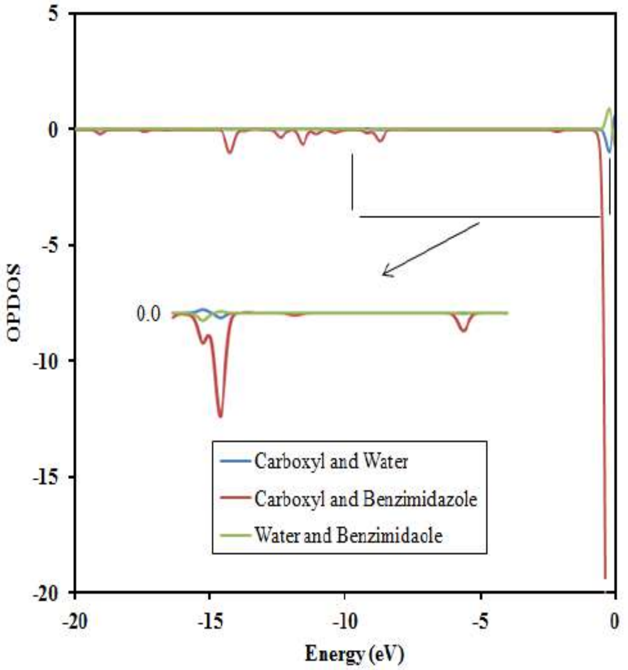

Figure 10 OPDOS diagram of 1HBCM in gas phase

The OPDOS spectrum shows the interaction of the bonding, anti-bonding, or non-bonding orbitals between two orbitals, atoms, or groups. Positive values in this spectrum indicate a bonding interaction (due to a positive overlap population), negative values indicate an anti-bonding interaction (due to a negative overlap population), and a value of zero indicates non-bonding interactions. [30]. The OPDOS diagram is shown in Figure 10 and can be easily identified by the colors and values of the interactions between the selected groups. According to this diagram, the carboxyl-benzimidazole system (red) is negative, i.e., it has an anti-bonding character. However, the water-benzimidazole system (green) is positive, i.e. it shows a binding interaction.

4.5. Molecular electrostatic potential surface

The molecular electronic surface (MEP) shapes are a technique used to represent the electrophilic, nucleophilic, and neutral domains in the molecule [32-33]. These regions are represented as a function of the specific colors and the degrees of the colors. The color scale ranges from dark red to dark blue. The red areas represent the regions where the electrophilic reactions occur, that is, the electron-donating atoms, the blue areas represent the regions of the nucleophilic reactions, the electron-accepting atoms, the yellow colors and green, and the neutral areas.

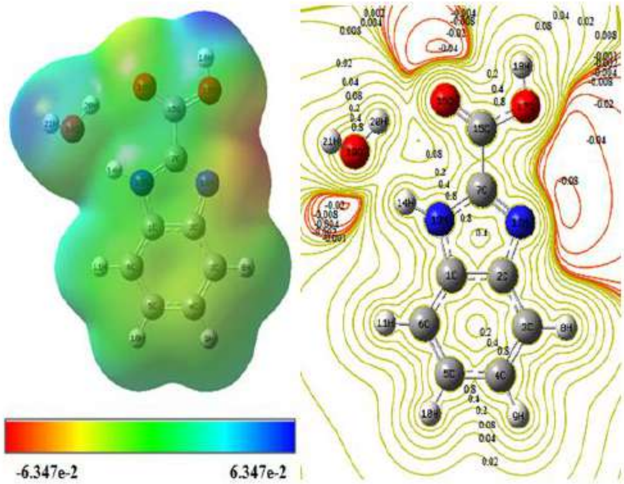

Figure 11 MEP map for 1HBCM molecules in gas phase

The electronic surface map for the 1HBCM molecule was found in the region of -6.347e2 and 6.347e2 (red to blue) and is shown in Figure 11. According to Figure 11, the nitrogen and oxygen atoms are the regions where the electrophilic reactions can occur in the molecule, and N11 is considered as the most electronegative atom in the molecule. The positive potential in the molecule was found at the hydrogen atoms in the monohydrate group. 2D peaks were drawn for the molecule and the red lines were concentrated around the electronegative atoms.

4.6. Mulliken atomic charges

Mulliken atomic charges are closely related to polarization, dipole moment, and acid-basic behavior of molecules. Since it plays an important role in quantum chemical calculations, it was calculated for this study as well, and the charge distribution was compared with the 1H-benzimidazole-2-carboxylic acid (1HBCA) molecule and given in Figure 12.

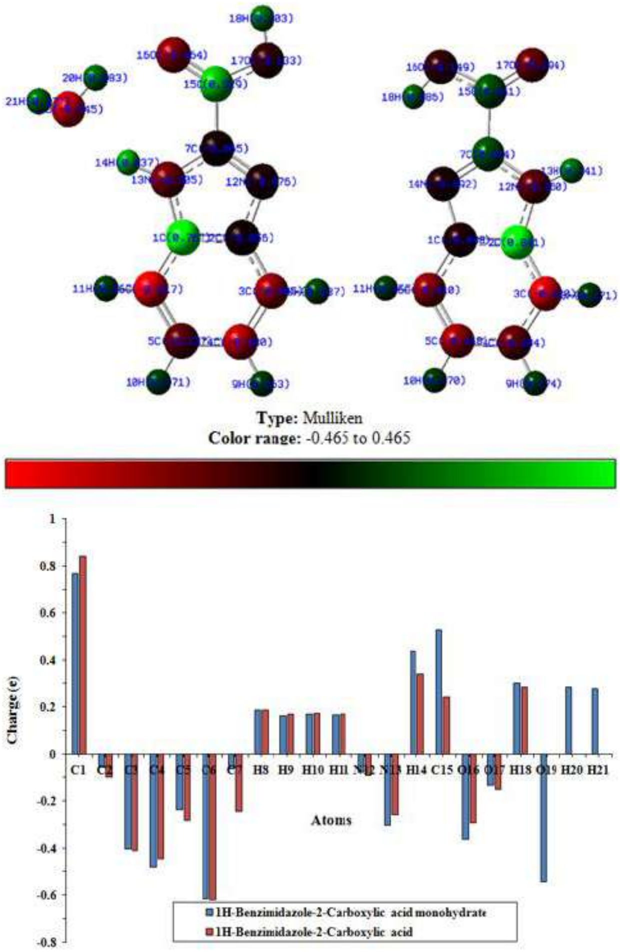

Figure 12 (a) In molecular form and (b) graphically the Mulliken charge distributions for 1HBCM and 1HBCA in gas phase

Looking at Figure 12, it is seen that the C1 atom has the highest positive value in both compounds (0.767 and 0.841 e). Although the C7 carbon atom is negative in both molecules, this value is smaller in the 1HBCM molecule. This difference is thought to be due to the monohydrate group in the molecule.

4.7. Thermodynamic properties

Parameters such as entropy (S), enthalpy (H) and specific heat (C) can be used to predict new reactions of the molecule [34]. While investigating the minimum energy state of the 1HBCM molecule, the thermodynamic parameters of the molecule were also calculated. Since the vibrational properties of molecules increase with temperature [35- 36], these parameters were also investigated in 1HBCM molecule with temperature change. As shown in Figure 13, it is seen that the thermodynamic parameters increase with temperature and become stable at a certain temperature in accordance with the thermodynamic laws.

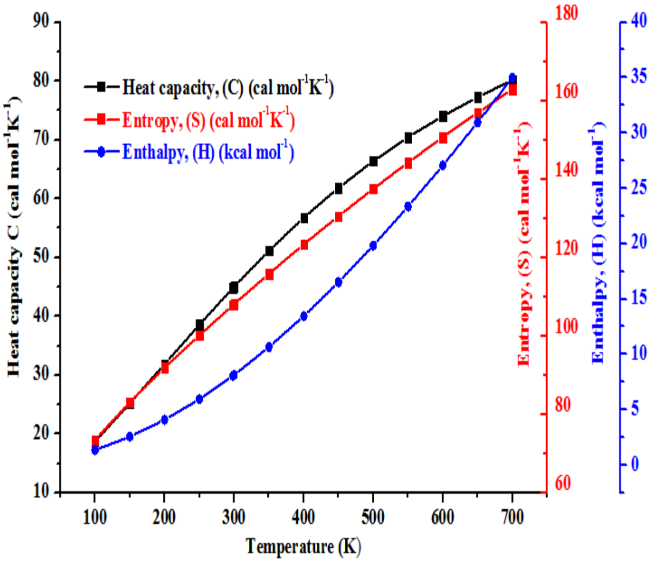

Figure 13 The correlation graphic of heat capacity, entropy, enthalpy and temperature for 1HBCM

5. CONCLUSION

As a result, the molecular structure, spectroscopic, optical and electronic properties of the 1HBCM molecule was investigated using experimental and quantum mechanical methods, and detailed information about these properties was given. The molecule was first optimized and the most suitable stable structure of the molecule was found. Geometric parameters and vibration spectra on the stable structure are given by comparing with similar molecules and experimental data. While the HOMO-LUMO band gap was calculated as 5.30 eV and 5.55 eV in similar molecules from the electronic properties of the molecule, this gap was calculated as 4.48 eV in 1HBCM molecule. When the Eg optical band gap values of the 1HBCM molecule were examined, it was observed experimentally as 3.68 eV (direct) and 3.57 eV (indirect). Considering the information presented, we hope that the usage areas of this structure will increase and that it will be used in health and semiconductor material applications.

Funding

This study is supported by Kırşehir Ahi Evran University Scientific Research Projects Coordination Unit. Project Number: TBY.A4.19.001.

Authors' Contribution

The authors contributed equally to the study.

The Declaration of Ethics Committee Approval

This study does not require ethics committee permission or any special permission.

The Declaration of Research and Publication Ethics

The authors of the paper declare that they comply with the scientific, ethical and quotation rules of SAUJS in all processes of the paper and that they do not make any falsification on the data collected. In addition, they declare that Sakarya University Journal of Science and its editorial board have no responsibility for any ethical violations that may be encountered, and that this study has not been evaluated in any academic publication environment other than Sakarya University Journal of Science.

REFERENCES

[1] W. Akhtar, M. F. Khan, G. Verma, M. Shaquiquzzaman, M. A. Rizvi, S. H. Mehdi, M. Akhter, M. M. Alam, "Therapeutic evolution of benzimidazole derivatives in the last quinquennial period" European Journal

of Medicinal Chemistry, vol. 126, no. 27, pp. 705-753, 2017.

[2] F. Fei, Z. Zhou, “New Substituted Benzimidazole Derivatives: a Patent Review (2010 - 2012)” Expert Opinion on Therapeutic Patents, vol. 23, pp. 1157–1179, 2013.

[3] M. Wang, X. Han, Z. Zhou, “New Substituted Benzimidazole Derivatives: A Patent Review (2013 - 2014)” Expert Opinion on Therapeutic, Patents no. 25, pp. 595–612, 2015.

[4] S. O. Podunavac-Kuzmonovic, L. M. Leovac, N. U. Perisicjanjic, J. Rogan, J. Balaz, “Complexes of cobalt(II), zinc(II) and copper(II) with some newly synthesized benzimidazole derivatives and their antibacterial activity” Journal of the Serbian Chemical Society, vol. 64, pp. 381-388, 1999.

[5] F. Vogetle, “Supramolecular Chemistry: An Introduction”, Wiley, New York, 1991.

[6] K. Takahasi, K. Horino, T. Komura, K. Murata, “Photovoltaic Properties of Porphyrin Thin Films Mixed with *o*-Chloranil” Bulletin of the Chemical Society of Japan, vol. 66, no. 3, pp. 733–738, 1993.

[7] R. S. Mulliken, “Structures of Complexes Formed by Halogen Molecules with Aromatic and with Oxygenated Solvents” Journal of the American Chemical Society, vol. 72, pp. 600–608, 1950.

[8] A. M. Mansour, “Coordination behavior of sulfamethazine drug towards Ru(III) and Pt(II) ions: Synthesis, spectral, DFT, magnetic, electrochemical and biological activity studies”, Inorganica Chimica Acta vol. 394, pp. 436–445, 2013.

[9] J. Tauc, A. Menth, “States in the gap” Journal of Non-Crystalline Solids, vol. 569, pp. 8–10, 1972.

[10] E. Babur Sas, M. Kurban, B. Gündüz, M.Kurt, “Photophysical, spectroscopic properties and electronic structure of BND: Experiment and theory”, Synthetic Metals, vol. 246, pp. 39-44, 2018.

[11] S. Krawczyk, M. Gdaniec, F. Saczewski, “1H-Benzimidazole-2-carboxylic acid monohydrate” Acta Crystallographica Section E, vol. 61 pp. 4185-4187, 2005.

[12] E. B. Sas, M. Kurt, M. Karabacak, A. Poiyamozhi, N. Sundaraganesan, “FT-IR, FT-Raman, dispersive Raman, NMR spectroscopic studies and NBO analysis of 2-Bromo-1H-Benzimidazol by density functional method” Journal of Molecular Structure, vol. 1081, pp. 506–518, 2015.

[13] E. B. Sas, M. Kurt, “Ft-raman, ft-ir, nmr and dft calculations of 5-bromo-1h benzimidazole” Sakarya University Journal of Science, vol. 1, no. 3, pp. 430-441, 2017.

[14] M. Karabacak, E. Kose, A. Atac, E. B. Sas, A. M. Asiri, M. Kurt, “Experimental (FT-IR, FT-Raman, UV–Vis, 1H and 13C NMR) and computational (density functional theory) studies on 3-bromophenylboronic acid” Journal of Molecular Structure, vol. 1076, pp. 358–372, 2014.

[15] V. Krishnakumar, R. Ramasamy, “Density functional and experimental studies on the FT-IR and FT-Raman spectra and structure of 2,6-diamino purine and 6-methoxy purine” Spectrochim. Acta A, vol. 69, pp. 8-17, 2008.

[16] O. R. Shehab, A. M. Mansour, “Charge transfer complexes of 2-arylaminomethyl-1H-benzimidazole with 2,3-dichloro-5,6-dicyano-1,4-benzoquinone: Experimental and DFT studies”, Journal of Molecular Structure, vol. 1047, pp. 121-135, 2013.

[17] N. T. A. Ghani, A. M. Mansour, “Molecular structure of 2-chloromethyl-1H-benzimidazole hydrochloride: Single crystal, spectral, biological studies, and DFT

calculations", Spectrochimica Acta Part A, vol. 86, pp. 605–613, 2012.

[18] T. S. Xavier, N. Rashid, I. H. Joe, "Vibrational spectra and DFT study of anticancer active molecule 2-(4-Bromophenyl)-1H-benzimidazole by normal coordinate analysis" Spectrochimica Acta Part A, vol. 78, pp. 319–326, 2011.

[19] V. Arjunan, A. Raj, C. V. Mythili, S. Mohan, "Structural, vibrational, electronic investigations and quantum chemical studies of 2-amino-4-methoxybenzothiazole" Journal of Molecular Structure, vol. 1036, pp. 327-340, 2013.

[20] G. Varsanyi, "Vibrational Spectra of Benzene Derivatives", Academic Press: New York, 1969.

[21] H. G. Silver, J. L. Wood, "Factors affecting torsional barriers in benzaldehyde derivatives", Transactions of the Faraday Society, vol. 60, pp. 5-11, 1964.

[22] R. Ramasamy, "Analysis of Vibrational Spectra of Pyridoxazinone Based on Density Functional Theory Calculations", Journal of Applied Spectroscopy, vol. 80, pp. 492–498, 2013.

[23] R. Ramasamy, "Vibrational spectroscopic studies of imidazole", Armenian Journal of Physics, vol. 8, pp. 51-55, 2015

[24] Y. Wang, R. A. Poirier, "Factors that influence the CN stretching frequency in imines", The Journal of Physical Chemistry A, vol. 101, no. 5, pp. 907–912, 1997.

[25] C. Y.Huang, T. Wang, F. Gai, "Temperature dependence of the CN stretching vibration of a nitrile-derivatized phenylalanine in water" Chemical Physics Letters, vol. 371, no. 5–6, pp. 731-738, 2003.

[26] I. Fleming, "Frontier Orbitals and Organic Chemical Reactions", Wiley, London, 1976.

[27] R. Hoffman, "Solids and Surfaces: A Chemist's View of Bonding in Extended Structures", Wiley- VCH Publisher, Newyork, 1988.

[28] W. Kohn, L. J. Sham, "Self-consistent equations including exchange and correlation effects" Physical Review, vol. 140, no. A, pp. 1133-1141, 1965.

[29] N. M. O'Boyle, A. L. Tenderholt, K. M. Langner "cclib: a library for package-independent computational chemistry algorithms" Journal of Computational Chemistry, vol. 29, pp. 839-845, 2008.

[30] S. Armaković, S. J. Armaković, J .P. Šetrajčić "Hydrogen storage properties of sumanene" International Journal of Hydrogen Energy, vol. 38, pp. 12190-12198, 2013.

[31] S. Armaković, S. J.Armaković, J. P. Setrajcic, S. K. Jacimovski, V. Holodkov, "Sumanene and its adsorption properties towards CO, CO_2 and NH_3 molecules" Journal of Molecular Modeling, vol. 20, pp. 2170-2177, 2014.

[32] N. Okulik, A. H. Jubert "Theoretical study on the structure and reactive sites of non-steroidal anti-inflammatory drugs" Journal of Molecular Structure: THEOCHEM, vol. 682, pp. 55-62, 2004.

[33] E. Scrocco, J. Tomasi, "Electronic molecular structure, reactivity and intermolecular forces: an euristic interpretation by means of electrostatic molecular potentials" Advances in Quantum Chemistry, vol. 11, pp. 115-193, 1978.

[34] H. P. Gümüş, Y. Atalay, "3-hidroksi-4-hidroksimiinometil-5-hidroksimetil-1,2-dimetilpiridinyum iyodid molekülünün geometrik yapısının incelenmesi" Sakarya University Journal of Science Institute, vol. 21, no. 3, pp. 564-571, 2017.

[35] J. B. Ott, J. Boerio-Goates, “Chemical Thermodynamics: Advanced Applications, Calculations from Statistical Thermodynamics”, Academic Press, 2000.

[36] E. B. Sas, N. Cankaya, M. Kurt, “Synthesis of 2-(bis (cyanomethyl) amino)-2-oxoethyl methacrylate monomer molecule and its characterization by experimental and theoretical methods” Journal of Molecular Structure, vol. 1161, pp. 433-441, 2018.

SAKARYA ÜNİVERSİTESİ
FEN BİLİMLERİ ENSTİTÜSÜ
DERGİSİ

Sakarya University Journal of Science
SAUJS

ISSN 1301-4048 | e-ISSN 2147-835X | Period Bimonthly | Founded: 1997 | Publisher Sakarya University |
http://www.saujs.sakarya.edu.tr/

Title: 24 January 2020 Sivrice-Elazığ Earthquake: Assessment of Seismic Characteristics of Earthquake, Earthquake Territory and Structural Performance of Reinforced Concrete Structures

Authors: İbrahim Özgür DEDEOĞLU, Musa YETKİN, Yusuf CALAYIR

Recieved: 2021-10-05 00:00:00

Accepted: 2022-08-10 00:00:00

Article Type: Research Article

Volume: 25
Issue: 5
Month: October
Year: 2022
Pages: 892-907

How to cite
İbrahim Özgür DEDEOĞLU, Musa YETKİN, Yusuf CALAYIR; (2022), 24 January 2020 Sivrice-Elazığ Earthquake: Assessment of Seismic Characteristics of Earthquake, Earthquake Territory and Structural Performance of Reinforced Concrete Structures. Sakarya University Journal of Science, 25(5), 892-907, DOI: 10.16984/saufenbilder.1005024
Access link
http://www.saujs.sakarya.edu.tr/en/pub/issue/73051/1005024

Sakarya University Journal of Science 25(5), 892-907, 2022

24 January 2020 Sivrice-Elazığ Earthquake: Assessment of Seismic Characteristics of Earthquake, Earthquake Territory and Structural Performance of Reinforced Concrete Structures

İbrahim Özgür DEDEOĞLU*[1], Musa YETKİN[2], Yusuf CALAYIR[2]

Abstract

An earthquake with a magnitude of 6.8 (M_w) has occurred in Sivrice district of Elazığ province in Eastern Turkey, on January 24, 2020. The main shock and long-term aftershocks felt fairly by near vicinities. Many structures have been damaged severely or demolished at this moderate earthquake that occurred on East Anatolia Fault (EAF) zone. Also resulted in sum 41 casualties, including 37 people in Elazığ and 4 people in Malatya. The purpose of this paper is to give information of the tectonic characteristics of the EAF zone, the seismic characteristics of the earthquake territory, the general characteristics of the main shock and after-shocks. In addition, another purpose of this article is to reveal the damages caused by the earthquake in the reinforced concrete (RC) buildings in Elazığ, with the post-earthquake field observations. The main reasons of damages have presented and discussed. The most important reason for damages of structures is the lack of engineering services, in other words, not being constructed properly with respect to the available building codes.

Keywords: 2020 Sivrice-Elazığ earthquake, reinforced concrete structures, earthquake damage survey, East Anatolia Fault zone, damage assessment

1. INTRODUCTION

On January 24, 2020, an earthquake with a magnitude of 6.8 (M_w) of according to Turkey Disaster Emergency and Management Agency (DEMA) [1] occurred in Sivrice district within the borders of Elazığ province in the Eastern Province of the Eastern Anatolian Region in Turkey. The earthquake was felt in 42 provincial centers and 26184 settlements, 750 km from the epicenter. The EAF zone is located between the Arabian Plate moving northward and the Anatolian Block moving westward. It has an average width of 30 km and a length of approximately 600 km and forms a left-lateral strike-slip transform boundary trending North-East. The EAF zone consists of

---

* Corresponding author: iozgur.dedeoglu@batman.edu.tr
[1] Batman University
ORCID: https://orcid.org/0000-0001-5356-6655
[2] Fırat University
E-mail: musayetkin@firat.edu.tr, ycalayir@firat.edu.tr
ORCID: https://orcid.org/0000-0002-6259-4137, https://orcid.org/0000-0002-6387-5360

segments ranging in length from 50 km to 145 km (Figure 1) [1].

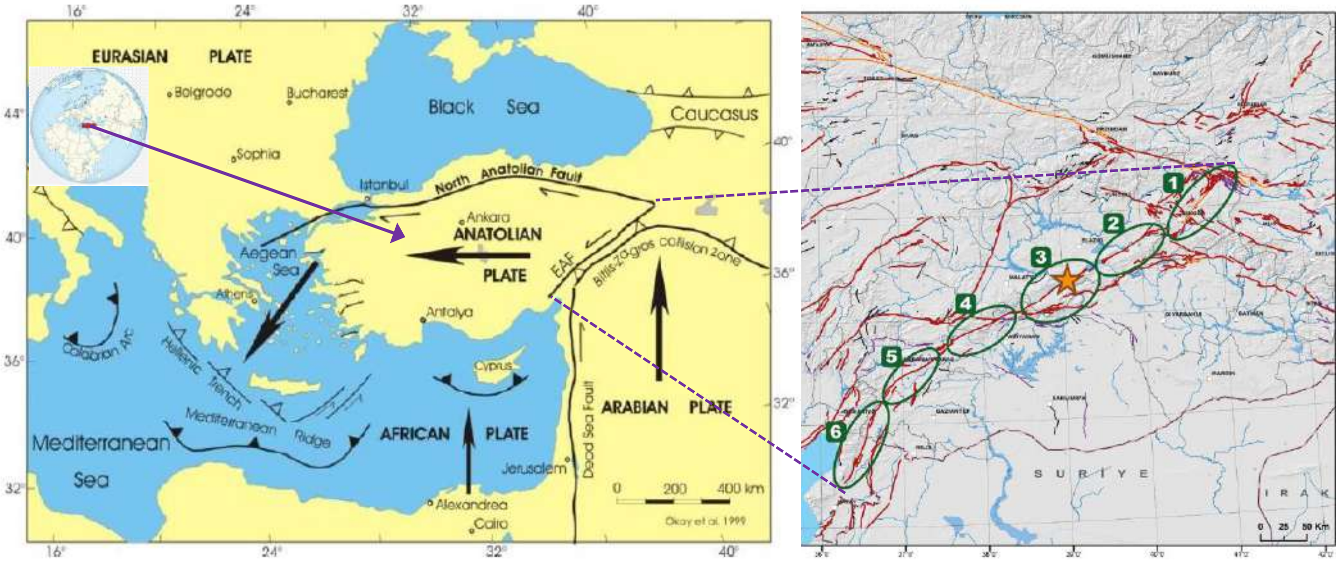

Figure 1 EAF zone (1:Karlıova-Bingöl, 2:Palu-Hazar Lake, 3:Hazar Lake-Sincik, 4:Çelikhan-Gölbaşı, 5:Gölbaşı-Türkoğlu, 6:Türkoğlu-Antakya) [1, 2]

Many devastating earthquakes have occurred on the EAF zone throughout history. Some of these earthquakes have been recorded historically and some instrumentally (Figure 2) [1]. The earthquakes of 1789-Palu, 1866-Elazığ, 1874-Elazığ, 1875-Bingöl-Elazığ and 1893-Malatya are some of the most important earthquakes recorded historically in the region (Table 1) [3- 11].

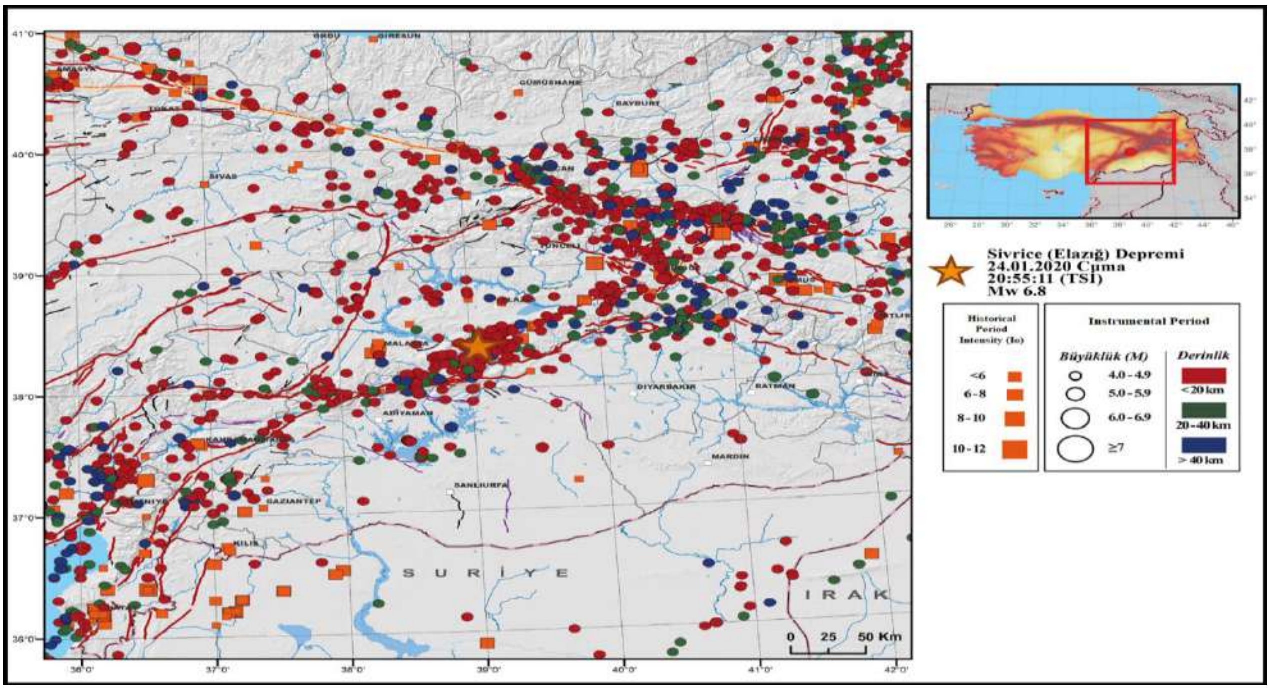

Figure 2 Earthquake activity in the historical and instrumental period along the EAF zone [1]

Table 1 Earthquake intensity in the historical period along the EAF zone

Year	Location	Intensity (I_o)
995	Elazığ (Palu, Sivrice)	VI
1513	Malatya	IX
1789	Elazığ (Palu)	VII
1866	Elazığ	IX
1874	Elazığ, Diyarbakır	X
1875	Elazığ, Bingöl	VII
1889	Elazığ (Palu)	VI
1890	Malatya	VI
1893	Malatya	X

When the earthquakes recorded instrumentally were examined, it was seen that 564 earthquakes over 4.0 occurred on the EAF zone. If we examine the earthquakes with magnitude 6 or more occurring on the main line and close segments of the EAF zone; the earthquakes of Pütürge (1905), Malatya (1908), Sincik-Adıyaman (1964), Varto-Muş (1966), Karlıova-Bingöl (1966), Bingöl (1971), Lice-Diyarbakır (1975) and Doğanşehir-Malatya (1986) earthquakes can be given as examples. During these earthquakes many people lost their lives and many houses were destroyed and heavily damaged [1].

When we entered the 21st century, earthquakes continued to occur in the EAF zone. Pülümür-Tunceli (2003) and Bingöl (2003) earthquakes are the first earthquakes to occur. After these earthquakes, there was a serious dynamism in the EAF system and there were always earthquakes at certain time intervals until 24 January 2020 Sivrice earthquake. In this time period, Sivrice-Elazığ (2004), Pütürge-Malatya (2005), Sivrice-Elazığ (Feb 9, 2007), Sivrice-Elazığ (Feb 21, 2007), Kovancılar-Elazığ (2010), Elazığ (2011), Sivrice-Elazığ (April 4, 2019) and Sivrice-Elazığ (December 27, 2019) earthquakes occurred (Figure 2). For the EAF zone, in the 17-year period since 2003, it is seen that there has been an increase in earthquake activity incomparable with previous periods. In addition, the Sivrice-Elazığ (2019) earthquakes occurred both on the same fault and in a very close location with the January 24, 2020 earthquake. Therefore, it is possible to interpret the 2019 Sivrice earthquakes as the foreshock of the January 24, 2020 earthquake [12].

Structural damages occurred with the past earthquakes in various regions had been investigated by many researchers according to the structure types. The earthquake performance of the RC structures is evaluated by Sezen et al. [13] for 1999 Kocaeli earthquake and by Doğangün [14] for 2003 Bingöl earthquake. Celep et al. [15] investigated failures of masonry and concrete buildings during the March 8, 2010 Kovancılar and Palu Earthquakes in Elazığ, Turkey. Calayır et al. [16] assessed damages of various structures (adobe, masonry, hımış, and RC structures, and minarets) in the rural area during the March 8, 2010 Kovancılar Earthquakes in Elazığ, Turkey. Sayın et al. [17] presented a comprehensive study on the 24 January 2020 Sivrice-Elazığ, Turkey. They summarized past and present seismic characteristics of the earthquake region. In addition, they also summarized the seismotectonic of the region, the general characteristics of the earthquake and more specifically to report on the structural damage, and structural damage caused by the earthquake, observed during the site investigation. Günaydın [18] et al. examined the case studies of damaged masonry buildings and as well as failure or collapse mechanisms. Yetkin et al. [19] investigated the damages occurred at the minarets in Elazig after the $M_w = 6.8$ magnitude earthquake that took place in Sivrice district of Elazig on January 24, 2020. In the examined minarets, the parts which the damages occurred in were determined and also the causes of these damages were evaluated. At the end of the study, some recommendations were made for the repair and strengthening of damaged minarets and the construction of new minarets.

The aim of this paper is to give information of the past and present seism tectonic characteristics of the EAF zone, the seismic characteristics of the earthquake territory, the general characteristics of the main shock and after-shocks. Also, the damages of RC buildings in Elazığ province were examined by the post-earthquake field observations. The observed damages was classified and discussed for RC structures.

2. ON JANUARY 24, 2020 SIVRICE-ELAZIĞ EARTHQUAKE

The closest settlement to the focal point of the earthquake that occurred on January 24, 2020 is Çevrimtaş village in Sivrice district. Çevrimtaş village is located 0.81 km from Sivrice (Figure 3).

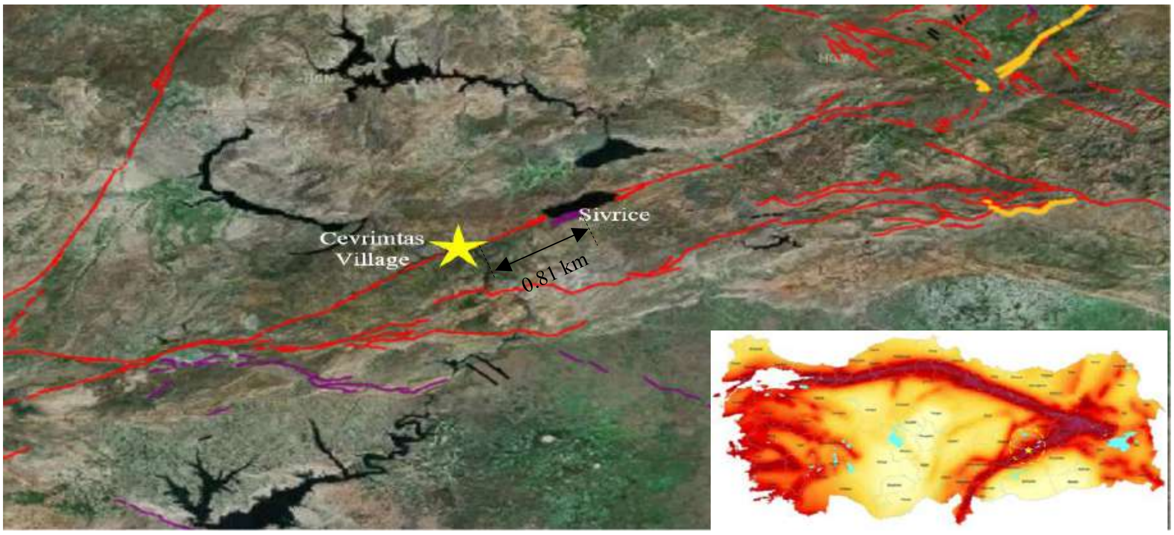

Figure 3 Location of the January 24, 2020 earthquake [11, 20]

This earthquake was felt in Elazığ and all its districts, and also in many other provinces, starting from the Çevrimtaş village. The magnitude of the earthquake has been announced by DEMA as 6.8 (M_w). Magnitude and source characteristics of the earthquake are defined by various institutions as given in Table 2. The depth at which the main shock occurred has been explained as different values by these institutions, and these values are in the range of 8.06-15.0 km. It is seen that aftershocks intensity in the depth range of 5 ~ 20 km (Figure 4). Therefore, earthquakes that occur are shallow earthquake.

Table 2 January 24, 2020 Sivrice-Elazığ earthquake characteristics for various institutions.

Institutions	Magnitude (M_w)	Depth (km)	Longitudinal	Latitude
Turkish Ministry of Interior Disaster and Emergency Management Agency (DEMA)	6.8	8.06	39.06	38.36
Kandilli Observatory and Earthquake Research Institute (KOERI)	6.5	5.0	39.24	38.37
European-Mediterranean Seismological Centre (France)	6.8	15.0	39.22	38.37
German Research Center for Geosciences	6.8	10.0	39.20	38.36
Instituto Nazionale di Geofisica e Vulcanologia (Roma)	6.8	11.0	39.12	38.39
United States Geological Survey	6.7	11.9	39.08	38.39

After the main shock, the aftershocks continued for days. The number of daily aftershocks for one month in the region is given in Figure 4. The aftershocks have gradually decreased. When 1-month data are evaluated in the region; it was observed that a total of 3080 earthquakes occurred, including the main shock, and 26 of these aftershocks were 4.0 (M_w) and above [1]. The distribution of earthquake aftershocks shows that the rupture started in the southwest of Sivrice. In addition, aftershocks are mostly concentrated in the northwest block very close to the Pütürge Segment. This data shows that the earthquake source fault is inclined to the northwest [12].

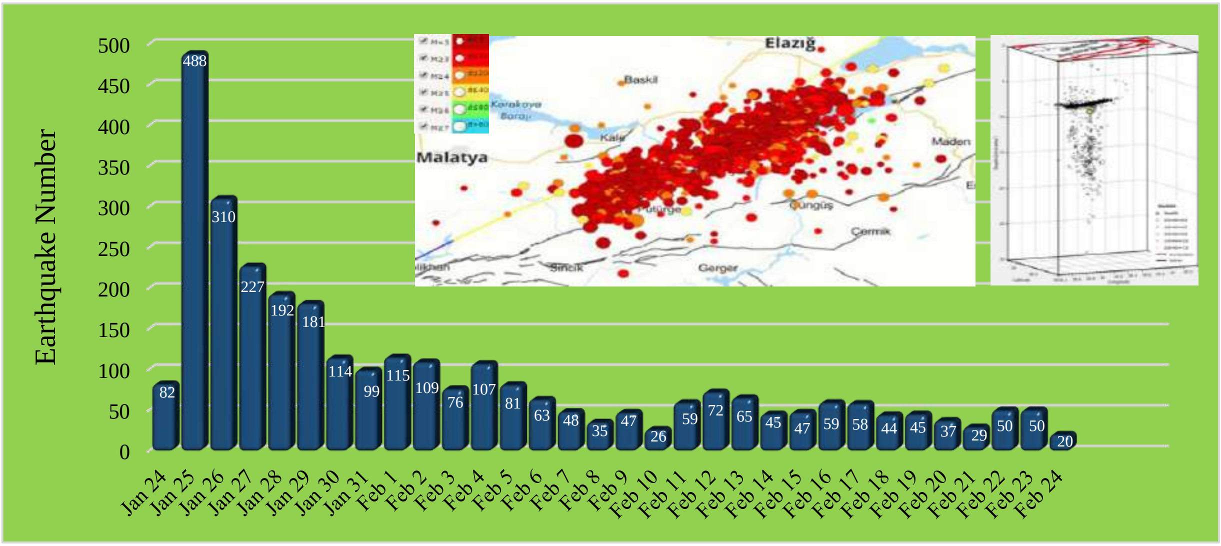

Figure 4 The number and location of daily aftershocks for one month [1, 21]

The main shock caused significant damage and resulted in sum of 41 which are 37 people in Elazığ and 4 in Malatya casualties. In addition, many buildings such as houses, workplaces, places of worship, animal shelters were damaged and some of these structures were demolished. As a result of the investigations made by the damage determination committees, the building damage states for Elazığ province are given in Figure 5.

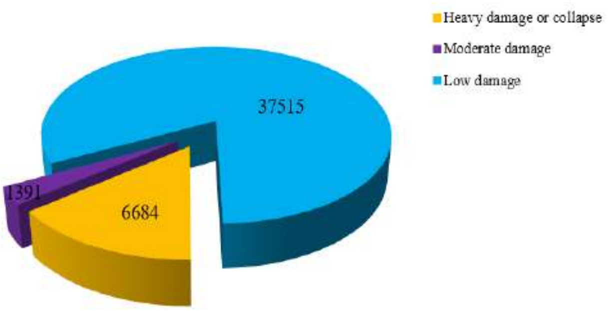

Figure 5 The building damage states for Elazığ province [22]

When the damage assessment results are examined, it is noteworthy that the number of damaged buildings is quite high. For some of these buildings, urgent demolition decision has been taken and some of them are determined as severely damaged and will be demolished. When the PGA data for the region on the Turkey Earthquake Hazard Map (DEMA) were evaluated, it was determined that the PGA-475 value (Design Earthquake) was 0.622 g, but the maximum acceleration values measured for the earthquake that occurred were 0.298 g [1]. Thus, it has been revealed that the maximum acceleration of the occurring earthquake has a smaller value than the Design Earthquake.

The spectral acceleration values of the records of Elazığ-Sivrice station were compared with the former Turkish Earthquake Code (TEC-2007) [23] and the current Turkish Building Earthquake Code (TBEC-2018) [24] design acceleration spectra in Figure 6. While calculating the design spectrum, the ground class of the region was accepted as Z3 according to TEC-2007 and ZC according to TBEC-2018. Elastic design spectrum was calculated for DD-2 earthquake ground motion level (design level, i.e., 10% probability of exceedance in 50 years-475 years return period) [20].

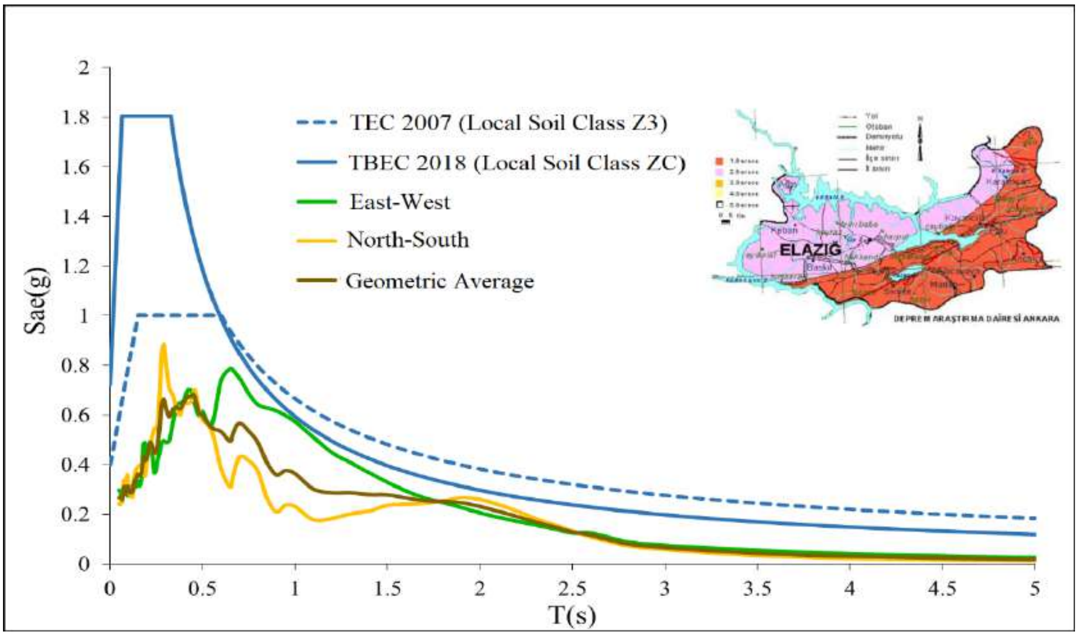

Figure 6 Comparison of the acceleration spectra of the Sivrice-Elazığ (2308) station horizontal acceleration records with the TEC-2007 and TBEC-2018 design spectra [1]

According to seismic codes, limiting permanent structural damage in order to ensure life safety in severe earthquakes is the basic principle of earthquake-resistant building design. Accordingly, it is desired that the structural elements consume the energy of a severe earthquake with plastic deformations (permanent displacement and damage), in other words, to act ductile. However, when the damage caused by the earthquake and the acceleration values recorded in the earthquake are examined, it is obvious that the level of damage to the buildings is higher than expected. This situation have shown that heavily damaged or collapsed structures weren't construct in accordance with seismic codes.

3. PERFORMANCE OF REINFORCED CONCRETE (RC) BUILDINGS

Many RC buildings were affected by the 6.8 (M_w) earthquake that occurred in the Sivrice district of Elazığ Province in Eastern Turkey on January 24, 2020. The damages were generally caused due to various engineering and structural deficiencies. Causes of damages of various types of RC buildings in the earthquake area are presented below.

3.1. Column Damage

The transverse reinforcement is of primary importance to ensure the adequate ductility capacity of the system in earthquake resistant building design. During the earthquake, shear forces is increased significantly, especially at end of column and beam, and beam-column joints. For this reason, we, as engineers, should pay special attention to the transverse reinforcement details during the project and construction of the building. However, in the field observations made after the earthquake, it was observed that the columns were damaged due to insufficient transverse reinforcement in the plastic hinge regions. Besides, it was seen that longitudinal reinforcement bar were also buckled owing to inadequate transverse reinforcement. This important deficiency caused the columns to display low performance against the shear forces of earthquake. In Figure 7-8, some of columns damaged in the earthquake due to insufficient transverse reinforcement have presented.

Figure 7 Column damage due to insufficient transverse reinforcement

Figure 8 Buckling longitudinal reinforcement bars of damaged column due to insufficient transverse reinforcement

3.2. Beam Damage

The beams are usually exposed to shear and bending damage because of the aforementioned structural deficiencies. In field observations for the Elazığ earthquake, shear and bending cracks were observed in the beams. In addition, damages were observed in the connected point the secondary beams to the supporting beams were as well. Some of the beams damaged in the earthquake have shown in Figure 9.

Figure 9 Beam damages

3.3. Strong Beam–Weak Column

In Turkey, especially available old RC structures stock was constructed with strong beam and weak column design. Accordingly, the beams are deep and rigid while the columns weak and flexible. Therefore, damage of these RC building in the event of an earthquake start at the ends of the columns. The design of strong beam-weak column was the main reason of the partial and total collapse of some buildings during the Sivrice-Elazığ earthquake. In Figure 10, columns of structures damaged due to strong beam-weak column design are presented.

Figure 10 Strong beam–weak column

To prevent this kind of damages or collapses arising from the strong beam-weak column design, current and former seismic codes require that sum of ultimate moment of columns framing into a beam-column joint should be at least 20% more than the sum of ultimate moment of beams framing into the same joint [23, 24]. Thus, plastic hinges occur at the ends of the beam in case of the earthquake and brittle failure prevents.

3.4. Damages of Infill Walls

In Turkey, the infill walls in the RC buildings are generally constructed by using brick and cement mortar. During an earthquake, the in-plane and out-of-plane behaviour of these infill walls is extremely complex and depends entirely on the interaction mechanism of the infill wall and RC frames. During the field observations, different type of infill damages were encountered as shown in Figure 11-14. During the earthquake, the diagonal cracks were observed in the infill walls due to the interaction with the RC frame. (Figure 11). Also partial or total out-of-plane mechanism was observed in the infill wall damages (Figure 12). The other type of observed damage in the infill wall is the separation of the infill wall from the frame (Figure 13). In addition, numerous overhang infill wall damages have been also observed in the earthquake-affected region with the aforementioned damages (Figure 14).

.

Figure 11 In-plane damage

Figure 12 Partial out-of-plane damage

Figure 13 Disconnection of infill wall from the frame

Figure 14 Damages of overhang infill walls

Infill walls are especially very sensitive to the inter-story drift ratio demand of the structural system. Therefore, TBEC (2018) limits these ratios. In order to prevent such damages, rules of earthquake code must strictly comply both during the project and the construction stage.

3.5. Inadequate Gaps between Adjacent Buildings

Today, due to the increase in the human population and the insufficiency of construction areas in city centers, adjacent buildings are often built. As a result of this, one or both facades of the buildings touch each other or there is little space between the buildings. Therefore, during an earthquake, these structures is collided because they do not have sufficient displacement space. A more dangerous situation is emerged when the story levels of adjacent structures are not same aligned. The slabs of the building can hit the columns of neighbor building, causing severely damage. Such damages were detected in the field observations made after the Elazığ earthquake (Figure 15).

Figure 15 Damages of adjacent buildings

To prevent such damages, there must be sufficient gaps between adjacent buildings. TBEC (2018) is required the construction of seismic joints that will maintain certain spacing between adjacent buildings. In this way, in the event of an earthquake, neighboring buildings can move independently without interfering with each other. According to the code, the minimum joint gap to be left will be at least 30 mm up to a height of 6 m and at least 10 mm will be added to this value for every 3 m of height after 6 m. Unless a more unfavorable value is obtained in accordance with requirement defined in previous statement, sizes of gaps should not be less than the sum of the absolute values of average story displacements multiplied by the coefficient α. If adjacent floor levels of buildings at all stories are same, then the amount of gap is $\alpha = 0.25\ (R/\mathrm{I})$, $\alpha = 0.50\ (R/\mathrm{I})$ if not. In these equations, R is the structural behavior factor and I building importance factor.

3.6. Poor Concrete Quality, Corrosion and Erroneous Applications

In Turkey, ready-mixed concrete has started to be used widely especially after 2000s. That's why, the majority of existing RC buildings were built with cast in-place concrete without any official control. As a result of this, many such buildings have low strength concrete due to high water-cement ratio, improper aggregate size and gradation, and reinforcement subjected to corrosion. In the field study, poor concrete quality, corroded reinforcement bars and erroneous applications which shown in Figure 16 were encountered in the structural members of the buildings.

(a)

(b)

(c)

Figure 16 a) Poor concrete quality b) corrosion c) erroneous application

In order to prevent these erroneous applications that negatively affect the behavior of structural members;

- Appropriate gradation concrete should be used.
- A vibrator should be used in order for the concrete to settle into the mold homogeneously.
- It should be ensured that the structural elements have sufficient concrete cover.
- Wrong applications that will weaken the RC system should be avoided.

4. CONCLUSIONS AND SUGGESTIONS

On January 24, 2020 an earthquake with a magnitude (M_w) of 6.8 hit the Elazığ Province, Turkey. Many structures have been damaged severely or demolished at this moderate earthquake that occurred on East Anatolia Fault zone. A total of 41 people died, including 37 people in Elazığ and 4 people in Malatya. The purpose of this paper is to summarize tectonic characteristics of the EAF zone, the seismic characteristics of the earthquake territory, the general characteristics of the main shock and after-shocks. In addition, another purpose of this article is to reveal the damages caused by the earthquake in the RC buildings in Elazığ, by the post-earthquake field observations. The main reasons of damages have assessed. The main factors of damages attained from this case study are given below.

- Using plain bar, large spacing transverse reinforcement, absence of crossties has caused significant damage to structural elements. In addition, the ends of the stirrups, which is an important detail, had not bent 135 degrees. Because of all of these, the wrapping effect of the stirrups in the concrete block has considerably reduced and the section integrity has been sufficiently not ensured. To avoid damage of structural members, attention should be paid to detailing of transverse reinforcement, and close-spaced stirrups should be used.
- During the earthquake, the diagonal cracks were observed in the infill walls due to the interaction with the RC frame. In addition, heavy overhangs in the building has increased the degree of damage. In order to prevent such damages, the infill wall should work independently from the frame. Also heavy overhangs should be avoided especially.
- Each building has different natural vibration periods due to their structural and material properties. During an earthquake, a hammering effect occurs between adjacent buildings or buildings with insufficient gap between them. This situation is devastating for buildings, especially when the neighbor buildings have different floor levels. To avoid this kind of damage, proper gaps should be left between the attached buildings.
- Material quality, proper workmanship and appropriate detailing are the main factors that positively affect the earthquake performance of structural systems. The information obtained the field observation shows that poor concrete quality, corrosion of reinforcement bars and wrong interventions reduce the structural performance of buildings. Hence, expected performance against earthquake cannot be provided. To prevent damage arising from this situation, selection and application of materials, workmanship and subsequent interventions should be paid attention.

RC buildings should be designed and built in accordance with the requirements of current seismic codes in order to reduce the damage of RC buildings and to prevent loss of property and life. In addition, construction workers should be taught that workmanship has an important role in the earthquake performance of the building. Building construction must be strictly controlled by engineers at every stage.

Acknowledgments
Authors would like to thank to Fırat University Rectorate for their support.

Funding
The authors received no financial support for the research, authorship or publication of this work

The Declaration of Conflict of Interest/ Common Interest

No conflict of interest or common interest has been declared by the authors

Authors' Contribution

The authors contributed equally to the study. All authors participated in discussions of results and manuscript preparation.

The Declaration of Ethics Committee Approval

This study does not require ethics committee permission or any special permission.

The Declaration of Research and Publication Ethics

The authors of the paper declare that they comply with the scientific, ethical and quotation rules of SAUJS in all processes of the paper and that they do not make any falsification on the data collected. In addition, they declare that Sakarya University Journal of Science and its editorial board have no responsibility for any ethical violations that may be encountered, and that this study has not been evaluated in any academic publication environment other than Sakarya University Journal of Science.

REFERENCES

[1] The Ministry of Interior, Disaster and Emergency Management Administration (DEMA), January 24, 2020 Sivrice (Elazığ) Earthquake Report, Turkey Republic, 2020.

[2] A. I. Okay, M. Zattın, W. Cavazza, “Apatite fissiontrack data for the Miocene Arabia-Eurasia collision,” Geology, vol. 38, pp. 35-38, 2010.

[3] K. Ergin, U. Güçlü, Z. Uz, “A catalog of earthquake for Turkey and surrounding area (11 A.D. to 1964 A.D.),” Istanbul Technical University, Faculty of Mining Engineering, Istanbul, Turkey, 1967.

[4] K. Ergin, U. Güçlü, G. Aksay, “A Catalog of Earthquakes of Turkey and Surrounding Area (1965–1970),” Istanbul Technical University, Faculty of Mining Engineering, Institute of Physics of the Earth, Technical Report 28, 1971.

[5] H. Eyidogan, U. Güçlü, Z. Utku, E. Değirmenci, “Macro-Seismic Directory of Major Earthquakes in Turkey (1900–1988),” ITU Mining Faculty, Department of Geophysical Engineering, Istanbul, 1991.

[6] N.N. Ambraseys, “Temporary seismic quiescence: SE Turkey,” Geophysical Journal, vol. 96, pp. 311-331, 1989.

[7] N. N. Ambraseys, C. Finkel, “Seismicity of Turkey and neighbouring regions 1500-1800,” Geophysical Journal of International, vol. 133, pp. 390-406, 1995.

[8] N. N. Ambraseys, J.A. Jackson, “Faulting associated with historical and recent earthquakes in the Eastern Mediterranean region,” Geophysical Journal International, vol. 133, pp. 390−406, 1998.

[9] O. Tan, M.C. Tapırdamaz, A. Yörük, “The Earthquakes Catalogues for Turkey,” Turkish Journal of Earth Science, vol. 17, pp. 405–418, 2008.

[10] D. Kalafat, Y. Güneş, K. Kekovalı, M. Yılmazer, “A revised and extended earthquake catalogue for Turkey since 1900 ($M \geq 4.0$) (in Turkish),” Boğaziçi University, Kandilli Observatory and Earthquake Research Institute, Istanbul, pp 640-1049, 2011.

[11] Ö. Emre, T.Y. Smoke, S. Özalp, H. Elmacı, Ş. Olgun, F. Şaroğlu, “1/1.250.000 Scaled Active Fault Map of Turkey,” General Directorate of Mineral Research and Exploration Special Publications Series, Ankara, Turkey, 2013.

[12] O. Tatar, H. Sözbilir, F. Koçbulut, E. Bozkurt, E. Aksoy, S. Eski, B. Özmen, H. Alan, Y. Metin, “Surface deformations of 24 January 2020 Sivrice (Elazığ)–Doğanyol (Malatya) earthquake (Mw= 6.8) along the Pütürge segment of the East Anatolian Fault Zone and its comparison with Turkey’s 100-year-surface ruptures,” Mediterranean Geoscience Reviews, vol. 2 (3), pp. 385-410, 2020.

[13] H. Sezen, A. S. Whittaker, K.J. Elwood, K.M. Mosalam, “Performance of reinforced concrete buildings during the August 17, 1999 Kocaeli, Turkey earthquake, and seismic design and construction practise in Turkey,” Engineering Structure, vol. 25, pp.103–114, 2003.

[14] A. Doğangün, “Performance of reinforced concrete buildings during the May 1, 2003 Bingöl earthquake in Turkey,” Engineering Structure, vol. 26, pp. 841–856, 2004.

[15] Z. Celep, A. Erken, B. Taskin, A. Ilki, “Failures of masonry and concrete buildings during the March 8, 2010 Kovancılar and Palu (Elazığ) Earthquakes in Turkey,” Engineering Failure Analysis, vol. 18, pp.868–889, 2011.

[16] Y. Calayır, E. Sayın, B. Yön, “Performance of structures in the rural area during the March 8, 2010 Elazığ-Kovancılar earthquake,” Natural Hazards, vol. 61(2), pp. 703-717, 2012.

[17] E. Sayın, B. Yön, O. Onat, M. Gör, M. E. Öncü, E. T. Tunç, D. Bakır, M. Karaton, Y. Calayır, “24 January 2020 Sivrice-Elazığ, Turkey earthquake: geotechnical evaluation and performance of structures,” Bulletin of Earthquake Engineering, vol. 19, pp. 657-684, 2021.

[18] M. Günaydın, B. Atmaca, S. Demir, A. C. Altınışık, M. Hüsem, S. Adanur Ş. Ateş, Z. Angın, “Seismic damage assessment of masonry buildings in Elazığ and Malatya following the 2020 Elazığ-Sivrice earthquake, Turkey,” Bulletin of Earthquake Engineering, vol. 19, pp. 2421-2456, 2021.

[19] M. Yetkin, İ. Ö. Dedeoğlu, Y. Calayır, “Investigation and Assessment of Damages in the Minarets Existing at Elazig After 24 January 2020 Sivrice Earthquake,” Fırat University Journal of Engineering Sciences, vol. 33 (2), pp. 379-389, Sep. 2021.

[20] URL-1. https://deprem.afad.gov.tr/deprem-tehlike-haritasi. Access: February 01, 2021.

[21]URL-2. http://udim.koeri.boun.edu.tr/zeqmap/osmap.asp. Access: February 01, 2021.

[22] Ministry of Environment and Urbanization-Elazığ Provincial Directorate of Environment and Urbanization Finalized damage assessment results for the 24 January 2020 earthquake. Elazığ, Turkey, 2020.

[23] Turkish Earthquake Code, Ministry of Public Works and Settlement, Ankara (in Turkish), 2007.

[24] Turkish Building Earthquake Code, Ministry of Environment and Urbanization, Ankara (in Turkish), 2018.

SAKARYA ÜNİVERSİTESİ
FEN BİLİMLERİ ENSTİTÜSÜ
DERGİSİ

Sakarya University Journal of Science
SAUJS

ISSN 1301-4048 | e-ISSN 2147-835X | Period Bimonthly | Founded: 1997 | Publisher Sakarya University |
http://www.saujs.sakarya.edu.tr/

Title: Mass Distributions and Neutron-Proton Ratios of Fragments in Peripheral Heavy-Ion Collisions

Authors: Hamide AVCI

Recieved: 2022-04-19 00:00:00

Accepted: 2022-08-10 00:00:00

Article Type: Research Article

Volume: 25
Issue: 5
Month: October
Year: 2022
Pages: 908-914

How to cite
Hamide AVCI; (2022), Mass Distributions and Neutron-Proton Ratios of Fragments in Peripheral Heavy-Ion Collisions. Sakarya University Journal of Science, 25(5), 908-914, DOI: 10.16984/saufenbilder.1105788
Access link
http://www.saujs.sakarya.edu.tr/en/pub/issue/73051/1105788

Sakarya University Journal of Science 25(5), 908-914, 2022

Mass Distributions and Neutron-Proton Ratios of Fragments in Peripheral Heavy-Ion Collisions

Hamide AVCI*[1]

Abstract

The mass and average neutron-proton ratio (N/Z) distributions of fragments from multifragmentation of excited projectile nuclei formed in heavy-ion collisions were reproduced theoretically. The experimental measurements in peripheral heavy-ion collisions of ^{124}Sn + ^{124}Sn and ^{112}Sn + ^{112}Sn at 1 GeV/nucleon were carried out with the Fragment Separator (FRS) of GSI. The mass distribution and N/Z ratios of the produced nuclear fragments are calculated in the frame of a statistical approach. Comparisons with the experimental data show that the statistical models are successfully reproduce the mass yields and N/Z measured in the both reaction systems. The calculations in the present paper were carried out for the first time and were not published anywhere else.

Keywords: Mass yield, nuclear multifragmentation, neutron-proton ratio (N/Z)

1. INTRODUCTION

One of the most important aims of current research in the field of nuclear physics is to describe the behavior of nuclear matter at extreme conditions at high temperature and pressure at various densities (to determine the equation of state related to the symmetry energy). For this reason, the properties of nuclear matter at extreme conditions have been under investigations by various groups both experimentally and theoretically. The results of these studies can be used in a wide range of research areas such as radiotherpy (treatment planning), space research, isotope production etc. The results are also used as a tool to investigate the stellar matter at extreme conditions as a fundamental research subject in astrophysical studies. The supernova explosion mechanism and neutron stars modelling may be examples of this kind of studies.

In order to simulate nuclear multifragmentation reactions the liquid-gas phase transition theory is widely used. In this theory, it is assumed that the hot and dense nuclear matter is formed when two heavy-ion collide at high energies. Then this matter expands as a result of strong repulsive forces at short distances and enters subsaturation densities. In this case the density fluctuations of the matter leads the system to thermodynamical equilibrium. At the end of this process the matter disintegrates into nuclear hot fragments. When there are at least 3 intermediate mass fragments satisfying the condition Z ≥ 3. At saturation density $\rho_0 = 0.15 fm^{-3}$, and freeze-out density $\rho \approx \frac{\rho_0}{3}$. The low temperature region is defined as $T \approx 3 - 8\, MeV$. The properties of large and

---

* Corresponding author: himal@selcuk.edu.tr
[1] Selçuk University
ORCID: https://orcid.org/0000-0003-2097-6054

small hot particles can be studies with statistical models relying on the phase transition theory.

Beside statistical models, dynamical models such as Time Dependent Hartree Fock, Molecular Dynamics and Quantum Molecular Dynamics are also widely used in modeling the nuclear reactions and astrophysical events. Nucleation theory of nuclear matter can also be studied on the basis of macroscopic models which rely on Fisher nucleation model, and kinetic theory of Boltzmann and Boltzmann-Uehling-Uhlenbeck (BUU) equation. Presently, we consider statistical multifragmentation model in this calculations. So far the results based on the statistical multifragmentation model show that this model is found to be very successful for reproducing the experimental data of nuclear reactions at low and high energies [1- 7].

For the additional important references we can cite for mid-peripheral heavy ion collision experiments as [8]. We also refer to the experiments performed at relativistic projectile energies around 1 GeV/nucleon in the high-resolution magnetic spectrometer, the Fragment Separator (FRS) at GSI laboratories for the ^{124}Sn + ^{124}Sn and ^{112}Sn + ^{112}Sn reactions, and the experimental results [9]. In the present paper, FRS (FRagment Separator) experiments were theoretically analysed in the framework of statistical multifragmentation model.

2. MATERIALS AND METHODS

We know that in the statistical approach to analyse the nuclear reactions, there is a concept of equilibrium as described: a) There are few stages of reactions leading to multifragmentation. b) There is a short time around 100fm/c for primary fragment production. c) We assume that freeze-out low density should be around 0.1 -0.6 ρ_0 (here ρ_0 is the normal nuclear matter density) d) There is a high degree of equilibration at the freeze-out volume.

Various models can be used for the definition of peripheral heavy-ion collisions. In this study, we have used the statistical multifragmentation model (SMM) [4]. According to the SMM, when two heavy-ion collide, a compressed and hot blob of nuclear matter is formed. This dense and hot substance will expand due to repulsive nucleon-nucleon forces. It will then enter a low-density freezing zone and the system reaches a statistical equilibrium. According to this model all fragmentation channels are composed of nucleons. It assumes that the laws of conservation of energy, momentum, angular momentum, mass number A and charge number Z are taken into account. It also includes compound nucleus channels and the competition between all channels is permitted. The statistical weight of fragmentation channels is defined in the Microcanonical approach as follows:

$$W_j = \frac{1}{\xi} \exp\left(S_j\left(E^*, A, Z\right)\right) \tag{2.1}$$

where Sj is the entropy of the system in channel j and ξ is the normalization constant.

Accessible states of decay channels are created by the Monte Carlo method considering the statistical weight of these channels. In this approach the particles with A ≤ 4 are considered as elementary particles or gase particles. The fragments with A>4 are considered as hot liquid droplets. In this case, the coexistence of the phases in the freezing volume can be studied on the liquid-gas phase transition theory. To express the free energy one may utilize the Weizecker's semi-empirical formula. In this formula, the F_{AZ} of each fragment is the sum of the bulk, surface, Coulomb and symmetry energy contributions as shown below:

$$F_{AZ} = F^B_{A,Z} + F^S_{A,Z} + E^C_{A,Z} + E^{sym}_{A,Z} \tag{2.2}$$

The terms are defined as follows:

$$F^B_{A,Z} = -\left(W_0 + \frac{T^2}{\varepsilon_0}\right)A \tag{2.3}$$

where, T is the temperature, ε_0 is related to the level density (approx. 16 MeV at normal nuclear matter density), and W_0 is the binding energy of infinite nuclear matter ($16MeV$),

$$F^{S}_{A,Z} = B_0 A^{2/3}\left(\frac{T_c^2 - T^2}{T_c^2 + T^2}\right)^{5/4} \tag{2.4}$$

where B_0 is the surface energy coefficient (18MeV), and *Tc* is the critical temperature of infinite nuclear matter (18 MeV);

$$E^{C}_{A,Z} = c\frac{Z^2}{A^{1/3}} \tag{2.5}$$

where

$$c = \left(\frac{3}{5}\right)\left(\frac{e^2}{r_0}\right)\left(1-\left(\frac{\rho}{\rho_0}\right)^{1/3}\right) \tag{2.6}$$

is the Coulomb parameter get from the Wigner-Seitz approach with the charge unit *e* and $r_0 =$ 1.17 fm;

$$E^{sym}_{A,Z} = \frac{\gamma(A-2Z)^2}{A} \tag{2.7}$$

where γ is the standard effective symmetry energy parameter (25 MeV). The parameters here are those in the Bethe-Weizsäcker formula and correspond to the conjecture of isolated fragments with normal density in the freeze-out configuration. These liquid drop paramaters including symmetry and surface terms should be reduced at low densities (for excited hot fragments) to reproduce the experimental data measured in the yields of fragments emitted from the heavy-ion collisions [5- 7].

3. RESULTS AND DISCUSSION

In the literature, important properties of nuclear multifragmentation have been studied in various studies. For examples; fragment multiplicity, charge distribution, mass distribution, isotopic distribution and isoscaling observables. In this study, we reproduced the fragment mass and neutron to proton ratio distributions in the ^{124}Sn + ^{124}Sn and ^{112}Sn + ^{112}Sn reactions performed at 1 GeV/nucleon at GSI laboratory. The initial neutron-to-proton ratios of these symmetrical systems are 1.24 and 1.48 for ^{112}Sn and ^{124}Sn, respectively. Now, we compare our results and experimental data [9]. In the calculations, the projectile and target nuclei were chosen to have the same N/Z so that isospin diffusions can be excluded. A statistical ensemble version of the SMM was used to define the properties of this isospin symmetric reaction systems. In our previous publication [10] we investigated the isotope and charge yields in the same reaction system of FRS experiments. Now, we have presently investigated mass yield and mean N/Z ratios of the fragmentation products of the same reactions. As for the comparison of our theoretical calculations and the experimental data, we normalized the data and predicted results with respect to the measured cross sections in the interval $20 \leq Z \leq 25$ as shown in Ref.[10]. The obtained factor was 0.00334 mb and 0.00344 mb per theoretical event for fragmentation of ^{124}Sn and for ^{112}Sn projectiles, respectively.

Figure 1 shows the present results that we obtained from the statistical ensemble calculations for the mass distribution of the final cold fragments in 500 000 reaction events. Here, red stars represent the experimental data and blue circles the theoretical predictions. Upper panel shows the mass distribution of the particles emitted from a neutron-rich projectile ^{124}Sn and lower panel the results for a neutron-poor projectile source ^{112}Sn.

The results were in agreement with the literature, that the U-shape of nuclear mass distributions were seen in Figure 1, both in upper and lower panels. Theoretical calculations for Z<10 are not shown in Figure 1. Because there is no experimental data that we can compare in this region. From these figures, one can see an agreement between theoretical and experimental values of the yields. Since the isotopes cannot be fully addressed in the experiments, such differences are, generally, observed in the distribution curves. See Refs [9, 11] for a comprehensive analysis of these differences.

Recently, we have carried out the calculations for weakly excited nuclear matter to reproduce the compound nuclei contribution at low excitation energies for Ex<1 MeV/nucleon [12]. In order to calculate the contribution of compound nuclei, the excitation energy interval was chosen, within weighting calculations, from 0 to 4 MeV per nucleon with the corresponding masses and charges of the excited source nuclei. Thus we demonstrated a connection of the compound nucleus regime with the multifragmentation regime.

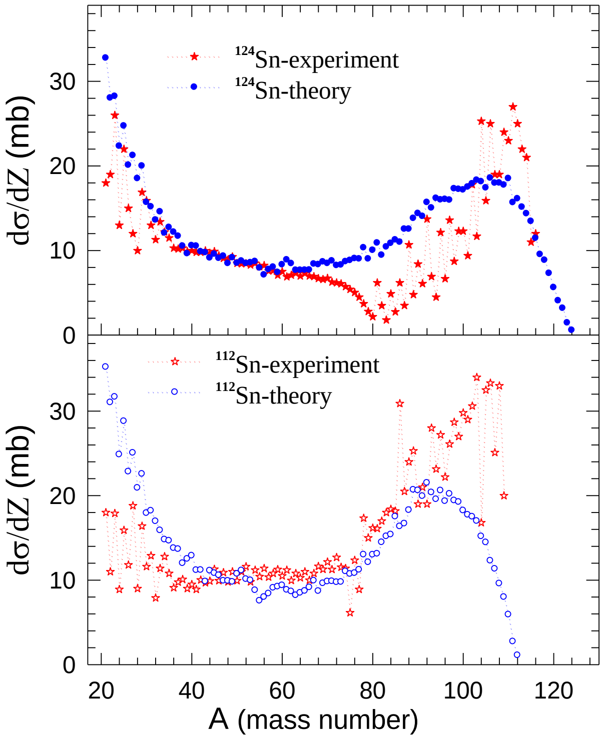

Figure 1 Production cross-sections of fragments emitted from two reaction systems as a function of mass number of the fragments

The final stage in the evolution of a highly excited nuclear system is the de-excitation stage of hot primary particles. Primary hot fragments are emitted from excited semi-projectile sources. This state in which all particles are considered hot can be described as "hot" fragmentation. When the system expands and the excitation of the hot primary particles is removed, cold fragmentation occurs. In the case of "cold" fragmentation the fragments preserve the Z/A ratio of initial nucleus. In contrast to that the "hot" fragmentation products, after the de-excitation stage, fall into the vicinity of the β-stability line, the so called exotic nuclei [4].

Figure 2 shows the present results that the average <N>/Z ratios of primary fragments (hot) and secondary fragments (cold) as a function of fragment charge number Z, in the interval 10 ≤ Z ≤ 25. Upper panel shows the results for a neutron-rich projectile ^{124}Sn (full circles) and lower panel shows the results for a neutron-poor projectile source ^{112}Sn (empty circles). In this figure, red stars show the experimental result. Blue symbols show the theoretical calculations for cold fragments and red symbols show theoretical calculations of the hot fragments formed before de-excitation process. These systems have a large difference in neutron-to-proton ratios of the fragments emitted from their quasiprojectile sources. The differences between the N/Z values of the hot fragments in the upper and lower panels of Figure 2, are also higher than the differences between the N/Z values of the cold fragments. This stems from the large difference in the initial isospin asymmetry of the reaction systems and de-excitation processes.

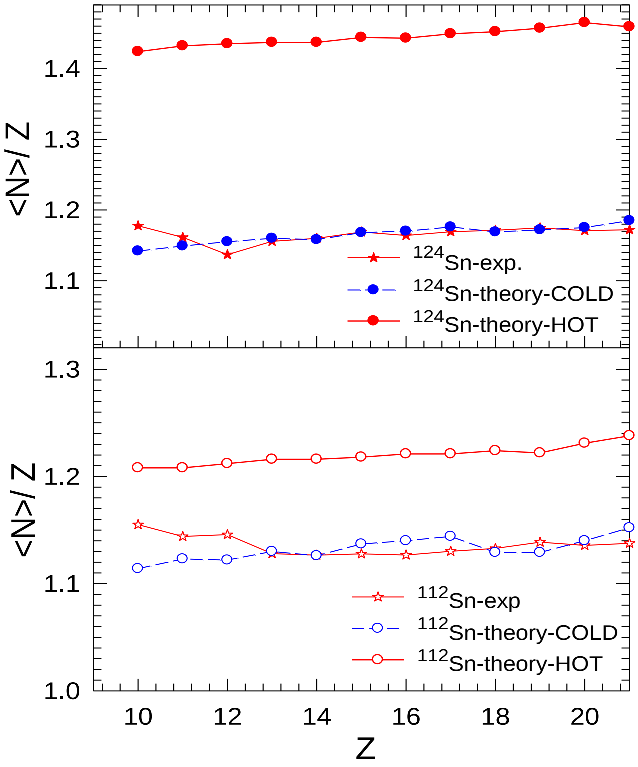

Figure 2 Mean N/Z values of the fragments emitted from two reaction systems

In the calculations of N/Z values we have used the reduced symmetry energy values for the optimization process in Ref. [10]. For a detailed discussion of the modifications of these model parameters in optimization calculations, we will refer the reader to Refs. [5, 13]. One can see in Figure 2 that, the most neutron-rich systems preferably populate the most neutron-rich isotopes, additionally the most proton-rich systems populate the most proton-rich isotopes. This result may be observed in Figure 2 that both in experimental and predicted theoretical calculation data. This is consistent with other findings in the literature (see e.g. Ref. [14]).

4. CONCLUSIONS

As a result, we have shown that statistical models successfully reproduce the experimental data for fragment production and mean N/Z values. It is remarkable that in the present calculations the isospin term (symmetry energy) is not subdivided into surface and volume parts, simply we have taken the effective values of the symmetry energy parameter into account as 25 MeV. One can see from the figures that there is a good agreement between theoretical and experimental results. We can argue that our results are in consistent with the existing studies in the literature [5-7, 10, 15]. It is shown in our calculations that the symmetry energy parameter should be reduced at low densities to be able to reproduce the experimental data. The effect of other liquid-drop parameters of nuclear matter are widely investigated in Ref. [5].

Consequently, our analysis of FRS experiments show that neutron-rich sources preferentially, produce neutron rich fragments when enough excitation energy is deposited in projectile nuclei. Thus, we have shown that the nuclear multifragmentation reactions become superior to produce neutron-rich and proton-rich isotopes, in relativistic energies (1 GeV/nucleon) [5, 9, 11], as well, as a continuation of the Fermi energy regime [16-18].

To investigate the properties of nuclear matter at extreme conditions in more details, further experiments are needed e.g., to extract information for the properties of neutron-rich exotic nuclei towards the neutron dripline in nuclear chart [19].

Acknowledgments
I gratefully acknowledge the enlightening discussions with R. Oğul and N. Büyükçizmeci during the calculations.

Funding
"The author has no received any financial support for the research, authorship or publication of this study."

The Declaration of Conflict of Interest/ Common Interest

No conflict of interest or common interest has been declared by the authors.

The Declaration of Ethics Committee Approval

The author declares that this document does not require an ethics committee approval or any special permission.

The Declaration of Research and Publication Ethics

The author of the paper declare that they comply with the scientific, ethical and quotation rules of SAUJS in all processes of the paper and that they do not make any falsification on the data collected. In addition, she declare that Sakarya University Journal of Science and its editorial board have no responsibility for any ethical violations that may be encountered, and that this study has not been evaluated in any academic publication environment other than Sakarya University Journal of Science.

REFERENCES

[1] N. Bohr, "Neutron capture and nuclear constitution," Nature (London) vol. 137: pp. 344-348, 1936.

[2] V. E. Viola, K. Kwiatkowski, L. Beaulieu, D. S. Bracken, H. Breuer, J. Brzychczyk, R. T. de Souza, D. S. Ginger, W-C. Hsi, R. G. Korteling, T. Lefort, W. G. Lynch, K. B. Morley, R. Legrain, L. Pienkowski, E. C. Pollacco, E. Renshaw, A. Ruangma, M. B.

Tsang, C. Volant, G. Wang, S. J. Yennello, N. R. Yoder, “Light-ion-induced multifragmentation; The ISiS project,” Physics Reports-Review Section of Physics Letters, vol. 434, no. 1-2, pp. 1-46, 2006.

[3] G. Bertsch, P. J. Siemens, “Nuclear fragmentation,” Physics Letters B, vol. 126, no. 1-2, pp. 9-12, 1983.

[4] J. P. Bondorf, A. S. Botvina, A. S. Iljinov, I. N. Mishustin, K. Sneppen, “Statistical multifragmentation of nuclei,” Physics Reports-Review Section of Physics Letters, vol. 257, no 3, pp.133-221, 1995.

[5] R. Ogul, A. S. Botvina, U. Atav, N. Buyukcizmeci, I. N. Mishustin, P. Adrich, T. Aumann, C. O. Bacri, T. Barczyk, R. Bassini, S. Bianchin, C. Boiano, A. Boudard, J. Brzychczyk, A. Chbihi, J. Cibor, B. Czech, M. De Napoli, J.-É. Ducret, H. Emling, J. D. Frankland, M. Hellström, D. Henzlova, G. Immè1, I. Iori, H. Johansson, K. Kezzar, A. Lafriakh, A. Le Fèvre, E. Le Gentil, Y. Leifels, J. Lühning, J. Łukasik, W. G. Lynch, U. Lynen, Z. Majka, M. Mocko, W. F. J. Müller, A. Mykulyak, H. Orth, A. N. Otte, R. Palit, P. Pawłowski, A. Pullia, G. Raciti, E. Rapisarda, H. Sann, C. Schwarz, C. Sfienti, H. Simon, K. Sümmerer, W. Trautmann, M. B. Tsang, G. Verde, C. Volant, M. Wallace, H. Weick, J. Wiechula, A. Wieloch, B. Zwiegliński, “Isospin-dependent multifragmentation of relativistic projectile,” Physical Review C, vol. 83, no. 2, article number 024608, 2011.

[6] N. Buyukcizmeci, R. Ogul, A. S. Botvina, “Isospin and symmetry energy effects on nuclear fragment production in liquid-gas phase transition region,” European Physical Journal A, vol. 25, no. 1, pp. 57-64, 2005.

[7] N. Buyukcizmeci, H. Imal, R. Ogul, A. S. Botvina, I. N. Mishustin, “Isotopic yields and symmetry energy in nuclear multifragmentation reactions,” Journal of Physics G- Nuclear Particle Physics, vol. 39, no. 11, article number 115102, 2012.

[8] S. P. Avdeyev, V. A. Karnaukhov, L. A. Petrov, V. K. Rodionov, P. A. Rukoyatkin, V. D. Toneev, H. Oeschler, O. V. Bochkarev, L. V. Chulkov, E. A. Kuzmin, A. Budzanowski, W. Karcz, M. Janicki, E. Norbeck, A. S. Botvina, K. K. Gudima, “Comparative study of multifragmentation of gold nuclei induced by relativistic protons, He-4 and C-12,” Nuclear Physics A, vol. 709, pp. 392-414, 2002.

[9] V. Föhr, A. Bacquias, E. Casarejos, T. Enqvist, A. R. Junghans, A. Kelić-Heil, T. Kurtukian, S. Lukić, D. Pérez-Loureiro, R. Pleskač, M. V. Ricciardi, K.-H. Schmidt, and J. Taïeb, “Experimental study of fragmentation products in the reactions 112Sn + 112Sn and 124Sn + 124Sn at 1A GeV,” Physical Review C, vol. 84, no. 5, article number 054605, 2011.

[10] H. Imal, A. Ergun, N. Buyukcizmeci, R. Ogul, A. S. Botvina, W. Trautmann, “Theoretical study of projectile fragmentation in the 112Sn+112Sn and 124Sn +124Sn reactions at 1 GeV/nucleon,” Physical Review C, vol. 91, no. 3, article number 034605, 2015.

[11] D. Henzlova, K.-H. Schmidt, M. V. Ricciardi et al., “Experimental investigation of the residues produced in the 136Xe+Pb and 124Xe+Pb fragmentation reactions at 1 A GeV,” Physical Review C, vol. 78, no. 4, article number 044616, 2008.

[12] H. Imal, R. Ogul, “Theoretical study of isotope production in the peripheral heavy-ion collision 136Xe + Pb at 1 GeV/nucleon,” Nuclear Physics A, vol. 1014, article number 122261, 2021.

[13] A. S. Botvina, N. Buyukcizmeci, M. Erdogan, J. Łukasik, I. N. Mishustin, R. Ogul, and W. Trautmann, “Modification of surface energy in nuclear multifragmentation,” Physical Review C, vol. 74, no. 4, article number 044609, 2006.

[14] A. Kaya, N. Buyukcizmeci, R. Ogul, “Isotopic distribution in projectile fragments

above the Coulomb barrier," Turkish Journal of Physics, vol. 42, no. 6, pp. 659-667, 2018.

[15] R. Ogul, N. Buyukcizmeci, A. Ergun, A. S. Botvina, "Production of neutron-rich exotic nuclei in projectile fragmentation at Fermi energies," Nuclear Science and Techniques, vol. 28, no. 2, article number 18, 2017.

[16] H. Imal, N. Buyukcizmeci, R. Ogul, A. S. Botvina, "Isospin dependence of fragment yields in peripheral heavy ion collisions," Europen Physical Journal A, vol. 56, no. 4, article number 110, 2020.

[17] M. B. Tsang, T. X. Liu, L. Shi, P. Danielewicz, C. K. Gelbke, X. D. Liu, W. G. Lynch, W. P. Tan, G. Verde, A. Wagner, H. S. Xu, W. A. Friedman, L. Beaulieu, B. Davin, R. T. de Souza, Y. Larochelle, T. Lefort, R. Yanez, V. E. Viola, Jr., R. J. Charity, L. G. Sobotka, "Isospin diffusion and the nuclear symmetry energy in heavy ion reactions," Physical Review Letters, vol. 92, no. 6, article number 062701, 2004.

[18] S. Piantelli, G. Casini, P. R. Maurenzig, A. Olmi, M. Bini, S. Carboni, G. Pasquali, G. Poggi, A. A. Stefanini, R. Bougault, E. Bonnet, B. Borderie, A. Chbihi, J. D. Frankland, D. Gruyer, O. Lopez, N. Le Neindre, M. Parlog, M. F. Rivet, E. Vient, E. Rosato, G. Spadaccini, M. Vigilante, M. Bruno, T. Marchi, L. Morelli, M. Cinausero, M. Degerlier, F. Gramegna, T. Kozik, T. Twarog, R. Alba, C. Maiolino, D. Santonocito, "Isospin transport in Kr-84+Sn-112, Sn-124Sn collisions at fermi energies," Physical Review C, vol. 87, no. 5, article number 054607, 2013.

[19] N. Buyukcizmeci,, A. S. Botvina, I. N. Mishustin, R. Ogul, M. Hempe, J. Schaffner-Bielich, F.-K. Thielemann, S. Furusawa, K. Sumiyoshi, S. Yamada, H. Suzuki, "A comparative study of statistical models for nuclear equation of state of stellar matter," Nuclear Physics A, vol. 907, pp. 13–54, 2013.

SAKARYA ÜNİVERSİTESİ

FEN BİLİMLERİ ENSTİTÜSÜ
DERGİSİ

Sakarya University Journal of Science
SAUJS

ISSN 1301-4048 | e-ISSN 2147-835X | Period Bimonthly | Founded: 1997 | Publisher Sakarya University |
http://www.saujs.sakarya.edu.tr/

Title: Characterization Of Jute/Aramid Hybrid Composite Materials with Using Different Resins

Authors: Berkay KARACOR, Mustafa ÖZCANLI

Recieved: 2022-02-28 00:00:00

Accepted: 2022-08-15 00:00:00

Article Type: Research Article

Volume: 25
Issue: 5
Month: October
Year: 2022
Pages: 915-930

How to cite
Berkay KARACOR, Mustafa ÖZCANLI; (2022), Characterization Of Jute/Aramid Hybrid Composite Materials with Using Different Resins. Sakarya University Journal of Science, 25(5), 915-930, DOI: 10.16984/saufenbilder.1080172

Sakarya University Journal of Science 25(5), 915-930, 2022

Characterization Of Jute/Aramid Hybrid Composite Materials with Using Different Resins

Berkay KARACOR*[1], Mustafa ÖZCANLI[1]

Abstract

For the last twenty to thirty years, interest in the use of hybrid fiber-reinforced composites has gradually increased due to their potential for various applications. The balanced strength and stiffness properties of hybrid composites, along with the advantages of lighter weight and lower cost, have made them an important step toward replacing traditional materials. In this study, a hybrid composite was made from a combination of Jute fabric from natural fibers, Aramid fabric from synthetic fibers, and two different resins (polyester and vinylester). This type of study was proposed because there is little research in the literature on how the use of polyester and vinyl ester resins affects the mechanical properties of homogeneous composites and hybrid composites. The vacuum assisted resin transfer molding process was used for the fabrication. The mechanical properties of the manufactured products were determined by tensile and hardness tests, and their morphological structures were examined by taking scanning electron microscope images. The results indicate that the value of tensile strength and elastic modulus of the Jute/Aramid hybrid samples in the productions prepared with polyester resin is 37.6% and %12.28, respectively, higher than in those made with vinyl ester resin. When comparing the values for microhardness, the results of the Jute/Aramid hybrid specimens produced with polyester resin were 1.20 times higher than those produced with vinyl ester resin. Scanning electron microscope images of the samples also clearly show that the bonding between matrix and fiber is better in polyester resin samples.

Keywords: Hybrid composites, jute fiber, aramid fiber, polyester resin, vinylester resin

1. INTRODUCTION

Hybrid composites are materials in which two or more materials form a combination, where the advantages and disadvantages of their components become a balance element. The hybridization process provides possibilities to obtain and develop customized material properties based on the unique properties of its constituent components. For a suitable hybridization process, the fiber and design must be compatible, and the performance-price balance of the composite materials would be well taken into account [1, 2]. Hybridization is indicated in many studies as a solution to reduce the disadvantageous properties of natural fibers and the applications of sustainable, non-environmental synthetic fibers. As a modern material, hybrid composites formed by synthetic-natural fibers have directed the attention of the

---

* Corresponding author: berkaykaracor01@gmail.com
[1] Çukurova University
ORCID: https://orcid.org/0000-0001-5208-366X, https://orcid.org/0000-0001-6088-2912
E-mail: ozcanli@cu.edu.tr

manufacturing sector to the use of hybrid composites and these materials have found various application areas such as marine, aviation and automotive sector, making hybridization an increasingly effective solution [3, 4]. In this context, natural fiber reinforced composites, which are expected to be used more in hybrid composites, come to the fore as an alternative and environmentally friendly option to synthetic fiber composites. Jute, flax, kenaf, hemp, ramie, and banana can be counted as the main stem type natural fibers. Among these fibers, jute is one of the strongest bast fibers grown in tropical countries and at low cost [5]. Jute is a widely used natural plant fiber with its easy availability and good insulating properties. In addition to being one of the most common agricultural fibers exhibiting moderately higher mechanical properties, jute has seen a significant increase in use as reinforcing materials in composites, along with flax fiber, over the past decade. This increased use can be attributed to the specific mechanical properties of the fiber obtained from the natural jute plant and its very good compatibility with polymers [6, 7]. In the search for alternatives to traditional materials, synthetic fiber-reinforced composite materials from fiber-reinforced composites have become the focus of attention due to the potential to replace these materials in various applications. Compared to traditional metallic materials, synthetic fibers are preferred due to their low weight, high mechanical properties, flexible structure, convenience in manufacturing, and corrosion resistance. Among these fibers, poly aramid fiber, called Kevlar fiber, stands out with its distinctive features [8]. Choosing Kevlar as a reinforcing element in composites has become popular due to its unique properties such as good strength, high impact and high energy absorption capacity, higher modulus, and higher strength per mass rate. In addition to its current use in helmets, bulletproof waistcoats, badminton and tennis rackets, airplanes, helicopter rotor blades, Kevlar fiber has a high potential for use in high-value applications, including vehicles, both for commercial purposes and as an innovative material in the future [9]. Polymer matrix composites are formed from polymer resin as matrix and fibers as reinforcement element. The matrix material generally determines the maximum service temperature because it normally softens, melts, or decomposes at a temperature much lower than the fiber reinforcement. The matrix materials commonly used in composite materials are thermosets and thermoplastics. Thermoset composite matrices include epoxies, phenolics, cyanate esters, bismaleimides, polyesters, polyimides, and vinyl esters [10]. Polyester resin is heat resistant, high strength, and tough. Polyester is a reactive solid and unsaturated in a polymerizable monomer. They are produced by a growth reaction between a glycol and an unsaturated (malic or fumaric) dibasic destructor [11]. Polyester resins are known for their fast curing, versatility, and long life at room temperature, but they also have disadvantages such as self-polymerization at higher temperatures compared to epoxy [12]. Vinyl esters, which are very similar to polyesters in molecular structure, differ from polyesters by having merely reactive groups at the ends of the molecular bond. The fact that vinyl esters have fewer ester groups than polyesters, and that the ester group is more sensitive to hydrolysis by water, increases their resistance to deterioration from water and moisture [13]. Vinylester materials are less sensitive at ambient temperature, with significant interfacial adhesion of natural fibers to the polymer matrix, but have a greater curing effect than polyester [14]. Little research has been done in the field of composite materials created using different resins reinforced with Kevlar and Jute fibers. Bhanupratap and Chittappa [15] investigated the effect of Kevlar fabric on the mechanical properties of hybrid composites they created by adding Kevlar fabric to homogeneous Jute fabric reinforced composites. As the Kevlar fiber ingredient increased in the hybrid composites, it was observed that the tensile strength and load carrying capacity of the jute reinforced epoxy composites increased. In another Jute/Kevlar fiber reinforced epoxy composite investigation [16], the effect of reinforcement elements on the thermal properties of the material designed using dynamic mechanical features was investigated. By adding increasing numbers of Kevlar and converting them to hybrid composites, it increased the storage modulus and loss modulus, glass transition temperature (T_g) compared to pure Jute composites. Maharana et al. [17] created Jute/Kevlar hybrid composites using a hand layup process and investigated how fiber orientation would affect mechanical features. While 20% Kevlar as a weight percent remained constant in the produced composites, the amount of jute changed with epoxy. The maximal tensile endurance value was determined at 30° orientation in the fiber orientation, and the bending strength value was determined the highest at 45° fiber orientation. In a different study [18], the impact absorption energy of hybrid composites formed with Jute fiber and Kevlar fiber was tested. A low velocity impact test was applied to the composites at heights between 50 mm and 250 mm, and energies were observed to vary between 0.4 J and 2.3 J. As the amount of Kevlar fiber increases in the hybrid composites formed, the impact energy of the composites and the absorbed energy increase with the increase in height and speed, and penetration is either absent or partial. Maharana et al. [19] created several hybrid array combinations of bidirectional woven Jute and Kevlar fabric, in which nanoscale fumed silica was used as the filler reinforcement. Double cantilever beam and end notch bending tests were applied to 13 different hybrid composite material combinations they produced. They determined the effect of layering sequence and nanofiller content on interlayer fracture toughness. In other examination [20], in which fumed silica was used as nanofiller and Jute fiber and Kevlar fiber were used as reinforcement elements, it was desired to observe the moisture absorption capacity of the hybrid materials produced. In the results, it was found that when the nanofiller reinforcement was increased up to 3%, the moisture absorption capacity of the hybrid composites decreased, the amount of more than 3% had an adverse effect on moisture absorption, the surface exposure of the jute fibers decreased and the moisture absorption decreased as the proximity of the Kevlar fiber to the surface in the composites increased. In a search in which Kevlar fiber and sisal fiber formed a hybrid composite, it was found that maximum mechanical properties were obtained when the nano silica additive to the polyester resin was 4%, and it was understood that increasing the nano silica ratio more than 4% had a negative effect on the mechanical properties [21]. In the study of Dogan et al. [22], they found that the absorbed energy and deformation amounts of graphene nanoplatelets added at different rates to the hybrid structure consisting of Aramid fiber and carbon fiber also had a significant effect. It was stated that 0.1% and 0.25% by weight nanoparticles added to the resin created the best effect on the structures. In the study of Cetin et al. [23], they analyzed the energy absorbed, deformation and damage in the composites they formed by reinforcing carbon and aramid fibers with halloysite nanotubes. In these analyzes carried out at different temperatures, they stated that the damage increased as the temperature decreased, and the nanoparticle additive had a positive effect on the mechanical properties of the material at the same temperatures. In another study where Cetin et al. [24] examined the effect of nanoparticles on wear in carbon-aramid fiber hybrid composites, they stated that as the percentage of halloysite nanotubes added to the composite material increased, the wear rate and friction coefficient decreased from 9% to 11%. In his study, Cetin [25] examined how the addition of multi-walled carbon nanotube filler (0.1% and 0.2% by weight) to sandwich composite materials affects low velocity impact energy, it was observed that 0.1% nanomaterials improved low velocity impact energy properties. In researches where glass fiber and Kevlar fiber are used as hybrid yarns and polyester resin is preferred as resin, the presence of Kevlar fiber in hybrid yarns significantly increases the mechanical properties, while the effects of fiber orientation and aging test applied on the results are seen [26, 27]. Kennedy and Inigo Raja [28] chose Jute fiber and glass fiber reinforcement material, polyester resin as matrix material in their studies. It has been observed that hybrid Jute/Glass fibers improve their mechanical properties compared to pure Jute fibers in tensile, bending, impact, and hardness tests, and even in some tests, hybrid material properties exceed those of pure glass fiber composite material. Hybrid composites formed by Kevlar fibers and natural fibers are used not only where mechanical properties are important but also where physical properties such as sound insulation are important. When the good mechanical strength properties of synthetic fibers are combined with the acoustic properties of natural fibers, these materials become a remarkable alternative in sound transmission loss performance [29]. Swami and Dabade [30] investigated the optimum fiber-resin combination in the study where different resin types (epoxy, polyester, vinylester) were reinforced with glass fiber. Inter-laminar shear stress and bending test results, it is stated that the highest mechanical properties were obtained in the sample with 60% fiber and 40% vinyl ester resin, while the polyester resin fiber combination showed the lowest mechanical properties. Khare et al. [31] produced composites using different percentages of jute and glass fibers by hand lay-up three different resins as epoxy, vinylester, and polyester. The highest tensile, flexural strengths, and impact energy were obtained with grewiaoptiva at 7.5 wt% in epoxy-based hybrid composites, while the value was found to be better when using grewiaoptiva at 5% wt for hardness compared to other resins. Bozkurt et al. [32] and Bulut et al. [33] performed impact behavior, damping and vibration analysis of hybrid structures formed by aramid fibers with basalt fibers. They showed that the volumetric percentage of aramid fibers in the hybrid structure and the variation of the sequence order with basalt fibers significantly affect the mechanical properties of the hybrid composites. The objective of this research is to examine the mechanical properties of hybrid composites produced in the combination of Jute and Kevlar fibers, rarely used in studies, with two different resins (vinylester and polyester). The mechanical properties of pure Jute and pure Aramid reinforced composites will be compared with the use of two different resins in the results of the study with the hybridization of natural Jute fibers and synthetic Kevlar fibers. The results of the analysis will shed light on the emergence of a low-cost material that can be used in the automotive industry, both in terms of the resin used and the use of natural fibers.

2. MATERIAL AND METHOD

2.1. Material

The reinforcing materials used were plain weave Jute fabric and Aramid twill fabric. Both fabrics were supplied by a company in Istanbul, Turkey. For this research, Table 1 contains the texture characteristics. Figure 1 indicates the texture specimens.

Table 1 Fabric features [34, 35]

Fabric	Weight (g/m²)	Thickness of fabric(mm)	Warp	Weft
Jute fabric	250	0.4	-	-
Aramid fabric	170	0.25	1270	1270

Figure 1 Texture samples: a) Jute texture b) Aramid texture

In the work, polyester resin with related additives and vinyl ester resin with related ingredients were benefitted for matrix materials. They were procured from the Poliya company. Technical specifications of the resins are demonstrated in Table 2 and Table 3. Mixing was carried out for both polyester and vinyl ester resins in a weight ratio of resin: cobalt nephthalate (as an accelerator): methyl ethyl ketone peroxide (MEKP) of 1:0.002:0.02.

Table 2 Polyester properties [36]

Maximum temperature (°C)	170
Flexural strength (MPa)	134
Elongation at break (%)	2.6
Viscosity (cps)	500-600
Tensile strength (MPa)	71
Barcol Hardness	40

Table 3 Vinylester properties [37]

Flexural strength (MPa)	155
Elongation at break (%)	5
Viscosity (cps)	200-250
Tensile strength (MPa)	76
Barcol Hardness	36

Twelve composite specimens were produced using two different resins and with different fabric stacking orders. Table 4 displays the pattern names for the texture laminas in the composite specimens.

Table 4 Naming pattern specimens

Pattern Names	**Texture kinds**
J	Jute fabric
A	Aramid fabric
JA	Jute/Aramid fiber hybrid composite
JP	Jute fiber reinforced polyester hybrid composite
AP	Aramid fiber reinforced polyester hybrid composite
JAP	Jute/Aramid fiber reinforced polyester hybrid composite
JV	Jute Fiber reinforced vinylester hybrid composite
AV	Aramid fiber reinforced vinylester hybrid composite
JAV	Jute/Aramid fiber reinforced vinylester hybrid composite

After curing at 60 °C for 1 hour, the composite specimens were cut off with a water jet machine in accordance with the test sizes determined in the norms, such as 250 mm length, 25 mm width, and 2.5 mm thickness. As the state of the produced samples before the tensile test is given in Figure 2, the stacking sequences of the fabrics are given in Figure 3 and Figure 4.

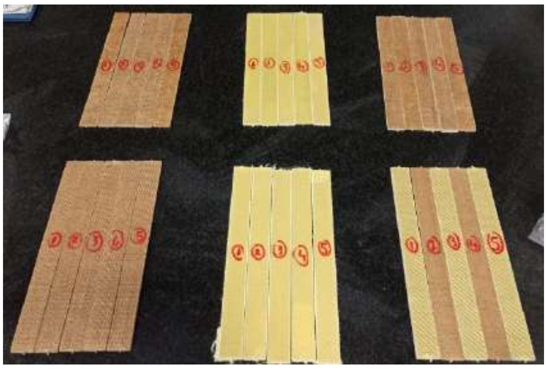

Figure 2 Composite samples after water jet machine application

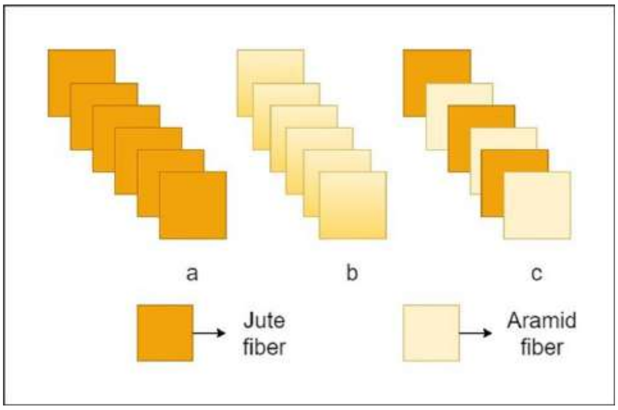

Figure 3 Fabric stacking sequences of a) JP b) AP c) JAP

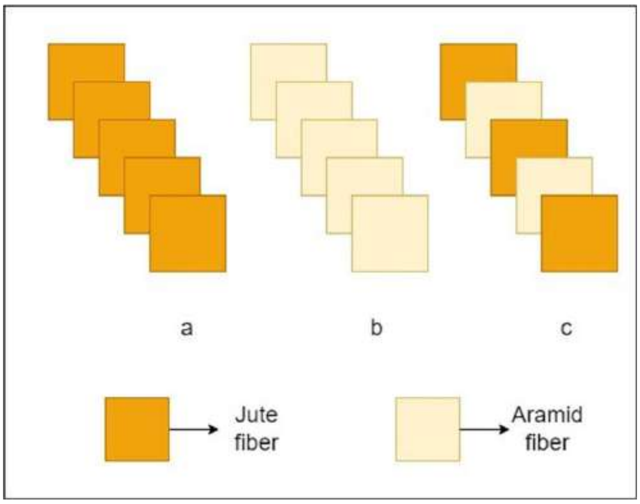

Figure 4 Fabric stacking sequences of a) JV b) AV c) JAV

2.2. Method

The vacuum-assisted resin transfer process was used to produce composite laminates reinforced with jute and aramid fibers. The composites were prepared at ambient temperature (20°C±2°C). This method uses a vacuum to remove the air from the reinforcing material so that the resin can penetrate the preform. The production area was created by using tempered glass for the composite production process. Firstly, the surface was sanitized and the area to be produced was determined with a vacuum sealing tape. Mold release wax was applied twice at specified times to the specified surface. Then the fabrics were laid in the predetermined sequence, and the peeling fabric and infusion net were set on top. The system was sealed with a vacuum bag, in an airtight manner, only two small holes were made for the resin inlet and outlet. During these procedures, the mixing ratio of resin and additional additives was specified, considering the values from prior manufacturing, and the blend was put together thence. Lastly, the vacuum pump was started to absorb the resin (Figure 5). The vacuum pump was operated for an average of 2 hours at a pressure of about 1 bar and was switched off as soon as the additional resin flow on the sample was interrupted. The products prepared to complete the curing process were left in this position for 24 hours. At the end of this period, the test samples were put into the oven and kept at 60°C for 1 hour.

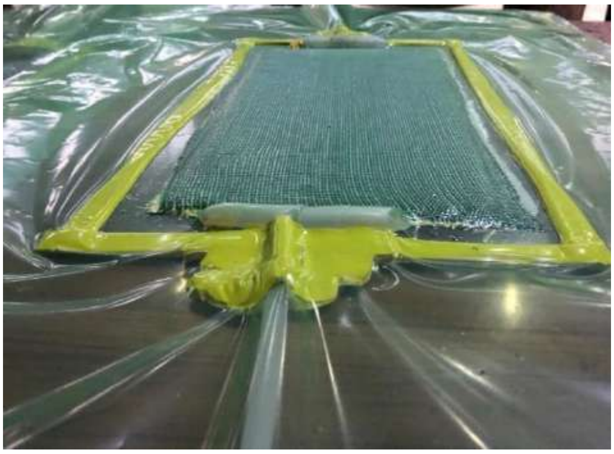

Figure 5 Vacuum assisted resin transfer molding process

2.3. Tensile Testing

The tensile experiment was performed to decide the mechanical properties of the produced composite specimens. Average tensile strength values were calculated by testing 5 samples from each configuration were tested, resulting in a total of 6 configurations. The tensile test was performed following the ASTM D 3039 standard [38]. The test was carried out with ALŞA hydraulic testing device (KOLUMAN Automotive Industry Laboratory) and 2 mm/min was adjusted as the cross-head speed on the machine with a 98000 kN load cell. Figure 6 displays the universal tensile tester. The tests were carried out at room temperature, and the sample sizes were recorded in the computer program before starting the tests. In addition to the automatic drawing of the engineering stress-strain diagram by a computer connected to the machine, the tensile strength, elastic modulus, and elongation ratios are calculated by the device.

Figure 6 Tensile testing machine

2.4. Hardness Testing

The definition of hardness in materials is known as resistance to local plastic deformation. In order to determine the hardness of the samples produced in this study, Vickers hardness tests, also called 136-degree diamond pyramid hardness tests, were performed. In hardness samples, the sample thickness was produced to be 1.5 mm. The Vickers hardness value was determined by measuring 15 hardness measurements from different areas of the surface of each sample, and the average of these values was found as the hardness value. While the hardness test of the samples was carried out with respect to the ASTM E92-17 standard [39], the AOB Lab hardness test measuring device was used. Figure 7 demonstrates the Vickers hardness test device.

Figure 7 Hardness testing machine

2.5. Morphological Analysis

The most suitable method for analyzing fiber surface morphology of materials is scanning electron microscopy (SEM). Owing to this method, fracture surfaces, fiber-matrix interactions, and fiber structures formed in composites can be observed as a result of tests. A Scanning Electron Microscope FEI Quanta 650 Field Emission instrument at an acceleration voltage of 100V-30kV was used for SEM analysis. In order to increase the superficies conductibility of the specimens, a gold overlay was done by spraying method. The machine seen in Figure 8 has a magnification capacity of 6-1,000,000 x. In order to see the hybridization effects, in addition to analyzing the quantitative data, the effects of mechanical fracture in a macroscopic way can be examined by SEM.

Figure 8 SEM analysis machine

3. RESULT AND DISCUSSION

3.1. Tensile Test Results

Figure 9 highlights that composite products prepared with polyester resin has higher tensile strength than those prepared with vinylester resin. It is understood from Figure 10 that this trend continues in the same way in the tensile modulus results. In the tensile strength results, it was found that the tensile strength value of the samples prepared with polyester resin was 1.37 times superior to the samples prepared with vinylester resin. In the tensile modulus outcomes, the samples using polyester resin were 1.12 times higher than the samples using vinylester resin. As seen in Figures 9 and 10, the highest tensile strength and tensile modulus values were obtained in pure aramid composite products. Pure jute composites, on the other hand, had the lowest values among the products produced in terms of both tensile strength and tensile modulus. The tensile strength results are also close in the studies where jute fibers and polyester resin are used together. The tensile strength values of the samples in the study are not far from each other. While the woven topology in the samples reduces the shrinkage in the fibers while the samples are breaking, it is stated that the progression of the crack formation is caused by the pulling of the fibers from the hollow structures in the matrix [40, 41]. When evaluated in terms of hybridization effect among the produced products, the tensile strength of JAP products was 3.89 times higher than that of JP products, and the tensile strength of JAV products was 3.09 times higher than JV products. This resulted in the value of the JAV product being 1.87 times higher than the value of the JV product, and the value of the JAP product being 1.88 times higher than the value of the JP product in the tensile modulus comparison. The low mechanical properties of jute fibers due to their nature are tried to be eliminated by using different fiber structures and by hybridization. In another study in which jute fibers were hybridized, an increase in tensile strengths of 4.79% and 6.14% were found depending on the warp and weft directions. In addition, it has been stated that the core-centered array creates an advantage in mechanical properties compared to the axial surface array in fiber fabric arrays [42]. In this study, the hybridization process with Aramid fibers provides improved tensile strength and tensile modulus values in the produced composites, but also provides a significant change in character. The use of polyester resin with jute fibers improved the tensile strength of the composite structure by 1.09 times compared to the use of vinylester resin with jute fibers, while the composite structures of aramid fibers prepared with polyester resin allowed an improvement in tensile strength by 1.32 times compared to structures prepared with vinylester resin. In the comparison of pure jute composites in the tensile modulus results, it was determined that the modulus value of JP was 1.12 times higher than that of JV, and the modulus value of AV was 1.55 times higher than that of AP. Considering the elongation rates in Figure 11, the elongation rates of the samples prepared with vinylester resin were higher than the samples prepared with polyester resin. The elongation rate values indicate the ductility of the sample. Since the factors that increase the yield and tensile strengths of material mostly decrease the ductility, it is seen that the samples prepared with polyester resin with high strength value results have less elongation rate. While the JAV structure showed 1.28 times higher elongation rate than the JAP structure, this difference was found to be 1.93 times in favor of AV between AV and AP and 1.11 times in favor of JV between JV and JP. Pure jute fiber polyester resin structures showed 1.81 times less elongation than hybrid jute/aramid fiber polyester resin structures. Structures formed with pure jute fiber polyester resin showed 1.57 times less elongation than structures formed with hybrid jute/aramid fiber polyester resin.

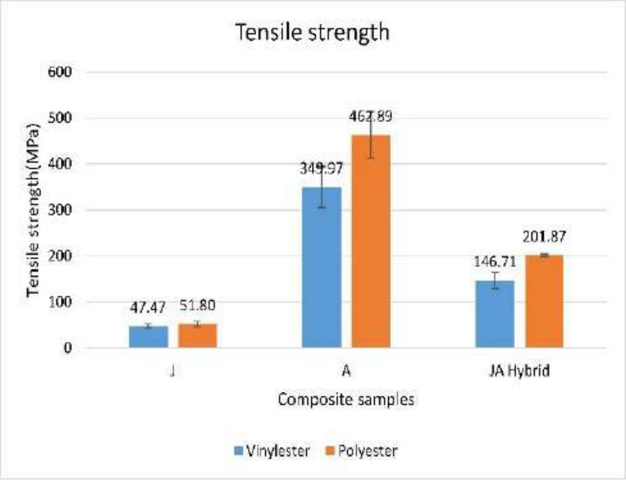

Figure 9 Tensile strength test results

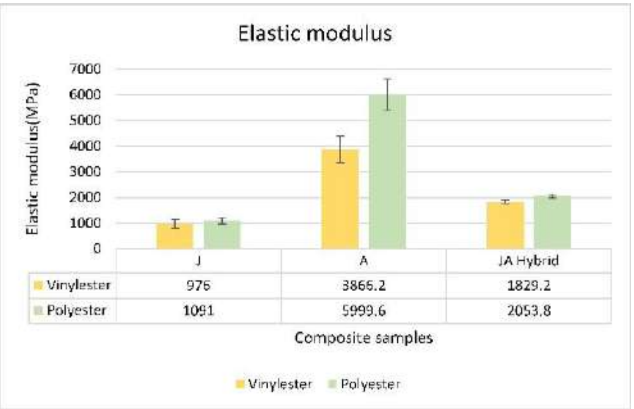

	J	A	JA Hybrid
Vinylester	976	3866.2	1829.2
Polyester	1091	5999.6	2053.8

Figure 10 Elastic modulus results

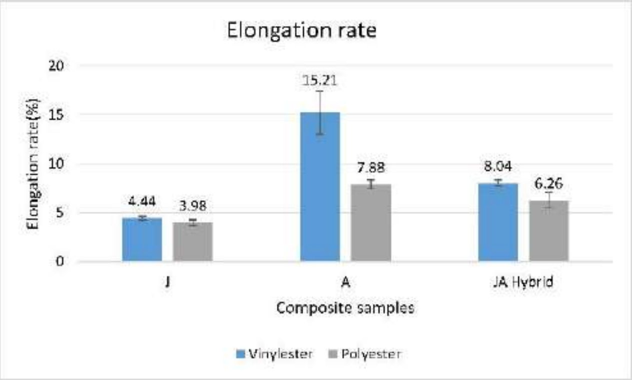

Figure 11 Elongation rate results

Figures 12- 17 indicate one of the stress-strain curves closest to the mean value from each configuration of the samples tested. As seen in Figures 12 and 13, rupture was observed at the maximum force of 4.2-4.63 kN with the brittle structure of the jute fiber. The fracture forces with the high elongation amount of aramid fibers were also determined at the values of 15.12-20.65 kN, as can be seen from Figures 14 and 15. As stated in Figures 16 and 17, in hybrid composites, on the other hand, a breaking force was determined between pure jute and pure aramid composites with a maximum breaking force of 11.35-16.02 kN, almost without departing from a linear curve.

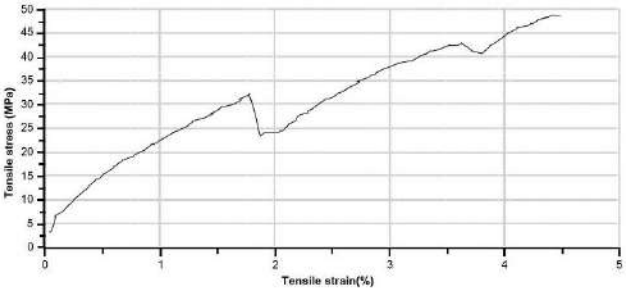

Figure 12 Stress-strain curve of JV sample

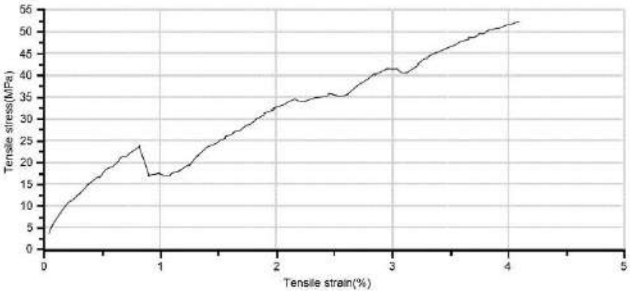

Figure 13 Stress-strain curve of JP sample

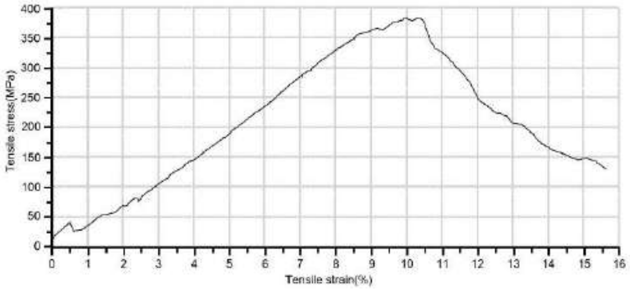

Figure 14 Stress-strain curve of AV sample

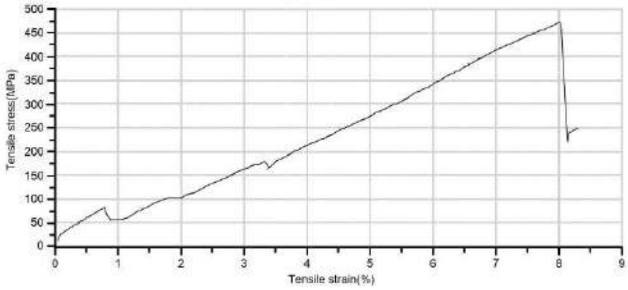

Figure 15 Stress-strain curve of AP sample

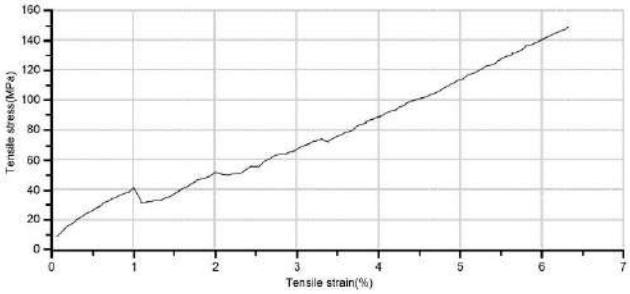

Figure 16 Stress-strain curve of JAV sample

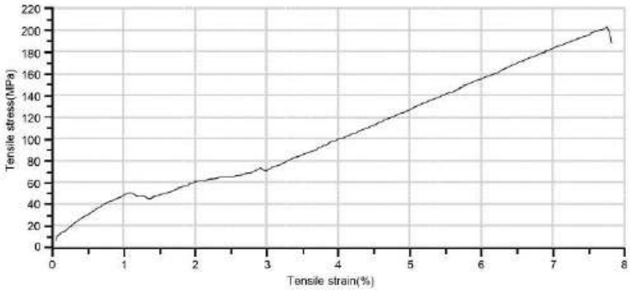

Figure 17 Stress-strain curve of JAP sample

Figure 18 and Figure 19 indicates the photographs of broken surfaces after the tensile test. From the sample images in Figure 18, it is understood that the ductile structure of aramid fibers manifests itself in the form of elongation of the fibers, while the jute fibers have a more fragile structure and break from the axial center. In hybrid jute/aramid structures, fiber tearing occurred on the outer surfaces, and unlike the breakage in pure jute fibers, aramid fibers tried to make breaking difficult. In the study examining the impact force applied to aramid and basalt, it was determined that the fibers showed slight ruptures and cracks occurred in the central region. High stresses where the impact force is applied have been the areas where the deformations are concentrated [3, 32].

Figure 18 Back side view(a) of JP, AP and JAP and front side view(b) of JP, AP and JAP

When the breaks in the vinylester resin samples in Figure 19 were examined, it was observed that there was no complete break in the aramid fibers. This explains why the percent elongation in tensile results is greater in samples prepared with vinylester resin. It was determined that the JV structures were completely broken, as in the JP structures in Figure 18. In the JAV structure, it was understood that the elongation of the fibers was less than that of the JAP structure, and it showed sharper breakage. In the study [2], in which aramid fiber and glass fiber were used as reinforcement elements, it was stated that the sequence types of the samples determined the tearing in the fabrics. Therefore, in the hybrid structures, the fibers in the outer layers of the fabrics were broken.

Figure 19 Back side view (a) of JV, AV and JAV and front side view (b) of JV, AV and JAV

3.2. Hardness Test Results

In view of Vickers hardness test outcomes as seen in Figure 20, products using polyester resin in composite production have higher Vickers hardness than products using vinylester resin. The use of aramid fabric as a reinforcement element in the use of both polyester and vinylester resin gave the highest Vickers hardness value. The use of jute fiber fabric as a reinforcing element showed the lowest Vickers hardness values in both resins. Hybridization of jute fabric with aramid fabric increased the hardness value in both resins compared to homogeneous composites using Jute fabric from the natural fiber fabric category. In this study [43], where the hybridization of Aramid fabric to natural fiber fabrics was investigated, it was observed that the addition of 5% Aramid fabric increased the hardness value by 14% compared to the pure vinylester resin composite.

While the Vickers hardness value of the JAP sample increased by 49.28% compared to the homogeneous JP sample, the hardness value of the JAV sample increased by 89.71% compared to the homogeneous JV sample. There is a difference of 20.2% between the JAP hybrid sample and the JAV hybrid sample in terms of hardness in favor of the composite sample using polyester resin. When the product specification values are also examined, the hardness value of pure polyester resin is higher than that of vinylester resin, as given in Tables 2 and 3. This difference is 52.75% on behalf of JP structure for JP and JV samples, while 10.24% is on behalf of AP structure for AP and AV samples. These results indicate that the highest hardness value difference is in the samples using Jute reinforced polyester resin and vinylester resin. In the study of Khare et al. [31], the hardness value in the samples produced by using polyester resin together with jute fiber was higher than the samples using vinylester resin, even though jute fiber was used in varying ratios such as 2.5% and 7.5%.

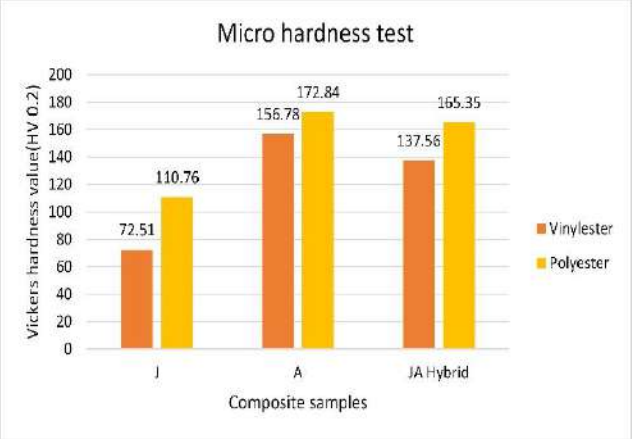

Figure 20 Micro hardness test results

3.3. SEM Analysis Results

The SEM images of Figures 21 displays the morphological structure of the JV after the tensile test, and also Figure 22 and 23 demonstrate morphologies the AV and JAV hybrid composite structures after the tensile test. In the JV composite structure as seen in Figure 21, fiber breaks are observed due to the brittle structure of the jute fibers, while in the AV composite structure in Figure 22, it is understood that the aramid fibers are broken homogeneously and there is no rupture. In the JAV composite structure in Figure 23, it has been determined that the Kevlar fiber provides a higher mechanical property by reducing the shrinkage effect on the jute fiber, with the effect of the hybrid structure, compared to the JV structure. It has also been noted in previous studies that hybridization of Kevlar fiber with jute provides a significant matrix fiber interaction [44, 45].

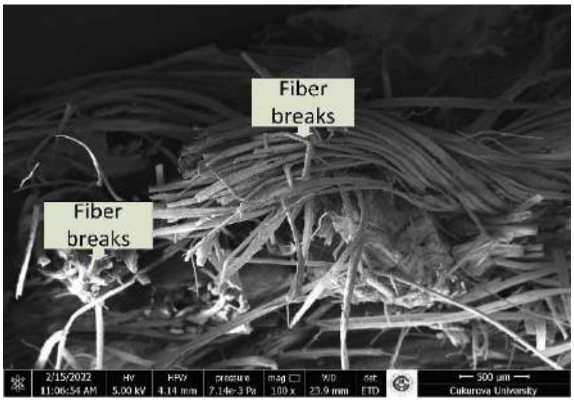

Figure 21 JV composites SEM micrograph

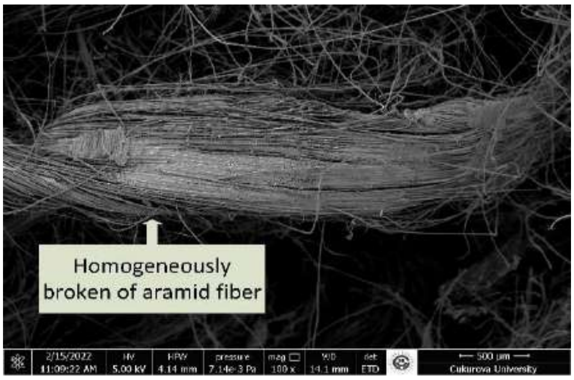

Figure 22 AV composites SEM micrograph

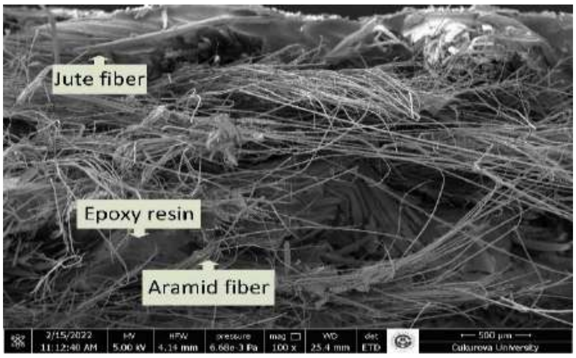

Figure 23 JAV hybrid composites SEM micrograph

Figures 24 shows the morphological forms of JP composite structures after the tensile test. Figures 25 and 26 indicate the morphological examination of AP and JAP composite structures after the tensile test prepared with polyester resin. Compared with the SEM images in Figures 21, 22, and 23, it is seen that JP, AP, and JAP hybrid composite structures have fewer voids, fewer air bubbles, and high toughness structure. In the tensile test results, better tensile strength values are obtained in the use of polyester resin compared to the use of vinylester resin, which is supported by these morphological analysis images. The absence of gaps around the fiber in the AP composite structure as in Figure 25 compared to the JP composite structures as in Figure 24 indicates that it provides a better adhesion with the resin. In structures where aramid fibers are used as reinforcing elements, fiber abrasion and fiber breakage occur as frequently encountered situations. Significant cases of rupture and micro buckling in Kevlar fibers have also been found in other studies [46]. In the JP composite structure, the fibers are not broken evenly, while a more homogeneous breakage is detected in the JAP composite structure in Figure 26.

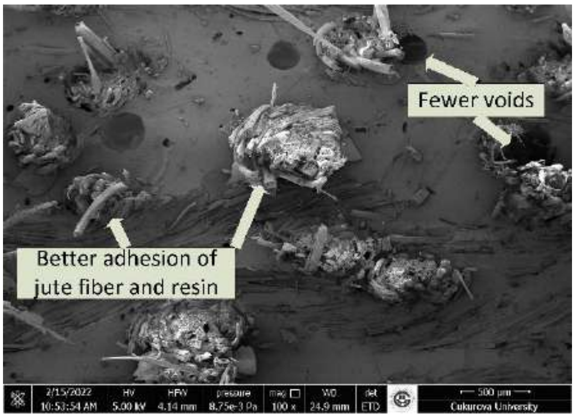

Figure 24 JP composites SEM micrograph

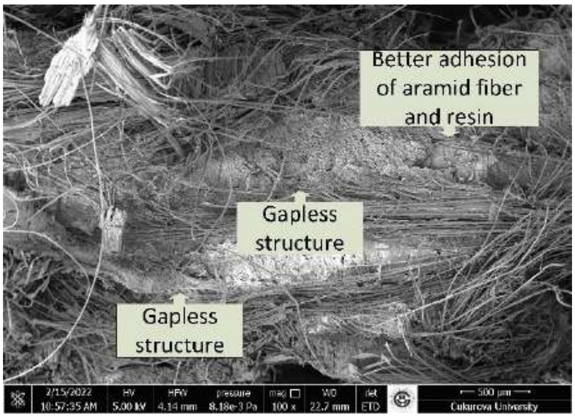

Figure 25 AP composites SEM micrograph

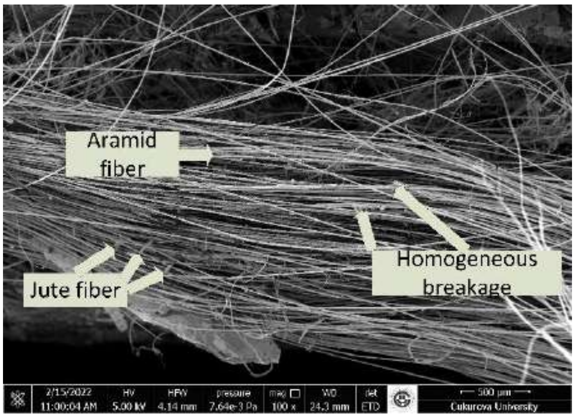

Figure 26 JAP hybrid composites SEM micrograph

4. CONCLUSION

In this work, jute fabric made of natural fibers and Kevlar fabric made of synthetic fibers were preferred as reinforcement elements, vinylester and polyester resins were preferred as matrix elements. The effects of using two different resins on the mechanical properties of the pure and hybrid composites were investigated. It has been determined that the use of polyester resin in hybrid jute/aramid composites improves the tensile strength, tensile modulus and microhardness value compared to the use of vinylester resin. The use of polyester resin, as understood from the SEM analysis results, provided better delamination resistance and structural integrity of the structures by creating better interfacial bonds between the fiber and the matrix and allowing less air gaps. In addition, it can be deduced from the results of this study that the mechanical properties of jute fibers in hybrid structures are improved by the hybridization process of jute fibers with aramid fibers in both resins. The results of this paper show that the use of polyester resin for reinforcement with jute and aramid fabrics results in better mechanical properties than vinylester resin. The use of polyester resin, which is more economical in terms of cost, instead of the commonly used epoxy resin, together with jute fibers, which are cheaper than Kevlar fibers and belong to natural fibers, points to an important point in terms of less harm to the environment and sustainability. In the light of the results of this study, these materials offer designers new ideas in terms of cost and weight without any loss in performance in the areas of the interior of the vehicle.

Funding

The authors have no received any financial support for the research, authorship or publication of this study.

The Declaration of Conflict of Interest/ Common Interest

No conflict of interest or common interest has been declared by the authors.

Authors' Contribution

The first author contributed 60%, the second author 40% to the study. BK: Literature research, conducting experiments, writing the article, MO: Literature research, writing the article.

The Declaration of Ethics Committee Approval

This study does not require ethics committee permission or any special permission.

The Declaration of Research and Publication Ethics

The authors of the paper declare that they comply with the scientific, ethical and quotation rules of SAUJS in all processes of the paper and that they do not make any falsification on the data collected. In addition, they declare that Sakarya University Journal of Science and its editorial board have no responsibility for any ethical violations that may be encountered, and that this study has not been evaluated in any academic publication environment other than Sakarya University Journal of Science.

REFERENCES

[1] K. Ganesan, C. Kailasanathan, N. Rajini, Sikiru O. Ismail, N. Ayrilmis, F. Mohammad et al., “Assessment on hybrid jute/coir fibers reinforced polyester composite with hybrid fillers under different environmental conditions,” Construction and Building Materials, vol. 301, no. June 2020, p. 124117, Sep. 2021.

[2] Z. A. Oguz, A. Erklig, O. Y. Bozkurt, “Degradation of hybrid aramid/glass/epoxy composites hydrothermally aged in distilled water,” Journal of Composite Materials, vol. 55, no. 15, pp. 2043-2059, 2020.

[3] Z. A. Oguz, A. Erklig, O. Y. Bozkurt, “Effects of hydrothermal seawater aging on the mechanical properties and water absorption of glass/aramid/epoxy hybrid composites,” International Polymer Processing, vol. 36, no. 1, pp. 79-93, 2021.

[4] M. J. Suriani, H. Z. Rapi, R. A. Ilyas, M. Petrů, S. M. Sapuan, “Delamination and Manufacturing Defects in Natural Fiber-Reinforced Hybrid Composite: A Review,” Polymers (Basel), vol. 13, no. 8, p. 1323, Apr. 2021.

[5] H. Chandekar, V. Chaudhari, S. Waigaonkar, “A review of jute fiber reinforced polymer composites,” Materials Today: Proceedings, vol. 26, pp. 2079–2082, 2020.

[6] P. Sai Shravan Kumar, K. Viswanath Allamraju, “A Review of Natural Fiber Composites [Jute, Sisal, Kenaf],” Materials Today: Proceedings, vol. 18, pp. 2556–2562, 2019.

[7] J. B. Sajin, P. Babu Aurtherson, J. S. Binoj, N. Manikandan, M. S. Senthil Saravanan, T. M. Haarison, “Influence of fiber length on mechanical properties and microstructural analysis of jute fiber reinforced polymer composites,” Materials Today: Proceedings, vol. 39, pp. 398–402, 2021.

[8] T. J. Singh, S. Samanta, “Characterization of Kevlar Fiber and Its Composites: A Review,” Materials Today: Proceedings, vol. 2, no. 4–5, pp. 1381–1387, 2015.

[9] S. Rajesh, B. Vijayaramnath, C. Elanchezhian, S. Vivek, M. H. Prasadh, M. Kesavan, “Experimental Investigation of Tensile and Impact Behavior of Aramid-Natural Fiber Composite,” Materials Today: Proceedings, vol. 16, pp. 699–705, 2019.

[10] B. Karacor, “The Usage of Natural Fiber Reinforced Hybrid Composite Materials as An Alternative to Automobile Interior Plastics,” MSc Thesis, Cukurova University, 2020.

[11] G. Santosh Gangappa, S. Sripad Kulkarni, “Experimentation and validation of basalt & jute fiber reinforced in polymer matrix hybrid composites,” Materials Today: Proceedings, vol. 38, pp. 2372–2379, 2021.

[12] A. T. Seyhan, F. H. Gojny, M. Tanoğlu, K. Schulte, “Critical aspects related to processing of carbon nanotube/unsaturated thermoset polyester nanocomposites,” European Polymer Journal, vol. 43, no. 2, pp. 374–379, 2007.

[13] F. C. Campbell, Structural Composite Materials, ASM International, pp.64-67,2010.

[14] S. Ravindran, G. G. Sozhamannan, L. Saravanan, V. S. K. Venkatachalapathy, “Study on mechanical behaviour of natural fiber reinforced vinylester hybrid composites,” Materials Today: Proceedings, vol. 45, pp. 4526–4530, 2021.

[15] Bhanupratap R, Dr H C Chittappa, “Study of Tensile Behaviour by Variation of Kevlar to the Jute Fibre Epoxy Hybrid Composites,” International Journal of Engineering Research and Technology, vol. V6, no. 06, pp. 1039–1043, Jun. 2017.

[16] R. Bhanupratap, “Jute/Kevlar Fibre Reinforced Epoxy Composites: A Dynamic Mechanical Study,” Materials Today: Proceedings, vol. 22, pp. 3145–3151, 2020.

[17] S. M. Maharana, P. Samal, J. Dehury, P. P. Mohanty, “Effect of fiber content and orientation on mechanical properties of epoxy composites reinforced with jute and Kevlar,” Materials Today: Proceedings, vol. 26, pp. 273–277, 2020.

[18] R. Bhanupratap, “Impact damage resistance of Jute/Kevlar hybrid composite laminates subjected to varying heights: An experimental approach,” Materials Today: Proceedings, vol. 39, pp. 1396–1401, 2021.

[19] S. M. Maharana, M. K. Pandit, A. K. Pradhan, “Influence of fumed silica nanofiller and stacking sequence on interlaminar fracture behaviour of bidirectional jute-kevlar hybrid nanocomposite,” Polymer Testing, vol. 93, no. September 2020, p. 106898, Jan. 2021.

[20] S. M. Maharana, A. K. Pradhan, M. K. Pandit, “Moisture absorption behaviour of nanofiller reinforced jute-kevlar hybrid polymer composite,” Materials Today: Proceedings, vol. 26, pp. 775–780, 2020.

[21] M. S. Chowdary, G. Raghavendra, M. S. R. N. Kumar, S. Ojha, V. Boggarapu, “Influence of Nano-Silica on Enhancing the Mechanical Properties of Sisal/Kevlar Fiber Reinforced Polyester Hybrid Composites,” Silicon, vol.14, no.2, pp. 539-546, 2022.

[22] N. F. Dogan, O. Ozbek, A. Erklig, “Effect of graphene nanoplatelets on mechanical and impact properties of an aramid/glass-reinforced epoxy composite,” Materials Testing, vol. 64, no. 4, pp. 490–501, 2022.

[23] M. E. Cetin, A. C. Tatar, O. Demir, G. Onal, A. Avcı, “Effects of cryogenic and warm temperatures on quasi-static penetration resistance of carbon-aramid hybrid nanocomposites reinforced using halloysite

nanotubes," Mechanics of Materials, vol. 155, no. November, p. 103780, 2021.

[24] M. E. Cetin, Y. Bastosun, A. C. Tatar, M. H. Cetin, O. Demir, G. Onal, A. Avcı, "The effect of halloysite nanotube modification on wear behavior of carbon-aramid fiber reinforced hybrid nanocomposites," Polymer Composites, vol. 43, no. 1, pp. 624–637, 2022.

[25] M. E. Cetin, "Increasing Low-Velocity Impact Strength of Glass Fiber Sandwich Composites with Nanoparticle Reinforced Adhesive," Gazi University Journal of Science Part C: Design and Technology, vol. 9, no. 3, pp. 492–504, 2021.

[26] T. G. Targino, S. R. L. Tinô, E. M. F. Aquino, "Anisotropy, hole, and hybridization influences in polyester polymer composites reinforced by glass and glass/Kevlar," Polymer Composites, vol. 40, no. 12, pp. 4669–4681, Dec. 2019.

[27] R. C. T. S. Felipe, R. N. B. Felipe, A. C. M. C. Batista, E. M. F. Aquino, "Influence of environmental aging in two polymer-reinforced composites using different hybridization methods: Glass/Kevlar fiber hybrid strands and in the weft and warp alternating Kevlar and glass fiber strands," Composites Part B: Engineering, vol. 174, no. June, p. 106994, Oct. 2019.

[28] Z. Edward Kennedy, A. Inigo Raja M, "Influence of stacking sequence and hybridization on the mechanical and tribological properties of glass and jute fiber composites," Materials Today: Proceedings, pp. 4–9, Jul. 2021.

[29] P. A. Thakare, N. Kumar, V. B. Ugale, "Sound transmission loss and flexural strength assessment of hybrid composite reinforced with natural fibers and kevlar," Materials Today: Proceedings, vol. 19, pp. 686–690, 2019.

[30] M. C. Swami, B. M. Dabade, "Flexural and Inter-laminar shear stress properties of glass fiber reinforced Iso-polyester, Epoxy & vinyl ester composites," Materials Today: Proceedings, vol. 51 pp. 646–650, 2022.

[31] J. M. Khare, S. Dahiya, B. Gangil, L. Ranakoti, "Influence of different resins on Physico-Mechanical properties of hybrid fiber reinforced polymer composites used in human prosthetics," Materials Today: Proceedings, vol. 38, pp. 345–349, 2021.

[32] O. Y. Bozkurt, A. Erklig, M. Bulut, "Hybridization effects on charpy impact behavior of basalt/aramid fiber reinforced hybrid composite laminates," Polymer Composites, vol. 39, no. 2, pp. 467–475, 2018.

[33] M. Bulut, O. Y. Bozkurt, A. Erklig, "Damping and vibration characteristics of basalt-aramid/epoxy hybrid composite laminates," Journal of Polymer Engineering, vol. 36, no. 2, pp. 173–180, 2016.

[34] Kumascı, "Technical characteristics of Jute fiber," 2021. [Online]. Available: https://www.kumasci.com/urun/kanavice-jut-telis-cuval-kumasi-ham-en-sik-jut-10-onz-150-cm-en/7392.

[35] Kompozitshop, "Technical properties of Aramid fiber," 2021. [Online]. Available: https://www.kompozitshop.com/aramid-fiber-kevlar-elyaf-takviyeler.

[36] Poliya, "Polyester Properties," 2021. [Online]. Available: https://www.poliya.com/tr/el-yatirmasi-ve-elyaf-puskurtme.

[37] Poliya, "Vinylester Properties," 2021. [Online]. Available: https://www.poliya.com/tr/bisfenol-a-epoksi-bazli-vinilester-recineler.

[38] ASTM D3039/D3039-M, "Standard Test Method for Tensile Properties of Polymer Matrix Composite Material," ASTM International, 2000.

[39] ASTM E92-17, “Standard Test Methods for Vickers Hardness and Knoop Hardness of Metallic Materials,” ASTM International 2017.

[40] Y. Dobah, M. Bourchak, A. Bezazi, A. Belaadi, F. Scarpa, “Multi-axial mechanical characterization of jute fiber/polyester composite materials,” Composites Part B: Engineering, vol. 90, pp. 450–456, Apr. 2016.

[41] A. P. Abhishek, B. S. K. Gowda, G. L. E. Prasad, R. Velmurugan, “Probabilistic Study of Tensile and Flexure Properties of Untreated Jute Fiber Reinforced Polyester Composite,” Materials Today: Proceedings, vol. 4, no. 10, pp. 11050–11055, 2017.

[42] C. Tezara, J.P. Siregar, M.H.M. Hamdan, T. Rihayat, D. Bachtiar, D. F. Fitriyana P. Prayitno, “Influence of layering sequences on tensile properties of hybrid woven Jute/Ramie fibre reinforced polyester composites,” Materials Today: Proceedings, vol. 48, pp. 1836–1841, 2022.

[43] T. Singh, B. Gangil, A. Patnaik, S. Kumar, A. Rishiraj, G. Fekete, “Physico-mechanical, thermal and dynamic mechanical behaviour of natural-synthetic fiber reinforced vinylester based homogenous and functionally graded composites,” Materials Research Express, vol. 6, no. 2, p. 025704, Nov. 2018.

[44] S. Anidha, N. Latha, M. Muthukkumar, “Reinforcement of Aramid fiber with bagasse epoxy bio-degradable composite: Investigations on mechanical properties and surface morphology,” Journal of Materials Research and Technology, vol. 8, no. 3, pp. 3198–3212, 2019.

[45] R. Bhanupratap, “Study on characterization and sorption behavior of jute reinforced epoxy composite: Hybridization effect of Kevlar fabric,” Materials Today: Proceedings, vol. 27, no. 2020, pp. 2017–2021, 2019.

[46] R. C. T. Dos Santos Felipe, R. N. B. Felipe, A. C. De Melo Caldas Batista, E. M. F. Aquino, “Polymer composites reinforced with hybrid fiber fabrics,” Materials Research, vol. 20, no. 2, pp. 555–567, 2017.

SAKARYA ÜNİVERSİTESİ

FEN BİLİMLERİ ENSTİTÜSÜ DERGİSİ

Sakarya University Journal of Science
SAUJS

ISSN 1301-4048 | e-ISSN 2147-835X | Period Bimonthly | Founded: 1997 | Publisher Sakarya University |
http://www.saujs.sakarya.edu.tr/

Title: Conformational Analysis and DFT Investigations of 1-(4-Fluorophenyl)Piperazine by ELF and LOL, Inhibitory Activity Against Alzheimer’s Disease, and ADME Prediction

Authors: Sibel ÇELİK

Recieved: 2022-06-06 00:00:00

Accepted: 2022-08-15 00:00:00

Article Type: Research Article

Volume: 25
Issue: 5
Month: October
Year: 2022
Pages: 931-941

How to cite
Sibel ÇELİK; (2022), Conformational Analysis and DFT Investigations of 1-(4-Fluorophenyl)Piperazine by ELF and LOL, Inhibitory Activity Against Alzheimer’s Disease, and ADME Prediction. Sakarya University Journal of Science, 25(5), 931-941, DOI: 10.16984/saufenbilder.1126853
Access link
http://www.saujs.sakarya.edu.tr/en/pub/issue/73051/1126853

Sakarya University Journal of Science 25(5), 931-941, 2022

Conformational Analysis and DFT Investigations of 1-(4-Fluorophenyl)Piperazine by ELF and LOL, Inhibitory Activity Against Alzheimer's Disease, and ADME Prediction

Sibel ÇELİK*[1]

Abstract

This study reports 1-(4-Fluorophenyl)Piperazine molecule structural and electronic properties calculated at the DFT/B3LYP level. A potential energy surface scan along the rotational bonds discovered the most stable minimum energy conformer of the title compound. Frontier molecular orbital (FMO) analyses, density of state (DOS), molecular electrostatic potential (MEP), and global and chemical reactivity descriptors were also used to investigate the reactivity of the pFPP molecule. In addition, ELF and LOL analysis were performed. In silico biological studies such as drug-likeness, ADME, and toxicity properties were also performed. Molecular docking studies are performed to predict the anti-Alzheimer agent enzyme (AChE) active site of the pFPP. The docking predicts the possibility of a potential drug to improve Alzheimer's disease (AD) treatment.

Keywords: 1-(4-fluorophenyl)piperazine, DFT, ADME, ELF, LOL, molecular docking

1. INTRODUCTION

The piperazine derivatives are important pharmacophores across several different therapeutic areas [1] and act as antibacterial [2], antifungal, antipsychotic, antimalarial [3], and anti-HIV proteases [4]. On the other hand, it is frequently employed to generate a variety of physiologically active compounds, including anticonvulsant, anxiolytic, neuroprotective, antioxidant, antidepressant, and anti-Alzheimer's [5]. A large number of well-known medications with a variety of uses contain piperazine, a six-membered heterocyclic molecule that contains nitrogen [6]. Due to their powerful biological activity and their involvement in the creation of promising pharmacological candidates, fluorine-containing heterocyclic compounds have attracted considerable attention [7]. Many commercially available drugs contain a piperazine ring, mainly on the nervous system. This pathology is characterized by a decline in memory, language, problem solving, and some other cognitive skills. This condition affects the ability of the person to perform daily duties. Alzheimer's disease causes neurons to die, which eventually affects parts of the brain that

---

* Corresponding author: sibelcelik@ahievran.edu.tr
[1] Kırşehir Ahi Evran University
ORCID: https://orcid.org/0000-0002-4852-3826

help a person do basic physical tasks like walking and swallowing [8].

1-(4-fluorophenyl)piperazine (pFPP) is a neuropharmacologically active compound [9]. The actual benefit of this molecular structure for pharmaceutical development is the potential for straightforward coupling of several aldehyde moieties by reductive amination to different phenylbenzyl-piperazines. Different neuroligands have important structural motives, such as ligands for D2-like dopamine receptors, serotonin receptors, sigma receptors [10], adrenergic receptors [11], and calcium channels [12]. Most of the time, adding an aromatic fluorine to a ligand increases its affinity and/or selectivity, which is important for radiodiagnostics [13, 14].

In this paper, the detailed conformational study of the pFPP molecule was performed using DFT. The study of the stable conformer has been performed by theoretical and in silico biological methods. In order to understand the structural and electronic properties of the title molecule, DFT results were compared. The molecular stability, softness, and chemical reactivity of the pFPP molecule are determined by the FMOs and global reactivity Electrophilic and nucleophilic centers were discovered by the MEP, which may interact with biological targets. Also, ELF and LOL analysis of the optimized most stable conformer structure were performed. The drug-likeness, pharmacokinetic (ADME) characteristics, and toxicity investigations were all predicted computationally. In relation to Alzheimer's disease (AD), an in silico molecular docking study was also done on the title compound with a protein target.

2. THEORETICAL CALCULATIONS

Density functional theory (DFT) calculations were performed with the B3LYP functional and the 6-311++G(d) basis sets by using the Gaussian 09 software [15]. The most stable conformer structure is used for the HOMO-LUMO orbitals and MEP analysis of the investigated chemical. The Gaussview molecular visualization program [16] was used to visualize the HOMO, LUMO, and MEP analyses. The Multiwfn software program [17] is used to do the ELF and LOL. The Autodock 2.2.6 software was used to molecular docking the chemical ligand-protein binding site [18]. The docked complexes were visualized using PYMOL [19] and Discover studio software [20]. The RSCB protein data bank provided the 3D dimensional structure of AChE (PDB ID: 1EVE) (www.pdb.org). The ADME and Drug-likeness parameters of the title compound are calculated using Pre-ADMET software [21] and the SwissADME program [22]. The Protox-II website [23] was used to figure out the LD50, as well as the organ toxicity and toxicological end points of the pFPP compound.

3. RESULT AND DISCUSSION

3.1. Conformational studies

The same molecule can be in different positions at room temperature [24]. As a result, conformation analysis was used in this section of our study to determine the lowest energy structure of the title structure at room temperature using the initial structure B3LYP/6-311++G(d, p). To determine the more stable conformer of the pFPP molecule, the PES was generated by shifting this dihedral angle (C10-C8-N2-C4) from 0° to 180° with a step of 10°. The potential energy surface (PES) curve drawn as a result of the calculations is given in Figure 1, according to which there are three different conformers of molecular geometry. The calculated energy as well as relative energies of these conformers are given in Table 1. The results of the PES scan show that conformer II is most stable with the lowest potential energy at an angle of 110° for the selected (C10-C8-N2-C4) dihedral angle.

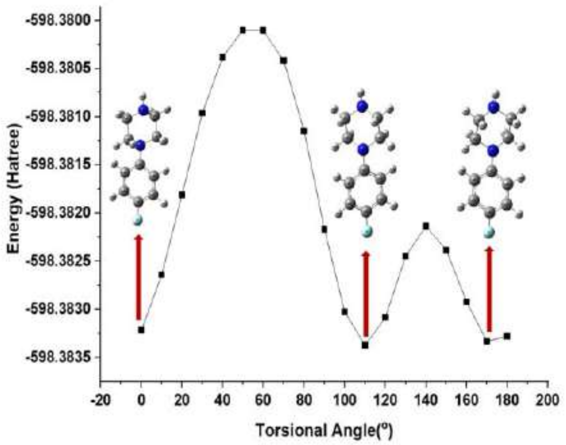

Figure 1 Scan of total energy of C10-C8-N2-C4 dihedral angle calculated by B3LYP/6–311++G(d,p) method.

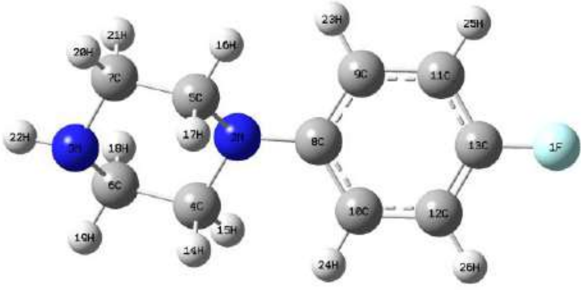

Figure 2 Optimized geometric structure

Table 1 Ground-state optimized energy and energy difference of all pFPP conformers

Conformer	Dihedral angle (°)	Energy (Hartree)	*Energy differ. (Hartree)
I	0	-598.383215640	0.000157
II	110	-598.383372769	0.000000
III	170	-598.383331269	0.000041

* Other conformers' relative energies in relation to the lowest energy of conformer I (Figure 2)

3.2. Frontier Molecular Orbitals and Chemical Reactivity Descriptors

The frontier molecular orbital (FMOs) analysis using quantum chemistry techniques is a well-known tool for explaining molecular transitions [25- 28]. The these orbitals control the mode of interaction between pharmaceuticals and other molecules, including interactions between drugs and their receptors [29]. Figure 3 shows the isodensity surface plots of HOMO and LUMO for the examined compound. Since HOMO is mostly delocalized on –phenyl ring and partially on the –piperazin ring, charge transfer within the system can be seen as LUMO is on phenyl ring. In this study, HOMO and LUMO are critical quantum chemical characteristics that are used to compute several significant parameters, such as chemical reactivity descriptors, and these are calculated and given in Table 2. The HOMO-LUMO energy gap is calculated as 4.99 eV. This band gap confirms that pFPP has a stable, bioactive structure and that charge transfer occurs within the molecule [30]. The lower chemical potential and higher electrophilicity index values calculated for the title molecule are similar to those of bioactive molecules.

The DOS spectrum graphically represents the occupied and unoccupied molecular orbitals of the corresponding molecule [31]. DOS contributions reinforced the information gathered by FMOs. Figure 4 depicts diagrams of DOS computations.

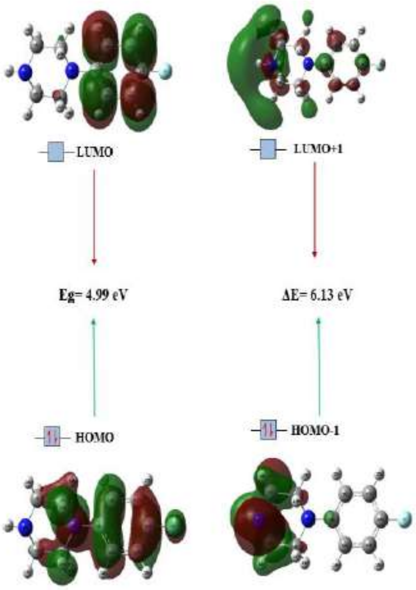

Figure 3 Frontier molecular orbitals of pFPP compound.

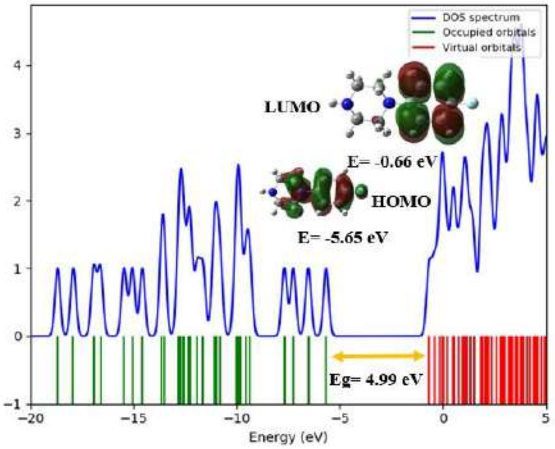

Figure 4 Density of states (DOS) diagram for pFPP molecule.

3.3. Molecular electrostatic potentials (MEP)

The molecular electrostatic potential (MEP) is a well-established computational approach for predicting reactive regions in molecules for nucleophilic and electrophilic attacks [32, 33]. As shown in Figure 5, MEP was estimated for the most stable conformer geometry. The most negative region on the MEP surface is -5.54e-2, which is depicted in red and is referred to as the electrophilic region. The most positive area, shown by the blue color and the nucleophilic region, is +5.54e-2. The various color coding on the MEP surface as displayed in Figure 5 reveals the yellow color regions around –phenyl and are electrophilic regions, whereas the blue color regions around hydrogen atoms show low electron density (nucleophilic). In the MEP, the most reactive location for electrophilic attack is the negative electrostatic potential (shown in red) localized on the fluorine and -NH group in the piperazin ring.

Table 2 Global reactivity descriptors of the pFPP compound

Parameters	Values
E_{HOMO}	-5.65 eV
E_{LUMO}	-0.66 eV
Energy band gap ($\Delta E = E_{LUMO} - E_{HOMO}$)	4.99 eV
Ionization potential ($I = -E_{HOMO}$)	5.66 eV
Electron affinity ($A = -E_{LUMO}$)	0.66 eV
Chemical hardness ($\eta = (I-A)/2$)	2.49 eV
Chemical softness ($\sigma = 1/2\eta$)	0.40(eV)$^{-1}$
Electronegativity ($\chi = (I + A)/2$)	3.16 eV
Chemical potential ($\mu = -(I + A)/2$	-3.16 eV
Electrophilicity index ($\omega = \mu 2 /2\eta$)	2.00 eV
Max. charge transfer index ($\Delta N_{max} = -\mu/\eta$)	1.27

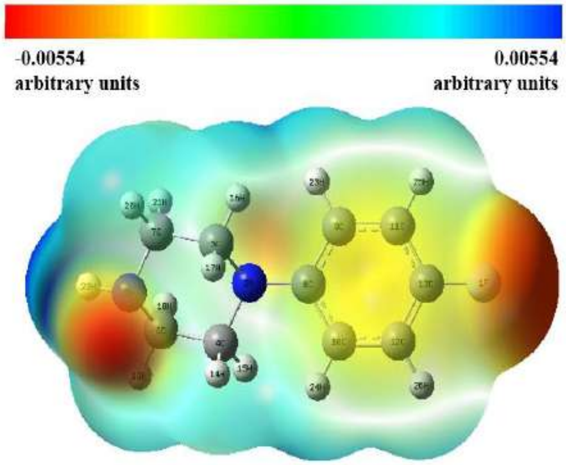

Figure 5 Molecular electrostatic potential maps of pFPP compound

3.4. ELF and LOL analyses

The electron localization function (ELF) and the localized orbital locator (LOL) are often used to show the structure of an atomic shell structure, chemical bonding classification, and charge-shift bond verification on the surface of a molecule. These surface analysis show that the high likelihood of discovering an electron pair on the molecular surface [33-35]. 2D and 3D depictions of the ELF and LOL isosurface for the pFPP compound in Fig. 6. The strong localized bonding and nonbonding electrons around hydrogen atoms are indicated by high ELF regions (red region) in Figure 6(a). The delocalized electron cloud around carbon and nitrogen atoms is shown by blue regions. The electron density is shown by the white color present in the central part of the hydrogen atom (H22) of the piperazin ring, as seen in Figure 6(b). The majority of the covalent region between carbon-carbon atoms and carbon-nitrogen atoms, represented by the red color. The blue circles around fluorine atom indicate the electron depletion.

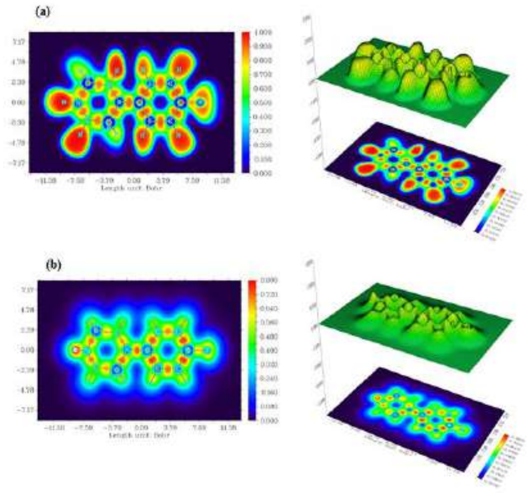

Figure 6 Relif map and Color filled map of (a) ELF and (b) LOL of pFPP compound

3.5. Molecular docking study

The pFPP molecule is an active substance for different neuroligands, and it is also involved in the structure of many drugs that act on the nervous system because it contains a piperazine ring. Since piperazines are under development as multifunctional agents for the treatment of Alzheimer's disease (AD) [36], anti-Alzheimer's receptor has been chosen as a biological target in the molecular docking. The most common treatment for AD is to improve cholinergic neurotransmission by blocking one of the major neurotransmitters, ACh, from being broken down by AChE, which maintains the brain's ACh level to compensate for the loss of functional brain cells. Therefore, the AChE enzyme was chosen as a biological target for our study. In order to study the most stable conformer, it was docked to the active sites of AChE. The in-silico molecular docking results, the binding energy, inhibition constant (Ki), and RMSD in the ligand-enzyme complex are -5.97 kcal/mol, 42.30 µM, and 92.61 Å, respectively. In drug design, the binding energy of compounds to anti-Alzheimer's receptors is crucial, while Ki is a measure of the ligand's protein binding affinity. The ligand-enzyme complex contains hydrophobic interactions and hydrogen bonds as shown in the Figure 7 given in 2D and 3D. The computational analyses of the molecular docking research show that the hydrogen bond interaction between the nitrogen atom N3 of piperazin ring and SER'286 residue of oxygen atom (N-H…O). Additionally, hydrophobic amino acids that are ordinarily incorporated inside the enzyme, such as TRY'334, PHE'331 and ARG'289, in the form of pi-pi interactions between title compounds (see Table 3). In molecular docking studies, it was concluded that the reactive sites obtained from MEP calculations are suitable for H-bond interaction with the selected enzyme.

Table 4 Toxicity prediction using the Protox II of pFPP

pFPP	**Values**
Toxicity Class	III
LD_{50} (mg/kg)	108
Organ Toxicity (Probability	
Hepatotoxicity	Inactive (0.83)
Carcinogenicity	Inactive (0.71)
Immunotoxicity	Inactive (0.96)
Mutagenicity	Inactive (0.82)
Cytotoxicity	Inactive (0.79)

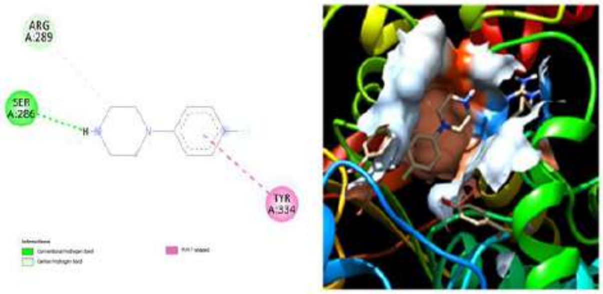

Figure 7 2D interaction and 3D bonding between amino acid residue and pFPP molecule with AChE

Table 3 The enzyme–ligand interaction parameters with hydrophobic contacts for pFPP compound

AChE (PDB ID)	Hydrogen bonding interaction		Hydrophobic interaction	
	R	D (Å)	R	D (Å)
1EVE	SER286	2.19	TRY334	3.38
			PHE331	3.35
			ARG289	3.53

R: Residues, D: Distance

3.6. Toxicity prediction

Piperazines have a reputation for being safe, and there are no studies of their toxicity at the cellular level that could help to understand their harmful effects [37]. Therefore, the aim of this work is to predict the organ toxicity, toxicological endpoints, and median lethal dose (LD_{50}) of the 1-(4-Fluorophenyl)piperazine) compound, which were obtained by using the Pro-Tox II web server [23]. As shown in Table 4, ProTox-II toxicity prediction software gave the predicted LD_{50} value of the pFPP molecule. The results of acute toxicity prediction, such as toxicity class classification [1 (toxic) to 6 (non-toxic), revealed that the listed chemical was classed as acute toxicity class 3 (toxic if swallowed). According to the findings, the title molecule is non-carcinogenic and has no immunotoxicity, cytotoxicity, or mutagenicity.

3.7. Drug-Likeness and ADME Analysis

In the present drug development, the potential of a novel chemical is commonly evaluated using initially through virtual tools [6]. The drug-likeness and ADME parameters of the pFPP molecule have been evaluated in order to determine its suitability for usage as an active substance in a variety of novel pharmaceutical products. Table 5 summarizes the calculated drug-likeness and ADME parameters, which should be interpreted using Lipinski's rule of five [38]. The Lipinski's rule of five states that the number of HBD (Hydrogen Bond Donor) and HBA (Hydrogen bond acceptor) must be fewer than 5 and 10, the miLogP value must be less than 5, and the molecular weight must be less than 500. Furthermore, TPSA (Total polar surface area) (≤140) is within acceptable limits. According to the analysis, the physicochemical properties of the title molecule definitely meet Lipinski's rule.

ADME analysis shows that the pFPP molecule is predicted by human intestinal absorption (HIA), Caco-2 (colorectal carcinoma) cell permeability and Blood-brain barrier penetration (BBB). The HIA value showed good oral absorption and the Caco-2 permeability values were considered good permeability of the compound. However, it was concluded that the BBB value of this molecule is not in the acceptable range for an ideal drug candidate. The bioavailability score was 0.55. In terms of bioavailability, drug-like behavior is critical to becoming an oral drug. These calculations show that the chemical in question shows promise as a pharmacological agent.

Table 5 Calculated ADME and Drug-Likeness properties of pFPP molecule

pFPP	**Values**
HBD ≤5	1
HBA ≤10	2
TPSA≤140 Å	15.27
miLogP	1.50
GI absorption	High
BBB	No
Caco2 permeability	57.77
HIA	100

4. CONCLUSION

We explored various properties of pFPP compound in this work, including conformation analysis, surface properties, pharmacokinetic and toxicity properties. The title molecule possesses three stable conformers. The intramolecular charge transfer was determined from the HOMO-LUMO orbitals, as well as the HOMO-LUMO energy values were used to compute and analyze various global reactivity parameters. The FMO shows the Egap of the pFPP molecule 4.99 eV, indicating that title compound is more chemically stable. The MEP map shows that the fluorine and NH group, which is deep red, has the most negative charge. ELF and LOL study shows that between C-C and C-N atoms, most of the covalent region is present. Pharmacological studies gave information about ADME, drug likeness, and value to identify the toxic activity of the molecule. The π–π staking interactions of the AChE inhibitors with title ligand molecule show the non-covalent binding sites in the structures. These sites were also justified by MEP surface. Hence, we predict the title compound pFPP might be used as a prospective drug after clinical and pharmaceutical research for Alzheimer’s disease.

Funding

The author (s) has no received any financial support for the research, authorship or publication of this study.

The Declaration of Conflict of Interest/ Common Interest

No conflict of interest or common interest has been declared by the authors.

The Declaration of Ethics Committee Approval

This study does not require ethics committee permission or any special permission.

The Declaration of Research and Publication Ethics

The author of the paper declare that they comply with the scientific, ethical and quotation rules of SAUJS in all processes of the paper and that they do not make any falsification on the data collected. In addition, I declare that Sakarya University Journal of Science and its editorial board have no responsibility for any ethical violations that may be encountered, and that this study has not been evaluated in any academic publication environment other than Sakarya University Journal of Science.

REFERENCES

[1] D. Y. Peng, Q. Sun, X. L. Zhu, H. Y. Lin, Q. Chen, N. X. Yu, W. C. Yang, G. F. Yang, "Design, synthesis, and bioevaluation of benzamides: Novel acetylcholinesterase inhibitors with multi-functions on butylcholinesterase, A*β* aggregation, and β-secretase,'' Bioorganic Medicinal Chemistry, vol. 20, pp. 6739-6750, 2012.

[2] Q. Sun, D. Y. Peng, S. G. Yang, X. L. Zhu, W. C. Yang, G. F. Yang, "Syntheses of coumarin–tacrine hybrids as dual-site acetylcholinesterase inhibitors and their activity against butylcholinesterase, Aβ aggregation, and β-secretase," Bioorganic Medicinal Chemistry, vol. 22, pp. 4784-4791, 2014.

[3] K. S. T. Diasa, C. Viegas, "Multi-Target Directed Drugs: A Modern Approach for Design of New Drugs for the treatment of Alzheimer's Disease," Current Neuropharmacology, vol. 12, pp. 239-255, 2014.

[4] E. M. H. Brewton, E. M. Hersh, G. Brewton, D. Abrams, J. Bartlett, J. Galpin, P. Gill, R. Gorter, M. Gottlieb, J. J. Jonikas, S. Landesman, A. Levine, A. Marcel, E. A. Petersen, M.Whiteside, J. Zahradnik, C. Negron, F. Boutitie, J. Caraux, J.-M. Dupuy, L. R. Salmi, "Dithiocarbsodium(diethyldithiocarbamate) therapy in patients with symptomatic HIV-infection. Aids a randomized, double-blind, placebo-controlled multicenter study, " American Medical Association, vol. 265, pp. 1538–1544, 1991.

[5] C. B. Mishra, A. Manral, S. Kumari, V. Saini, M. Tiwari, ‟Design, synthesis and evaluation of novel indandione derivatives as multifunctional agents with cholinesterase inhibition, anti-bamyloid aggregation, antioxidant and neuroprotection properties against Alzheimer's disease,'' Bioorganic Medicinal Chemistry, vol. 24, pp. 3829–384, 2016.

[6] H. S. N. Prasada, A.P. Ananda, T.N. Lohithd, P. Prabhuprasad, H.S. Jayanth, N.B. Krishnamurthy, M.A. Sridhar, L. Mallesha, P. Mallu, ‟Design, synthesis, molecular docking and DFT computational insight on the structure of Piperazine sulfynol derivatives as a new antibacterial contender against superbugs MRSA,'' Journal of Molecular Structure, vol. 1247, 131333, 2022.

[7] S. B. Ozdemir, N. Demirbas, A. Demirbas, N. Colak, F.A. Ayaz, ‟Design, Microwave-Assisted and Conventional Synthesis of New Hybrid Compounds Derived From 1-(4-Fluorophenyl) piperazine and Screening for Their Biological Activities,'' ChemistrySelect 3, pp. 2144 – 2151, 2018.

[8] A. Alzheimer, ‟Alzheimer's disease facts and figures,'' Alzheimer's & dementia: The Journal of the Alzheimer's Association, vol. 11, pp. 332-384, 2015.

[9] D. Scherman, M. Hamon, H. Gozlan, J .P. Henry, A. Lesage, M. Masson, ‟Molecular pharmacology of niaprazine,'' Progress in Neuropsychopharmacolgy and Biological. Psychiatry, vol. 12, pp. 989–1001, 1988.

[10] R. A. Glennon, M.Y. Yousif, A.M. Ismaiel, M.B. el-Ashmawy, J.L.

Herndon, J.B. Fischer, A.C Server, K.J.B.Howier, "Novel 1-phenylpiperazine and 4-phenylpiperidine derivatives as high-affinity sigma ligands,'' Journal of Medicinal Chemistry, vol. 34, pp. 3360–3365, 1991.

[11] W. N . Wu, L. A. McKown, G.H. Kuo, "Hepatic metabolism of two α-1A-adrenergic receptor antagonists, phthalimide-phenylpiperazine analogs (RWJ-69205 and RWJ-69471), in the rat, dog and human,'' European Journal of Drug Metabolism and Pharmacokinetics, vol. 31, pp. 271–276, 2006.

[12] B. G. Mockett, D. Guévremont, M. Wutte, S. R. Hulme, J .M. Williams, W. C. Abraham, "Calcium/Calmodulin-dependent protein kinase II mediates group I metabotropic glutamate receptor-dependent protein synthesis and long-term depression in rat hippocampus,'' Journal of Neuroscience, vol. 31, pp. 7380–7391, 2011.

[13] F. M. D. Ismail, "Important fluorinated drugs in experimental and clinical use,'' Journal Fluorine Chemistry, vol. 118, pp. 27–33. 25, 2002.

[14] A. A. Gakh, M.N. Burnett, "Extreme modulation properties of aromatic fluorine," Journal Fluorine Chemistry, 132, pp. 88–93, 2011.

[15] M. J. Frisch, G. W. Trucks, H. B. Schlegel, G. E. Scuseria, M. A. Robb, J. R. Cheeseman, G. Scalmani, V. Barone, B. Mennucci, G. A. Petersson, H. Nakatsuji, M. Caricato, X. Li, H. P. Hratchian, A. F. Izmaylov, J. Bloino, G. Zheng, J. L. Sonnenberg, M. Hada, M. Ehara, K. Toyota, R. Fukuda, J. Hasegawa, M. Ishida, T. Nakajima, Y. Honda, O. Kitao, H. Nakai, T. Vreven, J. A. Montgomery, Jr., J. E. Peralta, F. Ogliaro, M. Bearpark, J. J. Heyd, E. Brothers, K. N. Kudin, V. N. Staroverov, R. Kobayashi, J. Normand, K. Raghavachari, A. Rendell, J. C. Burant, S. S. Iyengar, J. Tomasi, M. Cossi, N. Rega, J. M. Millam, M. Klene, J. E. Knox, J. B. Cross, V. Bakken, C. Adamo, J. Jaramillo, R. Gomperts, R. E. Stratmann, O. Yazyev, A. J. Austin, R. Cammi, C. Pomelli, J. W. Ochterski, R.L. Martin, K. Morokuma, V.G. Zakrzewski, G. A. Voth, P. Salvador, J. J. Dannenberg, S. Dapprich, A.D. Daniels, O. Farkas, J. B. Foresman, J. V. Ortiz, J. Cioslowski, D. J. Fox., "Gaussian Inc,'' Wallingford CT, 2009.

[16] R. Dennington, T. Keith, J. Millam, "GaussView Version 5,'' Semichem Inc., Shawnee Mission KS., 2009.

[17] T. Lu, F. Chen, "Multiwfn: a Multifunctional Wavefunction Analyzer,'' Journal of Computaional Chemistry, vol. 33, pp. 580–592, 2012.

[18] G. M. Morris, D. S. Goodwill, R. S. Halliday, R. Huey, W. Hart, R. K. Belew, A. J. Olson, "Automated Docking Using a Lamarckian Genetic Algorithm and an Empirical Binding Free Energy Function,'' Journal of Computaional Chemistry, vol. 19, pp. 1639-1662, 1998.

[19] W. L. D. Pymol, "An open-source molecular graphics tool, CCP4 Newsletter on protein,'' Crystallography, vol. 40, pp. 82, 2002.

[20] Dassault Systemes BIOVIA, Discovery Studio Visualizer v17.2.0.16349, 2016. San Diego

[21] PreADMET Citation Statistics, (2022, May. 31). Available: www.preadmet.com

[22] Swiss Institute of Bioinformatics, (2022, May. 31). Available: www.swissadme.ch/index.php

[23] ProTox-II- Prediction of Toxicity of Chemicals, (2022, May. 31). Available: http://tox.charite.de/protox_II/

[24] T. Chaudharya, M. K. Chaudharya, B. D. Joshi, M. S. A. de Santana, A.P. Ayala, ‶Spectroscopic (FT-IR, Raman) analysis and computational study on conformational geometry, AIM and biological activity of cephalexin from DFT and molecular docking approach,'' Journal of Molecular Structure, vol. 1240, 130594, 2021.

[25] M. N. Ahmed, K. A. Yasin, K. Ayub, T. Mahmood, M. N. Tahir, B. A. Khan, M. Hafeez, M. Ahmed, I. ul-Haq, ‶Click one pot synthesis, spectral analyses, crystal structures, DFT studies and brine shrimp cytotoxicity assay of two newly synthesized 1,4,5-trisubstituted 1,2,3-triazoles,'' Journal of Molecular Structure, vol. 1106, pp. 430-439, 2016.

[26] M. Arshad, A. Bibi, T. Mahmood, A. Asiri, K. Ayub, ‶Synthesis, crystal structures and spectroscopic properties of triazine-based hydrazone derivatives; a comparative experimental-theoretical study, ‶ Molecules, vol. 20, pp. 5851-5874, 2015.

[27] M. Noreen, N. Rasool, Y. Gull, M. Zubair, T. Mahmood, K. Ayub, F.-H. Nasim, A. Yaqoob, M. Zia-Ul-Haq, V. Feo , ‶Synthesis, density functional theory (DFT), urease inhibition and antimicrobial activities of 5-aryl thiophenes bearing sulphonylacetamide moieties,'' Molecules, vol. 20, pp. 19914-19928, 2015.

[28] M. Evecen, "Structural, Conformational and Spectroscopic Properties of C16H16BrNO3 SchiffBase Molecule: A Theoretical Investigation," Sakarya Üniversitesi Fen Bilimleri Enstitüsü Dergisi, vol. 22, pp. 1591-1600, 2018.

[29] M. Hagar, H. A. Ahmed, G. Aljohani, O.A. Alhaddad, ‶Investigation of Some Antiviral N-Heterocycles as COVID 19 Drug: Molecular Docking and DFT Calculations,'' International Journalo of Molecular Sciences, vol. 21, pp. 3922, 2020.

[30] S. J. Basha, S. P. V. Chamundeeswari, S. Muthu, B. R. Raajaraman, ‶Quantum computational, spectroscopic investigations on 6- aminobenzimidazole by DFT/TD-DFT with different solvents and molecular docking studies,'' Journal of Molecular Liquids, vol. 296, pp. 11178, 2019.

[31] R. Mathammal, N. R. Monisha, S. Yasaswini, V. Krishnakumar, ‶Molecular structure, vibrational analysis (FT-IR, FT-Raman), NMR, UV, NBO and HOMO–LUMO analysis of N,N-Diphenyl Formamide based on DFT calculations,'' Spectrochimica Acta A, vol. 139, pp. 521-532, 2015.

[32] T. Chaudharya, M. K. Chaudharya , B. D. Joshi, M. S. A. de Santana, A. P. Ayala, ‶Spectroscopic (FT-IR, Raman) analysis and computational study on conformational geometry, AIM and biological activity of cephalexin from DFT and molecular docking approach,'' Journal of Molecular Structure, vol. 1240, pp. 130594, 2021.

[33] H. P. Gümüş, Ö. Tamer, Y. Atalay, "4-(Metoksimetil)-1,6-dimetil-2-okso-1,2-dihidropiridin-3-karbonitril molekülünün teorik olarak incelenmesi," Sakarya

Üniversitesi Fen Bilimleri Enstitüsü Dergisi, vol. 19 no 3, pp. 303-311, 2015.

[34] B. Silvi, A. Savin, "Classification of chemical bonds based on topological analysis of electron localization functions,'' Nature, 371, pp. 683-686, 1994.

[35] B. F. Rizwana, J. C. Prasana, S. Muthu, C. S. Abrahama, "Molecular docking studies, charge transfer excitation and wave function analyses (ESP, ELF, LOL) on valacyclovir : a potential antiviral drug,'' Computational Biological Chemistry, vol. 78, pp. 9-17, 2019.

[36] C. B. Mishra, A. Manral, S. Kumari, V. Saini, M. Tiwari, "Design, synthesis and evaluation of novel indandione derivatives as multifunctional agents with cholinesterase inhibition, anti-bamyloid aggregation, antioxidant and neuroprotection properties against Alzheimer's disease,'' Bioorganic Medicinal Chemistry, vol. 24, pp. 3829–3841, 2016.

[37] M.D. Arbo, R. Silva, D.J. Barbosa, D.D. da Silva, L.G. Rossato, M.L. Bastos, H. Carmo, "Piperazine designer drugs induce toxicity in cardiomyoblast h9c2 cells through mitochondrial impairment,'' Toxicology Letters, vol.229, pp. 178-189, 2014.

[38] A. Christopher, "Lipinski, Lead- and drug-like compounds: the rule-of-five revolution,'' Drug Discovery Today Technologies vol. 1 no 4,pp. 337-341, 2004.

SAKARYA ÜNİVERSİTESİ
FEN BİLİMLERİ ENSTİTÜSÜ
DERGİSİ

Sakarya University Journal of Science
SAUJS

ISSN 1301-4048 | e-ISSN 2147-835X | Period Bimonthly | Founded: 1997 | Publisher Sakarya University |
http://www.saujs.sakarya.edu.tr/

Title: Performance Analysis of MIMO Techniques for a Pyramid Receiver in an Indoor MIMO-VLC System

Authors: Aamir Ullah KHAN, Sultan ALDIRMAZ ÇOLAK, Yasin ÇELİK

Recieved: 2020-12-29 00:00:00

Accepted: 2022-08-15 00:00:00

Article Type: Research Article

Volume: 25
Issue: 5
Month: October
Year: 2022
Pages: 942-955

How to cite
Aamir Ullah KHAN, Sultan ALDIRMAZ ÇOLAK, Yasin ÇELİK; (2022), Performance Analysis of MIMO Techniques for a Pyramid Receiver in an Indoor MIMO-VLC System. Sakarya University Journal of Science, 25(5), 942-955, DOI: 10.16984/saufenbilder.849408
Access link
http://www.saujs.sakarya.edu.tr/en/pub/issue/73051/849408

Sakarya University Journal of Science 25(5), 942-955, 2022

Performance Analysis of MIMO Techniques for a Pyramid Receiver in an Indoor MIMO-VLC System

Aamir Ullah KHAN*[1], Sultan ALDIRMAZ ÇOLAK[1], Yasin ÇELİK[2]

Abstract

In an indoor multiple-input multiple-output (MIMO) visible light communication (VLC) system, line of sight (LoS) channel links are present between a light-emitting diode (LED) based transmitter and a photodetector (PD) based receiver. The PDs in the receiver are closely packed resulting in a high channel correlation. To overcome channel correlation and improve the performance of the MIMO-VLC system, angle diversity receivers (ADRs) are commonly employed. The channel matrix entries depend on the normal vectors of the PDs, which in turn depend on the elevation angle (EA) of the PDs. Thus, by having normal vectors pointing in different directions, the channel correlation can be considerably reduced. This paper considers a special type of ADR called pyramid receiver (PR) and employs a 4x4 MIMO-VLC system. In this paper, different MIMO algorithms such as repetition coding (RC) and spatial multiplexing (SMP) are considered to exhibit and compare the bit-error-rate (BER) performance of the fixed and variable EA MIMO-VLC systems. The results show that an SMP-employed MIMO-VLC system outperforms the RC-employed MIMO-VLC system. SMP results in an spatial multiplexing gain that varies linearly with the number of LEDs whereas RC does not yield any spatial multiplexing gain. To attain the same spectral efficiency i.e. 4 bit/s/Hz, a larger signal constellation size is required for RC employed MIMO-VLC system to achieve the same BER as of an SMP employed MIMO-VLC system. Similarly, the BER performance of variable EA MIMO-VLC systems is better as compared to fixed EA MIMO-VLC systems.

Keywords: Angle diversity receivers, optical wireless communications, pyramid receiver, visible light communication

---

* Corresponding author: aamir.khan770@gmail.com
[1] Kocaeli University
E-mail: sultan.aldirmaz@kocaeli.edu.tr,
ORCID: https://orcid.org/0000-0003-2352-5697, https://orcid.org/0000-0001-7154-0723
[2] Aksaray University
E-mail: yasincelik@aksaray.edu.tr
ORCID: https://orcid.org/0000-0001-8972-9970

1. INTRODUCTION

Wireless connectivity has become an absolute necessity nowadays. It is no more regarded as a luxury but as an utter need of time. Due to technical developments, the cost of handheld devices has become relatively lower over recent years, due to which their availability is no more an issue. According to the wireless world research forum, 7 billion people will be served by 7 trillion devices by the end of the year 2020. Similarly, it is also expected that the number of wirelessly connected devices will reach 1000 times the human population [1]. Similarly, a recent study [2] has anticipated that mobile networks will become the major source of data and around 77 exabytes of data traffic will be transmitted by mobile networks every month.

The number of digital users has been growing over recent years and there has been a rapid increase in the demand for wireless data communication. With the saturation of the radio frequency (RF) spectrum, it is very difficult to meet the growing demand for high-speed connectivity. In order to alleviate the looming spectrum crisis, scientists have started to look for new means to accommodate the new users. In recent years, optical wireless communications (OWC) specifically visible light communication (VLC) has become a prevalent wireless communication technique among researchers to complement traditional RF communications, especially for indoor environment-based communications. VLC is viewed as a very promising complementary technology to traditional RF-based indoor technologies, due to the inherent advantages of low-cost front-ends, unregulated spectrum, high data rates, and simultaneous illumination and data transmission.

In VLC, the visible part of the spectrum in 390nm-750nm is exploited for communication. In a VLC system, light-emitting diodes (LEDs) are used as transmitters, and photodetectors (PDs) are used as receivers. Air acts as a medium between source and destination. With the advancements in solid-state lighting technology over the years, it is now possible to modulate light at such high frequencies that human eyes cannot detect. Solid-state sources e.g. LEDs will substitute traditional illumination sources as they offer a greater lifetime, lower cost, and lower energy consumption. These properties, along with many others, make VLC an ideal, economic, and suitable choice for communication [3]. Employing white light LEDs as transmitters, VLC has been a rapidly-growing OWC technology and gained much consideration in recent years. In most cases, communication is a secondary function shadowed by illumination. This is what makes VLC different from other wireless communication standards having only the sole purpose of communication.

The modulation capability of commercially available LEDs is very limited. As a result of this limitation, the transmission bandwidth of the VLC systems is restricted to several MHz as compared to the available optical bandwidth of 400THz. As high data rates are required for high-speed communication, this restraint in bandwidth presents a challenge for researchers to design an effective VLC system [4].

Different approaches have been adopted by researchers to overcome the bandwidth limitations of VLC systems and design high-speed VLC systems. The performance of the VLC systems can be improved by employing high-order constellations orthogonal frequency division multiplexing (OFDM) [5]. In [6], OFDM has been shown as a suitable scheme for VLC for achieving high data rates because of combating inter-symbol interference and utilizing the spectrum more efficiently. Due to the physical nature of LEDs and PDs, intensity modulation direct detection (IM/DD) must be used in VLC systems [7]. The traditional OFDM results in polar signals. As IM/DD is employed in a VLC system, therefore, the transmitted signal must be real and positive all the time as negative signals cannot be modulated. Due to this limitation, in [8], different OFDM techniques are specifically designed for IM/DD based VLC systems are compared and analyzed.

With the use of multiple parallel LEDs for illumination and communication in an indoor environment, spectral efficiency can be improved by employing multiple-input multiple-output

(MIMO) techniques. MIMO can enhance the data rate without any additional bandwidth expansion. It was shown that optical MIMO has great potential in improving spectral efficiency for short-range high-speed data transmission [9]. A link adaptation method for the OFDM-based MIMO-VLC system is investigated in [10]. The proposed method supports repetition coding (RC) and spatial multiplexing (SMP) as MIMO modes. The switching of the spatial mode depends on the channel conditions. The proposed MIMO mode selection along with the bit loading scheme results in a more spectral efficient (SE) system while satisfying the target bit-error rate (BER).

In a line-of-sight (LoS) based indoor MIMO-VLC system, the entries of the channel matrix can be highly correlated. This correlation of channel matrix entries can yield a rank deficient channel matrix resulting in poor performance [11]. It is, therefore, important to have an uncorrelated channel matrix. The rank of the indoor MIMO-VLC system highly depends on the geometries of LEDs and PDs. In [12], authors have explored the impact of PDs placement on the performance of the MIMO-VLC system. It is shown that certain PD alignments result in a rank-deficient channel matrix. An irregular PD configuration has been proposed to overcome the issue of the rank deficient channel matrix.

Different methods have been adopted by the researchers to overcome the challenge of channel correlation in an indoor MIMO-VLC system. An aperture-based angular diversity receiver for the MIMO-VLC system is investigated in [13]. It is shown that a well-designed receiver can receive signals from different directions with low multi-stream interference. This results in a well-conditioned channel matrix. In order to obtain uncorrelated channels, an angle diversity receiver (ADR) has been proposed in [14]. A highly uncorrelated channel matrix is obtained by placing PDs on ADR in such a way that normal vectors of PDs point in different directions from one another. The performance of an ADR-based indoor MIMO-VLC can be reduced greatly as a result of inter-cell interference (ICI). In [5], a new angle diversity multi-element receiver is proposed. It is shown that this type of receiver cannot only overcome ICI but also results in robustness against the receiver's random rotations. Similarly, an interference management scheme to overcome the co-channel interference has been proposed in [15]. The authors have employed a constrained field-of-view (FOV) ADR along with least square channel estimation with maximum-likelihood (ML) detector. It is shown that the proposed system in [15] results in superior BER performance. Moreover, the proposed system outperforms the time division multiple access (TDMA) techniques at all positions and orientations of ADR. In [16], a comprehensive lighting configuration for an efficient VLC is presented. An efficient VLC system with mobility and link switching is considered along with illumination, signal-to-noise ratio (SNR), and received power constraints.

The use of pre-equalization methods to increase the bandwidth of white LEDs for VLC systems is discussed in [17]. The impact of different factors e.g., LED's array, FOV angle of the receiver, and the LED's transmission angle, influencing the performance of the MIMO-VLC systems are also elaborated and analyzed in [17]. Different diversity techniques such as select best combining, equal gain combining, and maximum ratio combining for LoS links are analyzed and compared in [7]. The performance of the ADR receiver is also compared with the traditional single PD receiver in terms of signal to interference plus noise ratio (SINR) and area spectral efficiency. It is shown that the ADR performs better as compared to the traditional receiver. Moreover, the SINR suffers from great fluctuations due to ICI in a multi-cell indoor MIMO-VLC system. To improve the performance of such a MIMO-VLC system, a generalized ADR is adopted by researchers in [18].

In [19], the authors have investigated the impact of MIMO modulation schemes on the performance of the indoor MIMO-VLC system. The authors have considered generalized spatial modulation (GSM) and SMP for the LOS and diffused channel links for vertical and angular detectors. It is shown that angular detectors result in a better BER performance compared to vertical detectors. Moreover, GSM outperforms SMP in terms of BER performance. Similarly, different transmission mechanisms such as spatial modulation (SC), RC, and SMP are compared and analyzed in [9]. The overall spectral efficiency is improved by the application of adaptive modulation and per antenna rate coding. Similarly, in [20], a pyramid receiver (PR) based on the principle of ADR is proposed in which the elevation angle (EA) of PDs was varied to generate uncorrelated channel matrix entries. The EA was kept constant for all the PDs for a constant receiver's position. A similar approach was implemented in [21] in which EAs of PDs were varied independently of one another resulting in optimum variable EAs for PDs. As a result of variable EAs, the throughput of the MIMO-VLC improves as compared to the fixed EA MIMO-VLC system.

In this paper, we compare the BER performance of a PR-based fixed and variable EA MIMO-VLC system. The authors in [21] have only addressed the channel throughput and provided a comparison in terms of throughput between fixed and variable EA MIMO-VLC systems. To the best of our knowledge, it is the first time where the BER performance of variable EA MIMO-VLC system for RC and SMP schemes is provided. Moreover, the comparison between fixed and variable EA MIMO-VLC systems has also been done for the first time. For both the fixed and variable EA MIMO-VLC systems, the optimum EA values given in [20, 21] are considered.

The rest of the paper is organized as follows. Section 2 presents the system model for both fixed and variable EA MIMO-VLC systems. Section 3 presents the simulation parameters and simulation results of BER for fixed and variable EA MIMO VLC systems. The paper is concluded and summarized in Section 4.

Throughout the introduction, we have used several abbreviations. To summarize, we have listed them in Table 1.

2. SYSTEM MODEL

In this paper, we have considered an M x N indoor MIMO-VLC system where M indicates the number of LEDs and N is the number of PDs. For optical modulation and demodulation, we have employed IM/DD schemes, respectively. We have only considered shot and thermal noises and they are modeled as additive white gaussian noise (AWGN) and added in the electrical domain at the receiver. We have assumed only LoS components in our scenario. The different stages of a VLC system are shown in Figure 1.

At first, the signal to transmit is modulated using unipolar K-PAM for its output being real and positive. The q_{th} modulated signal is represented as $\mathbf{s_q}$ $\mathcal{E}$ $[0, \ldots., (K-1)]$ where K is the modulation size of the constellation alphabet. This modulated signal is grouped into a vector of length M which is denoted by $\mathbf{s}$ $=[s_0, s_1, s_2, \ldots \ldots, s_{M-1}]^T$. The $\mathbf{s_q}$ signal is sent to

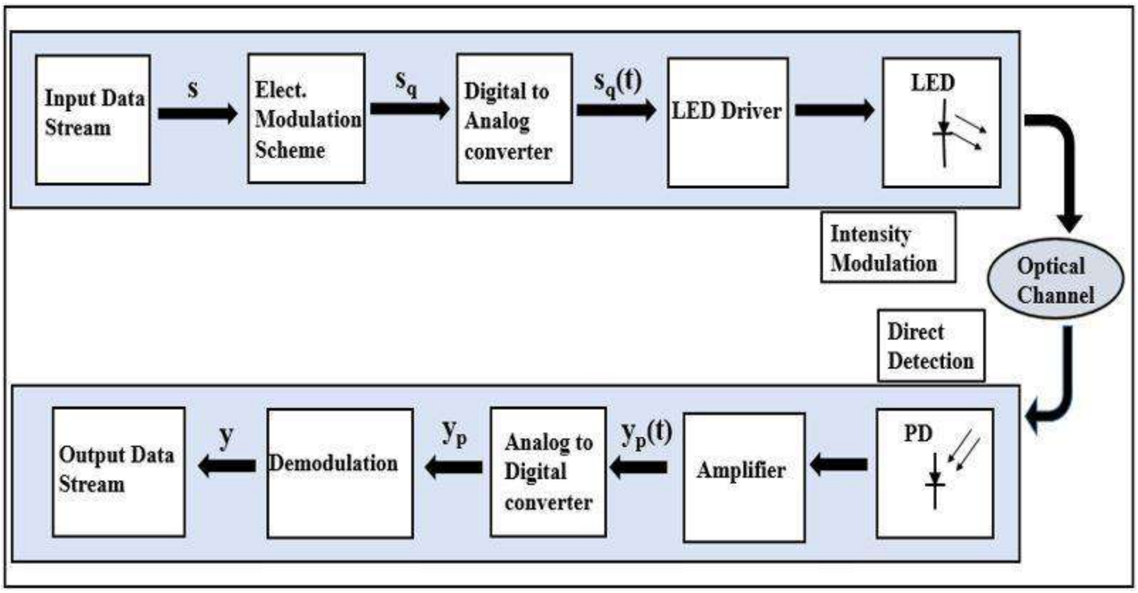

Figure 1 Block diagram of the VLC system adopted from [22]

Table 1 Abbreviations of systems under consideration

Abbr.	
ADR	Angle diversity receiver
EA	Elevation angle
FOV	Field-of-view
GSM	Generalized spatial modulation
IM/DD	Intensity modulation direct detection
LED	Light-emitting diode
ML	Maximum likelihood
PAM	Pulse amplitude modulation
PDs	Photodetectors
PR	Pyramid receiver
RC	Repetition coding
SC	Spatial modulation
SMP	Spatial multiplexing

the digital-to-analog converter (DAC) to form **s_q (t)** and is sent to the optical transmitter. In the optical transmitter, optical modulation i.e., IM is performed and data is sent to the optical receiver via the optical channel. The current generated at PD as a result of incident photons is sent to an amplifier. The amplified signal is sent to the analog-to-digital converter (ADC) to generate **y_p** to form a receive vector of length N as **y_p** = $[y_0, y_1, y_2, \dots\dots, y_{N-1}]^T$. The transmitted data is recovered by performing electrical demodulation on the received digital signal **y**. The description of the overall system is given in Equation 1:

$$\mathbf{Y} = \mathbf{HS} + \mathbf{W}, \tag{1}$$

where **S** is the (Mx1) transmitted signal vector, **Y** is the (Nx1) received signal vector whereas **W** is the (Nx1) noise signal vector. In Equation 1, **H** is the (NxM) channel matrix which can be represented as:

$$\mathrm{H} = \begin{bmatrix} \boldsymbol{h_{11}} & \dots & \boldsymbol{h_{1M}} \\ . & \vdots & . \\ . & \vdots & . \\ \boldsymbol{h_{N1}} & \dots & \boldsymbol{h_{NM}} \end{bmatrix} \tag{2}$$

In Equation 2, h_{mn} represents the channel between the n^th^ LED and m^th^ PD. It can be mathematically expressed as [14]:

$$h_{mn} = \frac{(\boldsymbol{p}+\mathbf{1})\, \boldsymbol{A_{PD}} \cos^{\boldsymbol{p}}(\boldsymbol{\alpha_{mn}}) \cos^{\mathbf{k}}(\boldsymbol{\beta_{mn}})}{\mathbf{2}\boldsymbol{\pi} \boldsymbol{d_{mn}^2}}, \tag{3}$$

where α_{mn} and β_{mn} should be in the range $\left[-\frac{\pi}{2}, \frac{\pi}{2}\right]$. The value of h_{mn} is considered to be 0 if it is outside the given range of α_{mn} and β_{mn}. In Equation 3, A_{PD} represents the PD's active area, d_{mn} is the distance between LED n and PD m, k is the FOV coefficient, α_{mn} represents the irradiance angle at LED n with respect to PD m, and β_{mn} is the angle of incidence at PD m with respect to LED n. The Lambertian emission order is represented by p in Equation 3 and can be mathematically given as [14]:

$$p = \frac{\ln 2}{\ln(\cos \emptyset_{1/2})}, \quad (4)$$

where $\emptyset_{1/2}$ is the LED's semi-angle that is calculated at half-power [11].

For a particular link between LED *n* and PD *m*, we have three vectors of interest. These vectors determine the values of α_{mn} and β_{mn}, which in turn determine the values of channel matrix entries as given in Equations 4 and 5 of [20]. As shown in Figure 2, these vectors include:

1. $\overrightarrow{A_n}$ is the normal vector in the direction irradiance from LED n,
2. $\overrightarrow{B_m}$ is the vector in the direction incidence from PD m,
3. $\overrightarrow{O_{mn}}$ is the vector from LED n to PD m.

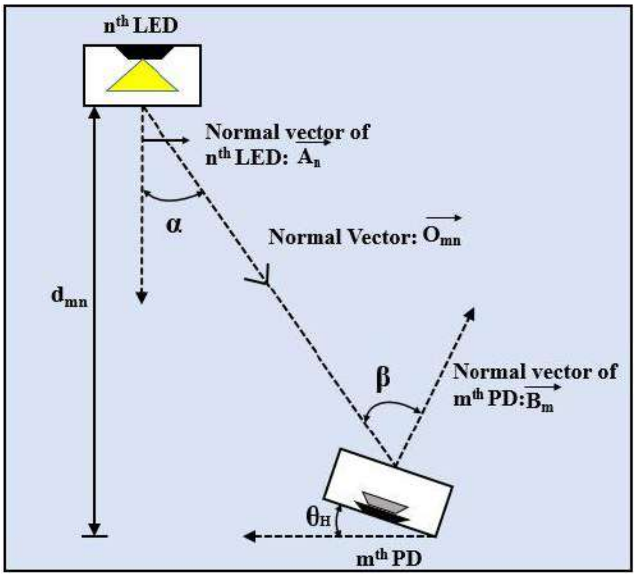

Figure 2 The geometry of LED-PD pair

In our system model, we have assumed channel state information is readily available at the receiver. Similarly, we have assumed that power is allocated uniformly among the M number of LEDs. In our system model, we have assumed different transmission techniques such as RC and SMP. All the considered MIMO-VLC systems employ an ML detector for the detection of the estimated received signal $\hat{s}$ at the receiver. The process of ML detection process can be mathematically expressed as [23]:

$$\hat{s} = arg\max_{S} \rho_y\,(\boldsymbol{y}|\mathbf{s},\mathbf{H}) = arg\min_{S} \|\boldsymbol{y} - \mathbf{Hs}\|_F^2, \quad (5)$$

where $\rho_y(\boldsymbol{y}|\mathbf{s},\mathbf{H})$ represents the conditional probability density function whereas $\|.\|_F$ is the Frobenius norm.

2.1. Transmission Schemes

In our paper, we have employed RC and SMP schemes for the transmission of information from source to destination. RC is the simpler of the two. In RC, the same information is transmitted from all the transmitters such that $s_1 = s_2 = \cdots = s_{M-1} = s_M$. The intensities from different LEDs add up constructively at the receiver enhancing the received optical power. As a result, RC achieves a good performance in free space OWCs. In this paper, a unipolar K-PAM together with RC is considered which results in spectral efficiency of $\log_2 K$ bit/s/Hz. The upper bound BER expression along with BER expression for RC employed MIMO-VLC system is given in Equations 7 and 8 of [23].

Another important transmission mechanism that is commonly adopted for the MIMO-VLC system is SMP. RC results in an increase in reliability. However, that comes at a cost of spectral efficiency as the same information is sent from all the transmitters. SMP results in a more spectral efficient system as independent data streams can be used from all the transmitters simultaneously for the transference of information. SMP employed MIMO-VLC system results in spectral efficiency of $M \log_2 K$ bit/s/Hz where M is the number of transmitters i.e., LEDs. The BER expression for an SMP-employed MIMO-VLC system is given in Equation 10 of [23].

In both the transmission mechanisms, the available optical power is divided equally among all the LEDs. Similarly, the mean transmission power and modulation scheme are also considered the same for both RC and SMP. The intensity levels for K-PAM is given as [23]:

$$I_i^{K-PAM} = \frac{2I}{K-1} i \text{ where } i = 0, 1, \ldots, K-1, \quad (6)$$

where I indicate the mean optical power emitted.

2.2. Coordinate System

In our system model, the respective positions of LEDs and PDs are displayed with the help of normal vectors in the $[x, y, z, \theta, \phi]$ format. The (x, y, z) represents the originating position of the respective normal vector. θ represents the EA from the positive z-axis whereas ϕ represents the azimuth angle from the positive x-axis. The range of θ and ϕ should be $[0, 180^0)$ and $[0, 360^0)$, respectively.

The normal vector $\overrightarrow{B_m}$ of the m^{th} PD located at $(x_{PD}^m, y_{PD}^m, z_{PD}^m)$ can be represented as $[x_{PD}^m, y_{PD}^m, z_{PD}^m, \theta_{PD}^m, \phi_{PD}^m]$ for $1 \leq m \leq N$ as shown in Figure 3. In a similar fashion, the n^{th} LED's normal vector $\overrightarrow{A_n}$ located at $(x_{LED}^n, y_{LED}^n, z_{LED}^n)$ can be represented as $[x_{LED}^n, y_{LED}^n, z_{LED}^n, \theta_{LED}^n, \phi_{LED}^n]$ for $1 \leq n \leq M$.

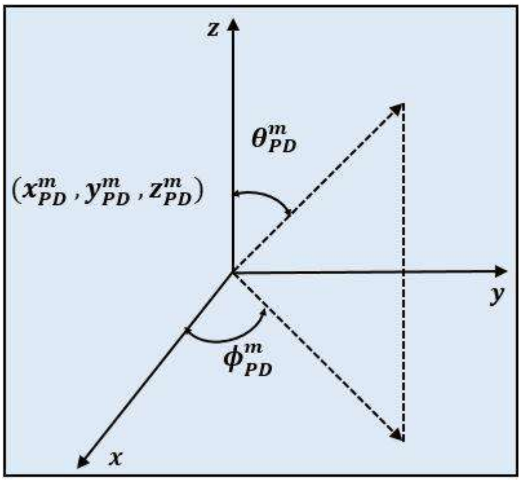

Figure 3 The coordinate system representation

2.3. Placement of PDs in PR

In our system model, we have assumed a circular arrangement of PDs in a circle of radius (r) for $1 \leq m \leq N$. The respective coordinates of PDs can be represented as [20]:

$$(x_{PD}^m, y_{PD}^m, z_{PD}^m) = \left(x_{PD} + \frac{r\cos 2(m-1)\pi}{N}, y_{PD} + \frac{r\cos 2(m-1)\pi}{N}, h_{PD}\right) \quad (7)$$

In Equation 7, (x_{PD}, y_{PD}) represents the (x, y) coordinates of the m^{th} PD whereas h_{PD} is the height of the receiver from the surface of the ground. As EAs of the PD m can be the same or different from one another depending upon the fixed and variable EA MIMO-VLC systems, the orientation can be defined as:

1. The EA can be different or the same for all the PDs,
2. The azimuth angle should be arranged as: $\phi_{PD} = \frac{2(m-1)\pi}{N}$ such that all the angles are symmetrically aligned.

The PR's horizontal orientation can be varied by ϕ_H resulting in a total azimuth angle of $\phi_{PD}+\phi_H$. The horizontal rotation can be introduced to improve the performance of the MIMO-VLC system as shown in Figure 4.

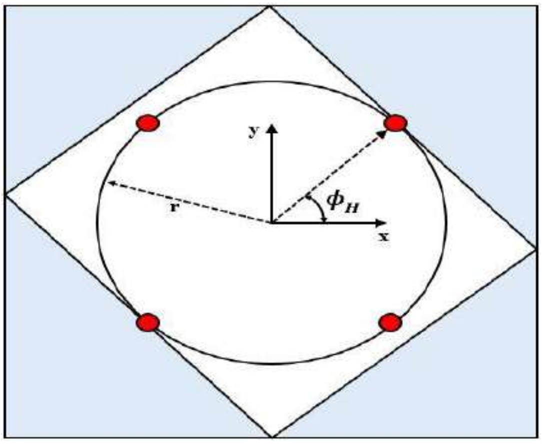

Figure 4 PD placement in PR

Similarly, the variation in the horizontal position of PR may also arise from the random orientation of the PR. Although the PDs are placed very close to one another in a PR, the orientation of PDs can be very different from one another as shown in Figure 5. Finally, the overall indoor setup is shown in Figure 6.

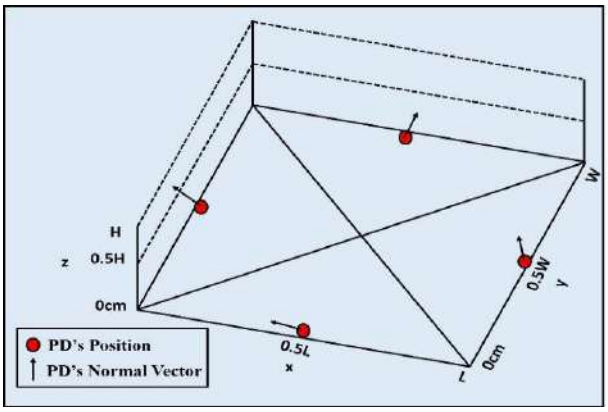

Figure 5 Normal vectors orientation in PR

3. SIMULATION PARAMETERS AND RESULTS DISCUSSION

In order to compare the BER performance of the 4x4 MIMO-VLC system, we have considered similar parameters as given in [20, 21]. A 4mx4mx2.7m dimension room is considered. The LEDs are placed in the ceiling at a height of 2.7m and are arranged in a square manner such that the center of the room and the center of the square coincide with one another. For all the LEDs, a similar normal downward angle is considered e.g. $\theta_{LED} = [0, 180^0]$. The separation distance between LEDs i.e.,d_{tx} is considered the same for all LED separations.

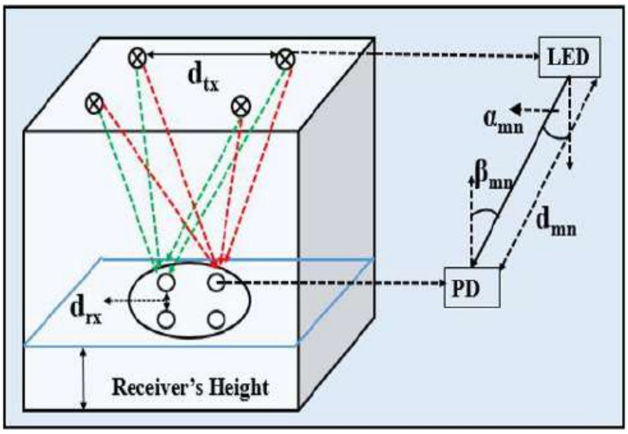

Figure 6 Indoor MIMO-VLC system

Similarly, we have also considered 7 receiver positions as given in Figure 7 according to [20].

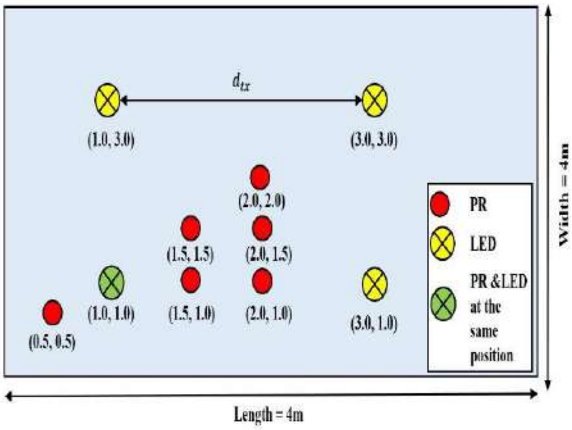

Figure 7 LEDs' placement and considered receiver positions adopted from [22]

The PDs are arranged in a circular manner according to Equation 7 with an r value of 0.5cm. The rest of the simulation parameters are given in Table 2.

Table 2 Parameters for MIMO-VLC system

Parameter	Value
Dimension of room	4m x 4m x 2.7m
Radius for PD placement	0.5cm
Separation between LEDs (d_{tx})	2m
Number of LEDs (M)	4
Number of PDs (N)	4
Active area of PD (A_{PD})	1.5mm^2
FOV coefficient (k)	1.4738
Semi-angle at half power($\emptyset_{1/2}$)	60^0
Height of LEDs (h_{LED})	2.7m
Height of PDs (h_{PD})	0.8m

As our goal is to compare the BER performance of RC and SMP employed MIMO-VLC systems, we evaluated the BER performance at all the considered receiver positions. The BER performance for fixed and variable EA MIMO-VLC systems is evaluated and compared with respect to optimum EA for both systems.

In Figure 8, we have considered the same optimum fixed EA values for respective receiver positions as given in [20]. It has been observed that position 1 performs the best, whereas, position 6 results in the worst performance. The performance gap between different receiver positions is very small i.e., a performance gap of around 2dB is observed for position 1 and position 6 for RC employed fixed EA MIMO-VLC system. Similarly, the BER performance of RC employed variable EA MIMO-VLC system is given in Figure 9. The variable EA values for considered receiver positions are adopted from [21]. For the variable EA MIMO-VLC system, every PD has its own independent EA angle. As can be seen from Figure 9, position 2 and 3 performs the best whereas position 0 results in the worst performance.

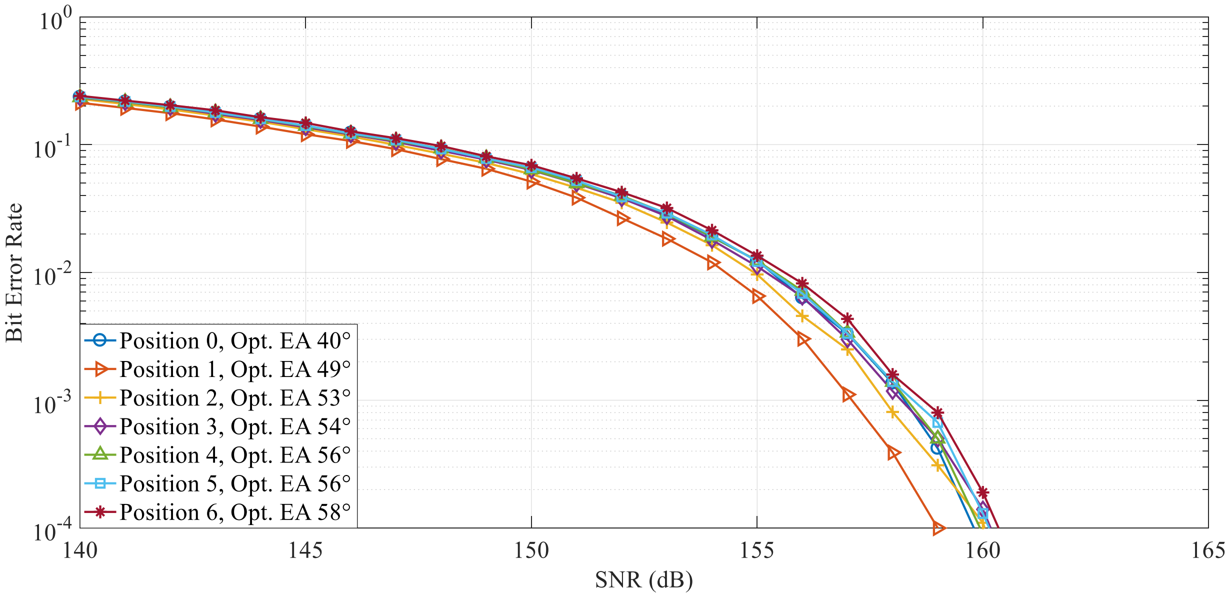

Figure 8 BER performance of RC employed fixed EA MIMO-VLC system

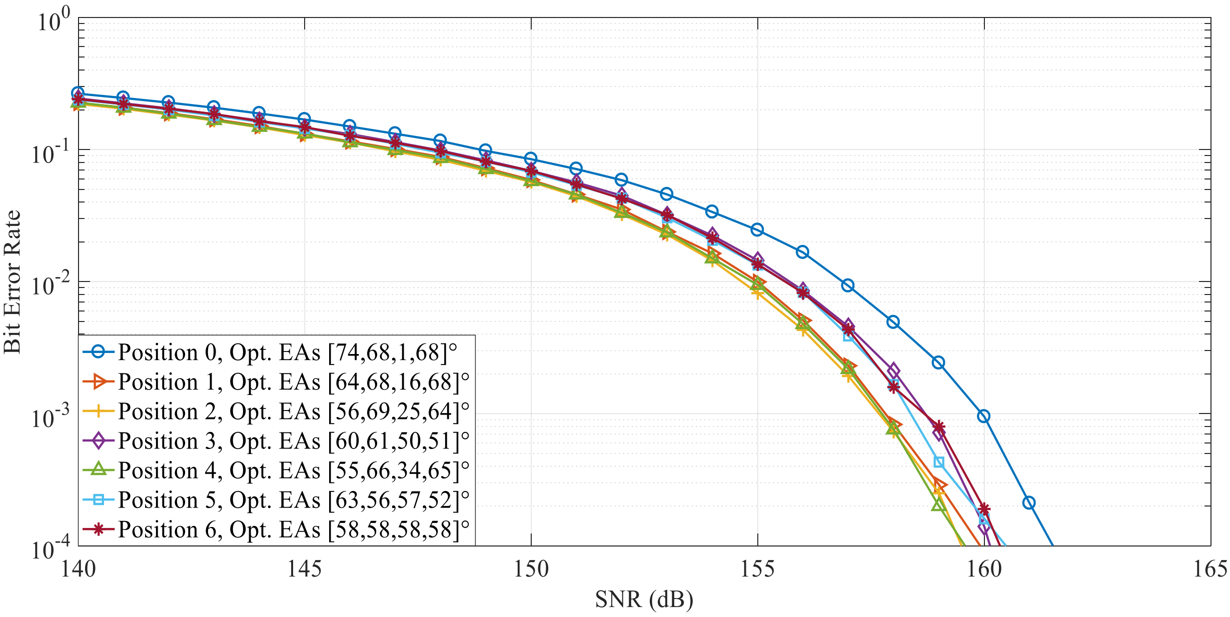

Figure 9 BER performance of RC employed variable EA MIMO-VLC system

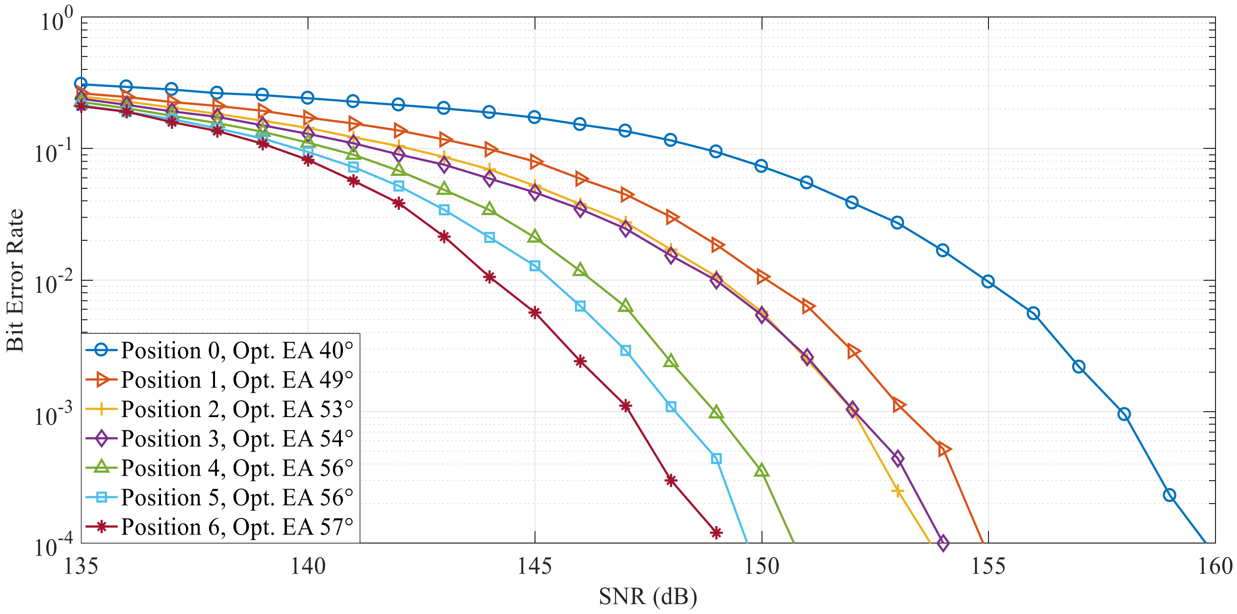

Figure 10 BER performance of SMP employed fixed EA MIMO-VLC system

Similarly, the BER performance of SMP employed fixed EA MIMO-VLC system is given in Figure 10. Position 6 performs the best as it is located at the center of the room. Position 0, which is located at the corner of the room, performs the worst. An SNR gap of 11dB is observed between positions 6 and 0. A similar trend is observed for the SMP employed variable EA MIMO-VLC system as given in Figure 11. As can be seen in Figure 11, an SNR gap of 11dB is observed between positions 6 and 0, where position 6 results in the best performance whereas position 0 results in the worst BER performance.

We have considered three positions i.e., position 1 (1.0, 1.0, 2.7), position 4 (1.5, 1.5, 2.7), and position 6 (2.0, 2.0, 2.7) for the BER performance comparison of RC and SMP employed MIMO-VLC systems. These positions are considered such that a fair comparison can be established between the RC and SMP employed MIMO-VLC systems. As it can be seen from Figure 12, the SMP employed MIMO-VLC system outperforms

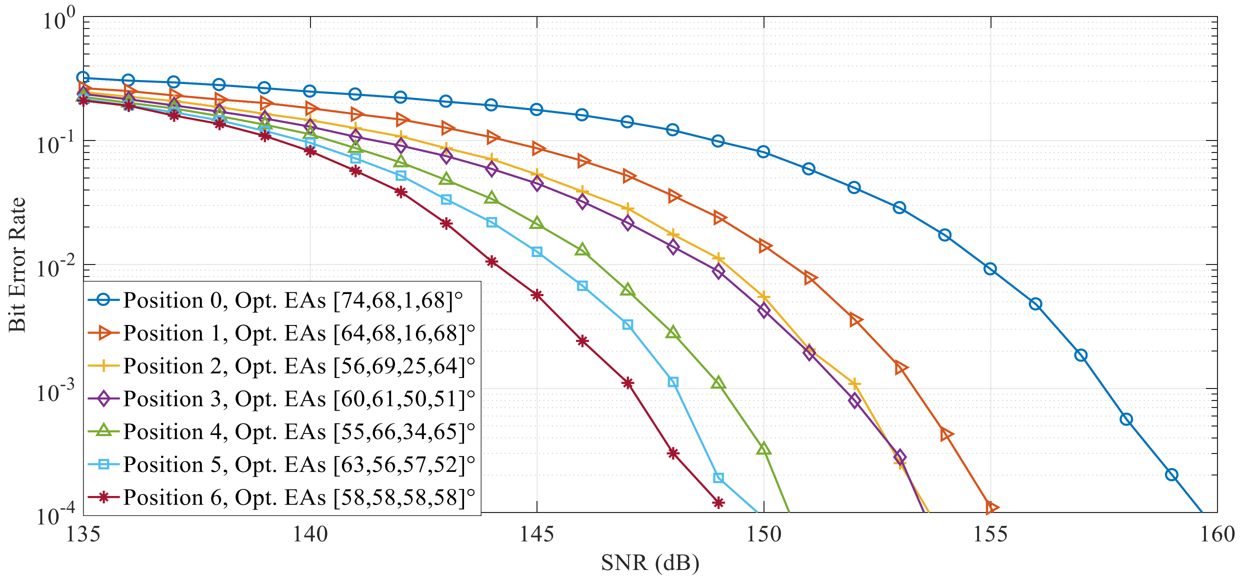

Figure 11 BER performance of SMP employed variable EA MIMO-VLC system

the RC employed the MIMO-VLC system. The performance of both systems depends on the difference between the channel factors. Depending upon the respective position of the receiver and the corresponding channel matrix entries, the performance of RC and SMP employed MIMO-VLC systems varies. The spatial multiplexing gain in an SMP-employed MIMO-VLC system increases linearly with the number of involved transmitters. However, there is no spatial multiplexing gain associated with an RC-employed MIMO-VLC system.

Similarly, to have the same spectral efficiency, we require a larger constellation size for RC as compared to SMP. That’s why we have used 16-PAM for RC employed MIMO-VLC system whereas 2-PAM is used for SMP employed MIMO-VLC system. The RC-employed MIMO-VLC system requires an additional SNR of 12.5dB to attain the same performance as SMP employed MIMO-VLC system. For all the considered receiver positions, the performance of the SMP employed MIMO-VLC system is better as compared to the RC employed MIMO-VLC system. A similar trend is observed for RC and SMP employed variable EA MIMO-VLC systems.

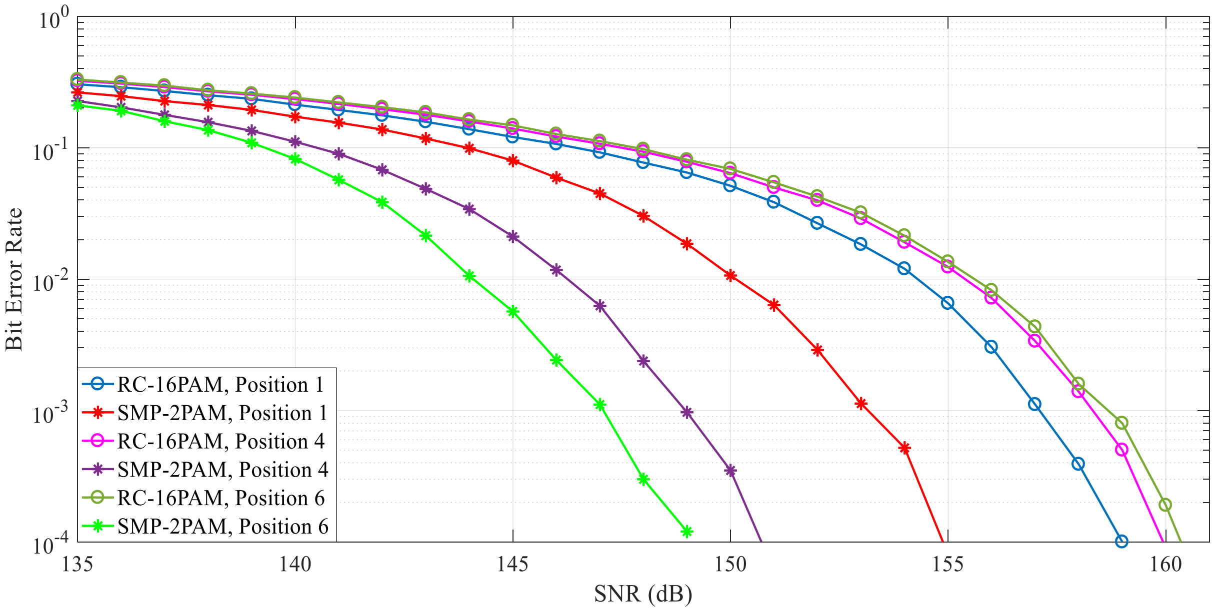

Figure 12 BER performance comparison of RC and SMP

4. CONCLUSION AND SUMMARY

In this paper, we have studied the BER performance of fixed and variable EA MIMO-VLC systems when different transmission schemes are employed for PR in an indoor environment. A 4x4 MIMO-VLC system with a static transmitter array is considered. Several receiver positions are considered across the room to evaluate the BER performance of the RC and SMP employed MIMO-VLC systems. We have shown that for a PR, the channel matrix entries depend on the EA of the PDs. The channel matrix correlation can be reduced by adopting a variable EA MIMO-VLC system. It has been exhibited that SMP results in an increase in the spectral efficiency of an IM/DD-employed MIMO-VLC system. However, a sufficiently low channel correlation is required to take full advantage of the spectrum efficiency presented by SMP. A PR-based MIMO-VLC system results in the low channel correlation required by an indoor SMP employed MIMO-VLC system. It has also been shown that the reliability of the MIMO-VLC system can be increased by adopting RC. The variable EA MIMO-VLC system results in better throughput as compared to the fixed EA MIMO-VLC system. However, the BER performance of fixed and variable EA MIMO-VLC systems is almost identical. It has been shown that SMP employed MIMO-VLC system outperforms RC employed MIMO-VLC systems for both fixed and variable EA employed systems. RC requires a larger signal constellation size to achieve the same spectral efficiency as SMP, which results in degrading the performance of an RC-employed MIMO-VLC system. An additional SNR of 12.5dB is required for an RC employed MIMO-VLC system as compared to SMP employed MIMO-VLC system to achieve a similar BER of 10^{-4} for position 6 of the receiver.

Acknowledgments

I would like to thank reviewers and editors for their effort and time.

Funding

"This work was supported by the Scientific and Technological Research Council of Turkey TUBITAK under the grant of Project No. 118E753."

The Declaration of Conflict of Interest/ Common Interest

No conflict of interest or common interest has been declared by the authors

Authors' Contribution

The first author contributed 50%, the second and third authors contributed 25% each.

The Declaration of Ethics Committee Approval

This study does not require ethics committee permission or any special permission.

The Declaration of Research and Publication Ethics

The authors of the paper declare that they comply with the scientific, ethical, and quotation rules of SAUJS in all processes of the paper and that they do not make any falsification on the data collected. In addition, they declare that Sakarya University Journal of Science and its editorial board have no responsibility for any ethical violations that may be encountered and that this study has not been evaluated in any academic publication environment other than Sakarya University Journal of Science.

REFERENCES

[1] L. Hanzo, H. Haas, S. Imre, D. O'Brien, M. Rupp, L. Gyongyosi, "Wireless myths, realities, and futures: From 3G/4G to optical and quantum wireless," Proceedings of the IEEE, vol. 100, no. SPL CONTENT, pp. 1853–1888, 2012.

[2] Cisco, "Cisco visual networking index (VNI) global mobile data traffic forecast update, 2017-2022 white paper," *Ca, Usa*, pp. 3–5, 2019.

[3] O. Ergul, E. Dinc, O. B. Akan, "Communicate to illuminate: State-of-the-art and research challenges for visible light communications," Physical Communication, vol. 17, pp. 72–85, 2015.

[4] D. C. O'Brien, L. Zeng, H. Le-Minh, G. Faulkner, J. W. Walewski, S. Randel, "Visible Light Communications: Challenges and possibilities," IEEE International Symposium on Personal, Indoor and Mobile Radio Communications, PIMRC, no. June 2014, 2008.

[5] W. De Zhong, C. Chen, H. Yang, P. Du, "Performance analysis of angle diversity multi-element receiver in indoor multi-cell visible light communication systems," International Conference on Transparent Optical Networks, vol. 1, pp. 2–5, 2017.

[6] Z. Zhan, M. Zhang, D. Han, P. Luo, X. Tang, Z. Ghassemlooy, L. Lang, "1.2 Gbps non-imaging MIMO-OFDM scheme based VLC over indoor lighting LED arrangments," Opto-Electronics Communication Conference, OECC 2015, pp. 3–5, 2015.

[7] Z. Chen, N. Serafimovski, H. Haas, "Angle diversity for an indoor cellular visible light communication system," IEEE Vehicular Technology Conference, vol. 2015, no. January, pp. 0–4, 2014.

[8] S. D. Dissanayake, J. Armstrong, “Comparison of ACO-OFDM , DCO-OFDM and ADO-OFDM in IM / DD Systems,” Journal of Lightwave Technology, vol. 31, no. 7, pp. 1063–1072, 2013.

[9] P. Fahamuel, J. Thompson, H. Haas, “Improved indoor VLC MIMO channel capacity using mobile receiver with angular diversity detectors,” IEEE Global Communications Conference 2014, pp. 2060–2065, 2014.

[10] O. Narmanlioglu, R. C. Kizilirmak, T. Baykas, M. Uysal, “Link adaptation for MIMO OFDM visible light communication systems,” IEEE Access, vol. 5, pp. 26006–26014, 2017.

[11] P. F. Mmbaga, J. Thompson, H. Haas, “Performance analysis of indoor diffuse VLC MIMO channels using angular diversity detectors,” Journal of Lightwave Technology, vol. 34, no. 4, pp. 1254–1266, 2016.

[12] A. A. Purwita, A. Yesilkaya, I. Tavakkolnia, M. Safari, H. Haas, “Effects of Irregular Photodiode Configurations for Indoor MIMO VLC with Mobile Users,” IEEE International Symposium on Personal, Indoor and Mobile Radio Communications, PIMRC, vol. 2019-September, pp. 1–7, 2019.

[13] T. Q. Wang, C. He, J. Armstrong, “Performance analysis of aperture-based receivers for MIMO IM/DD visible light communications,” Journal of Lightwave Technology, vol. 35, no. 9, pp. 1513–1523, 2017.

[14] A. Nuwanpriya, S. W. Ho, C. S. Chen, “Angle diversity receiver for indoor MIMO visible light communications,” 2014 IEEE Globecom Workshops 2014, pp. 444–449, 2014.

[15] M. Hosney, H. A. I. Selmy, A. Srivastava, and K. M. F. Elsayed, “Interference Mitigation Using Angular Diversity Receiver with Efficient Channel Estimation in MIMO VLC,” IEEE Access, vol. 8, pp. 54060–54073, 2020.

[16] T. C. Bui, S. Kiravittaya, K. Sripimanwat, N. H. Nguyen, “A Comprehensive Lighting Configuration for Efficient Indoor Visible Light Communication Networks,” International Journal of Optics, vol. 2016, 2016.

[17] M. H. Khadr, A. A. El Aziz, H. A. Fayed, M. Aly, “Bandwidth and BER improvement employing a pre-equalization circuit with white LED arrays in a MISO VLC system,” Applied Science, vol. 9, no. 5, 2019.

[18] C. Chen, W. De Zhong, H. Yang, S. Zhang, P. Du, “Reduction of SINR Fluctuation in Indoor Multi-Cell VLC Systems Using Optimized Angle Diversity Receiver,” Journal of Lightwave Technology, vol. 36, no. 17, pp. 3603–3610, 2018.

[19] M. L. N. Kumar, D. Sen, P. Mohapatra, “Performance evaluation of MIMO modulation schemes for indoor VLC channels with angular detectors,” IEEE Vehicular Technology Conference, vol. 2019-September, no. 1, pp. 1–6, 2019.

[20] A. Nuwanpriya, S. W. Ho, C. S. Chen, “Indoor MIMO Visible Light Communications: Novel Angle Diversity Receivers for Mobile Users,” IEEE Journal on Selected Areas in Communications, vol. 33, no. 9, pp. 1780–1792, 2015.

[21] A. U. Khan, Y. Çelik, S. Aldırmaz Çolak, “Capacity variation of an indoor MIMO VLC system for a pyramid receiver,” in 28th IEEE Conference on Signal Processing and Communications Applications (SİU), 2020.

[22] A. U. Khan, “Optimizing the performance of visible light communication system with angular diversity,” Kocaeli University, 2020.

[23] T. Fath, H. Haas, “Performance comparison of MIMO techniques for optical wireless communications in indoor environments,” IEEE Transactions on Communications, vol. 61, no. 2, pp. 733–742, 2013.

SAKARYA ÜNİVERSİTESİ

FEN BİLİMLERİ ENSTİTÜSÜ
DERGİSİ

Sakarya University Journal of Science
SAUJS

ISSN 1301-4048 | e-ISSN 2147-835X | Period Bimonthly | Founded: 1997 | Publisher Sakarya University |
http://www.saujs.sakarya.edu.tr/

Title: Characterization of a New Thermostable Carboxylesterase from Aneurinibacillus sp. PDF24

Authors: Meral BELDUZ KOLCU, Fulya AY SAL, Ali BELDÜZ, Sabriye ÇANAKÇI

Recieved: 2022-02-16 00:00:00

Accepted: 2022-08-16 00:00:00

Article Type: Research Article

Volume: 25
Issue: 5
Month: October
Year: 2022
Pages: 956-966

How to cite
Meral BELDUZ KOLCU, Fulya AY SAL, Ali BELDÜZ, Sabriye ÇANAKÇI; (2022), Characterization of a New Thermostable Carboxylesterase from Aneurinibacillus sp. PDF24. Sakarya University Journal of Science, 25(5), 956-966, DOI: 10.16984/saufenbilder.1074637
Access link
http://www.saujs.sakarya.edu.tr/en/pub/issue/73051/1074637

Sakarya University Journal of Science 25(5), 956-966, 2022

Characterization of a New Thermostable Carboxylesterase from *Aneurinibacillus* sp. PDF24

Meral BELDUZ KOLCU[1], Fulya AY SAL[2], Ali BELDÜZ*[2], Sabriye ÇANAKÇI[2]

Abstract

In this study, esterase of *Aneurinibacillus* sp. PDF24 strain, a thermophilic bacteria, was purified to homogenity (5.25 fold purification) by column chromotography, and characterized. The molecular weight of *Aneurinibacillus* sp. PDF24 esterase was determined about 40 kDa. The maximum activity of the purified esterase was analyzed at 55°C, pH 8.5. The esterase was found to be stable at 40ºC, 50ºC and 60ºC for 1 hour. K_m and V_{max} values for p-nitrophenyl butyrate were determined as 0.120 mM and 3164.8 U/mg, respectively. Considering K_m values in the literature, *Aneurinibacillus* sp. PDF24 esterase was found to have a good K_m value compared to other esterases. In the presence of 1 mM and 5 mM metal salts of Mg^{2+}, Li^{+}, Ca^{2+}, K^{+}, no significant change occured in enzyme activity. The activity of *Aneurinibacillus* sp PDF24 esterase was found to be stable also in the presence of ethanol, DMSO, EDTA, DTT and ß-mercaptoethanol. The data obtained suggest that the enzyme is a serine esterase, not a metalloprotein, and that disulfide bonds are not required to maintain enzyme conformation, and therefore, depending on its features, this esterase may be a suitable candidate for industrial applications.

Keywords: *Aneurinibacillus*, characterization, esterase, thermophilic

1. INTRODUCTION

Lipolytic enzymes are the most significant group of biocatalysts for biotechnological implementations. Hydrolases are a class of enzymes that displays a wide range of substrate specificity. Lipases (EC 3.1.1.3, triacylglycerol hydrolases) and esterases (EC 3.1.1.1, carboxyester hydrolases) which are two main groups of hydrolases are important biocatalysts with high industrial applications [1]. They catalyze the hydrolysis of ester bonds and are divided into some subclasses depending on the ester bonds they hydrolyze [2]. The three-dimensional structure of both groups of enzymes are characterized by the folding of the

---

* Corresponding author: belduz@ktu.edu.tr
[2] Karadeniz Technical University
ORCID: https://orcid.org/0000-0003-2240-7568
E-mail: fulyasal@gmail.com, sabriye@ktu.edu.tr
ORCID: https://orcid.org/0000-0002-0216-336X, https://orcid.org/0000-0003-0132-7198
[1] Avrasya University
E-mail: meralbelduz@hotmail.com
ORCID: https://orcid.org/0000-0002-9760-4817

characteristic α/β-hydrolase [3]. They are common in animals, plants and microorganisms. [4]. Esterases and lipases are found everywhere in nature and are produced by various plants, animals and microorganisms. Bacterial and fungal enzymes help in the classification of enzymes in organic chemistry and biotechnological applications [5]. Importance of scientific and biotechnological enzyme studies and the importance of microorganisms in obtaining enzymes are increasing day by day due to the increase in usage areas of enzymatic products in the industrial area and the importance of economic value. Esterases are used in processing the skin and post and in the removal of industrial wastewater by benefiting from the ability of esterases to cleave lipids [6]. The most important commercial area for hydrolytic esterases is detergents used in domestic and industrial washing machines and domestic dishwashers. The detergency of such detergents is at the highest level, all detergents contain similar ingredients and are based on similar detergent mechanisms. [7]. In particular, recent studies on fats have made biological processes more important than chemical processes. The most important reason for this is the formation of by-products in chemical processes and these by-products are high in number and also high temperature, pressure, pH etc. It requires exceptional circumstances. Furthermore, biotechnological methods are more economical than chemical methods. In recent years, esterases derived from thermophilic microorganisms have come to the forefront in industry. Thermophilic bacteria are organisms that are adapted to live in extreme temperature conditions, and the thermophilic enzymes are recently used in biotechnological and industrial fields. The stability of thermophilic enzymes against pH changes and high temperatures is the reason why these enzymes are preferred in industrial areas. Thermophilic enzymes are stable and active even at a temperature higher than the optimum growth temperature of microorganisms. These high temperatures significantly reduces the risk of contamination can occur during the reaction. Because most of the contaminating bacteria in the biological cycles are mesophilic. In the light of this information, in this study, a novel esterase was identified and purified from *Aneurinibacillus* sp. PDF24 strain and characterized to determine its suitability and potency for industrial processes or other applications in the field.

2. MATERIALS AND METHODS

2.1. Substrats and chemicals

p-nitrophenyl butyrate, p-nitrophenyl myristate, p-nitrophenyl deconoate, p-nitrophenyl laurate, p-nitrophenyl octanoate, p-nitrophenyl palmitate were purchased from Sigma (St. Louis, MO, USA). Protein ladder was purchased from NEB (Ipswich, MA) and all other chemicals were purchased from Merck AG (Darmstadt, Germany) and Sigma (St. Louis, MO, USA).

2.2. Bacterial strains and growth conditions

Aneurinibacillus sp. PDF 24 was isolated from Dikili Nebiler Hotspring in Turkey and identified as *Aneurinibacillus* sp. according to its morphological, physiologial, and biochemical properties and 16S rDNA sequences previously [8]. *Escherichia coli* JM101 was used as negative control of carboxylesterase activity because it does not have carboxylesterase. *Aneurinibacillus* sp. PDF 24 strain was grown at 50°C at pH 7.5 in Degryse medium and allowed to grow overnight.

2.3. Determination of carboxylesterase activity

Aneurinibacillus sp. PDF 24 and *Escherichia coli* JM101 were grown on Tributyrin agar plate. Plates were prepared by adding 1% tributyrin in Leura Bertani (LB) Broth. After inoculation, plates were incubated at 50°C for three days. Clear zone formation around the colonies indicated esterase activity.

2.4. Enzyme production

Overnight culture of *Aneurinibacillus* sp. PDF24 were inoculated into Degryse medium with an optical density (OD_{600}) of 0.1 and incubated at 50°C for 24 h with a shaking rate of 150 rpm. The cells were harvested by centrifugation at 10,000 rpm for 5 min at 4°C and pellet was resuspended in 50 mM Tris-HCl (pH 8.0) buffer, sonicated with Sartorius Labsonic M at 70% amplitude for 0.6 min at 5 min. To remove cell debris, the cell-free extract was centrifuged at 14,800 rpm for 15 min at 4°C and assayed for carboxylestrase activity.

2.5. Purification of carboxylesterase

A crude extract of *Aneurinibacillus* sp. PDF24 esterase was heated at 55°C for 15 min and precipitated proteins were removed by centrifugation at 14,800 rpm for 15 min at 4°C. After heat shock, ammonium sulfate precipitation was carried out between 20-80% $(NH_4)_2SO_4$ saturation. Resulting precipitates were dissolved in 50 mM Tris-HCl (pH 8.0) buffer and dialyzed overnight against the same buffer. The samples that have esterase activity were collected and loaded onto a Q sepharose Fast Flow column (50 x 1.5 cm) equilibrated with 20 mM Tris-HCl (pH 8.0). Elution was carried out with 500 mL gradient of NaCl (0.02–0.5 M) in the same buffer at a 1 mL/min flow rate. The fractions that have carboxylesterase activity were collected. The combined fractions was concentrated by centrifugation at 3,500 g for 15 min at 4°C using concentrator. The enzyme was then passed through a hydrophobic interaction column chromatography, Phenyl Sepharose 6 Fast Flow (20 x 0.75 cm). The column was equilibrated with 100 mL of 20 mM Tris-HCl (pH 8.0.) buffer including 1.3 M ammonium sulfate. Proteins were eluted with the gradient of ammonium sulfate from 1.3 M to 0 M and then 50 mL of 10% ethylene glycol was passed through the column with a flow rate of 0.5 mL/min. The amount of proteins in each fractions were determined by measurements at 280 nm wavelength in each purification step. In all eluted samples, the carboxylesterase activity was determined spectrophotometrically and fractions with the highest activity were selected. Protein concentration was determined by the Bradford method [9]. The purity and molecular mass were confirmed on SDS-PAGE (12% separating and 4.0% stacking) according to the method of Maniatis et al. [10].

2.6. Spectrophotometric carboxylesterase activity assay

The substrate (pNPB) solution for the determination of activity was prepared by mixing ethanol and 50 mM Tris–HCl (pH 8.0) to a final composition of 1:4:95 (v/v/v) of substrates dissolved in acetonitrile-isopropanol (1:1) /ethanol/buffer (50 mM Tris-HCl, pH 8,5), respectively.

Substrate solution (0.9 mL) and 50 mM Tris-HCl (pH 8.5) buffer (0.27 mL) were added to the enzyme (0.03 mL) and incubated at 55°C for 20 min [11]. After incubation, the enzyme activity was measured by monitoring the absorbance at 410 nm. One enzymatic unit was defined as 1 μmol p-nitrophenol formed in 1 minute from p-nitrophenyl butyrate (pNPB) at pH 8.5 and 55ºC. The molar absorption coefficient of p-nitrophenol at 410 nm was calculated as $1.457 x 10^5 cm^2 mol^{-1}$. All conditions that the reactions were carried out (reaction temperature, reaction pH, amount of enzyme) were rearranged as the enzymes optimum working conditions are determined.

2.7. Characterization of enzyme

2.7.1. Effects of temperature on activity and stability

Reactions, for determining the effects of temperatures on carboxylesterase activities were carried out at different temperatures ranging from 25ºC to 90ºC at pH 8.5 using pNPB as the substrate. Results were expressed as relative activity (%). For the stability of carboxylesterase, enzyme was incubated in 50 mM Tris-HCl (pH 8.5) buffer, at 40ºC, 50ºC, 60ºC, 65ºC, 70ºC and 75ºC for 20, 40 and 60 minutes. The residual activity (%) after incubation was calculated by comparison with untreated enzyme.

2.7.2. Effects of pH on activity and stability

Optimum pH of enzyme was determined by incubating enzyme in the range of pH from 5.0 to 10.0 at 55°C. pNPB was used as the substrate. The following buffers (50 mM) were used; sodium acetate (pH 5.0-5.5), potasium phosphate (pH

6.0), Tris-HCl (pH 7.0-8.0-8.5-9.0) and CAPS (pH 10.0). Results were expressed as relative activity (%).

To determine the stability of the enzyme at pH values of 5.0-10.0, a pre-incubation was performed at room temperature and 55°C for 60 min at each pH value. The residual enzyme activity was determined under the standard assay conditions.

2.7.3. Substrate specifity

To determine the substrate specificity of the esterase, p-nitrophenyl butyrate (4C), p-nitrophenyl caprylate (8C), p-nitrophenyl caprate (10C), p-nitrophenyl laurate (12C) p-nitrophenyl myristate (14C) and p-nitrophenyl palmitate (16C) were used. The relative activity (%) was determined under the standard assay conditions.

2.7.4. Effect of metal ions

Mg^{2+}, Li^{+}, Ca^{2+}, K^{+}, Zn^{2+}, and Co^{2+} were performed with chloride salts of metal ions. The enzyme was incubated with 1 mM metal ions for 15 minutes and 5 mM metal ions for 60 minutes at 55°C. To examine the effect of metal ions on the activity of carboxylesterase, incubated samples were assayed at 55ºC and pH 8.5 with pNPB as the substrate. The carboxylesterase activity of the enzyme without metal ions was defined as the 100% level. The residiul activity (%) was assayed spectrophotometrically.

2.7.5. Effect of detergents, potential inhibitors or organic solvents on the enzyme activity

To determine the effects of detergents, potential inhibitors or organic solvents such as 1% (v/v) of dimethyl sulfoxide (DMSO), β-Mercaptoethanol, ethanol and isopropanol, 0.1% of (v/v) Triton X-100, sodium dodecyl sulfate (SDS) and Tween 20, and 5 mM of EDTA, dithiothreitol (DTT), phenylmenthane sulfonyl fluoride (PMSF) were used. Carboxylesterase activity were assayed by the same procedure for 1 hour in 50 mM Tris-HCl (pH 8.5) buffer using pNPB as the substrate. The carboxylesterase activity of the enzyme without organic solvents, detergents and potantial inhibitors were defined as the 100% level. The residual activity (%) was assayed spectrophotometrically.

2.7.6. Kinetic parameters

The carboxylesterase activity was measured using various concentrations (25-1000 µM) of pNPB as substrate. The values of Michaelis-Menten kinetic parameters, V_{max} and K_m of the enzyme were calculated using a Lineweaver–Burk plot.

3. RESULTS AND DISCUSSION

3.1. Determination of carboxylesterase activity

Aneurinibacillus sp. PDF24 strain was shown to have esterase activity. *E.coli* JM101 strain that have no esterase activity and *Staphylococcus aureus* that have esterase activity were used as a positive and negative controls, respectively. After 3 days of incubation, the formation of clear zones around bacteria indicated the carboxylesterase activity (Figure 1).

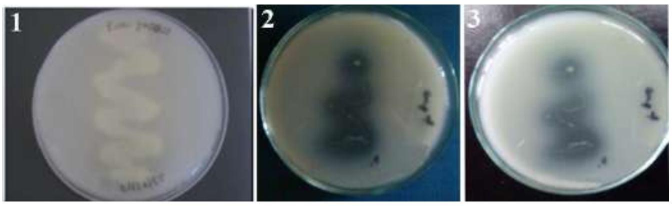

Figure 1 The esterase activity of the PDF24 bacterium on the Degryse-Tributrin agar. 1-*E.coli* JM101 esterase negative, 2-*Aneurinibacillus* sp. PDF24 esterase positive, 3-*Staphylococcus aureus* positive

3.2. Purification of the carboxylesterase

Aneurinibacillus sp. PDF24 carboxylesterase was expressed and purified by heat-shock, ammonium sulphate precipitation, ion exchange and hydrophobic interaction column chromatography. Protein concentrations and specific activities were determined after each purification steps. Enzyme purities were checked by SDS-PAGE analysis (Figure 2). Purifcation yields of enzymes after purifcation steps were shown in Table 1.

Table 1 Summary of purification steps

Purification step	Total volume (mL)	[Protein] (mg/mL)	Total protein (mg)	Total activity (U)	Spesific activity (U/mg)	Yield	Purification (fold)
Crude extract	17.0	1.9	32.5	116.9	3.6	100	1.0
Heat treatment	11.0	1.9	20.9	98.2	4,7	84.0	1.3
Ammonium sulfate precipitation	5.0	3.7	18.5	94.3	5.1	80.7	1.4
Ion exchange (Q-Sepharose)	4.1	0.7	2.9	45.8	15.7	39.2	4.4
Hydrophobic interaction	0.4	2.6	1.0	19.3	18.9	16.6	5.2

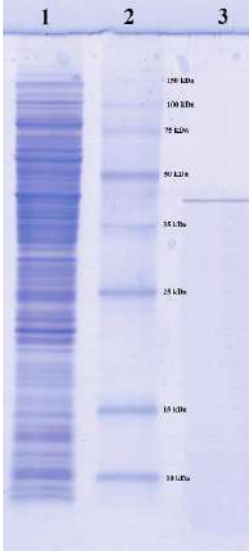

Figure 2 SDS-PAGE analysis of purified *Aneurinibacillus* sp. PDF24 esterase. Lane 1: Crude extract Lane 2: Moleculer weight marker Lane 3: Purified PDF24 esterase

3.3. Characterization of the carboxylesterase

3.3.1. Optimum pH and temperature

The optimum temperature for carboxylesterase was observed to be 55ºC and reactions were carried out at this temperature in subsequent experiments (Figure 3a)

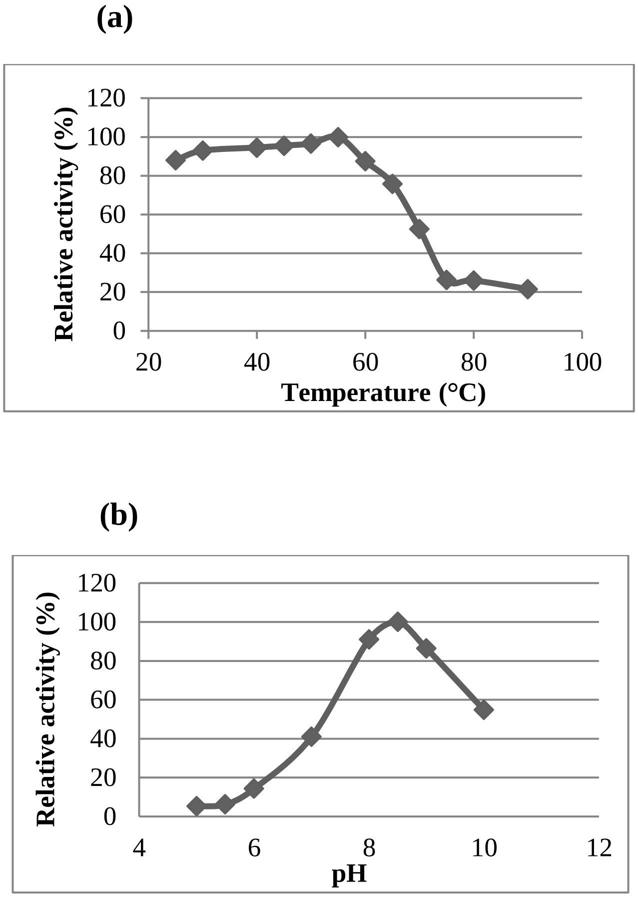

Figure 3 Effect of (a) temperature and (b) pH on activity of the purified PDF24

In literature, the optimum temperature of *Geobacillus thermodenitrificans* EstGtA2 and *Geobacillus* sp. DF20 esterases are reported to have 50°C [12, 13], *Geobacillus* sp. Est1, Est2 and Est3 esterases are reported to have 65°C [14] temperature optima. The optimum temperature of *Geobacillus thermoleovorans* YN EstA is reported as 60-65ºC [15]. When most of the esterases in the literature are reviewed, the optimum temperatures of the enzymes vary between 50-65ºC. The optimum temperature of *Aneurinibacillus* sp. PDF24 esterase is also in these ranges. However, there are also enzymes that operate at higher temperatures than these. For example, the optimum temperatures of *Thermoanaerobacterium thermosaccharolyticum* ThLip1 and ThLip2 are reported as 80ºC and 75ºC respectively [16].

The effect of pH on esterase activity was examined by a series reaction performed in buffers at pH 5.0-10.0. As shown in Figure 3b, optimum pH of *Aneurinibacillus* sp. PDF24 esterase was observed to be pH 8.5. Most of the previously studied esterases have been reported to operate at an optimum pH between 7.5 and 9.5 with a few exceptions, for example, *Thermoanaerobacterium thermosaccharolyticum* ThLip1 and ThLip2 have optimum pHs of 6.5 [16]. *Geobacillus thermodenitrificans* EstGtA2 esterase is reported to have a 8.0 optimum pH [12]. Optimum pH of *Geobacillus stearothermophilus* Est55 is in the range of 8.0-9.0. The optimum pH of *Geobacillus* sp. Est1 and Est3 is 9.5 [14] and the optimum pH of *Thermus* sp. NCCB 100425T is 7.5 [17]. Carboxylesterases in the literature generally have high optimum pHs. *Aneurinibacillus* sp. PDF24 esterase works better in alkaline environment than acidic environment and is compatible with other esterases in the literature.

3.3.2. pH and Temperature Stability

The enzyme was incubated at 40ºC, 50ºC, 60ºC, 65ºC, 70ºC and 75ºC for 1 hour to determine the effect of temperature on the stability of *Aneurinibacillus* sp PDF 24 esterase. At the end of incubation, there was no decrease in carboxylesterase activity at 40ºC, 50ºC and 60ºC. It was found that after 1 hour incubation at 65ºC, it retained 59% of its activity, 5% at 70ºC and 2% at 75ºC. (Figure 4a)

Comparing *Aneurinibacillus* sp PDF24 esterase to other similar esterases, *Geobacillus* sp Est1, Est2 and Est3 esterases retain 90% of their activities at 55-65°C for 1 hour [14], while *Geobacillus thermodenitrificans* EstGtA2 esterase retains 90% of the relevant activity at 55-60°C, however, only 15% at 75°C, and 83% at 65°C [12].

To determine the pH stability of the *Aneurinibacillus* sp PDF24 esterase, the pure enzyme was incubated at different pHs. There was no significant change in enzyme activity after 1.5 hours incubation at room temperature (data not shown). But, activity decreased to 90% at pH 5.0 and 97% at pH 6.0-10.0 after incubation at 55ºC for 1.5 hours. (Figure 4b)

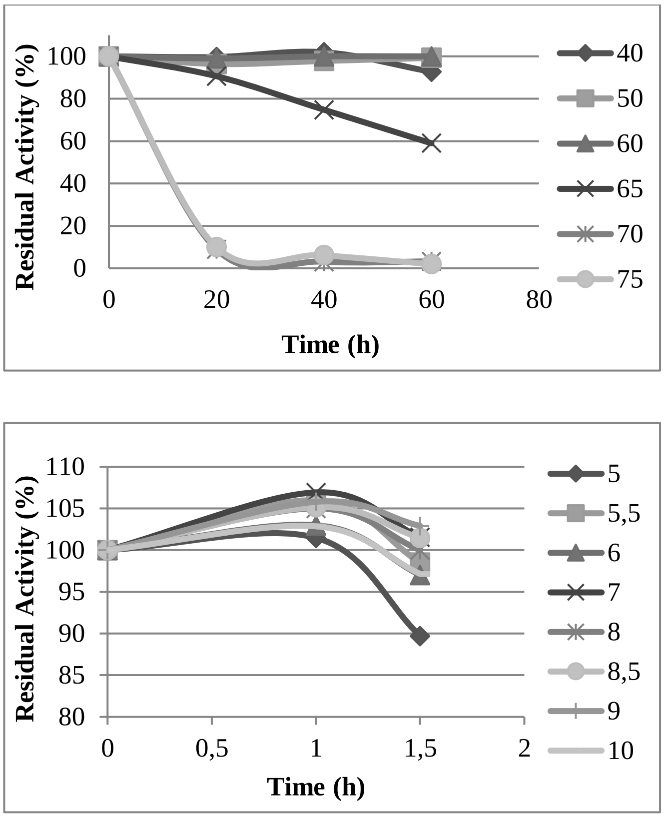

Figure 4 (a) Thermal stability of the purified PDF24 (b) pH stability of the purified PDF24 at 55 °C

The pH stability of *Geobacillus thermodenitrificans* EstGtA2 esterase at 50ºC was found to be 62%, and 36% at pH 6.0, and 11.0, respectively [12]. As a result, *Aneurinibacillus* sp. PDF24 esterase was found to have better pH stability than other esterases.

3.3.3. Substrate Specifity

The rates of hydrolysis of p-nitrophenyl acylates with chain length of C4, C8, C10, C12, C14, and C16 were determined for *Aneurinibacillus* sp. PDF24 esterase. The results demonstrated that *Aneurinibacillus* sp. PDF24 esterase has the maximal activity toward C4, while decreasing activities for C8, C10, C12, C14, and C16. *Aneurinibacillus* sp. PDF24 esterase prefers substrates with short-chain fatty acids instead of long-chain fatty acids (Table 2). The substrate specificity of esterases can vary, as the side chains of residues in the substrate binding pocket form steric hindrance. Esters with acyl chain lengths longer than C4 bind more difficult to the substrate binding site because of this steric hindrance [18]. Similarly, *Thermus* sp. NCCB 100425T, *Geobacillus* sp. DF20 and *Bacillus* sp. 4 [17, 13, 19] also showed a strong preference for the Hydrolysis of pNPB.

Table 2 Substrate specificity of the purified PDF24

Substrates	Relative activity (%)
***p*-NPB (C4)**	100
***p*-NPO (C8)**	74.5
***p*-NPD (C10)**	54.2
***p*-NPL (C12)**	28.9
***p*-NPM (C14)**	6.0
***p*-NPP (C16)**	1.8

3.3.4. Effect of Metal ions

For determining the effects of metal ions on esterase activity; chloride salts of Mg^{2+}, Li^{+}, Ca^{2+}, K^{+}, Zn^{2+}, and Co^{2+} were used. It was observed that in the presence of 1 mM metal salts of Mg^{2+}, Li^{+}, Ca^{2+}, K^{+}, no significant change occurs in activity, however Zn^{2+} decreased activity to 50% and Co^{2+} to 95%. In 1 hour incubation of enzyme with these salts (5 mM) Mg^{2+}, Li^{+}, Ca^{2+}, K^{+} showed still no significant change in activity, but Zn^{2+} decreased activity to 32% and Co^{2+} metal salt to 90%. (Figure 5)

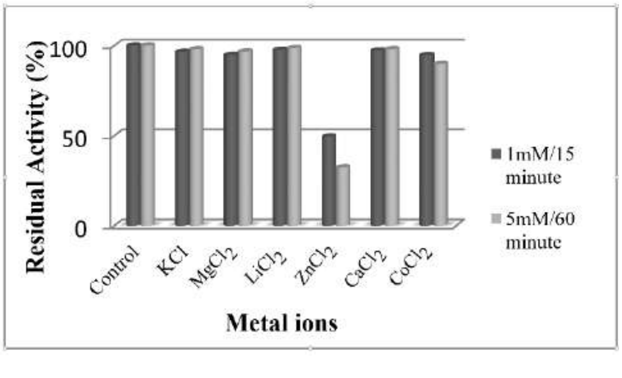

Figure 5 Effect of metal ions on PDF 24 activity

Metal ions have important roles in ensuring enzyme activity and structure by linking amino acids with negative charge in specific areas. *Geobacillus thermoleovorans* YN EstA esterase activity decreased to 17% with 1 mM Zn^{2+} but activity increased to 170% and 152% after incubations with Mg^{2+} and Ca^{+}, respectively [15]. The inhibition of esterase activity in the presence of Zn^{+2} has been reported in this study is in accordance with *Aneurinibacillus* sp. PDF24 esterase inhibition with Zn^{+2}. 1 mM Ca^{2+}, Zn^{2+}, K^{+} increased activity of *Geobacillus* sp Est1 esterase to 110%, 111%, 101% and 1 mM Cu^{2+}, Mg^{2+}, Li^{+} salts decreased activity to 88%, 92%, 89%, respectively [12]. 1 mM salts of Ca^{2+}, Zn^{2+}, K^{+}, Cu^{2+}, Mg^{2+}, Li^{+} increased *Geobacillus* sp Est2 esterase activity to 121%, 104%, and decreased activity to 98%, 81%, 95%, respectively [14]. Effect of metal ions on *Geobacillus* sp. Est3 esterase activity was determined and it was found that, Ca^{2+} and Zn^{2+} salts increase the activity of the enzyme to 103%, 115%, respectively. K^{+}, Cu^{2+}, Mg^{2+}, Li^{+} salts decrease the activity to 99%, 83%, 97% and 93%, respectively [14]. Considering all these datas, Ca^{2+} improves esterase activities in all these studies. Some esterases have a Ca^{2+} binding motif that increases enzyme activity and thermostability [20]. When the effect of Ca^{2+} on the activity of *Aneurinibacillus* sp. PDF24 esterase was examined, it was seen that the enzyme did not show Ca^{2+} dependent activation, which indicates that the enzyme does not have a Ca^{2+} binding site. Also the other metal ions that are used in this study (e.g Mg^{2+}, Zn^{2+}, K^{+}), don`t improve the activity of PDF24 esterase as they improve the activities of other enzymes as mentioned above.

3.3.5. Effect of detergents, organic solvents and potential inhibitors on the enzyme activity

The effects of detergent and organic solvents on the activity of *Aneurinibacillus* sp PDF4 esterase were investigated (Table 3). After treating the enzyme with these chemicals, the remaining activities at the end of 15, 30 and 60 minute incubations were calculated. The greatest inhibition was observed in the presence of SDS (an ionic detergent), which reduced *Aneurinibacillus* sp. PDF24 esterase activity to

7% after 1 hour incubation. Similarly, it was observed that SDS also inhibited Est1, Est2 and Est3 esterases of *Geobacillus* sp. [14]. Non-ionic detergents such as Triton X-100 and Tween 20 were found to reduce *Aneurinibacillus* sp. PDF24 esterase activity to 70% and 75%, respectively. Similarly, Triton X-100 and Tween 20 were also found to decrease the activity of *Geobacillus* sp. Est1, Est2 and Est3 esterases [14]. Most of the esterases and lipases contain a serine amino acid at their central active site [21]. The effect of PMSF, a serine inhibitor to *Aneurinibacillus* sp. PDF24 esterase, was found to reduce the activity of the enzyme to 10% after 1 hour incubation as expected for esterases with a serine in their active site. This data demonstrates that the enzyme is a serine esterase. *Geobacillus stearothermophilus* Est55 and Est30 esterase activity was reduced to 0% [22] and *Geobacillus* sp. Est1, Est2 and Est3 esterase activity were reduced to 45%, 58% and 55% respectively with PMSF as expected for esterases with a serine in their active site [14].

Organic solvents, which disrupt the hydrophobic interactions between the nonpolar side chains of amino acids, alter the natural structure of proteins. But activity of *Aneurinibacillus* sp. PDF24 esterase was found to be stable in the presence of organic solvents such as ethanol, DMSO and isopropanol, reducing agents that reduce disulfide bonds such as DTT and ß-Mercaptoethanol and in the presence of EDTA (a metal chelating agent). Studies on DTT and ß-mercaptoethanol, which are known as inhibitors of thiol groups, show that sulfhydryl groups do not have an important role in the active site of *Aneurinibacillus* sp. PDF24 esterase and suggesting that disulfide bonds are not obligatory to maintain the enzyme conformation [23]. As EDTA did not inhibit the enzyme, it can be suggested that this enzyme is not a metalloprotein [20]. In the literature, DMSO, EDTA and DTT were found to increase the activity of *Geobacillus* sp. Est1, Est2 and Est3 esterases [14]. Organic solvent such as isopropanol was found to reduce activity to 88% [14].

Table 3 Effect of inhibitors on PDF 24 activity

		Residual Activity (%)			
Inhibitors	**Concentration**	**0 min**	**15 min**	**30 min**	**60 min**
Control	0	100	100	100	100
DMSO	% 1 (v/v)	102	97	95	93
Ethanol	% 1 (v/v)	102	92	92	92
Isopropanol	% 1 (v/v)	101	92	92	88
β-Mercaptoethanol	% 1 (v/v)	104	102	101	100
EDTA	5 mM	98	95	94	92
PMSF	5 mM	50	5	11	10
DTT	5 mM	97	97	96	98
Triton X-100	%0,1 (v/v)	82	67	65	70
Tween 20	%0,1 (v/v)	83	75	70	75
SDS	%0,1 (v/v)	6	4	8	7

3.3.6. Kinetic Parameters

In determination of the kinetic parameters of *Aneurinibacillus* sp. PDF4 esterase, the substrate-activity graph was plotted in the presence of pNPB as the substrate and the enzyme was found to fit the simple Michaelis-Menten kinetics. The values of K_m and V_{max} were 0.120 mM and 3164.8 U/mg, respectively. K_m of esterases in the industrial applications was reported to be between 0.01 mM and 100 mM [24]. In the literature, K_m of *Geobacillus* sp. Est1 was found to be 0.095 mM [14], K_m of *Thermoanaerobacterium thermosaccharolyticum* esterase was 3.337 mM [16], K_m of *Thermus* sp. NCCB 100425T esterase was 18.32 mM [17], K_m of *Geobacillus* sp. DF20 esterase was 0.12 mM [13], K_m of *Geobacillus* sp. Est2 was 0.24 mM [14], K_m of *Geobacillus* sp. Est3 esterase was 0.17 mM [15], K_m of *Bacillus circulans* esterase was found to be 0.24 mM [25] Considering K_m values in the literature, *Aneurinibacillus* sp. PDF24 esterase was found to have a compatable K_m value compared to other esterases in the literature.

As a conclusion, in this study, a thermophilic esterase from the strain of *Aneurinibacillus* sp. PDF24 was purified and characterized. According to the results of SDS-PAGE, molecular weight of *Aneurinibacillus* sp. PDF24 esterase was determined to be 40 kDa. *Aneurinibacillus* sp. PDF24 esterase has an optimum pH of 8.5 and an optimum temperature of 55°C. Kinetic parameters of pNPB as the substrate of the enzyme were examined and K_m value was determined as 0.120 mM and V_{max} value was 3164.8 U/mg for this substrate. After incubation of enzyme for 1.5 hours at 55°C, the activity of the enzyme was decreased to 90% at pH 5.0, 97% at pH 6.0 and pH 10.0. In the presence of 1 mM $MgCl_2$, LiCl, $CaCl_2$, KCl, enzyme activity did not change significantly after 15 minutes incubation. It was observed that $ZnCl_2$ metal salt reduced activity to 50% and $CoCl_2$ metal salt reduced to 95%. The effects of detergents, organic solvents and other inhibitors on the activity of *Aneurinibacillus* sp. PDF24 esterase were investigated. The activity of *Aneurinibacillus* sp. PDF24 esterase was reduced down to 10% by PMSF (a serine inhibitor), down to 70% by Triton X-100, and down to 75% of Tween 20. SDS significantly reduced the activity. It was determined that activity remained stable in the presence of ß-Mercaptoethanol, DMSO, ethanol and EDTA, and activity decreased to 88% in isopropanol. Considering the obtained data, the biochemical features of the enzyme suggest the possible importance of the enzyme for industrial applications.

Funding
"The author (s) has no received any financial support for the research, authorship or publication of this study."

The Declaration of Conflict of Interest/ Common Interest

"No conflict of interest or common interest has been declared by the authors".

Authors' Contribution

"The authors contributed equally to the study"

The Declaration of Ethics Committee Approval

"This study does not require ethics committee permission or any special permission"

The Declaration of Research and Publication Ethics

"The authors of the paper declare that they comply with the scientific, ethical and quotation rules of SAUJS in all processes of the paper and that they do not make any falsification on the data collected. In addition, they declare that Sakarya University Journal of Science and its editorial board have no responsibility for any ethical violations that may be encountered, and that this study has not been evaluated in any academic publication environment other than Sakarya University Journal of Science."

REFERENCES

[1] S. Benjamin, A. Pandey, "*Candida rugosa* Lipases: Molecular Biology and Versatility In Biotechnology," Yeast, vol. 14, pp. 1069–1087, 1998.

[2] R. D. Schmid, R. Verger, "Lipases: Interfacial Enzymes with Attractive Applications," Angewandte Chemie-International Edition, vol. 37, pp. 1608-1633, 1998.

[3] A. Svendsen, P. Woolley, S. B. Petersen, "Lipases—Their Structure, Biochemistry and Applications." Cambridge University Press, Cambridge, pp. 1–21, 1994.

[4] U. T. Bornscheuer, R. J. Kazlauskas, "Hydrolayses In Organic Synthesis Regio and Stereoselective Biotransformations," Wiley Vch, Weinheim, pp. 105, 1999.

[5] P. K. Ghosh, R. K. Saxena, R. Gupta, R. P. Yadav, S. Davidson, “Microbial Lipases Production and Applications” Science Progress, vol. 79, no. 2, pp. 119-157, 1996.

[6] E. W. Seitz, “Industrial Applications of Microbial Lipases-A Review,” Journal of American Oil Chemists Society, vol. 51,pp. 12–16, 1974.

[7] S. Ito, T. Kobayashi, K. Ara, K. Ozaki, S. Kawai, Y. Hatada, “Detergent Enzymes From Alkaliphiles: Enzymatic Properties, Genetics and Structures,” Extremophiles vol. 2, pp. 90-185, 1998.

[8] K. İnan, “İzmir ve Aydın illerindeki bazı kaplıcalardan izole edilen termofilik bakteri izolatlarının moleküler taksonomisi ve D1021 izolatının glukoz izomerazının karakterizasyonu, Doktora Tezi,” 2011.

[9] M M. Bradford, “A rapid and sensitive method for the quantitation of microgram quantities of protein utilizing the principle of protein-dye binding,” Analytical Biochemistry vol. 72, pp. 248–254, 1976.

[10] T. Maniatis, E. F. Fritsch, J. Sambrook, “Molecular Cloning: a Laboratory Manual,” Cold Spring Har, 1982.

[11] D. Lee, Y. Koh, K. Kim, B. Kim, H. Choi, D. Kim, M.T. Suhartono, Y. Pyun, “Isolation and characterization of a thermophilic lipase from bacillus thermoleovorans ID-1” FEMS Microbiology Letters, vol. 179, pp. 393-400, 1999.

[12] D. M. Charbonneau, F. Meddeb-Mouelhi, and M. Beauregard, “A novel thermostable carboxylesterase from Geobacillus thermodenitrificans: evidence for a new carboxylesterase family,” The Journal of Biochemistry, vol. 148, pp. 299–308, 2010.

[13] E. Özbek, Y. Kolcuoğlu, L. Konak, A. Çolak, F. ÖZ, “Partial purification and biochemical characterization of an extremely thermo-and pH-stable esterase with great substrate affinity,” Turhish Journal of Chemistary, vol. 38, pp. 538-546, 2014.

[14] H. C. Tekedar, G. Şanlı-Mohamed, “Molecular cloning, over expression and characterization of thermoalkalophilic esterases isolated from Geobacillus sp.” Extremophiles, vol. 15, pp. 203–211, 2011.

[15] N. A. Soliman, M. Knoll, Y. R. Abdel-Fattah, R. D. Schmid, S. Lange, “Molecular cloning and characterization of thermostable esterase and lipase from Geobacillus thermoleovorans YN isolated from desert soil in Egypt,” Process Biochemistry, vol. 42, pp. 1090-1100, 2007.

[16] W. Li, H. Shi, H. Ding, L. Wang, Y. Zhang, X. Li, F. Wang, “Charcterization of two thermostable esterases from Thermoanaerobacterium thermosaccharolyticum,” Protein Expression and Purification, vol. 152, pp. 64-70, 2018.

[17] M. A. Tekincanli, M. Y. Akatin, A. ÇOLAK, “Purification and characterization of anovel thermostable esterase from Thermus sp. NCCB 100425^{T},” Turkish Journal of Biochemistry, vol. 40, no. 2, pp. 116-124, 2015.

[18] S. Yang, Z. Qin, X. Duan, Q. Yan, Z. Jiang, “Structural insights into the substrate specifi city of two esterases from the thermophilic Rhizomucor miehei,” Journal of Lipid Research, vol. 56, 2015.

[19] Z. B. Bakır Ateşlier, K. Metin, “Production and Partial Characterization of A Novel Thermostable Esterase From A Thermophilic Bacillus sp.,” Enzyme and Microbial Technology, vol. 38, pp. 628–635, 2006.

[20] F. Ay, H. Karaoglu, K Inan, S. Canakci, A. O. Belduz, “Cloning, purification and

characterization of a thermostable carboxylesterase from Anoxybacillus sp. PDF1," Protein Expression and Purification vol. 80, pp. 74–79, 2011.

[21] P. Fojan, P. H Jonson, M. T. Petersen, S. B. Petersen, "What Distinguishes an Esterase From A Lipase: A novel Structural Approach," Biochimie., vol. 82, pp. 1033-1041, 2000.

[22] H. E. Ewis, A. T. Abdelal, C.-D. Lu, "Molecular cloning and characterization of two thermostable carboxyl esterases from Geobacillus stearothermophilus," Gene, vol. 329, pp. 187-195, *2004.*

[23] J. de Cassia Pereira, E. C. Giese, M.. M. de Souza Moretti, A. C. dos Santos Gomes, O. M. Perrone, M. Boscolo, R. da Silva, E. Gomes and D. A. B. Martins, "Effect of Metal Ions, Chemical Agents and Organic Compounds on Lignocellulolytic Enzymes Activities,"Enzyme Inhibitors and Activators (Ed. M. Senturk), Chapter 6, 2017.

[24] P D. Fullbrook, "Practical Applied Kinetics. In: Godfrey T, West S (eds) Industrial enzymology. 2nd edition" Stockholm Press, New York, pp 483–540, 1996.

[25] A. Kademi, N. A¨ıt-Abdelkader, L. Fakhreddine, J. C. Baratti, "Characterization of A New Thermostable Esterase From The Moderate Thermophilic Bacterium Bacillus circulans," Journal of Molecular Catalysis B: Enzymatic, Vol.10, no. 4, pp. 395–401, 2000.

SAKARYA ÜNİVERSİTESİ

FEN BİLİMLERİ ENSTİTÜSÜ
DERGİSİ

Sakarya University Journal of Science
SAUJS

ISSN 1301-4048 | e-ISSN 2147-835X | Period Bimonthly | Founded: 1997 | Publisher Sakarya University |
http://www.saujs.sakarya.edu.tr/

Title: First Theoretical Identification of the Magnetic Dipole Moment of the 97.43 keV State in 153Eu

Authors: Elif KEMAH, Emre TABAR, Hakan YAKUT, Gamze HOŞGÖR

Recieved: 2022-05-31 00:00:00

Accepted: 2022-08-19 00:00:00

Article Type: Research Article

Volume: 25
Issue: 5
Month: October
Year: 2022
Pages: 967-973

How to cite
Elif KEMAH, Emre TABAR, Hakan YAKUT, Gamze HOŞGÖR; (2022), First Theoretical Identification of the Magnetic Dipole Moment of the 97.43 keV State in 153Eu. Sakarya University Journal of Science, 25(5), 967-973, DOI: 10.16984/saufenbilder.1123474

Sakarya University Journal of Science 25(5), 967-973, 2022

First Theoretical Identification of the Magnetic Dipole Moment of the 97.43 keV State in ^{153}Eu

Elif KEMAH[1], Emre TABAR*[1], Hakan YAKUT[1], Gamze HOŞGÖR[1]

Abstract

Two alternative values, +3.21±0.22 μ_N and-0.52±0.22 μ_N, for the magnetic dipole (M1) moment of the excited [532] $5/2^-$ state at 97.43 keV in ^{153}Eu were reported in the Mossbauer-effect study. The Quasiparticle Phonon Nuclear Model (QPNM) has been used to determine the correct value of the magnetic moment of this state. According to the QPNM calculations, the experimental 97.43 keV level is the [532] $5/2^-$ Nilsson state occurring at 79 keV. The QPNM predicted the magnetic moment of this state to be +3.2162 μ_N, which agrees well with one of the experimental values, i.e., +3.21±0.22 μ_N. Therefore, the correct value for the magnetic moment of the 97.43 keV level of ^{153}Eu is most probably +3.21±0.22 μ_N. The measured value (+3.4717±0.006 μ_N) of the magnetic moment of $5/2^-$ ground-state, which is probably a [532] Nilsson state according to our QPNM calculations, supports our prediction.

Keywords: Odd-mass nuclei, ^{153}Eu, magnetic dipole, *M*1, qpnm

1. INTRODUCTION

The deformed nuclei in the rare-earth mass region of the periodic table exhibit a rich variety of nuclear structure phenomena, such as multipole excitations, shape changes and shape coexistence [1]. Determining the magnetic dipole moments of odd-mass nuclei in this region allows us to obtain directly or indirectly information on the underlying structure of these nuclear phenomena due to the direct relationship between the magnetic moments and the single particle configurations [2]. Therefore, magnetic moments are crucial to clarify whether the single particle or the collective motion is responsible for the observed nuclear features [3].

---

* Corresponding author: elif.kemah2@ogr.sakarya.edu.tr

[1] Sakarya University

E-mail: etabar@sakarya.edu.tr, hyakut@sakarya.edu.tr, gamze.hosgor2@ogr.sakarya.edu.tr

ORCID: https://orcid.org/0000-0001-9512-5524, https://orcid.org/0000-0002-5093-9409, https://orcid.org/0000-0002-3903-5863, https://orcid.org/0000-0001-5589-9824

Considerable experimental data are available on the magnetic moment of the ground- and some low-lying excited-states of the rare-earth odd-mass nuclei [4]. Extensive theoretical investigations have also been carried out on the ground-state magnetic moments of these nuclei [5-10]. However, a limited number of theoretical studies are available for the magnetic moments of the excited-states in odd-mass deformed nuclei [11].

The problem of correctly describing the observed magnetic moments of the odd-mass nuclei is required proper interpretation of the core-polarization which is directly affect the magnetic moments [1]. The core polarization in the odd-mass nuclei arises as a result of interaction between the valance nucleon and the M1 excitations of the core [1, 12, 13]. The core polarization effect has been subject of several theoretical works in which the importance of the requirement of considering core-polarization in the calculation of magnetic moments has been pointed out [11-17]. Recently, a microscopic method [14-17] within the framework of the Quasiparticle Phonon Nuclear Model (QPNM) [18] has been introduced for the magnetic moment calculation of odd-mass deformed nuclei. It has been demonstrated with numerical results that this method not only reproduce the experimental magnetic moments and intrinsic factors but also gives a theoretical explanation for the effective spin gyromagnetic factors, which are assumed to be 0.6-0.7 in several calculations [14-17].

Undoubtedly, investigation of the magnetic moment of an excited-state would be an important challenge for this model to test whether it retains its success in calculating the ground-state magnetic properties for excited states. In light of the above-mentioned fact, in the present paper, the magnetic dipole ($M1$) moment of the excited [532] $5/2^-$ state at 97.43 keV in ^{153}Eu nucleus is studied in detail using the method based on the QPNM [14-18]. It is an intriguing nucleus to study since there are two alternative experimental values, +3.21±0.22 μ_N and -0.52±0.22 μ_N, for the 97.43 keV state [19]. Therefore, it constitutes an invaluable ground to test the possibility of describing the magnetic properties of the excited-states in odd-mass deformed nuclei within the framework of the QPNM. Naturally, determining the correct value of the M1 moment of this state is another purpose of the current work.

In Sec. II, the way of treating the magnetic properties within the QPNM is described, and related analytical expressions are presented. In Sec. III, the results of the calculation are given and discussed. Sec. IV is a summary of the obtained results.

2. THEORY

In order to investigate the magnetic properties of an odd-mass nucleus, a model nuclear Hamiltonian taking into account the pairing and residual spin-spin interactions is constructed as follows [14-17]:

$$H \approx H_{sqp} + H_{coll.} + H_{\text{int.}} \tag{1}$$

where the H_{sqp} and $H_{coll.}$ described the single-quasiparticle and collective motion in axially-symmetric mean-field, respectively, and $H_{\text{int.}}$ represents the interaction between single quasiparticles and phonons of collective motion. The ecliptic expressions of H_{sqp}, $H_{coll.}$ and $H_{\text{int.}}$, and the detail of the notations used in this study can be found in refs [14-17].

For the states with K>1/2, the wave function of odd-mass deformed nuclei includes the one-quasiparticle term as well as the single-quasiparticles⊗phonon mixing term:

$$\Psi_K^j(\tau) = \left\{ N_K^j \alpha_K^+(\tau) + \sum_{i\nu} G_{ij}^{K\nu} \alpha_\nu^+(\tau) Q_i^+ \right\} \left| \psi_0 \right\rangle \tag{2}$$

Here the index j defines the number of the states for a given K$^{\pi}$. N_K^j and $G_{ij}^{K\nu}$ are the one-quasiparticle and the quasiparticle⊗phonon amplitudes of the wave function, respectively [14-17].

Within the framework of the well-known variational method, the analytical expression of the secular equation can be found as follows:

$$-P(\eta) \equiv \varepsilon_K - \eta_K - \\ -\sum_{i\nu} \frac{1}{Z(\omega_i)} \frac{q^2 \sigma_{K\nu}^2 M_{K\nu}^2}{\left(1+\chi F_p^i\right)^2 \left(\omega_i + \varepsilon_\nu - \eta_K\right)} = 0 \tag{3}$$

where

$$Z(\omega_i) = \frac{1}{\left(-\chi F_n\right)^2} Y_n(\omega_i) + \frac{q^2}{\left(1+\chi F_p\right)^2} Y_p(\omega_i)$$

$$Y_\tau = 4\omega_i \sum_{ss'} \frac{\varepsilon_{ss'} \sigma_{ss'}^2 L_{ss'}^2}{\left(\varepsilon_{ss'}^2 - \omega_i^2\right)^2} \;\; ; \;\; F_\tau = 2 \sum_{ss'} \frac{\varepsilon_{ss'} \sigma_{ss'}^2 L_{ss'}^2}{\varepsilon_{ss'}^2 - \omega_i^2} \tag{4}$$

here, ω_i is the energies of the collective 1^+ states of the even-even core. The roots (η_K) of Eq.(3) are the ground- and excited-states energies of the non-rotational states of the odd-mass nucleus under investigation. The analytical expressions for $G_{ij}^{K\nu}$ and N_K^j can be easily obtained by using the secular Eq. (3) and the normalization condition of the wave function. The explicit form of the $G_{ij}^{K\nu}$ and N_K^j can be found in refs [14-17].

For a K>1/2 state of an odd-mass nucleus, the intrinsic magnetic moment i.e. $\mu_K = g_K K$ is the expectation value of μ_z [14-17]:

$$\mu_K = \left\{ \begin{array}{l} (g_s^p - g_\ell^p)\left(1 + N_K^2 \frac{1}{Z(\omega_i)} \frac{2M_{K\upsilon}(1+\chi F_n)}{\left(\chi^2 F_n\right)\left(1+\chi F_p\right)\left(\varepsilon_\upsilon + \omega_i - \eta_K\right)}\right) - \\ -g_s^n N_K^2 \frac{1}{Z(\omega_i)} \frac{2qM_{K\upsilon}}{\chi\left(1+\chi F_p\right)\left(\varepsilon_\upsilon + \omega_i - \eta_K\right)} \end{array} \right\} \left\langle K \left| s_z \right| K \right\rangle + g_\ell^p K \tag{5}$$

Omitting the details and considering the $K = \upsilon$ for $\mu = 0$ following analytical expression for g_s^{eff} can be easily found from the comparison of Eq. (5) and the well-known Nilsson formula [14-17].

$$g_s^{eff} - g_l^p = \\ = \left(g_s^p - g_\ell^p\right)\left(1 + 2N_K^2 \sum_i \frac{\left(1+\chi F_n\right)}{\chi^2 Z(\omega_i) F_n \left(1+\chi F_p\right)} \frac{1}{(\varepsilon_K + \omega_i - \eta_K)}\right) - \\ - g_s^n N_K^2 \sum_i \frac{2q}{\chi Z(\omega)\left(1+\chi F_p\right)(\varepsilon_K + \omega_i - \eta_K)} \tag{6}$$

As can be seen from Eq. (6), the mixing of one-quasiparticle and phonon terms caused the quenching of the spin gyromagnetic factor in odd-Z nuclei. According to the Unified Model [1], the magnetic moment of an odd-mass nucleus for a K>1/2 state includes contribution both from the rotational and intrinsic motion of the nucleus [14- 17]:

$$\mu = \frac{K}{I+1}\left(g_K K + g_R\right) \tag{7}$$

In order to take into account the rotational contribution in our calculations, the rotational gyromagnetic factors (g_R) calculated within the Inglis-Belyaev cranking model [20] is used.

3. RESULT AND DISCUSSIONS

The calculations were performed with the single particle scheme of levels for an axially symmetric Woods-Saxon potential [21]. The quadrupole deformation parameter β_2=0.3064 taken from the work of Raman [22]. The neutron and proton pairing constants are Δ_n=0.986 MeV and Δ_p=1.053 MeV, respectively from the odd-even mass differences [23]. The chemical potentials for neutrons and protons were calculated to be λ_n=-7.159 and λ_p=-7.993 following the same procedure of Ref [18].

The calculations show that the interaction between the odd-particle and the *M*1 excitations of the core causes shifting of the energy of the single quasiparticle state. However, this shift is small and usually does not exceed 0.006 MeV.

Figure 1(a) compares the theoretical and experimental structure of the ground- and 97.43 keV excited-state. As shown in Figure 1(a), the calculated and experimental energies and the Nilsson quantum numbers are in good agreement. It is important to state that the QPNM results for the structure of these two states are consistent with the results reported by Soloviev et al. [24]. The $5/2^-$ ground- and $5/2^+$ excited-state in ^{153}Eu can be assumed to have one-quasiparticle character since the single-quasiparticle contributions to the wave function of these two states exceed 99%. On the other hand, the structure of these states calculated within QPNM contains quasiparticle⊗phonon admixtures. Although the quasiparticle⊗phonon terms in the wave functions do not exceeds the 0.05%, the coherent contribution of these small admixtures leads to a quenching of spin gyromagnetic factors. The effective gyromagnetic ratio for the excited-state at 97.43 keV is found to be $g_s^{eff} = 0.798\, g_s^{free}$.

As seen from Figure 1(b) when the spin-spin interaction strength equals to /=20, the g_K value for the excited-state at 97.43 keV is in excellent agreement with the semi-empirical g_K value calculated using μ=+3.21±0.22 μ_N experimental magnetic moment. On the other hand, the semi-empirical value of g_K calculated using the other experimental value, i.e. μ=-0.522±0.22 μ_N is considerably smaller than the theoretical results. Therefore, the actual value of the experimental magnetic moment of the states at 97.43 keV in ^{153}Eu is most probably μ=+3.21 ±0.22 μ_N.

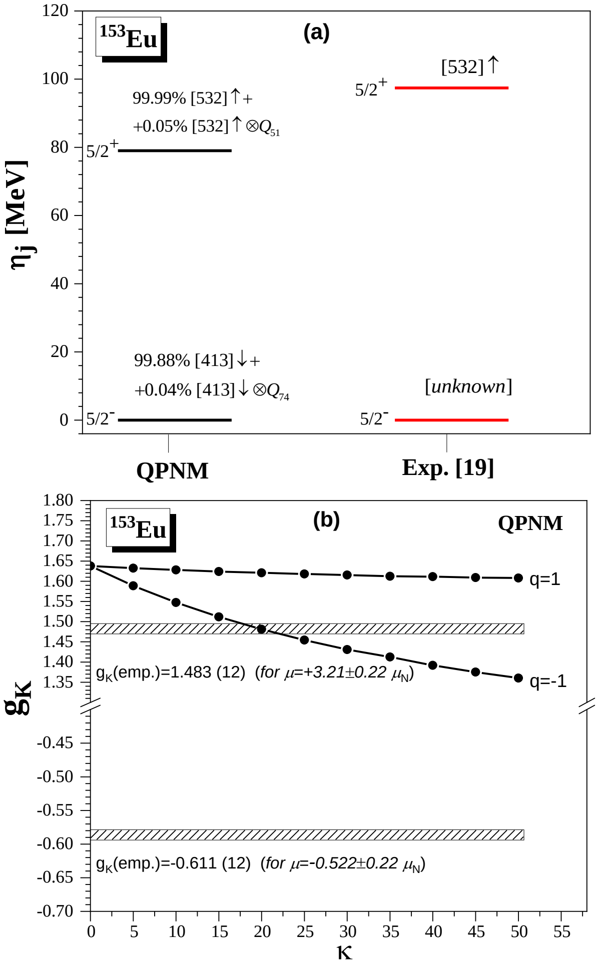

Figure 1 **(a)** Comparison of the theoretical and experimental structure of the ground- and 97.43 keV excited-state in ^{153}Eu. **(b)** Intrinsic magnetic moment (g_K) of the excited-state at 97.43 keV as a function of q and | where *q*=1 and *q*=-1 correspond to the isovector and isoscalar part, respectively

Figure 1(b) shows the intrinsic magnetic moment (g_K) of the excited-state at 97.43 keV as a function of q and κ.

Using the g_R=0.42 determined from the cranking model and taking into account the g_K factor calculated within QPNM, the magnetic moment of this excited state is predicted to be μ=+3.2162 μ_N.which agrees well with one of the experimental values, μ=+3.21±0.22 μ_N. According to the single particle model calculations, μ=+3.493 μ_N which is also consistent with our result. Besides, the measured value (μ=+3.4717 ± 0.006 μ_N) of the magnetic moment of $5/2^-$ ground-state, which is probably a [532] 5/2 Nilsson state according to our QPNM calculations, support our prediction.

4. CONCLUSION

The magnetic moment of the state at 97.43 keV in ^{153}Eu has been theoretically investigated using the QPNM. There are two different experimental magnetic moments values (+3.21±0.22 μ_N and -0.52±0.22 μ_N) fo these state. According to QPNM calculations the true value of the magnetic moment of this excited states is likely +3.21±0.22 μ_N. This prediction is supported by the result of the single particle model calculation and the magnetic moment values of the ground-state of ^{151}Eu which has the same Nilsson quantum numbers as the state at 97.43 keV in ^{153}Eu.

In the light of the above mentioned results it is possible to state that the method based on the QPNM is succesful not only in the determination of the magnetic properties of ground-states, but also in description of the magnetic properties of low-lying states in odd-mass nuclei.

Acknowledgements

Funding

The author (s) has no received any financial support for the research, authorship or publication of this study.

Authors' Contribution

The authors contributed equally to the study.

The Declaration of Conflict of Interest/ Common Interest

No conflict of interest or common interest has been declared by the authors.

The Declaration of Ethics Committee Approval

This study does not require ethics committee permission or any special permission.

The Declaration of Research and Publication Ethics

The authors of the paper declare that they comply with the scientific, ethical and quotation rules of SAUJS in all processes of the paper and that they do not make any falsification on the data collected. In addition, they declare that Sakarya University Journal of Science and its editorial board have no responsibility for any ethical violations that may be encountered, and that this study has not been evaluated in any academic publication environment other than Sakarya University Journal of Science.

REFERENCES

[1] A. Bohr, B. Mottelson, “Nuclear Structure”, Vol. 1, 2, Benjamin, 1975.

[2] N. Benczer-Koller, G. Lenner F, R. Tanczyn, A. Pakou, G. Kumbartzki, A. Pique, “Magnetic moments of low-lying states in medium weight odd nuclei” Hyperfine Interactions vol. 43, pp. 457-467, 1988.

[3] R. Neugart, G. Neyens, “Nuclear Moments”, Lecture Notes in Physics, vol. 700, 135–189, Springer-Verlag Berlin Heidelberg, 2006.

[4] N. J. Stone, “Table of Nuclear Magnetic Dipole and Electric Quadrupole

Moments”, IAEA Vienna Report No. INDC(NDS)-0658, 2014.

[5] I. L. Lamm, ‘‘Shell-model calculations on deformed nuclei,’’ Nuclear Physics A, vol. 125, pp. 504-530, 1969.

[6] R. R. Chasman, I. Ahmad, A. M. Friedman, J.R. Erskine, ‘‘Survey of single-particle states in the mass region A>228’’ Reviews of Modern Physics, vol. 49, no 4, pp. 833-891, 1977.

[7] A. K. Jain, R. K. Sheline, P. C. Sood, K. Jain, ‘‘Intrinsic states of deformed odd-A nuclei in the mass regions (151≤A≤193) and (A≥221)’’, Reviews of Modern Physics, vol. 62, no 2, pp. 293-509, 1990.

[8] L. Bonneau, J. Le Bloas, P.Quentin, ‘‘Effects Of Core Polarization And Pairing Correlations On Some Ground-State Properties Of Deformed Odd-Mass Nuclei Within The Higher Tamm–Dancoff Approach,’’ International Journal of Modern Physics E, vol. 20, no 2, pp. 252–258, 2011.

[9] L. Bonneau, P. Quentin, N. Minkov, J. Bartel, J. Le Bloas, ‘‘Effects of Core Polarization and Pairing Correlations on Magnetic Moments of Deformed Odd Nuclei’’, Nuclear Theory, vol. 31, pp. 164-174, 2012.

[10] L. Bonneau, N. Minkov, Dao Duy Duc, P. Quentin, J. Bartel, ‘‘Effect of core polarization on magnetic dipole moments in deformed odd-mass nuclei,’’ Physical Review C, vol. 91, p. 054307, 2015.

[11] A.A. Kuliev, N.I. Pyatov, ‘‘Magnetic Dipole Interactions in Deformed Nuclei, Soviet Journal of Nuclear Physics’’, Soviet Journal of Nuclear Physics-Ussr, pp. 185-189, 1969.

[12] Z. Bochnacki, S. Ogaza, ‘‘Spin polarization effect and the magnetic moments of odd-mass deformed nuclei’’, Nuclear Physics, vol. 69, no 1, pp. 186-192, 1965.

[13] J. De Boer, J.D. Rogers, ‘‘Concerning the magnetic properties of deformed nuclei in region 153 ≤ A ≤ 187’’, Physics Letters, vol. 3, no 6, pp. 304–306, 1963.

[14] H. Yakut, E. Guliyev, M. Guner, E. Tabar, Z. Yildirim, ‘‘QPNM calculation for the ground state magnetic moments of odd-mass deformed nuclei: $^{157-167}$Er,’’ Nuclear Physics A, vol. 888, pp. 23-33, 2012.

[15] H. Yakut, E. Tabar, A. A. Kuilev, Z. Zengnerler, P. Kaplan, ‘‘Ground state magnetic properties of odd neutron Dy isotopes’’, International Journal of Modern Physics E, vol. 22, no 10, p. 1350076, 2013.

[16] H. Yakut, E. Tabar, A. A. Kuliev, E. Guliyev, ‘‘The ground-state magnetic moments of odd-mass Hf isotopes’,’ Central European Journal of Physics, vol. 12, no 12, pp. 843-850, 2014.

[17] H. Yakut, E. Tabar, A. A. Kuliev, E. Guliyev, H. Quliyev, G. Hoşgör, “Magnetic Moments and g factors in odd-mass Ho isotopes’’, Chinese Physics C, vol. 41, no 7, p. 074101, 2017.

[18] V. G. Soloviev, “Theory of Complex Nuclei” Pergamon Press, 1976.

[19] U. Atzmony, S. Ofer, ‘‘Mössbauer-Effect Studies of the 97-keV Level of Eu^{153}’’, Physical Review, vol. 145, no 3, pp. 915-917, 1966.

[20] O. Prior, F. Boehm, S.G. Nilsson, ‘‘Collective gyromagnetic ratios of deformed nuclei’’ Nuclear Physics A, vol. 110, pp. 257-272, 1968.

[21] J. Dudek, T. Werner, ‘‘New parameters of the deformed Woods-Saxon potential for A=110-210 nuclei,’’ Journal of Physics G: Nuclear and Particle Physics, vol. 4, pp. 1543-1561, 1978.

[22] S. Raman, C.W. Nestor Jr., P. Tikkanen, Atomic Data and Nuclear Data Tables, vol. 78, pp. 1-128, 2001.

[23] P. Moller, W. D. M. J. R. Nix, W. J. Swiateck, Atomic Data Nuclear Data Tables, vol. 59, pp. 185-381, 1995

[24] V.G. Soloviev, S.I. Fedotov, ‘‘Nonrotational States in Odd-Z Deformed Nuclei with 153 < A < 177,’’ Izvestiya Akademii Nauk SSR, Seriya Fizicheskaya, vol. 36, pp. 706-710, 1972.

SAKARYA ÜNİVERSİTESİ
FEN BİLİMLERİ ENSTİTÜSÜ
DERGİSİ

Sakarya University Journal of Science
SAUJS

ISSN 1301-4048 | e-ISSN 2147-835X | Period Bimonthly | Founded: 1997 | Publisher Sakarya University |
http://www.saujs.sakarya.edu.tr/

Title: Mold Design and Analysis for Multi-Component Plastic Injection Parts with Contrasting Functional Features: Case Study

Authors: Akın Oğuz KAPTI, Erdi ERTEKİN, Uğur ACUN

Recieved: 2022-07-01 00:00:00

Accepted: 2022-08-25 00:00:00

Article Type: Research Article

Volume: 25
Issue: 5
Month: October
Year: 2022
Pages: 974-989

How to cite
Akın Oğuz KAPTI, Erdi ERTEKİN, Uğur ACUN; (2022), Mold Design and Analysis for Multi-Component Plastic Injection Parts with Contrasting Functional Features: Case Study. Sakarya University Journal of Science, 25(5), 974-989, DOI: 10.16984/saufenbilder.1138590
Access link
http://www.saujs.sakarya.edu.tr/en/pub/issue/73051/1138590

Sakarya University Journal of Science 25(5), 974-989, 2022

Mold Design and Analysis for Multi-Component Plastic Injection Parts with Contrasting Functional Features: Case Study

Akın Oğuz KAPTI*[1], Erdi ERTEKİN[1], Uğur ACUN[1]

Abstract

The classical plastic injection method is based on the principle of injecting a single color of a single polymeric material into the mold cavity under high pressure. In cases where the products are expected to have contrasted functional features and different colors, the classic injection process and the conventional injection molds are not sufficient. This paper proposes a new design approach for multi-component injection molds required by products containing different polymeric materials or different colors of the same polymeric material at the same time. It also presents a case study including the design of the hot runner, electromechanical rotary-cross, cooling, and ejection systems of a two-component, eight-cavity toothbrush mold. The polymeric materials are polypropylene for the first component, and styrene based thermoplastic elastomer for the second component, which exhibit good bonding properties with each other. In addition, an analysis study covering the filling parameters and production defect generations is also provided. The adopted design approach provides a production rate of 1600 parts per hour, corresponding to 18 s cycle time and 200 cycles per hour, and makes it sufficient to rotate only the 80 kg core plate instead of 1120 kg entire core side. Compared to existing methods, the results show that the proposed multi-component injection mold design method eliminates the need for particular injection machines and robotic systems, shortens the cycle time, and reduces energy consumption.

Keywords: Multi-component mold, plastic injection, mold design, rotary-cross method, toothbrush mold

1. INTRODUCTION

Plastic injection molding is one of the most used plastic part production approaches. It provides many advantages such as the suitability for mass production of identical parts, automation compatibility, the desired dimensional accuracy, flexibility in product geometry, unnecessity for additional processing, ease of metal attachments adding to the mold before injection, and ease of recycling [1, 2]. It offers a suitable option for giving the permanent shape of thermoplastic shape memory polyurethane [3]. Despite its superior features, this method is insufficient when

---

* Corresponding author: aokapti@sakarya.edu.tr

[1] Sakarya University

E-mail: ertekinerdi@hotmail.com, uguracunn01@gmail.com

ORCID: https://orcid.org/0000-0003-2059-6086, https://orcid.org/0000-0002-7719-5622, https://orcid.org/0000-0002-7609-431X

the final product requires the contrasted functional properties [4, 5]. Plastic parts often require a combination of rigid and flexible structures together. For example, a screwdriver handle should be both rigid enough not to deform under applied tightening torque and flexible enough not to hurt or slip out of the user's hand simultaneously. Such situations, where different properties are expected from the same product, require multi-component molds (MCMs).

In MCMs, different types of plastic materials or different colors of the same plastic material are injected into the same mold. It is applied in many areas including car front/rear lights, pediatric products, mobile phone covers, stationery products, hand tools, buttons, etc. Such molds offer extra significant advantages such as better mechanical properties, esthetic appearance, low light, and sound insulation. MCMs reduce costs and are environmentally friendly since they allow recycling plastics material to be used inside of the product. On the other hand, they are difficult and costly to manufacture and require special and expensive injection molding machines [6, 7].

There are six current approaches applied in MCMs. These methods are the inter-machines transfer, core-back, sandwich molding, in-mold automated transfer, rotary-table, and vertical-turn methods [8-10]. In the inter-machines transfer method, a separate mold and a separate injection machine are required for each component. The part injected in a mold working on an injection machine is manually transferred to the other mold working on another injection machine. Although a multi-component product can be produced with this method, it cannot be considered a multi-component mold application since it requires as many molds and injection machines as the number of components.

In the core-back method, the jig drawn back on the core plate generates a space in the cavity for the second component to be injected in the second stage. The number of extruders of the injection machine should be two in this method.

In the sandwich molding method (or co-injection), at first, the plastic material to form the surface portion of the product is injected, and then, the plastic material to form the inner part of the product is injected. The material of the inner portion pushes the surface portion just injected, thereby allowing the mold's walls to be wrapped by the first injected material. The number of extruders of the injection machine should also be two in this method. However, both materials are injected from the same pathway.

In the in-mold automated transfer method, the parts injected in the first cavity group are transferred to the second cavity group of the same mold by a robotic manipulator. This method requires complicated robotic manipulators that increase the investment cost and the cycle time.

In the rotary-table method, the core side of the mold is rotated 180° for two-component molds (or 120° for three-component molds) as a feature of the injection machine. The core side designs are the same for both components, while the cavity side designs vary according to the geometric profile of the product. The number of extruders of the machine should also be two in this method. Each component is injected into the mold cavity from separate pathways.

In the vertical turn method, it is necessary to design a middle plate with the cavity groups looking in both directions. The blank portions that remained in the first injection are filled in the second injection after the central plate is rotated 180° around the vertical axis.

All these methods mentioned above have some disadvantages. In the inter-machines transfer method, the product cost is very high, and the processing time is quite long since it requires as many molds and machines as the number of components. The core-back method can only be applied to the parts with simple geometry due to the limitations it has in terms of part geometry and component number. In the sandwich molding method, it cannot be seen from the outside that it is a multi-component part since the components are in the form of a shell and a core. In the in-mold automated transfer method, the robotic manipulator required for the transfer process increases both mold cost and cycle time. In the rotary-table method, the half or one-third rotation of the core side in each cycle is considered a feature provided by the injection machine. Therefore, this method cannot be applied to a conventional injection machine. Similarly, the vertical turn method also requires a particular injection machine. The middle plate, which needs to rotate half turn around the vertical axis, extends the mold opening distance and thus the cycle time.

This study proposes a new method, called the rotary-cross method, eliminating the disadvantages of the other six methods mentioned above [11]. The rotary-cross method can be compared to the rotary-table method among the methods mentioned above. The new idea of the rotary-cross method is that only a part of the core plate is rotated by a mechanism placed in the mold instead of the entire core side of the mold being rotated by the injection machine. Thus, the need for a particular and expensive injection machine is eliminated. In addition, the mass that must be rotated by half or one-third turn in each cycle is significantly reduced. This study presents a case study investigating the design process of a MCM equipped with the rotary-cross system. The selected sample product is a two-component, eight-cavity toothbrush (180°–2C–2x8). The design study covers the cavity and core portions of the mold and the calculations of the hot runner, rotary-cross, cooling, and ejecting systems. In addition, an analysis study, including the filling time, filling easiness, post-filling temperature, post-cooling temperature, sink mark generation, trapped air, and weld line investigations is also provided.

2. MATERIALS and METHOD

2.1. General Design Considerations

The number of cavities is 2x8. The total cycle time is 18 s, including 2 s injection time, 11 s holding and cooling time, and 5 s manipulating (opening, pushing forward, rotating, pulling backward, ejecting, closing) time. The design principles specified in the mold design handbooks [12-16], articles [17, 18], and thesis studies [19, 20] related to this research area are considered in the design of this two-component toothbrush mold.

Figure 1 The solid model and parting line of the molded two-component toothbrush

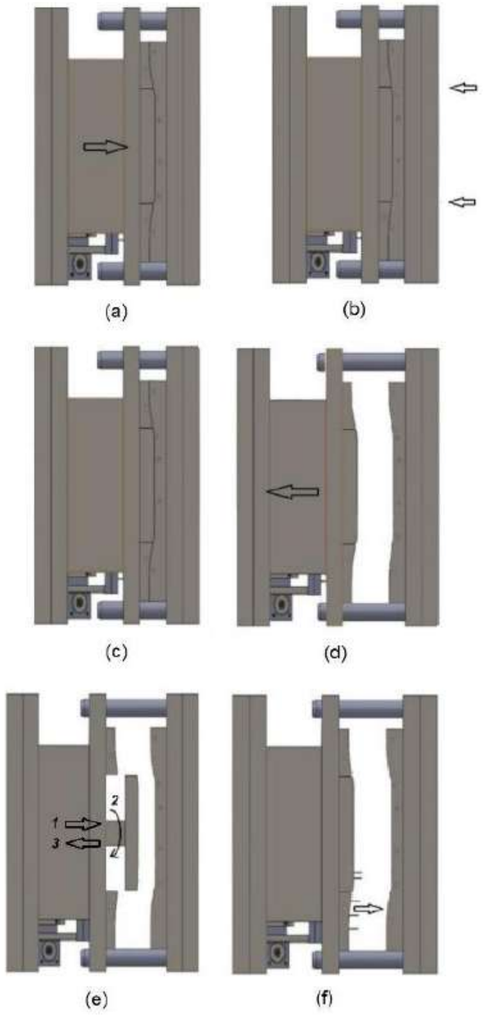

Figure 2 Stages of the cycle: a) The mold is closed and locked, b) PP and TPE polymers are injected, c) Waiting for holding and cooling, d) The mold is opened, e) The core plate is pushed forward, rotated, and pulled backward by the rotary-cross system, f) The entirely manufactured products are ejected

A mold design study starts with the part design. The solid model and parting line of the molded two-component toothbrush are shown in Figure 1. The molded toothbrush components' volumes, masses, and projection areas are obtained from the computer model as 8.1 cm^3, 7.3 g, and 10.4 cm^2 for the first component, 5.2 cm^3, 5.7 g, and 8.3 cm^2 for the second component, respectively.

In MCMs, the selection of polymeric materials is quite essential because the materials must bond with each other. We selected Polypropylene (PP) as the first component and styrene-based thermoplastic elastomer (TPE) as the second component. PP is the hard plastic material forming the toothbrush body, and TPE is the soft plastic material providing an aesthetic appearance and ease of holding to the toothbrush. Among the major categories, TPEs are the most widely used due to that they can combine well with many other materials, including fillers, extenders, modifiers, and other resins. The material properties of these polymers are given in Table 1.

Table 1 Material properties of the selected polymers [21, 22]

	First component Polypropylene (PP)	Second component Thermoplastic elastomer (TPE)
Density (g/cm^3)	0.9	1.1
Molding temperature (°C)	240	220
Specific heat (kJ/kg·K)	1.9	1.3
Thermal conductivity (W/m·K)	0.18	0.21
Thermal expansion coefficient (1/°C)	$1.46 \cdot 10^{-4}$	$2.35 \cdot 10^{-4}$
Young module (MPa)	1300	3
Yield strength (MPa)	33	-
Tensile strength (MPa)	41	15
Elongation at rupture (%)	100	500
Poisson ratio	0.4	-
Hardness (Shore)	66D	40A
Viscosity (Pa·s)	60	55
Shrinkage (%)	2	2

2.2. Structure of the Mold

A classical plastic injection mold consists of two main groups. One of them is the cavity group, which is the fixed side of the mold, and the other is the core group, which is the moving side of the mold. The process sequence in a classical mold is as follows: closing, clamping, injection, holding, cooling, opening, and ejecting. The MCM designed in this study has these classical sequential features, too. In addition to these, it also has some additional features. The stages of the cycle are shown in Figure 2. The process starts with the closing and clamping of the mold (Figure 2a). The polymers for the first and second components (PP and TPE) are injected into the mold (Figure 2b). After the holding and cooling process (Figure 2c), the mold is opened (Figure 2d). The core plate is pushed forward, is rotated 180°, and is pulled backward by the rotary-cross system, including two servomotors (Figure 2e). The eight entirely manufactured toothbrushes are ejected from the mold by the ejector system (Figure 2f). The mold is closed and locked again in the next cycle.

2.3. Hot Runner System

While the hot runner system is optional in conventional molds, it is strictly necessary for the MCM designed in this study. A hot runner system is a melt polymer feeding system that allows injection directly into the mold cavities without heat losses. It consists of manifolds, nozzles, heating resistances, thermocouples, and a control unit. There are many advantages provided by the hot runner system compared to conventional runner molds. It provides savings in energy, time, material, space, and labor. It makes it possible to produce better quality products [23- 26].

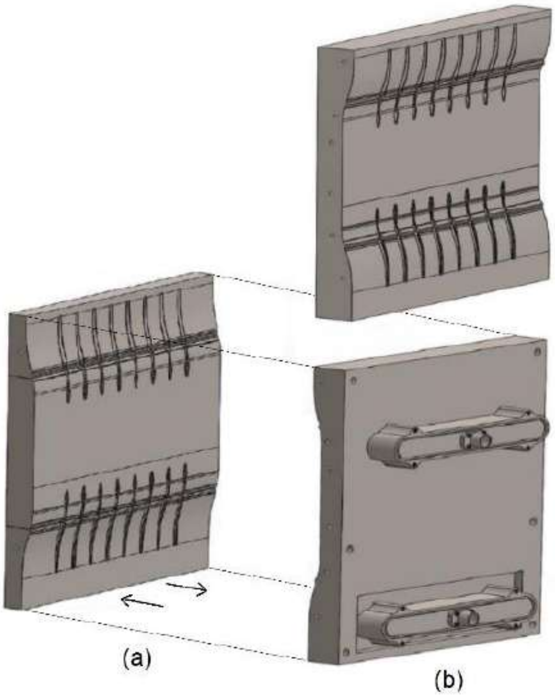

Figure 3 a) Front view of the core plate, b) Front and back views of the cavity plate and hot runner manifolds

The core and cavity plates and the hot runner manifolds at the backside of the cavity plate are shown in Figure 3. Two nozzle sets, each consisting of eight nozzles with diameters of 1.8 mm, and a gate length of 2 mm, are selected for both components. The pressure losses occurring in the gates are calculated by Equation (1) for the first and second components as follows:

$$\Delta p = \frac{8\cdot\mu\cdot l_g\cdot V_p}{\pi\cdot r_g^4\cdot t_{inj}} \tag{1}$$

Where Δp, μ, l_g, V_p, r_g, and t_{inj} are the pressure loss, melt viscosity, gate length, part volume, gate radius, and injection time, respectively.

By considering the average in-cavity cross-sections (A_c), which are 0.14 and 0.11 cm^2 for the components, the flow lengths are calculated by Equation (2) as follows:

$$L_f = \frac{t_p^2\cdot p_{inj}\cdot t_{inj}\cdot A_c}{50\cdot V_p\cdot\mu} \tag{2}$$

Where L_f, t_p, and p_{inj} are the in-cavity flow length, part thickness, and injection pressure, respectively. Calculated in-cavity flow lengths and pressure losses are within reasonable limits.

Two 16 kg mass-I type manifolds are selected for PP and TPE materials. The total heating power required to activate the manifolds of the hot runner system in 7 minutes with 65% efficiency in the first run are calculated by Equation (3) as follows:

$$P = \frac{m_m\cdot c_s\cdot\Delta T}{t\cdot\eta} \tag{3}$$

Where P, m_m, c_s, ΔT, t, and η are the heating power, the manifold mass, the specific heat of the manifold material, temperature difference, warm-up time, and heating efficiency, respectively. The appropriate flexible and cartridge resistances for manifold and spiral resistances for nozzles are selected to provide the calculated heating power.

2.4. Mold Set

The standard mold set is selected considering the part sizes and the cavity number. Accordingly, the main dimensions of the mold cross-section are 590x780 mm, the thickness of the cavity and core plates is 90 mm, and the distance between the parallel side blocks is 390 mm (see Figure 4). According to the projection areas of the components and 25 MPa injection pressure, the force to open the mold during injection is calculated by Equation (4), and the deflection occurring on the cavity plate during injection is calculated by Equation (5) as follows:

$$F_r = \sum_{i=1}^{2} \frac{A_{prj}\cdot n_c\cdot(p_{inj}-\Delta p)}{10^3} \tag{4}$$

$$l_{def} = \frac{5\cdot L_{def}^4\cdot Q_{dst}}{384\cdot E_s\cdot I_b} \tag{5}$$

where F_r, A_{prj}, p_{inj}, n_c, l_{def}, L_{def}, Q_{dst}, E_s, and I_b are the force to open the mold during injection, projection area, injection pressure, cavity number, deflection occurring on the cavity plate during injection, deflection length (i.e., the distance between the parallel side blocks), distributed load on the cavity plate, elasticity module of the mold steel, and bending moment of inertia of the cavity plate, respectively. The calculated deflection value is safe because it is lower than the flash gap of the polymeric materials.

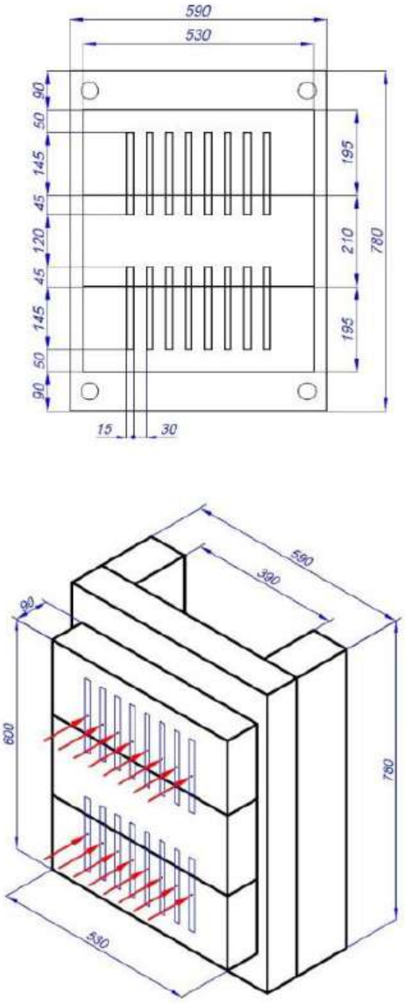

Figure 4 Dimensions of the selected mold set

2.5. Rotary-Cross System

The working principle of the rotary-cross system designed in this study is shown in Figure 5.

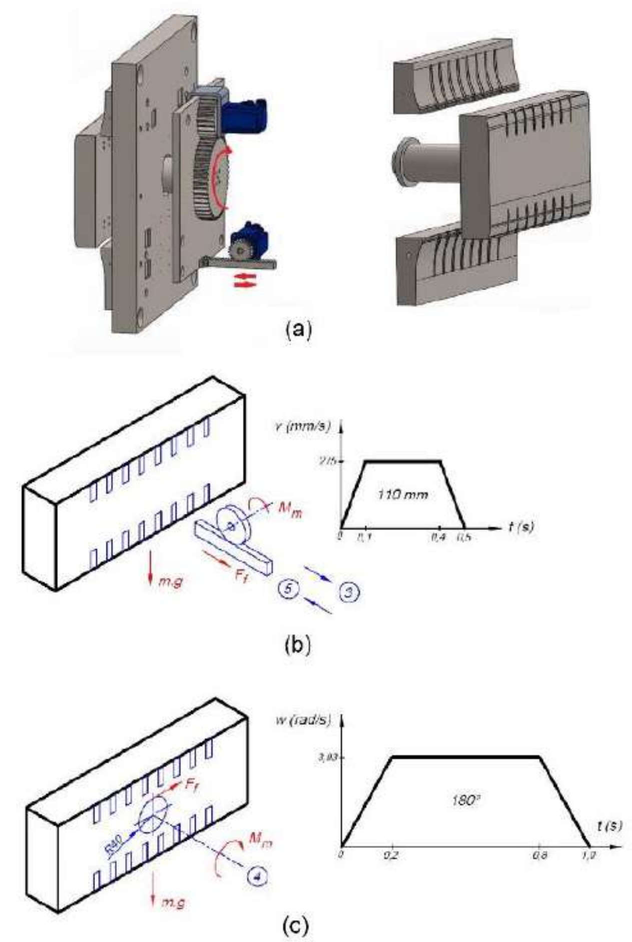

Figure 5 a) Schematic of the rotary-cross system, b) Pushing forward and pulling back, c) Rotating

The main feature of this system is that a portion of the core plate is pushed forward when the mold is opened, then it is rotated 180°, consecutively in reverse each time, and then it is pulled back to the neutral position. Total manipulating time is considered 5 s (including 1 s for opening, 0.5 s for pushing forward, 1 s for rotating, 0.5 s for pulling backward, 1 s for ejecting, and 1 s for closing). There are two stepper motors in the system for translational and rotational movements. The first stepper motor torque output required to activate the translational motion is calculated by Equation (6) as follows:

$$M_{m1} = \frac{m \cdot R_p \cdot (g \cdot \mu + a) \cdot s}{\eta} \quad (6)$$

where M_m, m, R_p, g, μ, a, s, and η are the stepper motor torque output, totally shifted mass, the radius of the pinion gear, gravitational acceleration, sliding frictional coefficient, translational acceleration, safety coefficient, and mechanical efficiency, respectively.

The second stepper motor torque output required to activate the rotational movement of the rotary-cross system is calculated by Equation (7) as follows:

$$M_{m2} = \frac{(m \cdot f \cdot g \cdot R_f + J \cdot \alpha) \cdot s}{i_r \cdot \eta} \qquad (7)$$

Where f, R_f, w, h, α, and i_r are the rolling frictional coefficient, frictional radius, width and height dimensions of the rotating core plate, angular acceleration, and gear reduction ratio, respectively.

2.6. Cooling System

An effective cooling system is essential to keep the cycle time within an appropriate range. It is also strictly necessary to maintain the process correctly, to prevent the occurrence of product defects, and to keep the mold temperature constant at a specific value by transferring the heat load of the injected polymeric material [27, 28]. Water circulation in circular cross-section channels processed in the cavity and core plates is adopted in cooling system design. Considering the melt temperatures of the first and second components (240 and 220 °C) and the exit temperature of the molded part (50 °C), the total heat load to be transferred from the mold is calculated by Equation (8) as follows:

$$Q_h = \left[(m \cdot c \cdot \Delta T)_{pp} + (m \cdot c \cdot \Delta T)_{tpe}\right] \cdot n_c \cdot n_{cc} \qquad (8)$$

Where Q_h is the heat load that needs to be transferred from the mold; m, c, and ΔT are the mass, specific heat, and temperature difference of each component; n_c and n_{cc} are the number of the cavity and the number of the cycle per hour, respectively.

Based on the heat load to be transferred from the mold, the diameter of the circular cross section-cooling channels, needed cooling water flow rate, the length of the cooling channel network, and cooling time are calculated by Equations (9 – 12) [19], and the turbulent flow regime in the cooling network is checked by Equations (13) as follows:

$$\frac{Q_h}{3600} = \frac{\pi \cdot {d_c}^2}{4} \cdot \vartheta_w \cdot c_w \cdot d_w \cdot (T_{out} - T_{in}) \qquad (9)$$

$$Q_w = \frac{\pi}{4} \cdot {d_c}^2 \cdot \vartheta_w \qquad (10)$$

$$L_c = \frac{Q_h \cdot d_c}{3.53 \cdot Q_w \cdot (1 + 0.015.T_w) \cdot (T_m - T_w)} \qquad (11)$$

$$t_c = \frac{{t_p}^2 \cdot d \cdot c}{\pi^2 \cdot k} \cdot ln\left(\frac{4}{\pi} \cdot \frac{T_{mlt} - T_m}{T_{pe} - T_m}\right) \qquad (12)$$

$$R_e = \frac{d_c \cdot \vartheta_w}{v_w} \qquad (13)$$

Where υ_w, c_w, d_w, Q_w and ν_w are the velocity, specific heat, density, flow rate, and kinematic viscosity of the cooling water; T_{in}, T_{out}, and T_w are the inlet, exit, and medium temperatures (15, 25 and 20 °C) of the cooling water; d_c and L_c are the diameter of the circular cross-sectional cooling channel, and the total length of the channel network; T_m, T_{mlt} and T_{pe} are the mold, melt, and product exit temperatures; t_c, t_p and k are the cooling time, product thickness, and thermal conductivity, respectively. The results show that the cooling channel network with 10.5 mm diameter and 2.19 m length is required. The cooling water flow rate is 2.6 lt/min at 15 °C inlet temperature. The cooling times are calculated as 30.6 and 10.7 s for the first and second components. The design of the cooling system is completed by circulating the channel network in the appropriate zones.

2.7. Ejecting system

To eject the fully manufactured toothbrushes from the mold when the mold is opened, it is necessary to equip the mold with an ejector system. The usage of pin type ejector system is adopted. The lengths of the ejector pins are varied due to the geometry of the cavity. The ejector pins are subjected to compression stress and buckling under the influence of 25 MPa injection pressure. Five ejector pins with a diameter of 3 mm were used for each cavity. The general structure of the ejector system is shown in Figure 6.

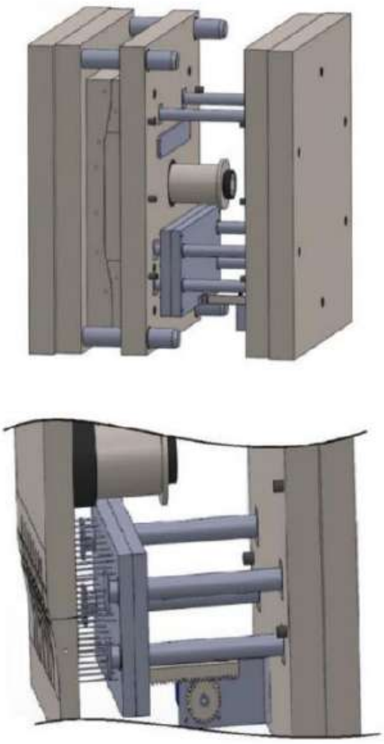

Figure 6 Plates and the rock-pinyon mechanism of the ejector system

2.8. Mold Assembly

There are many standard elements such as centering columns, bushings, lifting lugs, cooling water connection fittings, pins, and bolts that should be used in formwork assembly. The assembly of the mold has been completed after selecting these standard complementary elements. The exploded view of the mold components and the assembled mold are shown in Figure 7.

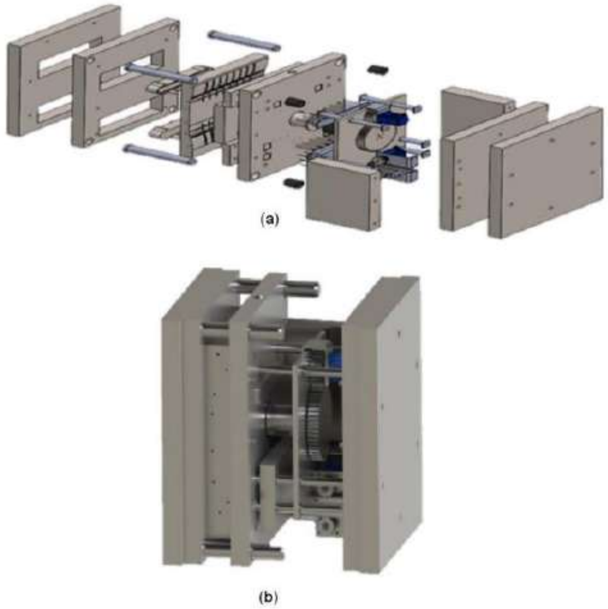

Figure 7 Exploded (a) and assembled (b) views of the mold

3. RESULTS and DISCUSSION

3.1. Design

The MCM design parameters obtained in the design study are listed in Table 2. When these results are examined, it is seen that a production rate of 1600 parts per hour, corresponding to 18 s cycle time and 200 cycles per hour, is achieved. The total mass of the mold is 1840 kg, of which the core side is 1120 kg, and the cavity side is 720 kg. The rotary-cross method proposed in this study provides improvements in product cost and cycle time when compared to the other five methods, except for the rotary-table method. The rotary-cross method also provides some advantages when compared to the rotary-table method, which is the closest alternative. First, it eliminates the need for a special injection machine. In addition, it makes that rotating only the 80 kg core plate is sufficient, instead of 1120 kg core side entirely. These improvements provide the side benefits of the more straightforward design, smaller stepper motors, and reduction in energy consumption.

Table 2 Summary of the design parameters

Design parameter	First Component Polypropylene (PP)	Second Component Thermoplastic elastomer (TPE)
Cavity number	8	8
Volume (cm^3)	8.1	5.2
Mass (g)	7.3	5.7
Projection area (cm^2)	10.4	8.3
Average cross section (cm^2)	0.14	0.11
Average thickness (mm)	3.5	2.5
Nozzle diameter (mm)	1.8	1.8
Gate length (mm)	2	2
Flow length (cm)	32.6	23
Injection time (s)	2	2
Injection pressure (MPa)	25	25
Pressure loss (MPa)	1.9	1.1
Manifold mass (kg)	16	16
Manifold heating power (kW)	6.2	5.6
Cooling time (s)	30.6	10.7
Mold cross-section (mm)	590x780	
The thickness of the plates (mm)	90	
Distance between parallels (mm)	390	
Force to open the mold (kN)	351	
Distributed load (N/mm)	595	
Deflection of the core plate (μm)	18	
Mass of the core plate (kg)	80.14	
Inertia of the core plate ($kg \cdot m^2$)	2.17	
Linear acceleration (m/s^2)	2.75	
Angular acceleration (rad/s^2)	19.6	
Mass of the mold (kg)	1840	
Cycle time (s)	18	
Stepper motor torques (N·m)	11.5; 32	
Heat load (kCal/h)	1490	
Cooling water velocity (m/s)	0.5	
Reynolds number	6105	
Inlet/exit temperatures (°C)	15/25	
Flow rate (m^3/h)	0.156	
Cooling channel diameter (mm)	10.5	
Length of the cooling channel (m)	2.19	

Both values of in-cavity flow lengths are longer than the product length. This result shows that there is no difficulty in filling the cavities, and a single gate is sufficient for each cavity. The 10.7 s cooling time of the second component is appropriate since it is already shorter than the applied cooling time (11 s). On the other hand, the 30.6 s cooling time of the first component does not seem appropriate because it is far longer than the selected cooling time. At this point, it is necessary to remember an essential feature of MCMs. While the second component is ejected from the mold at the end of the cycle in which it is injected, the first component remains in the mold for two consecutive cycles. As a result, it can be said that both calculated cooling times are provided within the appropriate limit. A turbulent flow regime desired in injection molds is also provided. In this case, study focusing on the MCM design, the ratio of the entire core side mass to the rotating portion of the core plate mass is 14. This ratio indicates a significant gain in energy requirement.

3.2. Analysis

Computer-aided analysis studies assist designers in all areas of engineering by showing problems before they arise. Therefore, it has a wide range of applications in mold making as well as in all other areas. It provides foresight about the parameters such as filling time, filling temperature, injection and holding pressures, temperature after cooling, and production defect generations such as the air bubbles, sink marks, and weld lines. This foresight makes it possible to optimize the mold design before starting mold manufacturing [29- 32].

A number of production defects occur due to material properties, mold design, and machine process parameters. The most important of these defects are short shot, burrs, warpage caused by uneven shrinkage, jetting, hot ejected part caused by insufficient cooling, sink marks, sear caused by trapped air, and weld line. Accordingly, the analyses of the filling time, filling easiness, temperatures at the end of the filling and cooling, generations of the sink mark, trapped air, and weld line are performed. The results obtained in this analysis study run in SolidWorks software are given in Figures 8-14.

The filling time analysis given in Figure 8 shows that no difficulties are encountered in filing the mold cavities. The color distribution is from blue to red in this analysis. The red zone represents the region where the polymer flow has last arrived. It is seen from the analysis study that the filling time of both components is realized as 2 s in the framework of the selected hot runner system elements and working parameters.

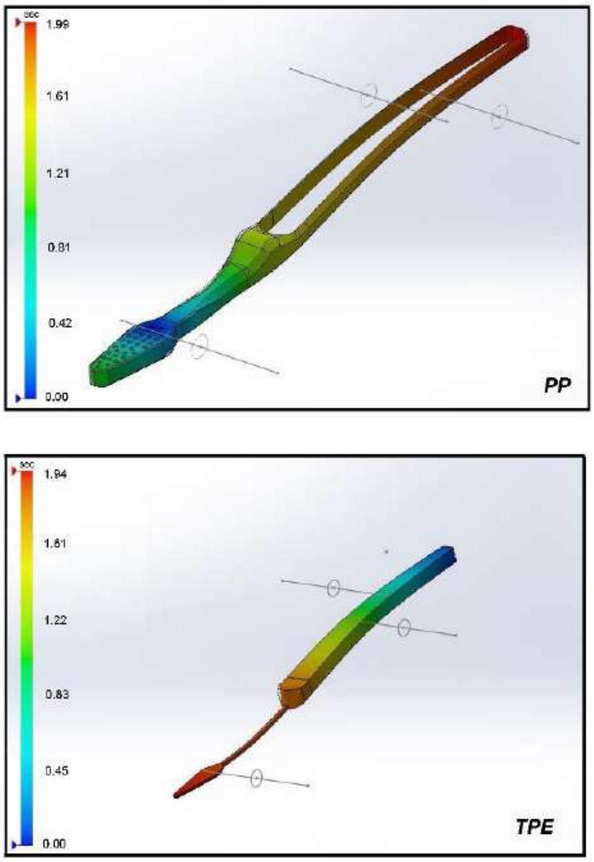

Figure 8 Filling time analysis

The short shot is the inability to fill the mold cavity completely; the burr is the polymeric material overflowing from the parting line due to the excessive injected material quantity or high injection pressure, and the jetting is the trace resulting from the entry of the material into the mold cavity by snaking with high injection speed. The green color in the filling easiness analysis given in Figure 9 indicates that no difficulties are encountered in filling the cavities in terms of the number and position of the gate, injection velocity, and the part geometry. No short shot, burr, or jetting were observed in this analysis.

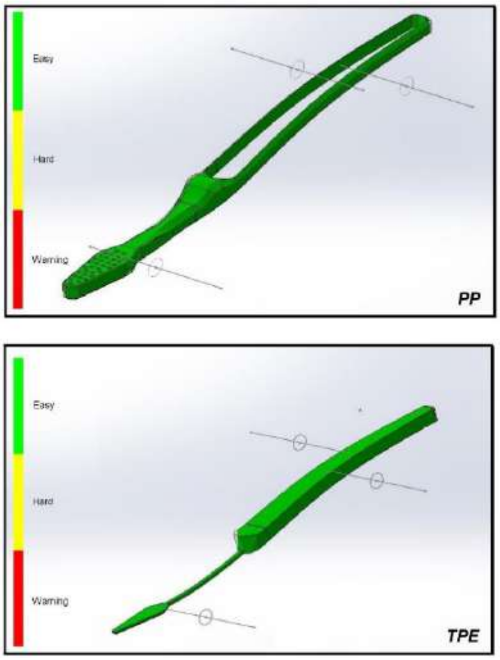

Figure 9 Filling easiness analysis

In the end-of-filling temperature analysis, as expected, the temperature appeared as 240 °C for PP, and 220 °C for TPE, in proximity to the gate and in fleshy regions (Figure 10). In the end-of-cooling temperature analysis, it is seen that the temperature values are reduced to 50 °C, which is the expected temperature for the ejected part, but the cooling is not enough near the gate location. This result suggests that the cooling system should be revised or the cooling period should be extended (Figure 11)

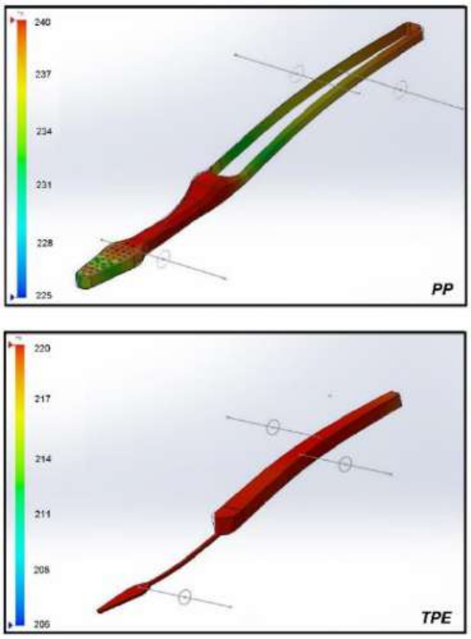

Figure 10 End-of-filling temperature analysis

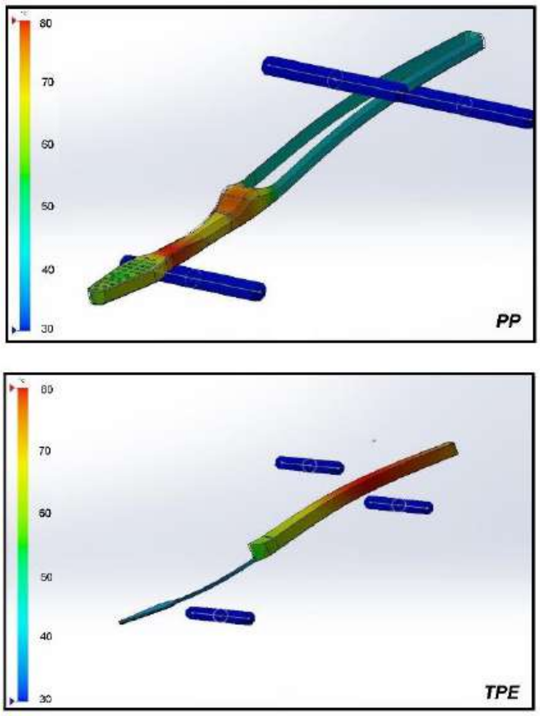

Figure 11 End-of-cooling temperature analysis

A sink mark is a defect caused by excessive shrinkage in the areas of material condensation due to part design. Other reasons are inadequacy of holding pressure and time, injected material quantity, and gate cross-section. The sink mark values encountered in the analysis given in Figure 12 are 0.031 mm for PP and 0.044 mm for TPE. These values are within reasonable limits.

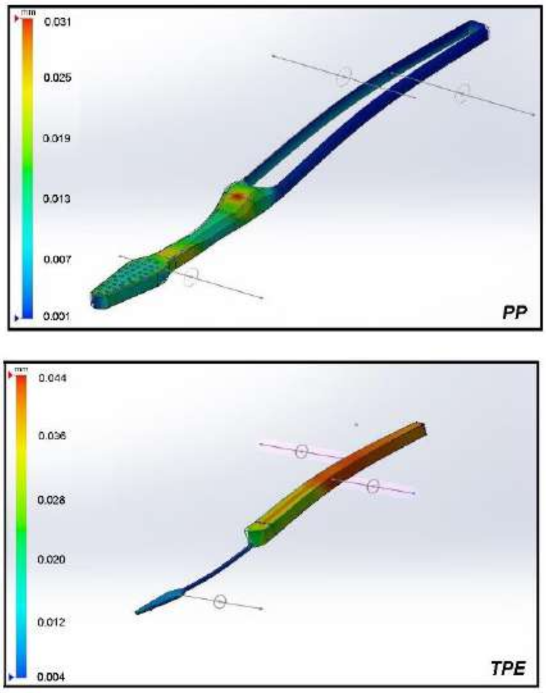

Figure 12 Sink marks analysis

Burn mark or sear is described as a blackening or yellowing of a part of the part. The most important reason for this is that the air cannot evacuate the mold cavity during the injection and is trapped in a region. When the air in the mold cavity is not fully evacuated from the mold to the outside during injection, due to the high injection speed and the inadequacy of the air channels, it causes a burn mark at the regions where the air is trapped. From the analysis, it is seen that air is trapped at the points specified on the Figure 13. It is necessary to open the air duct from these points for air release. The dimension of these air ducts should be smaller than the flash gap limit of the polymeric materials.

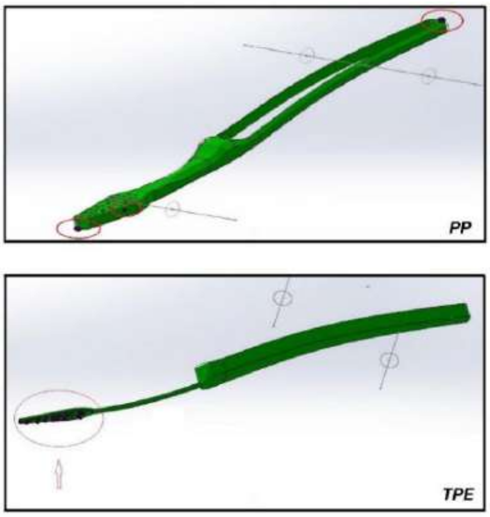

Figure 13 Trapped air analysis

Weld line is a flow trace formed where the polymeric material from the multi-gate or multi-flow line joins and fuses. In addition to being a visually disturbing trace, it also causes the weak cross-section of the part that can easily break even at low loads. In the weld line analysis given in Figure 14, it is seen that there is a weld line in the region specified for the first component, and there is no weld line for the second component.

The analysis results show that the approaches adopted in the multi-component mold design are appropriate and compatible with the literature. For the composite products produced by the multi-component injection method, it is necessary to provide the interface compatibility between the components regarding shrinkage and stiffness. In this respect, the selection of the component materials crucially influences the properties of the composites. In addition, the adjustment of the ratio between the component volumes must also be carefully adjusted. Moreover, the position of the sprue and the design of the molded parts are more important than the processing parameters. The uniformity of the layer thicknesses is primarily determined by the viscosity of the components. To prevent flow instabilities, the ratio of the viscosities of the core to the skin material should be around one. Otherwise, poor filling behavior, varying wall thickness distribution, and ruptures can be encountered.

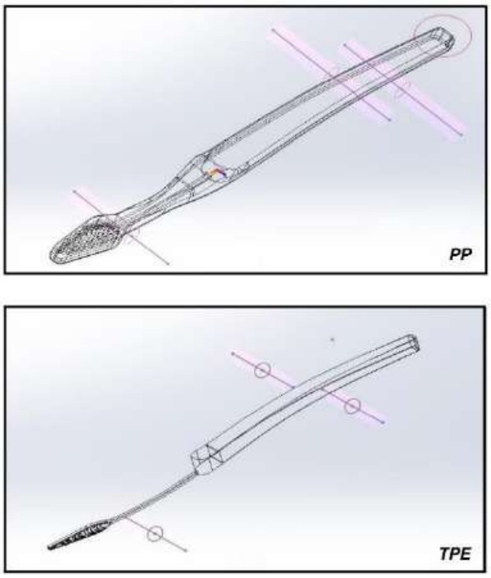

Figure 14 Weld line analysis

4. CONCLUSION

Although MCMs have many superior features compared to conventional injection molds, their applications are limited due to their more expensive and challenging design and production procedures. This study aims to contribute to facilitating the design of such molds. To achieve this goal, the rotary-cross method eliminating the disadvantages of the current methods is proposed. The idea of the proposed method is that only a part of the core plate is rotated by a mechanism placed in the mold instead of the entire core side of the mold being rotated by the injection machine. This idea eliminates the need for a particular and expensive plastic injection machine. A mold using this method can also be worked on a conventional injection molding machine. These improvements provide the side benefits of the more straightforward design, smaller stepper motors, and reduction in energy consumption.

It is also aimed to contribute to the awareness and widespread of such molds. For this aim to be fulfilled, this study presents a case study investigating the design process of a MCM equipped with the rotary-cross system. The selected sample product is a two-component, 8-cavity toothbrush (180°–2C–2x8). The case study covers the design of the cavity and core portions of the mold and the calculations of the hot runner, rotary-cross, cooling, and ejecting systems. In addition, the analysis study including the filling time, filling easiness, post-filling temperature, post-cooling temperature, sink mark generation, trapped air, and weld line investigations is also provided.

According to obtained results, the filling time was 2 s for both components. No difficulties are encountered in filling the cavities in terms of the number and position of the gates. No short shot, burr, or jetting were observed. The end-of-filling and end-of-cooling temperatures were appeared as expected. The inadequacy of cooling near the gate location shows that more meticulous work should be done on the cooling system in MCMs. The sink marks were within reasonable limits. No weld lines and air traps were found at a level that could be considered a problem. These results show that the MCM design approach adopted in the study is appropriate.

APPENDIX

Symbols		**Subscripts**	
A, a	Area (m^2), Linear acceleration (m/s^2)	b	Bending
c	Specific heat (kJ/kg·K)	c	Cycle, Cooling, Cavity, Core plate
d	Diameter (mm), Density (g/cm^3)	def	Deflection
E	Modulus of elasticity (MPa)	dst	Distributed
f	Rolling frictional coefficient	f	Frictional, Flow
g	Gravitational acceleration (m/s^2)	g	Gate
h, w	Dimensions of the rotating core plate (mm)	h	Heat
I	Moment of inertia (m^4)	inj	injection
i	Gear reduction ratio	m	Mold, Manifold, Motor
J	Mass moment of inertia ($kg\cdot m^2$)	mlt	Melt
k	Thermal conductivity (W/m·°C)	p	Product, pinion gear
L, l	Length (m)	pe	Product exit
M, m	Torque (N·m), Mass (kg)	prj	Projection
n	Number	pp	Polypropylene (1st component)
P, p	Power (kW), Pressure (Pa)	tpe	Thermoplastic elastomer (2nd component)
Q	Heat load (kCal/h), Flow rate (m^3/s)	s	Steel
R, r	Radius	w	Water
t	Time (s), Thickness (m)		
T	Temperature (°C)		
V	Volume (m^3), Velocity (m/s)		
η	Efficiency		
α	Angular acceleration ($1/s^2$)		
μ	Frictional coefficient, Viscosity (Pa·s)		

Funding

The authors have not received any financial support for the research, authorship, or publication of this study.

The Declaration of Conflict of Interest/ Common Interest

No potential conflict of interest was declared by the authors.

Authors' Contribution

The first author contributed 50%, the second author 25%, and the second author 25%.

The Declaration of Ethics Committee Approval

This study does not require ethics committee permission or any special permission.

The Declaration of Research and Publication Ethics

The authors of the paper declare that they comply with the scientific, ethical and quotation rules of SAUJS in all processes of the paper and that they do not make any falsification on the data collected. In addition, they declare that Sakarya University Journal of Science and its editorial board have no responsibility for any ethical violations that may be encountered, and that this study has not been evaluated in any academic publication environment other than Sakarya University Journal of Science.

REFERENCES

[1] C. A. Harper, “Handbook of Plastic Processes”, ISBN: 978-0-471-66255-6, New Jersey, USA, Wiley, 2006.

[2] T. Oswald, L. S. Turng, P. Gramann, “Injection Molding Handbook”, 2nd ed., ISBN: 9783446407817, Munich, Germany, Hanser, 2007.

[3] Ş. Katmer, Ç. Karataş, “Part quality in Injection Molding of Shape Memory Polyurethane”, Pamukkale University Journal of Engineering Sciences, vol. 27, no. 4, pp. 472-477, 2021.

[4] R. Dangel, “Injection Molds for Beginners”, ISBN: 978-1-56990-631-6. Munich, Germany, Hanser, 2016.

[5] V. Goodship, B. Middleton, R. Cherrington, “Design and Manufacture of Plastic Components for Multifunctionality, Structural Composites, Injection Molding, and 3D Printing”, ISBN: 978-0-323-34061-8, Elsevier, 2016.

[6] G. Menges, W. Michaeli, P. Mohren, “How to Make Injection Molds”, 3rd ed., ISBN: 978-3-446-40180-8, Munich, Germany, Hanser, 2001.

[7] R. A. Malloy, “Plastic Part Design for Injection Molding”, 2nd ed., ISBN: 978-1-56990-436-7, Munich, Germany, Hanser, 2010.

[8] E. Yapıcıoğlu, “Co-injection: Multiple Component Injection Molds”, TurkCADCAM Design and Manufacturing Technologies Portal, 2007.

[9] H. Şahin, “Co-injection”, TurkCADCAM Design and Manufacturing Technologies Portal, 2008.

[10] H. Wu, G. Zhao, G. Wang, W. Zhang, Y. Li, “A new Core-Back Foam Injection Molding Method with Chemical Blowing Agents”, Materials and Design, vol. 144, pp. 331-342, 2018.

[11] E. Ertekin, U. Acun, “Two-Component Plastic Injection Mold and Rotary Cross System Design”, BSc Thesis, Sakarya University, Türkiye, 2018.

[12] P. Jones, “The Mould Design Guide”, ISBN: 978-1-84735-088-6, Smithers Rapra, 2008.

[13] G. Mennig, K. Stoeckhert, “Mold Making Handbook”, 3rd ed., ISBN 978-1-56990-446-6, Munich, Germany, Hanser, 2013.

[14] J. M. Fischer, "Handbook of Molded Part Shrinkage and Warpage", 2nd ed., ISBN: 978-1-4557-2597-7, Elsevier, 2013.

[15] D. O. Kazmer, "Injection Mold Design Engineering", 2nd ed., ISBN: 978-1-56990-570-8, Munich, Germany, Hanser, 2016.

[16] M. Moayyedian, "Intelligent Optimization of Mold Design and Process Parameters in Injection Molding", ISBN 978-3-030-03355-2, Springer, 2019.

[17] K. Çetinkaya, H. Başak, "Computer Aided Three Dimensional Design of Mold Components", Pamukkale University Journal of Engineering Sciences, vol. 6, no. 2, pp. 155-160, 2000.

[18] M. O. Yağır, O. H. Mete, "Numerical Model Analysis of an Industrial Product, Drilling and Tapping Operations on Reducing the Mold Design Process", Sakarya University Journal of Science, vol. 21, no. 2, pp. 131-140, 2017.

[19] D. Şafak, "Examination of Plastic Injection Mold Design and Applied Design Example", MSc Thesis, Istanbul Technical University, Türkiye, 2001.

[20] C. Koyun, "Computer Aided Plastic Injection Mold Design and Analysis", MSc Thesis, Yıldız Technical University, Türkiye, 2005.

[21] W. D. Callister, D. G. Rethwisch, "Materials Science and Engineering", 8th ed., ISBN 978-605-133-418-9, Nobel Publishing, 2013.

[22] Y. Kanbur, Ü. Tayfun, "Mechanical, Physical and Morphological Properties of Polypropylene/Huntite Composites", Sakarya University Journal of Science, vol. 21, no. 5, pp. 1045-1050, 2017.

[23] R. Spina, "Injection Molding of Automotive Components: Comparison Between Hot Runner Systems for a Case Study", Journal of Materials Processing Technology, vol. 155, pp. 1497-1504, 2004.

[24] T. Öztürk, A. Özkan, "Comparison of Hot and Cold Runner System", Düzce University Journal of Science and Technology, vol. 3, no. 1, pp. 283-298, 2015.

[25] A. Khan, "Injection Mold Design Optimization Based on Runner System Design and Operating Process Conditions Through Simulation", MSc Thesis, Lamar University, USA, 2015.

[26] J. P. Beaumont, "Runner and Gating Design Handbook Tools for Successful Injection Molding", 3rd ed., ISBN: 978-1-56990-590-6, Munich, Germany, Hanser, 2019.

[27] H. Gürün, A. Özdemir, T. Acar, "Computer Aided Design of the Cooling System for Plastic Injection Molds". Pamukkale University Journal of Engineering Sciences, vol. 15, no. 2, pp. 263-268, 2009.

[28] M. T. Oktaç, M. Timur, H. Kılıç, "Impact of Dehumidification Devices on Production Efficiency in Plastic Injection", Sakarya University Journal of Science, vol. 25, no. 5, pp. 1129-1135, 2021.

[29] R. Selden, "Co-injection Molding: Effect of Processing on Material Distribution and Mechanical Properties of a Sandwich Molded Plate", Polymer Engineering and Science, vol. 40, no. 5, pp. 1165-1176, 2004.

[30] H. Zhou, "Computer Modeling for Injection Molding Simulation, Optimization, and Control", ISBN 978-0-470-60299-7, Wiley, 2013.

[31] Ö. Erkan, "Plastic Analysis by Autodesk Moldflow Ultimate", ISBN: 978-975-02-2632-8, Ankara, Türkiye, Seçkin Publishing, 2014.

[32] F. Mieth, M. Tromm, H. P. Heim, “Specialized Injection Molding Techniques”, ISBN 978-0-323-34100-4, Elsevier, 2015.

SAKARYA ÜNİVERSİTESİ
FEN BİLİMLERİ ENSTİTÜSÜ
DERGİSİ

Sakarya University Journal of Science
SAUJS

ISSN 1301-4048 | e-ISSN 2147-835X | Period Bimonthly | Founded: 1997 | Publisher Sakarya University |
http://www.saujs.sakarya.edu.tr/

Title: Effect of Glutaraldehyde Crosslinking Parameters on Mechanical and Wetting Properties of PVA/NaAlg Electrospun Mat

Authors: Ayben PAKOLPAKÇIL

Recieved: 2022-03-17 00:00:00

Accepted: 2022-08-28 00:00:00

Article Type: Research Article

Volume: 25
Issue: 5
Month: October
Year: 2022
Pages: 990-999

How to cite
Ayben PAKOLPAKÇIL; (2022), Effect of Glutaraldehyde Crosslinking Parameters on Mechanical and Wetting Properties of PVA/NaAlg Electrospun Mat. Sakarya University Journal of Science, 25(5), 990-999, DOI: 10.16984/saufenbilder.1089304
Access link
http://www.saujs.sakarya.edu.tr/en/pub/issue/73051/1089304

Sakarya University Journal of Science 25(5), 990-999, 2022

Effect of Glutaraldehyde Crosslinking Parameters on Mechanical and Wetting Properties of PVA/NaAlg Electrospun Mat

Ayben PAKOLPAKÇIL*[1]

Abstract

Electrospun alginate-based materials are used in a wide range of applications, including wound dressings, tissue engineering, batteries, water treatment, bioremediation, and food packaging. However, they have low resistance to water. Crosslinking is usually used to enhance the mechanical properties of water-soluble polymers. Process parameters also play a key role in the crosslinking process. In this study, materials from sodium alginate (NaAlg) and poly (vinyl alcohol) (PVA) were prepared using the electrospinning method. To investigate the effect of the process parameters on the mechanical properties of the materials, different concentrations (1.25, 2.5 and 5 v %) and different application times (10 min, 60 min and 24 h) of the crosslinking agent were used. The wettability and mechanical properties of the electrospun mats were evaluated using a water contact angle device and a tensile strength tester, respectively. The maximum tensile strength was measured at 7 MPa which is the sample treated at 5% glutaraldehyde (GA) concentration and 60 min of application time. The sample treated with 2.5% GA concentration and 60 min of treatment time had the highest measured elongation of 11.5%. The sample treated with 2.5% GA concentration and for 10 min had the lowest water contact angle, which was measured at 27.5°. The intended usage of the materials should be considered, as the concentration of the crosslinking process and duration might affect the water-soluble polymers' mechanical and wetting properties.

Keywords: Crosslinking, glutaraldehyde, mechanical property, wettability, contact angle

1. INTRODUCTION

Biopolymers are widely used in many applications, such as in biomedical, textile, food packaging, cosmetic, energy storage and environmental applications [1]. Specifically, sodium alginate (NaAlg) as a biopolymer, is a valuable natural polymer. It is derived from brown algae. It is hydrophilic, biocompatible, and biodegradable. It has, therefore, been widely used in several applications, including paper, textiles, the food industry, pharmaceuticals and cosmetics [2, 3]. In 2020, the worldwide alginate market was valued at USD 728.4 million, with an expected increase to USD 759.8 million in 2021 [4].

---

* Corresponding author: ayben_p@yahoo.com
[1] Nişantaşı University
ORCID: https://orcid.org/0000-0002-6981-4980

The electrospinning technique is an easy way to produce nanomaterials based on alginates. It is a versatile, simple, and inexpensive technique capable of producing continuous micro-nano fibers. Electrospun structures have superior properties, such as a high surface area and adjustable porosity; therefore, intensive research has been conducted on the use of these materials in many fields, such as textiles, packaging, and filtration. This technique, with a 100-year history, is based on the concepts of electromagnetic forces. However, over the last two decades, nanotechnology has become more sensitive to the production of nanofiber from biopolymers [5-8].

Electrospun alginate-based fibers have attracted a lot of attention due to their unique characteristics such as low toxicity, biocompatibility, their relatively low cost, and gelling properties under certain conditions. Many researchers have studied the development of alginate-based materials for a variety of applications, such as food packaging [9], bioremediation [10, 11] water treatment [12, 13], batteries [14], wound dressings [15, 16] and scaffolding [17, 18]. However, due to the rigid and extended chain characteristics of the alginate, the electrospinning method cannot be achieved on its own. For this reason, poly (ethylene oxide) (PEO) and poly (vinyl alcohol) (PVA) polymers are accompanied by electrospinning to produce alginate nanofibers. PVA has many desirable properties, such as thermal properties, water solubility, strength, and gas permeability [19, 20]. It is used extensively in a variety of ways, including industrial, food, packaging and medical applications, textiles, paper, antimicrobial packaging, wound dressings, and contact lenses. PVA solubility in water is high due to the significant amount of hydroxyl groups it contains; hence its stability must be increased before it can be used in aqueous environments. Both PVA and NaAlg are water-soluble polymers. Physical and chemical crosslinking have been examined as strategies for PVA-based nanofibers in the literature. Chemical crosslinking forms stable covalent bonds between polymer chains, enhancing mechanical characteristics and resulting in a water-insoluble material [21-23]. There are many chemicals for crosslinking processes such as citric acid, dextran dialdehyde, genipin, carboxylic acids, etc [19]. The use of a glutaraldehyde (GA) crosslinking agent is a widely employed method for the preparation of biopolymers. GA has high reactivity and is both inexpensive and easily available. GA is also employed in pharmaceutical sciences enzyme technology, histochemistry, biomedical applications, and chemical sterilization. It is an organic chemical compound from the group of aldehydes. It is a colorless to pale straw-colored, pungent, oily liquid. It is used for crosslinking biopolymers. A variety of factors influence the crosslinking process and crystallinity, including chemical compositions, concentrations, temperatures, and reaction times [24, 25]. Kim et al. investigated the effects of the degree of GA crosslinking time on the properties of PVA pervaporation membranes. These effects included pervaporation characteristics, contact angles, swelling characteristics and critical surfaces [26]. Mansur et al. prepared the GA crosslinked PVA hydrogels with different degrees of hydrolysis and their chemical structure was investigated by using Synchroton small-angle X-ray scattering and Fourier transform infrared spectroscopy [27]. The effects of the concentration of GA and the temperature of the crosslinking process on the thermal and chemical changes in the PVA membrane have been investigated by Figueiredo et al [28]. Ahmad et al. examined the effects of the GA crosslinking time on the pore size distribution of PVA films [29]. Qin et al. investigated the mechanical characteristics, thermal stability, water stability, and changes in the degree of crystallinity of PVA nanofibrous mats using a variety of concentrations of GA solutions [30]. Matty et al. worked on the effect of GA as a crosslinking agent with different weight ratios on the swelling behavior of PVA hydrogels [31]. Shivakumara and Demapp examined sodium alginate /PVA hydrogels which had been crosslinked with different GA concentrations; the chemical functional groups, morphology, and swelling properties of the hydrogels were investigated at different pH values, and using indifferent salts at different temperatures, and indifferent acids and bases [32]. Gadhave et al. evaluated the changes in thermal and mechanical properties caused by crosslinking different concentrations of GA on starch and PVA blended films [33]. Musa and Hameed worked on the effect of GA as a crosslinking agent with different weight ratios on the mechanical properties of PVA/starch and PVA/polyethylene glycol blend films [34]. Nagamadhu and Kivade investigated the mechanical and dynamic mechanical analysis of PVA-GA polymers [35]. Although the effect of concentrations on mechanical properties was investigated in some studies, reaction time was not emphasized. As far as the author is aware, no study has been carried out to evaluate the mechanical and wettability effects of crosslinking agent concentrations and duration parameters on the electrospun PVA/NaAlg materials.

This work aims to present a systematic investigation of some of the physical features occurring after the crosslinking process of PVA/NaAlg electrospun mats in the presence of GA. PVA/NaAlg electrospun mats are used for various applications, such as filtration, packaging, and wound dressings, and for this purpose, it is important to control the physical features and to understand how process parameters like concentration and time influence mechanical ability and wettability. Given this, the effects of crosslinker concentration and time on the wettability and mechanical properties of PVA/NaAlg electrospun mats after the crosslinking process are investigated. In this way, it is hoped to gain a basic insight into the crosslinking processes that affect wettability and strength properties.

2. EXPERIMENTAL STUDY

2.1. Materials

The PVA polymer (a molecular weight of 85,000-124,000 g/mol with 87-89% hydrolyzed), and hydrochloric acid (HCl) (37%) came from Sigma Aldrich (Germany). NaAlg was acquired from Cargill (France). GA (50%) was supplied by Kimetsan (Turkey). Ethyl alcohol, acetone, sodium chloride, potassium chloride, sodium phosphate dibasic, and potassium phosphate monobasics were supplied from Merck (Germany). The experiments were carried out with distilled water, and all the chemicals were employed without being purified.

2.2. Fabrication of NaAlg/PVA electrospun mats

To prepare a PVA aqueous solution, 12 g PVA polymer was completely dissolved in 100 mL distilled water over 12 hours at 90°C with continuous stirring. To prepare a NaAlg aqueous solution, 1 g NaAlg powder was fully dissolved in 100 mL distilled water over 4 hours at 50°C with constant stirring. Following that, the PVA and NaAlg were combined in a 70:30 (v:v) ratio and mixed for 6 hours to get a homogeneous solution. A 20 mL syringe was filled with NaAlg/PVA solution, and the electrospinning of the solutions was performed in a single-nozzle electrospinning setup (Figure 1). Before starting the electrospinning equipment, the spinning parameters were set as follows: rotational speed 180 rpm/min, voltage 18 kV, spinning distance 12 cm, and extrusion speed 0.7 mL/h. The electrospun mats were collected on aluminum foil.

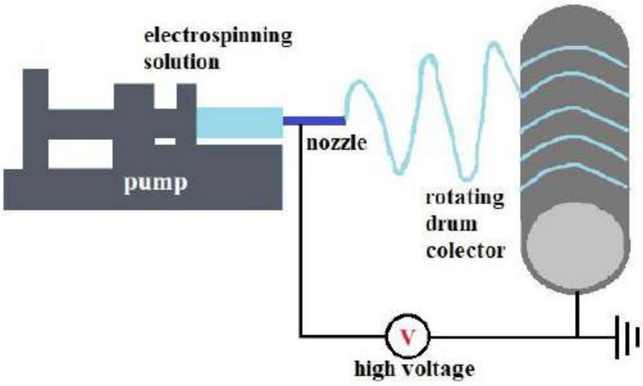

Figure 1 Illustration scheme of electrospinning setup

2.3. Crosslinking

The obtained electrospun PVA/NaAlg mats were soaked in a reaction solution consisting of three different (1.25, 2.5 and 5 v %) GA concentration. The recipes of the prepared solutions are given in Table 1 and a schematic diagram of the crosslinked PVA/NaAlg is shown in Figure 2. The samples were treated with the prepared solutions at room conditions (temperature = 25 ± 2 °C; relative humidity = 50 ± 5%) three separate times (10 min, 60 min, and 24 h) for chemical crosslinking and then washed with ethyl alcohol. Subsequently, the electrospun PVA/NaAlg mats were carefully washed several times with a phosphate buffer solution to remove the remaining GA.

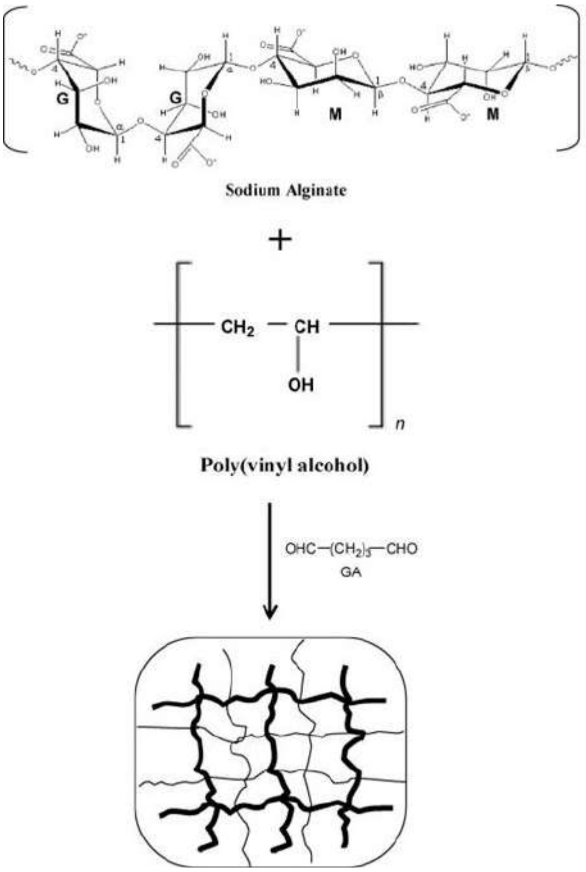

Figure 2 Schematic representation of the prepared crosslinked PVA/NaAlg [25]

Table 1 Recipes of crosslinking solution

	Concentrations		
Chemicals	1.25 %	2.5 %	5 %
Glutaraldehyde (mL)	1.25	2.5	5
Hydrochloric acid (mL)	0.5	0.5	0.5
Acetone (mL)	98.25	97	94.5

2.4. Mechanical strength

The tensile properties of the crosslinked electrospun mats were measured using the universal materials testing machine (Shimazhu AG-X plus) at room conditions (temperature = 25 ± 2 °C; relative humidity = 50 ± 5%). ISO 9073-3 Nonwovens — Test methods — Part 3: determination of tensile strength and elongation at break using the strip method was used for this study and modified according to the obtained electrospun mats. The tensile strength and elongation at break were determined using samples cut from the electrospun mats, which were 50 mm in length, 10 mm in width and at a crosshead speed of 10 mm/min. A digital micrometer was used to measure the thicknesses of the crosslinked electrospun mats (30-70 μm). The measurements were taken in triplicate, and the average values and standard deviations were determined.

2.5. Wettability

Contact angle measurements were performed using the sessile drop method with an Attension Theta (Biolin Scientific Inc.) system and distilled water. The crosslinked electrospun samples measuring 3 x 1 cm^2 were employed for the contact angle analysis. Water droplets (5 μL) were softly deposited on the surface, and the angle formed between the drop and the surface was determined by image analysis via software. Three different times (0 s, 10 s, and 30 s) were monitored as the droplets of water were released onto the electrospun mats. Three measurements were taken, and the mean values and standard deviations were determined by taking both the left-side and right-side angles into account.

3. RESULTS AND DISCUSSION

3.1. Mechanical strength of the electrospun mats

One of the most important and widely estimated properties of materials used in many applications is their ability to resist breaking under tensile stress [36]. This characterization was performed to study the effect of the condition of crosslinking duration and concentration on the tensile strength

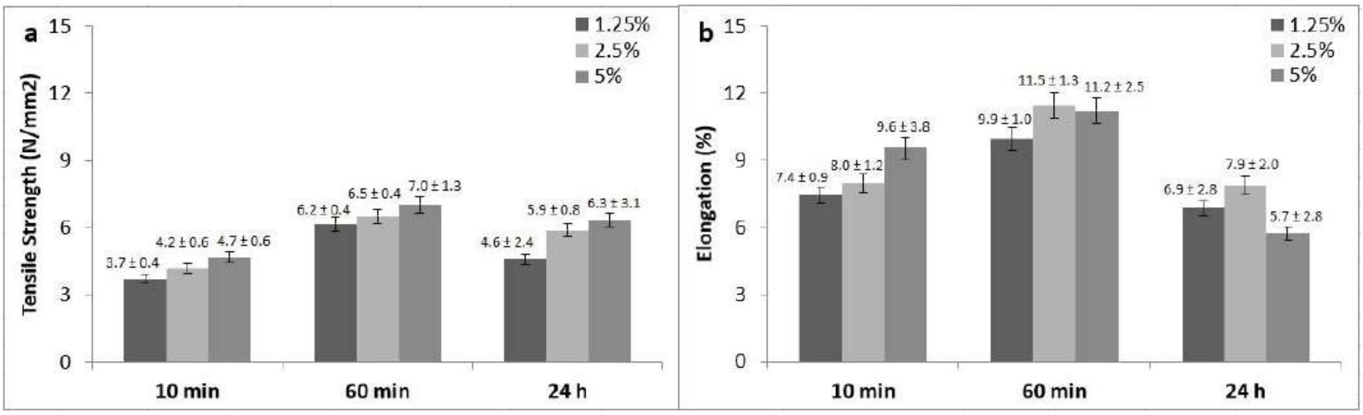

Figure 3 a) Influence of GA toward tensile strength and b) Influence of GA toward elongation

behavior of the electrospun mats. Figure 3 shows the mechanical properties of the electrospun mats using different concentrations (1.25, 2.5 and 5 v %) and application times (10 min, 60 min, and 24 h) of GA. With the increasing exposure time of GA, the tensile strength and elongation at break of the electrospun mats increased steadily at first but then decreased gradually when the application time of GA was 24 h. The improved tensile strength and elongation properties were attributed to an increase in acetal bonds between the aldehyde groups of crosslinking agents and the interaction of the hydrogen bond between the hydrophilic PVA and NaAlg. However, when the application duration approached 24 h, free hydroxyl and crosslinking points tended to become saturated. Excess GA tangled with the NaAlg/PVA molecular chains, meanwhile reducing the strength of the electrospun mats. The efficiency of GA on the crosslinking of NaAlg and PVA is due to the strong reactivity of the aldehyde groups, which quickly form imine bonds (Schiff's base) with amino groups and acetal bonds with hydroxyl groups [37]. The formation of a crosslinked network of electrospun mats, which limited the mobility of the molecular chains, was related to the improvement in tensile strength and the decrease in elongation at break. The highest tensile strength was 7.0 MPa for 5 % GA at 60 min. The high strength is usually related to high crystallinity [23]. It is thought that the maximum possible crystallinity for the samples had been reached under these operating conditions. The highest elongation was 11.5 % for 2.5 % GA at 60 min. This study showed us that although the increase in crosslinker concentrations initially gave an increase in elongation, at a certain point, higher crosslinking density protected the fiber from elongation and it became harder thus, elongation decreased. Because of the presence of two extremely reactive alpha protons the GA become more reactive and acidic in nature [33]. Due to the greater reactivity of GA, particularly at higher doses, the H-bond between the PVA chains is reduced. Mansur et al. showed that when PVA hydrogen was prepared with different GA concentrations in FTIR spectroscopy, the reaction of the PVA with the GA resulted in a significant reduction in the intensity of O-H peaks at higher GA concentrations [27].

In summary, the electrospun PVA/NaAlg mats may require different strength and flexibility properties depending on their use. Therefore, the process parameters should be optimized before crosslinking.

3.2. Water contact angle measurements of the electrospun mats

Wetting is a natural phenomenon with significant consequences for both nature and human existence. When a liquid interacts with a solid, it generates a liquid coating that spreads across the solid's surface. Materials have varying wetting qualities due to the different intermolecular interactions between the liquid and the solid. The contact angle is a numerical representation of the sample's wetting features. The contact angle of water has a considerable influence on the wetting of micro-sized droplets on solid surfaces [38]. Figure 4 shows the water contact angles of the

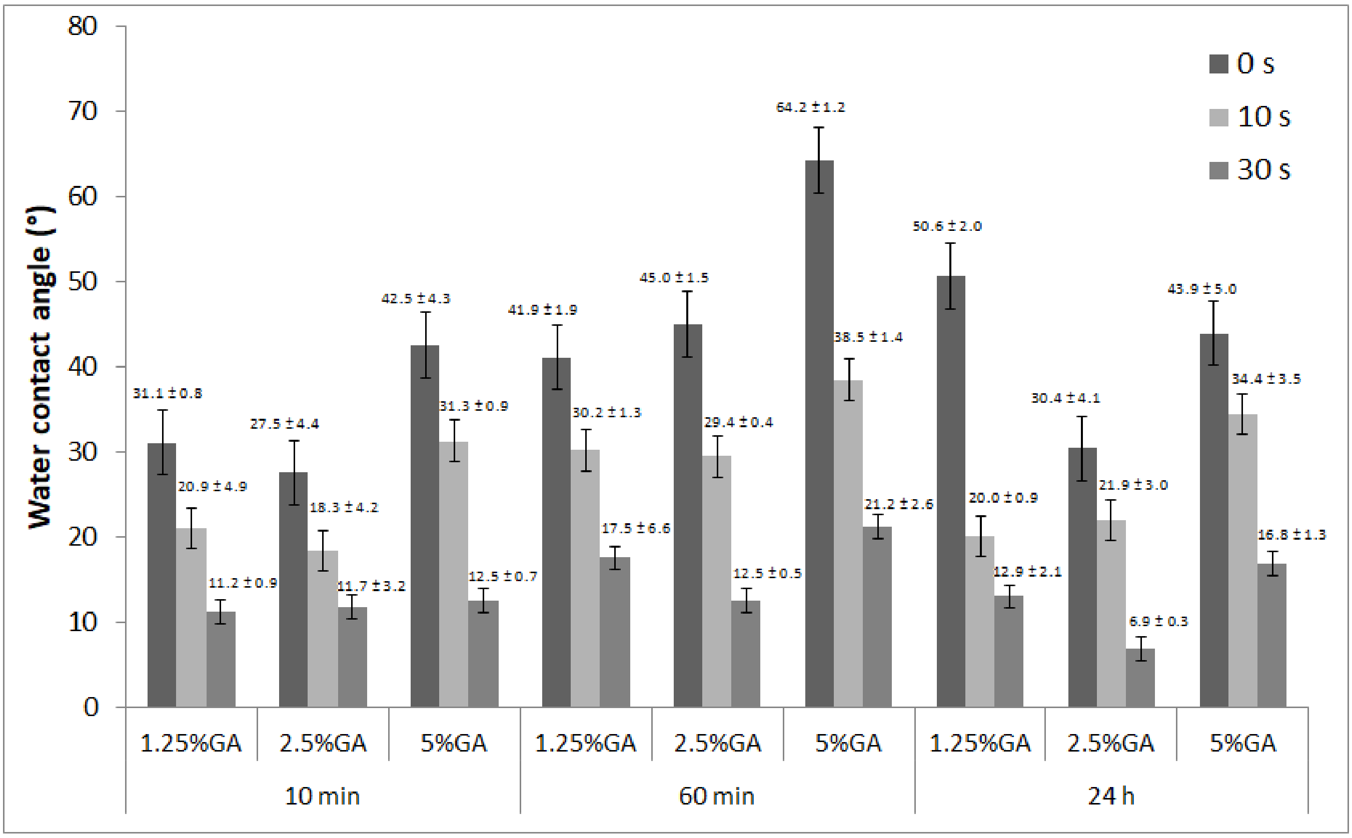

Figure 4 Water contact angles values of PVA/NaAlg electrospun mats at 0 s, 10 s and 30 s

electrospun mats at 0 s, 10 s and 30 s, with different concentrations and application times of GA. As shown in Figure 4, the electrospun mats demonstrated low water contact angles (27-64°). The water contact angle values were found to be consistent with those reported by Pakolpakçıl et al, where the GA crosslinked red cabbage extract loaded Alg/PVA contact angle value was ~46° [13].

The application time of GA was 10 min, it was observed that the electrospun mats exhibited the hydrophilic surfaces characteristics of more low contact angles (27-42°) when compared to the other application times. PVA and NaAlg's hydroxyl groups are hydrophilic, which means they can form hydrogen bonds with water and absorb a lot of it. This results in a decreased degree of water contact angle.

The highest contact angle value of 64° was obtained at 5% GA concentration and 60 min treatment time. The finding can be explained by increasing the crosslinking of the network; in other words the concentration of GA. The highest results were relatively consistent with the strength measurement at the same concentration and the time of application. It is thought that the water molecules are unable to find any spaces to enter, as the attraction force between the polymer molecules is high and the sample is too compressed [39]. This results in an increased degree of water contact angle. Pakolpakçıl and Draczynski showed that the water contact angle value of the EDC/NHS crosslinked PVA/alginate nanofiber mat increased as the EDC/NHS concentration increased [8].

The results show that the crosslinking concentration and time influenced the water contact angle of the electrospun mats, which can be attributed to the chemical interaction of the polymers and the crosslinker.

4. CONCLUSION

The PVA and NaAlg structures both include hydroxyl groups, which makes the reaction with GA possible. In this study, the PVA/NaAlg electrospun mats were fabricated successfully by the electrospinning method. To investigate the effect of the concentration and application time of GA crosslinking agent on the electrospun PVA/NaAlg mats, different concentrations (1.25, 2.5 and 5 v %) and duration times (10 min, 60 min and 24 h) of the GA were applied. According to the findings, the longest application time (24 h) has a negative effect on elongation. The highest strength values were obtained at all concentrations at 60 min of application time. In general, the highest contact angle values were observed at a concentration of 5%. The results of the investigation revealed that the crosslinking process parameter, the application time and the concentration influenced the development of the PVA/NaAlg electrospun mats' mechanical and wetting properties.

The end-use of the materials should be considered, where the choice of concentration and the duration of the crosslinking process have an impact on the mechanical and wetting ability of the water-soluble polymers. Mechanically strong fibers are generally preferred in many areas of use. However, since high water absorbance is required in applications such as wound dressings, wettability may be at the forefront.

The Declaration of Conflict of Interest/ Common Interest

No conflict of interest or common interest has been declared by the author.

The Declaration of Ethics Committee Approval

This study does not require ethics committee permission or any special permission.

The Declaration of Research and Publication Ethics

The author of the paper declare that they comply with the scientific, ethical and quotation rules of SAUJS in all processes of the paper and that they do not make any falsification on the data collected. In addition, they declare that Sakarya University Journal of Science and its editorial board have no responsibility for any ethical violations that may be encountered, and that this study has not been evaluated in any academic publication environment other than Sakarya University Journal of Science.

REFERENCES

[1] S. Thomas, S. Gopi, A. Amalraj, Biopolymers and their industrial applications from plant, animal, and marine sources, to Functional Products, 1st ed. Elsevier, 2020.

[2] M. A. Taemeh, A. Shiravandi, M. A. Korayem and H. Daemi, "Fabrication challenges and trends in biomedical applications of alginate electrospun nanofibers," Carbohydrate Polymers, vol. 228, 115419, 2020.

[3] I. P. S. Fernando, W. W. Lee, E. J. Han, G. Ahna, "Alginate-based nanomaterials: Fabrication techniques, properties, and applications," Chemical Engineering Journal, vol. 391, 123823, 2020.

[4] Grand View Research, Inc., Alginate Market Size, Share & Trends Analysis Report By Type (High M, High G), By Product (Sodium, Propylene Glycol), By Application (Pharmaceutical, Industrial), By Region, And Segment Forecasts, 2021-2028, https://www.grandviewresearch.com/industry-analysis/alginate-market (accessed on 16 March 2022).

[5] S. Ramakrishna, K. Fujihara, W. Teo, T. Lim, Z. Ma, An Introduction to Electrospinning and Nanofibers, World Scientific Publishing Co., Singapore, 2005.

[6] W. Xu, R. Shen, Y. Yan, J. Gao, "Preparation and characterization of electrospun alginate/PLA nanofibers as tissue engineering material by emulsion eletrospinning," Journal of the Mechanical Behavior of Biomedical Materials, vol. 65, pp 428-438, 2017.

[7] M. A. Teixeira, M. T. P. Amorim, H. P. Felgueiras, "Poly(vinyl alcohol)-based nanofibrous electrospun scaffolds for tissue engineering applications," Polymers, 12, 7, 2020.

[8] A. Pakolpakçıl, Z. Draczynski, “Preparation and characterization of the advanced alginate-based nanofibrous nonwoven using EDC/NHS coupling agent by electrospinning,” The Journal of the Textile Institute, vol. 113, pp. 1908-1916, 2021.

[9] S. Amjadi, H. Almasi, M.Ghorbani, S. Ramazani, “Preparation and characterization of TiO2NPs and betanin loaded zein/ sodium alginate nanofibers,” Food Package and Shelf Life, vol. 24, 100504, 2020.

[10] M. Wang, X. Li, T. Zhang, L. Deng, P. Li, X. Wang, B. S. Hsiao, “Eco-friendly poly(acrylic acid)-sodium alginate nanofibrous hydrogel: A multifunctional platform for superior removal of Cu(II) and sustainable catalytic applications,” Colloids and Surfaces A: Physicochemical and Engineering Aspects, vol. 558, pp. 228-241, 2018.

[11] Q. Wang, J. Ju, Y. Tan, L. Hao, Y. Ma, Y. Wu, H. Zhang, Y. Xia, K. Sui, “Controlled synthesis of sodium alginate electrospun nanofiber membranes for multi-occasion adsorption and separation of methylene blue,” Carbohydrate Polymers, vol. 205, pp. 125-134, 2019.

[12] T. C. Mokhena, N. V. Jacobs, A. S. Luyt, “Electrospun alginate nanofibres as potential bio-sorption agent of heavy metals in water treatment,” Express Polymer Letters, vol. 11, pp. 652–663, 2017.

[13] T. C. Mokhena, N. V. Jacobs, A. S. Luyt, “Nanofibrous alginate membrane coated with cellulose nanowhiskers for water purification,” Cellulose, vol. 25, pp. 417–427, 2018.

[14] L. Tan, Z. Li, R. Shi, F. Quan, B. Wang, X. Ma, Q. Ji, X. Tian, Y. Xia, “Preparation and properties of an alginate-based fiber separator for lithium-ıon batteries,” ACS Applied Materials and Interfaces, vol. 12, pp. 38175–38182, 2020.

[15] A. Pakolpakçıl, B. Osman, G. Göktalay, E. T. Özer, Y. Şahan, B. Becerir, E. Karaca, “Design and in vivo evaluation of alginate-based pH-sensing electrospun wound dressing containing anthocyanins,” Journal of Polymer Research, vol. 28, 50, 2021.

[16] A. Pakolpakçıl, Z. Draczynski, “Green approach to develop bee pollen-loaded alginate based nanofibrous mat,” Materials, vol. 14, 2775, 2021.

[17] K. R. Aadil, A. Nathani, C. S. Sharma, N. Lenka, P. Gupta, “Fabrication of biocompatible alginate-poly(vinyl alcohol) nanofibers scaffolds for tissue engineering applications,” Materials Technology, vol. 33, pp. 507-512, 2018.

[18] G. Ma, D. Fang, Y. Liu, X. Zhu, J. Nie, “Electrospun sodium alginate / poly (ethylene oxide) core –shell nanofibers scaffolds potential for tissue engineering applications,” Carbohydrate Polymers, vol. 87, pp. 737-743, 2012.

[19] N. Reddy, R. Reddy, Q. Jiang, “Crosslinking biopolymers for biomedical applications,” Trends in Biotechnology, vol. 33, pp. 362-369, 2015.

[20] K. Pal, A. T. Paulson, D. Rousseau, “14- Biopolymers in Controlled-Release Delivery Systems” Handbook of Biopolymers and Biodegradable Plastics, S. Ebnesajjad, Eds. William Andrew Publishing, 2013, pp. 329-363.

[21] E. Yang, X. Qin, S. Wang, “Electrospun crosslinked polyvinyl alcohol membrane,” Materials Letters, vol. 62, pp. 3555-3557, 2008.

[22] G. Acik, “A comprehensive study on electrospinning of poly (vinyl alcohol): effects of the TCD, applied voltage, flow rate, and solution concentration,” Journal

of the Turkish Chemical Society Section A: Chemistry, vol. 7, pp. 609-616, 2020.

[23] I. Gurol, C. Altinkok, E. Agel, C. Tasaltin, M. Durmus, G. Acik, “Phthalocyanine functionalized poly(vinyl alcohol)s via CuAAC click chemistry and their antibacterial properties,” Journal of Coatings Technology and Research, vol. 17, pp. 1587–1596, 2020.

[24] I. Migneault, C. Dartiguenave, M. J. Bertrand, K. C. Waldron “Glutaraldehyde: behavior in aqueous solution, reaction with proteins, and application to enzyme crosslinking” BioTechniques, vol. 37, pp. 790-802, 2004.

[25] R. V. Kulkarni, V. Sreedhar, S. Mutalik, C. M. Setty, B. Sa, “Interpenetrating network hydrogel membranes of sodium alginate and poly(vinyl alcohol) for controlled release of prazosin hydrochloride through skin,” International Journal of Biological Macromolecules, vol. 47, pp. 520-527, 2010.

[26] K. J. Kim, S. B. Lee, N. W. Han, “Effects of the degree of crosslinking on properties of poly(vinyl alcohol) membranes”, Polymer Journal, vol. 25, pp. 1295–1302, 1993.

[27] S. Mansur, M. S. Carolina, A. N. Souza, A. A. P. Mansur, “FTIR spectroscopy characterization of poly (vinyl alcohol) hydrogel with different hydrolysis degree and chemically crosslinked with glutaraldehyde,” Materials Science and Engineering C, vol. 28, pp. 539-548, 2008.

[28] K. C. S. Figueiredo, T. L. M. Alves, C. P. Borges, “Poly(vinyl alcohol) films crosslinked by glutaraldehyde under mild conditions,” Journal of Applied Polymer Science, vol. 111, pp. 3074–3080, 2009.

[29] A. L. Ahmad, N. M. Yusuf, B. S. Ooi, “Preparation and modification of poly (vinyl) alcohol membrane: Effect of crosslinking time towards its morphology,” Desalination, vol. 287, pp. 35–40, 2012.

[30] X. Qin, G. Dou, G. Jiang and S. Zhang, “Characterization of poly(vinyl alcohol) nanofiber mats cross-linked with glutaraldehyde,” Journal of Industrial Textiles, vol. 43, pp. 34–44, 2012.

[31] F. S. Matty, M. T. Sultan, A. K. Amine, “Swelling Behavior of Cross-link PVA with Glutaraldehyde”, Ibn Al-Haitham Journal for Pure and Applied Sciences, vol. 28, no. 2, pp. 136-146, 2015.

[32] L. R. Shivakumara, D. Thippaiah, “Synthesis and swelling behavior of sodium alginate/poly(vinyl alcohol) hydrogels,” Turkish Journal Pharmaceutical Sciences, vol. 16, pp.252-260, 2019.

[33] R. V. Gadhave, P. A. Mahanwar, P. T. Gadekar, “Effect of glutaraldehyde on thermal and mechanical properties of starch and polyvinyl alcohol blends,” Designed Monomers and Polymers, vol. 22, pp. 164-170, 2019.

[34] B. H. Musa, N. J. Hameed, “Effect of crosslinking agent (glutaraldehyde) on the mechanical properties of (PVA/Starch) blend and (PVA/PEG) binary blend films,” Journal of Physics: Conference Series, 1795, 012064, 2021.

[35] M. Nagamadhu, S. B. Kivade, “Effect of multifrequency, boundary conditions of Polyvinyl Alcohol (PVA) crosslinked with Glutaraldehyde (GA) using dynamic mechanical analyzer,” Advances in Materials and Processing Technologies, 2021.

[36] Y. Elmogahzy, R. Farag, “7- Tensile properties of cotton fibers: Importance, research, and limitations” In The Textile Institute Book Series, Handbook of Properties of Textile and Technical Fibres, A. R. Bunsell Eds. (Second

Edition), Cambridege: Woodhead Publishing, 2018, pp. 223-273.

[37] E. Campos, P. Coimbra, M. H. Gil, “An improved method for preparing glutaraldehyde cross-linked chitosan–poly(vinyl alcohol) microparticles,” Polymer Bulletin, vol. 70, pp. 549–561, 2013.

[38] T. Zhao, L. Jiang, “Contact angle measurement of natural materials,” Colloids and Surfaces B: Biointerfaces, vol. 161, pp. 324-330, 2018.

[39] M. Miraftab, A. N. Saifullah, A. Çay, “Physical stabilisation of electrospun poly(vinyl alcohol) nanofibres: Comparative study on methanol and heat-based crosslinking,” Journal of Materials Science, vol. 50, pp. 1943–1957, 2015.

SAKARYA ÜNİVERSİTESİ
FEN BİLİMLERİ ENSTİTÜSÜ
DERGİSİ

Sakarya University Journal of Science
SAUJS

ISSN 1301-4048 | e-ISSN 2147-835X | Period Bimonthly | Founded: 1997 | Publisher Sakarya University |
http://www.saujs.sakarya.edu.tr/

Title: Some Electrical and Photoelectrical Properties of Conducting Polymer Graphene Composite /n-Silicon Heterojunction Diode

Authors: Elif DAŞ

Recieved: 2022-06-14 00:00:00

Accepted: 2022-08-31 00:00:00

Article Type: Research Article

Volume: 25
Issue: 5
Month: October
Year: 2022
Pages: 1000-1009

How to cite
Elif DAŞ; (2022), Some Electrical and Photoelectrical Properties of Conducting Polymer Graphene Composite /n-Silicon Heterojunction Diode. Sakarya University Journal of Science, 25(5), 1000-1009, DOI: 10.16984/saufenbilder.1129742
Access link
http://www.saujs.sakarya.edu.tr/en/pub/issue/73051/1129742

Sakarya University Journal of Science 25(5), 1000-1009, 2022

Some Electrical and Photoelectrical Properties of Conducting Polymer Graphene Composite /n-Silicon Heterojunction Diode

Elif DAŞ*[1]

Abstract

In this study, polythiophene-graphene (PTh-G) composite thin film was prepared on the n-type silicon (n-Si) semiconductor wafer by the spin coating method. Subsequently, the current-voltage (I-V) measurements were made on the fabricated Au/PTh-G/n-Si/Al device to ascertain the impact of the PTh-G interfacial layer on the device performance. The main device parameters such as ideality factor (n), barrier height (Φ_b), series resistance (R_s) were calculated by using the thermionic emission (TE) and Norde functions, and then, the obtained results were discussed in detail. Additionally, the capacitance-voltage (C-V) characteristic of the device was examined as a function of the frequency, and the device parameters such as diffusion potential (V_d), Fermi energy level (E_f), carrier concentration (N_d), Φ_b were detemined. Finally, the light intensity-dependent I-V measurements were taken to obtain information about the photoelectrical characteristics of the fabricated device. The obtained results have shown that the prepared composite material has a good potential to be used in optoelectronic applications such as photodiode, and photodetector.

Keywords: Polythiophene, graphene, composite material, photoresponse, photosensitivity

1. INTRODUCTION

The metal-semiconductor (MS) Schottky barrier diode (SBD), formed by putting a metal in contact with a semiconductor, is the simplest known form of the electronic rectifier [1-3]. Despite its simple structure, it offers tremendous performance and is used in many different applications. In an SBD, the electrical properties of the device are mainly related to the interface and depletion region of the junction. So, if an interlayer material is positioned between the semiconductor and the metal, the performance of the device will depend on the physical characteristics of the material [4-6]. Thus, it is possible to fabricate semiconductor devices with higher electrical performance. Many researchers have been researching on using conducting polymer-based materials as interface materials to alter the electrical characteristics of MS junctions in recent years [7, 8].

Conducting polymers and/or their composites have the potential to dissolve in different solvents,

---

* Corresponding author: das.elif@gmail.com
[1] Atatürk University
ORCID: https://orcid.org/0000-0002-3149-6016

which allows them to be easily used in device fabrication via spin coating and drop-casting. Up to now, a wide range of conducting polymers and their derivatives have been developed, such as poly (1,4-phenylenevinylene) (PPV), poly(p-phenylene) (PPP), polyfluorene (PF), and polythiophene (PTh) [8, 9]. Among these conducting polymers, polythiophene (PTh) has been much interested material due to its good chemical and thermal stability as well as excellent electronic and optical properties [10, 11]. Additionally, many composites of PTh have been reported for different applications [9, 12]. The obtained results have shown that composite materials possess properties that may not be achieved by either component separately. Also, these reports have shown that there are many factors affect the PTh composite properties, like synthesis methods, types of fillers, fillers morphology, polymer matrix, etc.

In the last few years, the fantastic properties of carbon-based materials make them very promising and favorable as fillers for production of a new class of polymeric heterostructures. For example, Wang et al. [13] prepared ordered PTh/fullerene composite core-shell nanorod arrays by using melt-assisted wetting of porous alumina templates. Experimental results showed that the synthesized material has promising potential in solar cells. Also, Karim et al. [14] prepared PTh/single-wall carbon nanotube composites using a polymerization method. The obtained results showed that the composite material was better in terms of thermal and electrical conductivity compared to pure PTh. In another study, Bachhac and Patil [15] synthesized PTh-coated multiwalled carbon nanotube (MWCNT) composites by simple, cost-effective, in-situ oxidative polymerization method. They highlight that synergistic effects of the PTh-coated MWCNTs improve the gas sensing properties. In a nutshell, combining conducting polymers with carbon-based materials allows engineers to create flexible composites with favorable electrical, optical, or mechanical properties. In the light of this information, within the scope of the presented study, the synthesis of PTh-graphene (PTh-G) composite material and its analysis in terms of electrical and photoelectrical properties at the metal-semiconductor interface are discussed. When the studies in the literature are analyzed, this study is the first research study conducted for the stated purpose. In this sense, I believe that the presented study will make significant contributions to the literature and optoelectronic technology.

2. MATERIALS AND METHODS

2.1. Materials

Thiophene (Sigma-Aldrich), Graphene nanoplatelet (Nanografi, surface area: 320 m^2g^{-1}), choloform, anhydrous ferric chloride ($FeCI_3$), acetone and methanol (Sigma-Aldrich) were used as obtained. Additionally, in the SBDs fabrication process, n-type Si wafer was preferred. A well-known cleaning procedure was used to clean the Si wafers, as specified in ref [16].

2.2. Preparation of PTh-G Composite Materials

Composite materials synthesis were carried out according to a literature method developed by Melo et al. [17] with some modification. In this method, in-situ chemical oxidative polymerization technique was used for the synthesis of composite materials. Briefly, 0.03 g of thiophene monomer was added to chloroform and thoroughly mixed. Then, 0.1 g of graphene was added to the prepared suspension and mixed for a while. On the other hand, 3 g of oxidizing agent $FeCI_3$ was dispersed in a different beaker with a chloroform solution until it formed a homogeneous suspension. Subsequently, the $FeCI_3$ suspension was added drop by drop to the thiophene-graphene suspension and stirred for one day at room temperature. After that the PTh-G composite was filtered and attentively washed many times by methanol, water, and acetone, respectively. Finally, the resultant composite material was dried in a vacuum oven.

2.3. Fabrication of Au/PTh-G/n-Si/Al SBD

In this stage, firstly, the aluminum (Al) metal coating process was carried out to obtain ohmic contact onto the unpolished surface of the Si wafer under 10^{-6} torr pressure. Then, the n-Si/Al structure was maintained at 450 ˚C for 5 minutes to enhance the ohmic contact's quality. Next stage, the composite material was dispersed in ethanol, then spin-coated onto Si substrate at the rotation of 1000 rpm for one minute, and air-dried overnight at room temperature. Gold (Au) dots were made on the surface of the composite thin film by using thermal evaporation system through a shadow mask. As a result, the fabrication of the Au/PTh-G/n-Si/Al device was completed. The schematic representation of the obtained device structure is given in Figure 1. In addition, reference device (Au/n-Si/Al) fabrication was also performed in order to observe the effect of the composite interfacial material on the junction parameters.

2.4. I-V and C-V Measurements

The I-V measurements of the device were carried out under darkness and illumination conditions using Keithley source-meter. Additionally, the impedance analyzer system ((HP 4192A LF Model) was used to determine the C-V behaviors at various frequencies. The measurements were performed at ambient conditions. More information on measurement systems can be found in previous studies [5,6].

3. RESULTS AND DISCUSSION

3.1. I-V Results of the Fabricated Devices

The forward and reverse biased log (I)-V characteristics of the PTh-G/n-Si and reference diode are shown at dark ambient in Figure 2. According to the literature reports, the non-linear current-voltage characteristics of the metal/polymer junction could be owing to the thermionic emission (TE), space charge limited conduction (SCLC), or Poole-Frenkel emission [18]. The current through a Schottky barrier diode under a forward bias voltage is formulated by the eq. (1)

$$I = I_0 \left[exp\left(\frac{qV}{nkT}\right) - 1 \right] \qquad (1)$$

In eq. (1), electronic charge, voltage, ideality factor, Boltzmann constant, temperature, and saturation current are represented by the terms q, V, n, k, T and I_o, respectively. I_o, namely, the reverse sturation current can be calculated using the equation (2) [19].

$$I_0 = AA^{*}T^{2} exp(-q\Phi_b/kT) \qquad (2)$$

herein, the A is the diode area, A* is the effective Richardson constant, and Φ_b is Schottky barrier height. If we rearrange the eqs. (1) and (2), the value of n and Φ_b can be calculated from the following equations [20].

$$n = \frac{q}{kT}\left(\frac{dV}{dIn\, I}\right) \qquad (3)$$

and

$$\Phi_b = \frac{kT}{q} ln\left(\frac{AA^{*}T^{2}}{I_0}\right) \qquad (4)$$

In the heterojunction devices, the current transport mechanism is generally analyzed using the TE model. According to the TE model, the n and the Φ_b values of the prepared devices were calculated and the results were tabulated in Table 1. It is clearly seen that the n value of the device obtained with the conductive polymer composite material is lower than the reference diode. The value of n generally expresses the dependence of the diode current on the applied potential and gives information about the quality of the fabricated device. For an ideal SBD, the value of n is equal to one, but, in application, n always exceed unity. In the present study, the value of n is small and closer to unity for the PTh-G/n-Si device. Additionally, the leakage current of the PTh-G/n-Si device is lower than the reference diode as seen in Figure 2. Therefore, it can be said that the electrical properties of the reference diode were improved after the insertion of the PTh-G composite layer between Au and n-Si wafer. On the other hand, Φ_b is a main parameter to specify the attitude of the depletion region in the SBD.

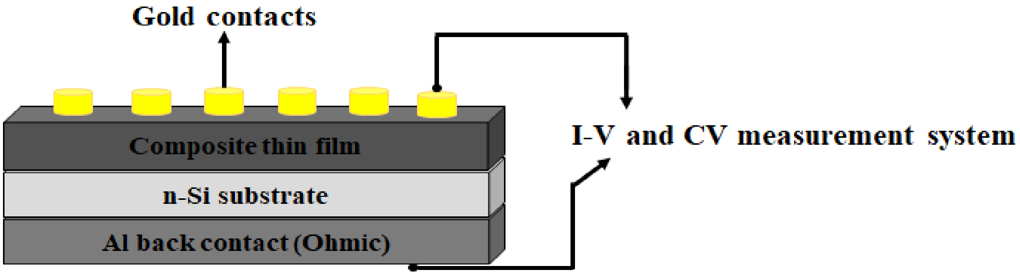

Figure 1 A schematic representation of Au/PTh-G/n-Si/Al SBD

The Φ_b value of the PTh-G/n-Si diode was found as 0.78 eV, which is higher than that of the reference diode (0.74 eV). This situation can be attributed to the presence of the PTh-G composite interlayer. Since the composite thin film separates the metal from the semiconductor material, thereby, an increase in the Φ_b of MS junction is observed.

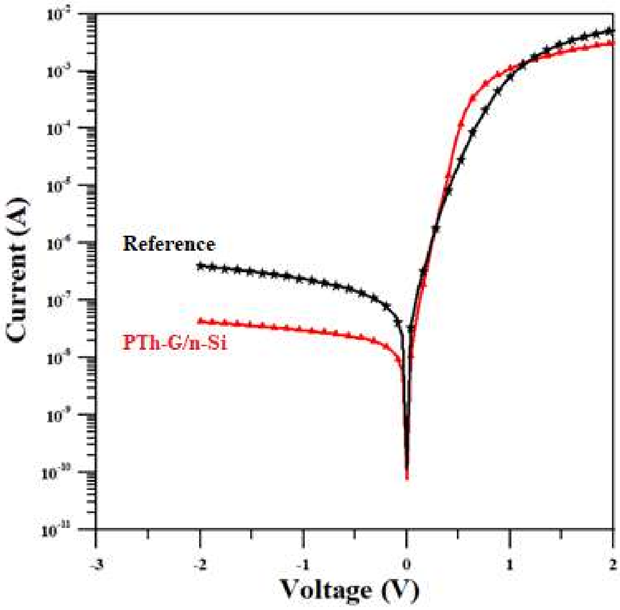

Figure 2 The log (I)-V plots of the PTh-G/n-Si and reference diode at room temperature

In order to get further insight into the electrical properties of the prepared device, determining the value of the series resistance (R_s) is also quite important. The value of R_s can be easily calculated by the Norde method which is described as [21]:

$$F(V) = \frac{V}{\gamma} - \frac{kT}{q}\, In\,\left(\frac{I(V)}{AA^{*}T^{2}}\right) \qquad (5)$$

here, γ is the first integer greater than n. The value of Rs is determined using the following equation:

$$R_s = \frac{kT(\gamma - n)}{qI} \qquad (6)$$

here the n value obtained from the In(I)-V plot is used. Moreover, the value of the Φ_b can be computed using this method. The Φ_b is given as

$$\Phi_b = F(V_{min}) + \frac{V_{min}}{\gamma} - \frac{kT}{q} \qquad (7)$$

The lowest level of F(V) is $F(V_{min})$, and V_{min} is the corresponding voltage value. Figure 3 shows Norde's function against the potential for the PTh-G/n-Si heterojunction device. Based on equations (6) and (7), the Φ_b and R_s values of the devices were calculated and summarized in Table 1. According to acquired the results, the values of Φ_b are in good agreement with those obtained from I-V characteristics.

3.2. C-V Results of the PTh-G/n-Si SBD

The C-V measurement provides important information about the interfacial properties of the diode. For this purpose, the C-V measurements of the PTh-G/n-Si heterojunction device were carried out at room temperature, with a frequency range of 100-1000 kHz. The obtained C-V characteristics for the PTh-G/n-Si device are shown in Figure 4, and the relationship for C^{-2}-V characteristics are shown in Figure 5. In Figure 4, the capacitance increases with the applied voltage in the forward bias region upto a point where it

Table 1 Main device parameters of the fabricated devices

Device (dark ambient)	**I-V**		**Norde**	
	n	**Φ_b (eV)**	**Φ_b (eV)**	**R_s (Ω)**
Au/n-Si/Al	2.67	0.74	0.74	2762
Au/PTh-G/n-Si/Al	1.84	0.78	0.77	3479

reaches a maximum value. Also, the value of the capacitance at the peak tends to decrease with increasing frequency. The increase in peak value of the capacitance occurs because the interface states at lower frequencies can follow the alternative current (AC) signal and yield an excess capacitance which depends on the frequency [22]. However, in the high frequency limit, the contribution of the interface states which can follow the AC signal, to the total capacitance is negligibly small. Hence, the capacitance peak tends to decrease as frequency increases.

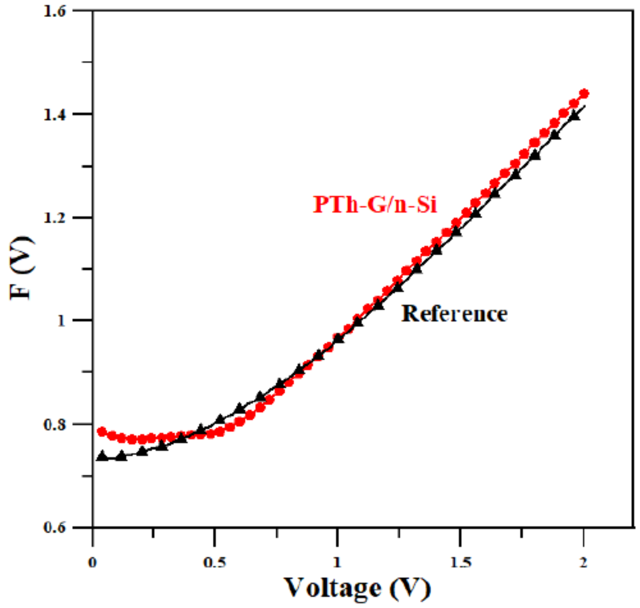

Figure 3 The F(V)-V plots of the PTh-G/n-Si and reference device

Additionally, in Figure 5, C^{-2}-V plot of the PTh-G/n-Si diode exhibits a linear behavior in the negative voltage range for all frequency values, and at this region, the equation for the connection between C^{-2} and V_d can be given as eq.(8) [22, 23].

$$C^{-2} = \frac{2(V_d+V)}{q\varepsilon_s N_d A^2} \tag{8}$$

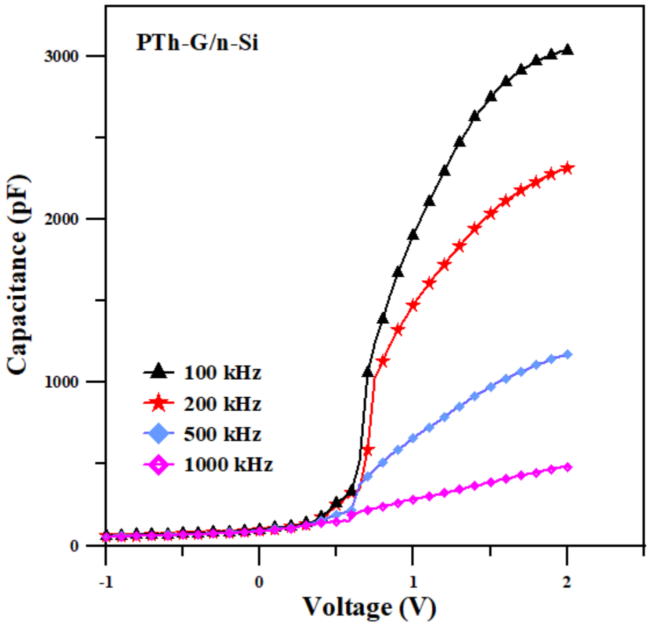

Figure 4 The C-V curves of the PTh-G/n-Si SBD for different frequencies

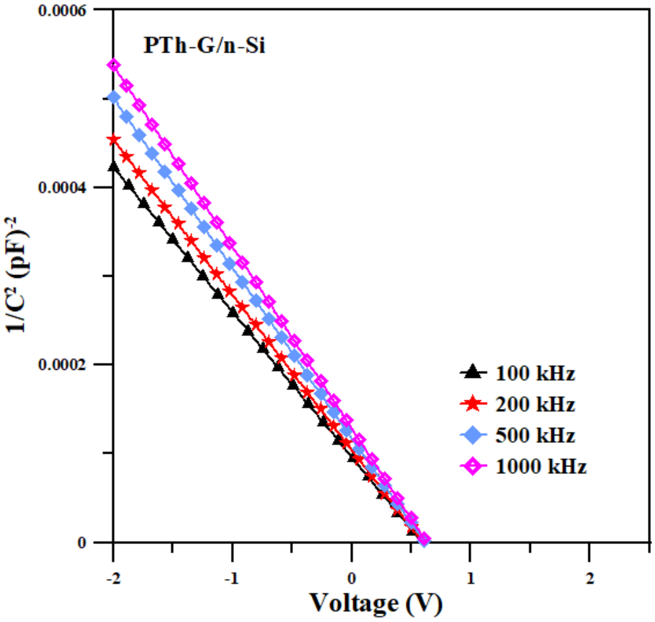

Figure 5 The C^{-2}-V curves of the PTh-G/n-Si SBD for different frequencies

Table 2 The device parameters obtained from C^{-2}-V plot for characteristics of the Au/PTh-G/n-Si/Al SBD between 100 and 1000 kHz at the room temperature

Frequency (kHz)	V_d (V)	N_d (cm^{-3})	E_f (eV)	Φ_b (eV)
1000	0.651	$9.68*10^{14}$	0.265	0.60
500	0.628	$1.02*10^{15}$	0.264	0.59
200	0.605	$1.11*10^{15}$	0.262	0.57
100	0.590	$1.18*10^{15}$	0.260	0.56

herein, V_d is the diffusion potential at zero bias which is determined from the extrapolation of the linear C^{-2}-V plot to V axis. Also, ε_s is the dielectric constant of semiconductor, A is the effective area of the diode and N_d is the concentration of ionized donors.

In order to determine device parameters of the PTh-G/n-Si diode, the C-V curves were used, and the obtained results were given in Table 2. According to the results, it can be said that the paramaters show a weak frequency dependency in the applied frequency range. The similar results for these paramaters can be found in the literature reports [24, 25].

3.3. Photocurrent and Responsivity Measurements

Figure 6 show the effect of illumination on the PTh-G/n-Si device. It is seen that the diode current does not change in the forward bias region under white light illumination, on the other hand, it increases with increasing light intensity in the reverse bias region. Such behavior implies that the device has a photodiode characteristic. Furthermore, at zero bias, the short circuit current (I_{sc}) is sensitive to the intensity of the light. So, it can be said that self-powered light detection can be achieved with the PTh-G/n-Si SBD [26].

In the literature, the photoresponsivity (R) and photosensitivity (S) behavior of the SBDs are usually investigated for photoconductivity measurements [26-29]. In this sense, we can say that the responsivity is a way to show the photoconductivity or the light-induced current of a material. The value of R is defined as the ratio of electrical output to its optical input in Amperes/Watt (AW^{-1}), as shown in equation (9).

$$R = \frac{J_{ph}}{P_{in}} \tag{9}$$

where, J_{ph} is the photocurrent dentisty, P_{in} is the incident light power. On the other hand, the photosensitivity is simply the ON/OFF ratio for current output in the light compared to that in the dark, as shown in equation (10).

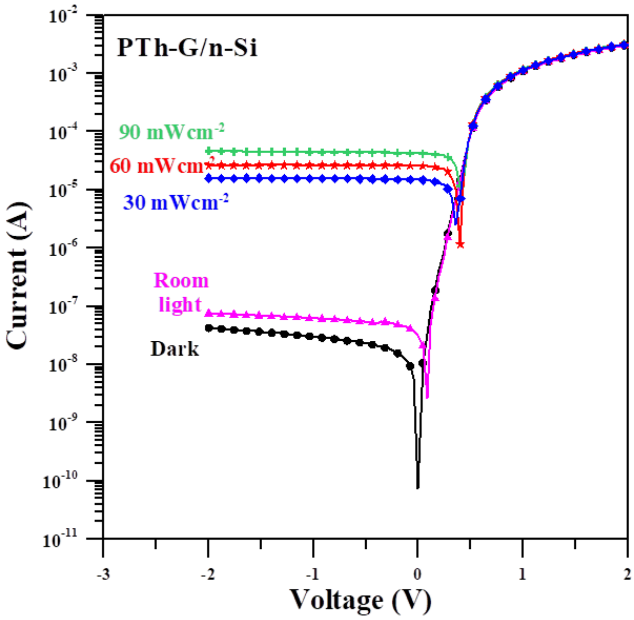

Figure 6 The I-V plots of the PTh-G/n-Si device under dark and different light illumunations

$$S = \frac{I_{ph}}{I_{dark}} \tag{10}$$

In the light of this information, the R and S values of the PTh-G/n-Si device were calculated at different voltages for various light intensities and the obtained results were tabulated in Table 3. It is seen that the R and S values of the device vary depending on the incident light power. Additionally, open-circuit voltage (V_{oc}) and (I_{sc})

Table 3 Photodiode parameters of the PTh-G/n-Si SBD at various light intensities

Light Intensity ($mWcm^{-2}$)	**I_{sc} (μA)**	**V_{oc} (V)**	**Photosensivity (S)**		**Photoresponsivity (R) (AW^{-1})**	
			(@-0.5 V)	**(@-1 V)**	**(@-0.5 V)**	**(@-1 V)**
30	13.2	0.37	676.4	517.1	$6.5*10^{-2}$	$6.6*10^{-2}$
60	23.8	0.40	1159.4	875.6	$5.6*10^{-2}$	$5.6*10^{-2}$
90	36.8	0.41	1936.1	1480.9	$6.2*10^{-2}$	$6.3*10^{-2}$

Table 4 Photovoltaic parameters of the PTh-G/n-Si and reported polymer/Si based junctions

Device configuration	**Light Intensity ($mWcm^{-2}$)**	**I_{sc} (μA)**	**V_{oc} (V)**	**References**
PTh-G/n-Si	90	36.8	0.41	present work
CU:rGO/n-Si	10	0.48	0.22	[30]
	150	12.18	0.37	
bisTPAT/n-Si	100	15	0.40	[31]
PVA(Co-doped)/n-Si	100	19.30	0.28	[32]
PVA (Bi-doped)/n-Si	250	88.53	0.22	[33]
PVA (Ni-doped)/n-Si	100	33.2	0.42	[34]
Pentacene/n-Si	100	~7	~0.15	[35]
Sunset Yellow/n-Si	40	25.45	~0.15	[36]
	100	91.84	~0.18	
Eosin y/n-Si	100	10	0.02	[37]
Eosin y/p-Si	100	9	0.10	

values of the PTh-G/n-Si device were also given in Table 3. The results demonstrated that when light intensity increased, the photovoltaic parameters improved. Furthermore, the photovoltaic parameters were compared with the relevant literature reports in the Table 4. The obtained values suggest that the PTh-G/n-Si device can be operated as a heterojunction photodiode.

4. CONCLUSION

In recent years, extensive research has been carried out on conductive polymer carbon-based composite materials for various applications due to their extraordinary properties. In the presented study, the performance of PTh-G composite material as an interface layer in the Au/PTh-G/n-Si/Al SBD structure was evaluated for the first time in the literature. For this purpose, firstly, PTh-G composite material synthesis was made by using the in-situ chemical oxidative polymerization method, and then device fabrication was carried out. The I-V characteristics of the prepared device were measured under dark and illuminated conditions (30-90 $mWcm^{-2}$) to provide information about important device parameters such as n, Φ_b, R_s, R, and S. The obtained results show that the device is highly sensitive to light and exhibits a self-powering feature under illumination. Additionally, C-V measurements show that the fabricated device has capacitance feature and this capacity change as a function of the frequency. So, based on the obtained results, it can be said that the fabricated Au/PTh-G/n-Si/Al SBD can be used in optoelectronic applications.

Funding
The author has no received any financial support for the research, authorship or publication of this study.

Acknowledgements
I would like to thank the NANOGRAFI Company (Turkey) for supplying graphene in this study. Also, I would like to express my special thanks to Mr. Zafar Alam Queraishi for his valuable time and useful suggestions.

The Declaration of Conflict of Interest/ Common Interest
No conflict of interest or common interest has been declared by the author.

Authors' Contribution
ED: This paper is a single-author study. Everything was done by the author.

The Declaration of Ethics Committee Approval
The author declares that this document does not require an ethics committee approval or any special permission.

The Declaration of Research and Publication Ethics
The author of the paper declares that they comply with the scientific, ethical and quotation rules of SAUJS in all processes of the paper and that they do not make any falsification on the data collected. In addition, they declare that Sakarya University Journal of Science and its editorial board have no responsibility for any ethical violations that may be encountered, and that this study has not been evaluated in any academic publication environment other than Sakarya University Journal of Science.

REFERENCES

[1] S. M. Sze, “Physics of Semiconductor Devices,” 2nd ed. Wiley, New York, 1981.

[2] E. H. Rhoderick, R. H. Williams, Metal-Semiconductor Contacts, 2nd ed., Clarendon Press, Oxford, 1988.

[3] R. T. Tung, “Recent advances in Schottky barrier concepts,” Materials Science and Engineering R, vol. 35, pp. 1-138, 2001.

[4] Z. Çaldıran, “Modification of Schottky barrier height using an inorganic compound interface layer for various contact metals in the metal/p-Si device structure,” Journal of Alloy and Compound, vol. 865, pp. 158856, 2021.

[5] E. Daş, “Electrical and photoelectrical properties of Schottky diode construction with three-dimensional (3D) graphene aerogel interlayer,” Optical Materials, vol. 121, pp. 111633, 2021.

[6] E. Daş, “Green synthesis of reduced graphene oxide and device fabrication for optoelectronic applications,” Erzincan University Journal of Science and Technology, vol. 14, pp. 524-541, 2021.

[7] S. Mahato, “Composition analysis of two different PEDOT:PSS commercial products used as an interface layer in Au/n-Si Schottky diode,” RSC Advances, vol. 7, pp. 47125, 2017.

[8] S.Ying, Z. Ma, Z. Zhou, R. Tao, K.Yan, M. Xin, Y. Li, L. Pan, A. Y. Shi, “Device based on polymer Schottky junctions and their applications: A review,” IEEE Acces, vol. 8, pp. 189646-189660, 2020.

[9] F. Vatansever, J. Hacaloglu, U. Akbulut, L. Toppare, “A conducting composite of polythiophene: synthesis and characterization,” Polymer International, vol. 41, pp. 237-244, 1996.

[10] K. R. Nemade and S. A. Waghuley, “Synthesis, characterization and thermal properties of polythiophene composites,” Asian Journal of Chemistry, vol. 24, pp. 5947-5948, 2012.

[11] S. Sivrikaya, A. Dalmaz, S. Durmuş, “Synthesis of nano poly(2-thiophenecarboxaldehyde) and characterization of structure,” Sakarya

University Journal of Science, vol. 22, pp. 1571-1575, 2018.

[12] C. Zanardi, F. Terzi, R. Seeber, "Polythiophenes and polythiophene-based composites in amperometric sensing," Analytical and Bioanalytical Chemistry, vol. 405, pp. 509-531, 2013.

[13] H. S. Wang, L. H. Lin, S. Y. Chen, Y. L. Wang, K. H. Wei, "Ordered polythiophene/fullerene composite core-shell nanorod arrays for solar cell applications," Nanotechnology, vol. 20, pp. 075201, 2009.

[14] M. R. Karim, C. J. Lee, M. S. Lee, "Synthesis and characterization of conducting polythiophene/carbon nanotubes composites," Journal of Polymer Science (Part A) Polymer Chemistry, vol. 44, pp. 5283-5290, 2006.

[15] S. G. Bachhav and D. R. Patil, "Preparation and Characterization of Multiwalled Carbon Nanotubes-Polythiophene Nanocomposites and its Gas Sensitivity Study at Room Temperature," Journal of Nanostructures, vol. 7, pp. 247-257, 2017.

[16] Z. Çaldıran, "Fabrication of Schottky barrier diodes with the lithium fluoride interface layer and electrical characterization in a wide temperature range," Journal of Alloy and Compounds, vol. 816, pp. 152601, 2020.

[17] J. P. Melo, E. N. Schulz, C. M. Verdejo, S. L. Horswell, M. B. Camarada, "Synthesis and Characterization of Graphene/Polythiophene (GR/PT) Nanocomposites: Evaluation as High-Performance Supercapacitor Electrodes," International Journal of Electrochemical Science, vol. 12, pp. 2933-2948, 2017.

[18] R. Singh, D. N. Srivastava, R. A. Singh, "Schottky diodes based on some semiconducting polymers," Synthetic Metals, vol. 121, pp. 1439-1440, 2001.

[19] R. K. Gupta and R. A. Singh, "Schottky diode based on composite organic semiconductors," Material Science in Semiconductor Processing, vol. 7, pp. 83-87, 2004.

[20] R. K. Gupta, K. Ghosh, P. K. Kahol, "Fabrication and electrical characterization of Au/p-Si/STO/Au contact," Current Applied Physics, vol. 9, pp. 933-936, 2009.

[21] H. Norde, "A modified forward I-V plot for Schottky diodes with high series resistance," Journal of Applied Physics, vol. 50, pp. 5052-5053, 1979.

[22] S. A. Yerişkin, M. Balbaşı, İ. Orak, "Frequency dependent electrical characteristics and origin of anomalous capacitance-voltage (C-V) peak in Au/(graphene-doped PVA)/n-Si capacitors," Journal of Materials Science: Materials in Electronics, vol. 28, pp. 7819-7826, 2017.

[23] A. Chelkowski, "Dielektrik Physics," Elsevier, Amsterdam, pp. 97-105, 1980.

[24] S. Demirezen, İ. Orak, Y. Azizian-Kalandaragh, Ş.Altındal, "Series resistance and interface states effects on the C-V and G/w-V characteristics in Au/(Co_3O_4-doped PVA)/n-Si structure at room temperature," Journal of Materials Science: Materials in Electronics, vol. 28, pp. 1296-12976, 2017.

[25] A. Nikravan, Y. Badalı, Ş. Altındal, I. Uslu, İ. Orak, "On the Frequency and Voltage-Dependent Profiles of the Surface States and Series Resistance of Au/ZnO/n-Si Structures in a Wide Range of Frequency and Voltage," Journal of Electronic Materials, vol. 46, pp. 5728-5736, 2017.

[26] K. Chandra Sekhar Reddy, P. Sahatiya, I. Santos-Saucesa, O. Cortazar, R. Ramirez-Bon, "One-step fabrication of 1D p-NiO nanowire/n-Si heterojunction: Development of self-powered ultraviolet

photodetector,” Applied Surface Science, vol. 513, pp. 145804, 2020.

[27] E. Daş, U. Incekara, Ş. Aydoğan, “A comparative study on electrical characteristics of Ni/n-Si and Ni/n-Pi Schottky diodes with Pinus Sylvestris Resin interfacial layer in dark and under illumination at room temperature,” Optical Materials, vol. 119, pp. 111380, 2021.

[28] Ö. Sevgili and İ. Orak, “The investigation of current condition mechanism of Al/Y_2O_3/p-Si Schottky barrier diodes in wide range temperature and illuminate,” Microelectronics Reliability, vol. 117, pp. 114040, 2021.

[29] A. Koçyiğit, A. Sarılmaz, T. Öztürk, F. Özel, M.Yıldırım, “A Au/$CuNiCoS_4$/p-Si photodiode: electrical and morphological characterization,” Beilstein Journal of Nanotechnology, vol. 12, pp. 984-994, 2021.

[30] H. O. Doğan, Z. Orhan, F. Yıldırım, S. Aydoğan, “Self-powered photosensor based on curcumin:reduced graphene oxide (Cu:rGO)/n-Si heterojunction in visible and UV regions,” Journal of Alloys and Compounds, vol. 915, pp. 165428, 2022.

[31] M. Erdogan, Z. Orhan, E. Daş, “ Synthesis of electron-rich thiophene triphenylamine based organic materials for photodiode applications,” Optical Materials, vol. 128, pp. 112446, 2022.

[32] M. Gökçen, T. Tunç, Ş. Altındal, İ. Uslu, “Electrical and photocurrent characteristics of Au/PVA(Co-doped)/n-Si photoconductive diodes,” Materials Science and Engineering B, vol. 177, pp. 416-420, 2012.

[33] S. Demirezen, Ş. Altındal, İ.Uslu, “Two diodes model and illumination effect on the forward and reverse bias I-V and C-V characteristic of Au/PVA (Bi-doped)/n-Si photodiode at room temperature,” Current Applied Physics, vol. 13, pp. 53-59, 2013.

[34] T. Tunç, M. Gökçen, “Preparation and electrical characterization of Au/n-Si (110) structure with PVA-nickel acetate composite film interfacial layer,” Journal of Composite Materials, vol. 46, pp. 2843-2850, 2012.

[35] H. Kacus, M.Yılmaz, A. Koçyiğit, U. İncekara, Ş. Aydoğan, “ Optoelectronic properties of Co/pentacene/Si MIS heterojunction photodiode,” Physica B: Condensed Matter, vol. 597, pp. 412408, 2020.

[36] A. G. Imer, E. Kaya, A. Dere, A. G. Al-Sehemi, A. A. Al-Ghamdi, A. Karabulut, F. Yakuphanoğlu, “Illumination impact on the electrical characteristics of Au/Sunset Yellow/n-Si/Au hybrid Schootky diode,” Journal of Materials Science:Materials in Electronics, vol. 31, pp. 14665-14673, 2020.

[37] M.Yılmaz, A. Koçyiğit, S. Aydoğan, U. İncekara, Y. Şahin, H. Kacus, “Influence of illumination intensity on electrical characteristics of Eosin y dye based hybrid photodiode:comparative study,” Applied Physics A, vol. 126, pp. 781, 2020.

SAKARYA ÜNİVERSİTESİ
FEN BİLİMLERİ ENSTİTÜSÜ
DERGİSİ

Sakarya University Journal of Science
SAUJS

ISSN 1301-4048 | e-ISSN 2147-835X | Period Bimonthly | Founded: 1997 | Publisher Sakarya University |
http://www.saujs.sakarya.edu.tr/

Title: Copper(II) Complexes of a New Hydrazones with Aliphatic Groups: Synthesis, Characterisation and Nuclease Activity

Authors: Cansu TOPKAYA

Recieved: 2022-04-26 00:00:00

Accepted: 2022-09-02 00:00:00

Article Type: Research Article

Volume: 25
Issue: 5
Month: October
Year: 2022
Pages: 1010-1021

How to cite
Cansu TOPKAYA; (2022), Copper(II) Complexes of a New Hydrazones with Aliphatic Groups: Synthesis, Characterisation and Nuclease Activity. Sakarya University Journal of Science, 25(5), 1010-1021, DOI: 10.16984/saufenbilder.1109011
Access link
http://www.saujs.sakarya.edu.tr/en/pub/issue/73051/1109011

Sakarya University Journal of Science 25(5), 1010-1021, 2022

Copper(II) Complexes of a New Hydrazones with Aliphatic Groups: Synthesis, Characterisation and Nuclease Activity

Cansu TOPKAYA*[1]

Abstract

Two new copper(II) complexes of bidentate arylhydrazone ligands have prepared and studied. Elemental analysis, SEM-EDS, thermal gravimetric analysis (TGA), powder X-ray diffraction (XRD), and a number of spectroscopic techniques were used to determine the structures of the compounds (FTIR, UV-Vis, ^{1}H and ^{13}C-NMR). Using agarose gel electrophoresis, the DNA cleavage activities of the produced copper complexes were investigated in the absence and presence of hydrogen peroxide. It was also investigated the influence of compound dose on the DNA cleavage process. The results show that in the presence of an oxidant agent, all of the complexes break pBR322 DNA. At the concentration of 10 μM, $[Cu(L^1)_2]$ converted the supercoil DNA into two forms, while $[Cu(L^1)_2]$ formed only the nicked form. The mechanistic analyses show that the active oxidative species for DNA breakage is a species generated by hydrogen peroxide and the copper(II) metal. The compounds also cleaveged pBR322 DNA in the absence of H_2O_2, marginally.

Keywords: Arylhydrazone, copper(II) complex, DNA-cleavage, ROS

1. INTRODUCTION

Hydrazone derivatives' bioinorganic chemistry is fascinating and vital since they have exceptional biological activity. As a result, arylhydrazones and their transition metal complexes have been investigated for their biological features such as antibacterial, antifungal, antioxidant, and anticancer activities [1-9]. Furthermore, hydrazone derivatives are flexible ligands that may be used in a variety of ways to coordinate with transition metal ions found in biological systems. Arylhydrazone complexes have been discovered to serve as enzyme inhibitors, and their pharmacological uses make them valuable [10-13].

Since transition metal complexes play a critical role in anticancer treatment, the interaction between transition metal complexs and DNA has been widely explored in recent years. Cisplatin is a metal-based anticancer medicine that is extensively used in cancer treatment, although it has a number of drawbacks, including high toxicity, side effects, and a low administration dose. As a result, continuing efforts throughout the world are aimed at discovering new metal-based compounds with lower toxicity and unique methods of action. Copper ions are recognized as

---

* Corresponding author: cansutopkaya@mu.edu.tr
[1] Muğla Sutkı Koçman University
ORCID: https://orcid.org/0000-0002-6834-4841

pharmacological agents and play a key function in biological systems. Also, copper is one of the essential components of biologically important metalloproteins. The use of a number of metal complexes to cleave DNA via hydrolytic or oxidative processes has been investigated [3, 14-18]. In the presence of oxidizing or reducing co-reactants, Cu(II) complexes frequently demonstrate DNA cleavage activity. A variety of copper complexes have been demonstrated to be active both *in vitro* and *in vivo* [19]. Copper(II) complexes have been reported to behave as possible anticancer and cancer suppressing agents. The synthesis and characterisation of novel Cu(II) complexes of arylhydrazones with long chain groups was detailed in this work, as well as the DNA cleavage activities of these complexes.

2. METHODOLOGY

2.1. Materials and Instrumentation

Solvents and chemicals used in the laboratory were obtained commercially from Merck and Sigma. Solvents used in synthesis and measurements were freshly distilled and dried according to the appropriate procedure. pBR322 DNA was obtained from Fermentas. On an LECO 932 CHNS analyzer, analysis of elemenets (C, N, and H) was done and On a DV 2000 Perkin Elber ICP-AES, also, copper values were measured using atomic absorption spectroscopy. A Sherwood Scientific MK1 Model Gouy Magnetic Susceptibility Balance was used to assess magnetic susceptibility on powdered materials at room temperature. NMR spectra were recorded on a Bruker 400 MHz spectrometer in DMSO_d$_6$ with TMS as the internal standard. Thermo-Scientific Nicolet iS10-ATR IR spectra were acquired using the ATR (attenuated total reflectance) method. A PG Instruments T80+ UV/Vis Spectrophotometer was used to record the electronic spectra of the ligands and complexes. The thermogravimetric analysis was performed at the Central Laboratory at METU with a Perkin Elmer Pyris 1 TGA thermal analyzer. The XRD and SEM-EDS experiments were carried out at Mugla Sıtkı Koçman University's Research Centre Laboratory. A JEOL SEM 7700F was used for scanning electron microscopy (SEM) and Energy-dispersive X-ray spectroscopy (EDS). Powder X-ray diffraction (XRD) patterns were acquired on a Rigaku-SmartLab diffractometer.

2.2. Synthesis

4-Hydroxy-N'-[(1E)-1-(4-methylphenyl) ethylidene] benzohydrazide [III] and 4-butoxy-N'-[(1E)-1-(4-methylphenyl)ethylidene] benzohydrazide (HL^1) were synthesized as described previously [9, 20].

2.2.1. Synthesis of 4-hexyloxy-N'-[(1E)-1-(4-methylphenyl)ethylidene]benzohydrazide (HL^2)

A mixture of compound III (1 mmol), 1-bromohexane (1 mmol) and dry K_2CO_3 in 30 mL acetone (1 mmol) were stirred for 24 hours under reflux and ice water (150 mL) was added to the mixture. The white precipitate was filtered and washed with water several times and dried. The product crystallized in ethanol.

Yield 69 %; Mp 147 °C; UV (EtOH, nm) 297; IR (KBr) (ν, cm^{-1}) 3283 (NH), 2871-2956 (CH), 1650 (C=O), 1610 (C=N), 1397 (C-N), 1263 (C-O); ^{1}H NMR (CDCl$_3$, ppm) δ 0.92 (t, 3H J=7.03, $^{f}CH3$), 1.33-153 (sex, 4H, $^{e}CH_2{}^{d}CH_2$), 1.68 (p, 2H, J= 7, $^{c}CH_2$), 1.84 (p, 2H, $^{b}CH_2$), 2.30 (s, 3H, H_3C^h-Ar), 2.43 (s, 3H, N=C-$^{g}CH_3$), 3.02 (t, 2H, J= 6,6, $^{a}CH_2$), 6.98 and 7.52 (dd, 4H, *J*=9.0, Ar-H), 7.81-8.13 (m, 4H, Ar-H),8.94 (s, 1H, NH); ^{13}C NMR (DMSO_d$_6$, ppm) 162.0 (C8), 154.8 (C6), 140.1 (C12), 133.8 (C5), 131.1 (C2), 129.3 (C9), 129.1 (C4), 128.7 (C10), 125.2 (C3), 114.0, (C11), 66.3 (C13), 32.4 (C14), 21.2 (C7), 20.3 (C1), 19.8 (C15), 18.2 (17), 19.4 (C18) and 14.1 (C16). Analysis (%Calculated/found) for $C_{22}H_{28}N_2O_2$; C: 74.89/74.56, H: 7.94/8.10, N: 7.94/8.30.

2.2.2. Preparation of copper(II) hydrazone complexes

After adding equivalent amounts of triethylamine to the solutions of HL^1 and HL^2 ligands (2 mmol) in ethanol (20 mL) separately, $(CH_3COO)_2Cu.H_2O$ (1 mmol) dissolved in ethanol (10 mL) was added dropwise. two separate mixtures. The reaction was run under reflux for 3 hours. After standing overnight, the copper(II) complexes separated and were collected by filtering. Water was used to wash the complexes.

For [Cu(L^1)$_2$]: Dark brown complex; yield: 78%; m.p.: 160 ºC. μ_{eff} = 1.86 B.M.; UV (DMF, nm) 385, 299; FT-IR (KBr, cm^{-1}): 2871-2957 (CH), 1608 s (C=N−N=C), 1372 m (C-N), 1244 s and 1169 m (C−O−C). Analysis (%Calculated/found) for $C_{40}H_{46}CuN_4O_4$; C: 67.63/67.84, H: 6.53/6.39, N: 7.89/8.05, Cu: 8.95/9.69.

For [Cu(L^2)$_2$]: Brown complex; yield: 71%; m.p.: 137 ºC. μ_{eff} = 1.65 B.M.; UV (DMF, nm) 382.5, 299.0; FT-IR (KBr, cm^{-1}): 2857-2926 (CH), 1608 s (C=N−N=C), 1373 s (C-N), 1246 s and 1169 m (C−O−C). Analysis (%Calculated/found) for $C_{44}H_{54}CuN_4O_4$; C: 68.95/69.18, H: 7.10/6.99, N: 7.31/7.58, Cu: 8.29/8.15.

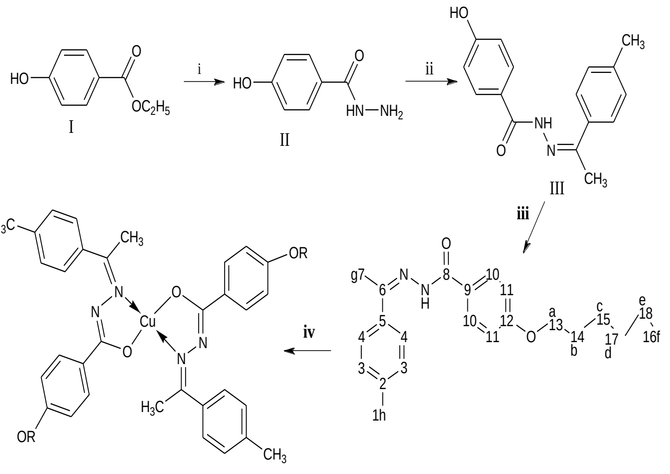

Scheme 1 Synthesis of ligands and complexes

2.3. DNA Cleavage

DNA cleavage tests were monitored by agarose gel electrophoresis. DMF was used to dissolve different amounts of complexes (10-100 M) were combined with 5 µl pBR322 (50 ng/l). After adding 5 µl H_2O_2 (5 mM) to the reaction mixture, it was diluted with tris buffer (100 mM Tris, pH: 8) to a total volume of 30 µl. After incubation at 37 ºC for two hours, samples (20 µl) were loaded onto a 1% agarose gel according to the procedure described above [8- 9]. The gel was operated at 100 V for 3 hours and imaged under UV light. Reactive oxygen scavengers (ROS) (100 µM), such as DMSO, KI, NaN_3, and EDTA, were added alternatively to the reaction mixture to test for the existence of reactive oxygen species formed during strand scission. The samples were processed in the same way as stated previously.

3. RESULT AND DISCUSSION

Compound III and HL^1 were synthesized as described previously [9, 20] while the arylhydrazones derivative HL^2 bearing hexyl chain group was reported for the first time. The reactions of III with 1-bromobutane and 1-bromohexane stoichiometrically in the presence of dry K_2CO_3 in dry acetone gave HL^1 and HL^2. The reactions performed successfully, yielding excellent yields of the relevant arylhydrazones (Scheme 1). They are water insoluble but soluble in typical organic solvents. The structure of the hydrazine ligands were determined using a variety of spectroscopic approaches. The complexes were created by reacting Arylhydrazones with copper(II) acetate at a 2:1 molar ratio. It was unable to extract crystals appropriate for single X-ray diffraction. As a result, analytical and spectroscopic findings for the hydrazone and copper(II) complexes correspond well with the chemical formula provided.

In the solid state, arylhydrazones like the ones generated in this work can be found in keto or enol tautomeric forms (Figure. 1-a). In the infrared spectra of the HL^2, the strong absorption band ν(C = O) suggests that the ligand is in the solid state in the keto form, as in arylhydrazones [9, 21]. Furthermore, in solutions, these arylhydrazones, such as those produced in our study, may leave in an *E* or *Z* configuration (Figure. 1-b). The ^{1}H and ^{13}C-NMR spectra of HL^2 revealed just one signal for each hydrogen and carbon, indicating that arylhydrazones are in the *E* configuration [9, 22-23].

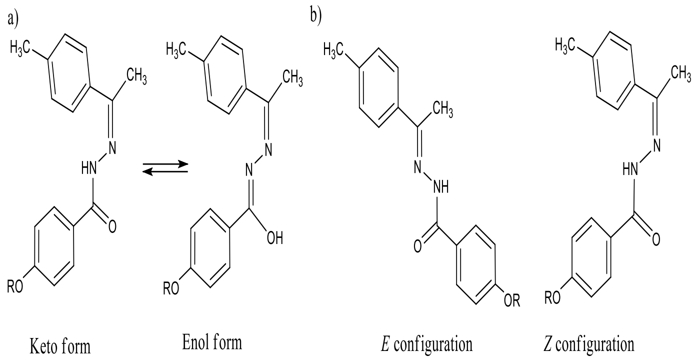

Figure 1 a) Keto-enol arylhydrazone tautomeric forms b) Structural configuration

3.1. NMR spectroscopy

The ^{1}H NMR spectra of the HL^2 was recorded at 25 ^oC in DMSO_d_6. The removal of the OH proton signal verified the development of the novel arylhydrazone (HL^2), present in the starting material of **III** and observed at 10.18 ppm. The NH proton is ascribed to the D_2O exchangeable singlet resonance that emerged at 8.94 ppm for the HL^2 ligand. The ^{1}H NMR spectra of the HL^2 exhibits two singlet peaks at 2.30 and 2.43 ppm due to CH_3 protons. The first is made up of methyl protons (^{h}CH3) attached to the aromatic ring, whereas the second is made up of ^{g}CH3 protons near the imine group. On the other hands, the resonance observed as triplet at 0.92 ppm in the ^{1}H NMR spectra of HL^2 ligand is assigned to aliphatic methyl protons ($^fCH_3$). The spectrum also exhibits signals corresponding to protons of methylene groups in the ligand framework. These findings are consistent with earlier research on comparable substances [9, 21-27].

The structural characterisation of the hydrazone compounds is further supported by the ^{13}C-NMR spectra. The amide carbonyl (C8) and azomethine (C6) groups of the HL^2 arylhydrazones have unique chemical shifts of 162.5 ppm and 154.8 ppm, respectively. The ^{13}C NMR spectrum of the ligand exhibits signals between 140.1 and 114.0 ppm due to the carbon atoms of the aromatic rings. The signals corresponding to the carbon atoms in aliphatic rings are viewed between 14.1 and 68.1 ppm. These evaluated data show good agreement with previously published similar compounds. [9, 21-27]. The results obtained strongly indicate that the title arylhydrazone ligand is formed [28- 29].

3.2. IR spectroscopy

The free ligands' IR spectra and their copper complexes' IR spectra, which are important for identifying the ligands' mode of coordination. The starting material III has a large OH stretching vibration at 3296 cm^{-1} that is gone in the IR spectra of the HL^2, suggested that total condensation has occurred. The novel HL^2 arylhydrazones have an amide NH stretching band at 3283 cm^{-1}. The amide I band emerges at 1650 cm^{-1} for HL^2, whereas the other distinctive band owing to the azomethine group appears at 1610 cm^{-1}. The experimental section lists the additional peaks seen in the IR spectra of the arylhydrazones ligand produced in this study [21, 22, 24-27, 30-33].

C=O, C=N imine, and N-H bound bands were not detected in the IR spectra of both copper(II) complexes. Instead, around 1608 cm^{-1}, a new band arises, perhaps due to the newly created moiety of C=N-N=C. This showed that the azomethine nitrogen and enolic oxygen were coordinated with copper [21, 22, 28-30, 33]. According to the results obtained from the FTIR spectrum, the arylhydrazones, which are the subject of the study, are in coordination with the nitrogen atom of azomethine through the dehydrogenation of the tautomeric enolic form, and they are classified as mono anionic bidentate ligands.

3.3. X-ray diffraction analysis

Powder X-ray diffraction recorded at $2\theta = 0–70^{\circ}$ was used to get more information about the structure of the copper(II) complexes. The copper(II) complexes exhibit well-defined crystalline structures, as demonstrated in Figure 2's X-ray diffraction pattern. But very less number of peaks were observed in the case of $[Cu(L^1)_2]$ complexes. The sharp peaks are indicative of complex $[Cu(L^2)_2]$ having higher crystallinity than complex $[Cu(L^1)_2]$.

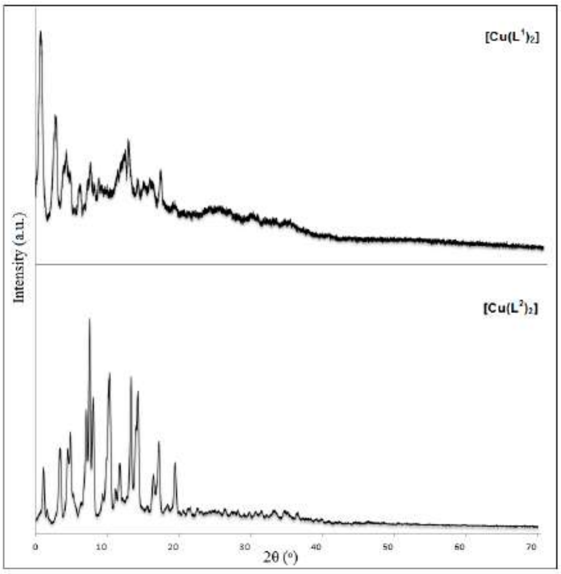

Figure 2 Copper(II) complexes X-ray diffraction patterns.

3.4. Analyses of SEM and EDS

SEM images taken to reveal the surface morphology of the ligand and its complex were obtained at 15 kV acceleration voltage and x500 magnification (Figure 3). Figure 4 shows the SEM image of the HL^2 ligand with a pyramidal structure and rod-shaped blocks vertically and horizontally, while the copper(II) complex shows non-uniformly sharp crystalline species (Figure 3). The HL^2 and its Cu(II) complex have average particle diameters of ~300 μm and 100 μm, respectively. The morphological structure of the hydrazone ligand following association with the copper ion, as observed in SEM pictures, has undergone a significant shift.

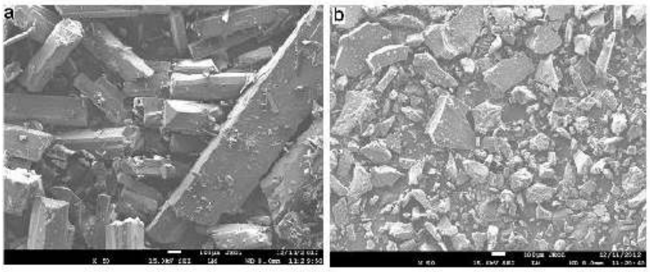

Figure 3 Comparison of SEM images of complex and ligand (a) HL^2; (b) $[Cu(L^2)_2]$

The composition of the $[Cu(L^2)_2]$ complex was defined by Energy dispersive spectroscopy (EDS) analysis (Figure 4). The EDS corroborates the presence of copper in the Arylhydrazones-copper derivative which confirms the formation of the copper complex. The C, N, O and Cu peaks were only observed in the Figure 4. indicating that the $[Cu(L^2)_2]$ complex powder has high purity.

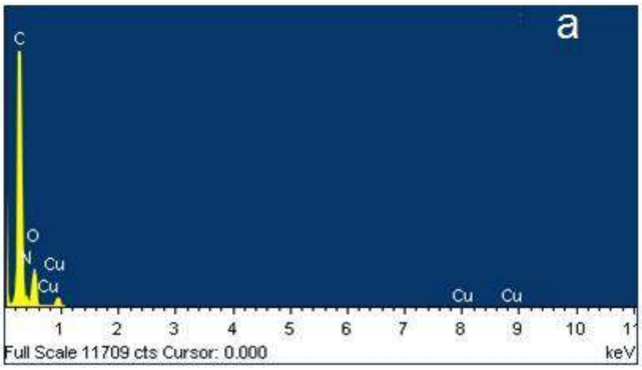

Figure 4 Energy dispersive spectrometer of the $[Cu(L^2)_2]$

3.5. Thermal analyses

Figure 5 shows the copper complexes' thermal gravimetric analysis (TGA) curves. Thermal decomposition of copper complexes happened in one step, according to TGA curves, and they are stable below 280 °C. When the temperature increases to 280 °C, both complexes decompose. The deterioration observed in the curves of the complexes as the temperature rises to the range of 280-530 °C corresponds to the detachment of arylhydrazone copper(II) complexes from the organic structure and the formation of a copper deposit as a residue.

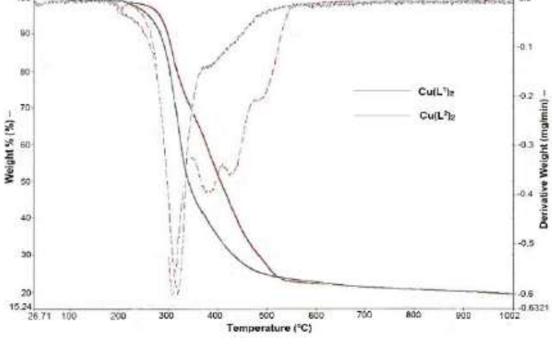

Figure 5 TGA curves of Cu(II) complexes.

3.6. Electronic absorption spectra

Two absorbance peaks corresponding to n→π* electronic transitions were observed for HL^1 and HL^2 arylhydrazones at 298 nm and 297 nm, respectively. In DMF solution, the complexes' electronic absorption spectra were obtained. When the absorption spectrums of arylhydrazone ligands and their copper(II) complexes were compared, it was discovered the metal free ligands' maximum bands had a red shift, which might be due to the arylhydrazone ligands' enol form as well as coordination of the copper(II) ion. Moreover, there is a band in the visible range of the electronic spectrums of copper complexes, 385 nm for $[Cu(L^1)_2]$ and 383 nm for $[Cu(L^2)_2]$, which can be ascribed to the LMCT transition. Interestingly, even in concentrated solution, the predicted weak d-d transition in the visible range for the one-electron paramagnetic (μ_{eff} = 1.86 and 1.65 BM) complexes cannot be identified. It might be lost in the charge transfer transition's low-energy tail [21, 22, 34- 35].

3.7. Nuclease activity

The DNA cleavage studies of the compounds were determined using agarose gel electrophoresis under physiological circumstances with/without H_2O_2 as an oxidant agent. The capacity of the complex to convert the supercoiled form (Form I) of DNA to its open circular form (Form II) and linear form (Form III) was used to assess its DNA cleavage activities [36-38].

The complex-mediated cleavage reactions were carried out at 37 °C with various concentrations of complex (10-100 μM). In the presence of hydrogen peroxide, the copper complexes of the HL^1 and HL^2 ligands showed efficient DNA cleavage activity, transforming the plasmid supercoiled DNA into its cleavage forms (Form II and III), as illustrated in Figure 6. ($[Cu(L^1)_2]$ lane 1-5 and $[Cu(L^1)_2]$ lane 13-17.) It is apparent that when the concentration of all complexes rises, the quantity of supercoiled DNA (Form I) decreases.

The cleavage reactions meditated by the complexes were performed under different concentration of complex (10-100 μM) at 37 ºC. Figure 6 represents the gel electrophoretic separations of pBR322 DNA with increasing concentrations of complexes (10-100 μM) at 37 ºC in their optimum incubation times in the presence and absence of H_2O_2. The copper(II) complexes of the HL^1 and HL^2 ligands exhibit effective DNA cleavage activity converting the plasmid supercoiled DNA into its cleavage forms (Form II and III) in the presence of hydrogen peroxide as shown in Figure 6. (Lane 1-5 for $[Cu(L^1)_2]$ and lane 13-17 for $[Cu(L^1)_2]$). It is apparent that when the concentration of all complexes rises, the quantity of supercoiled DNA (Form I) decreases. Interestingly, the complex $[Cu(L^2)_2]$ can only formed of nickeded DNA, while the copper complex $[Cu(L^1)_2]$ can simultaneously separate supercoiled DNA into Form (II) and Form (III).

At a concentration of 10 μM, lane 1, the plasmid DNA was slightly cleaved by the complex $[Cu(L^1)_2]$ and all three forms of DNA are observed. The percentage of the nicked DNA molecules is higher than those of form I and form III. On the other hand, when the concentration of the complex was greater than 10 μM, the supercoiled DNA is disappeared completely and form II and form III are present for complex $[Cu(L^1)_2]$, lane 2-4, as a result of double-strand breaks over the plasmid molecule. Finally, at the concentration of 100 μM (lane 5), the supercoiled DNA degrades completely into small pieces as no bands is observed.

In the presence of $[Cu(L^2)_2]$ at 10 μM, it scarcely catalyzed the cleavage of plasmid DNA. However, when the concentration of the complex was increased to 25 μM, the cleavage of DNA was clearly observed. It was found that with the increase of the complex concentration, the density of supercoil DNA on the gel decreased, whereas the density of the nicked DNA increased significantly (lanes 14- 16), indicating that the DNA was fragmented by the complex by a single-stranded cleavage. Finally when the complex concentration is at 100 μM, lane 17, the supercoiled DNA is completely cleaved to nicked form.

Both copper complexes exhibit mild nuclease activity as an oxidative agent even under hydrolytic conditions. However, it can be concluded from the data in Figure 6. that $[Cu(L^1)_2]$ is much more effective artificial nuclease than that of $[Cu(L^2)_2]$ in the absence of an oxidative agent. It was observed that the percentage of nicked DNA increased, with increasing concentration of $[Cu\ (L^1)_2]$. On the other hand, in the case of the DNA cleavage by $[Cu(L^2)_2]$, a small amount of supercoiled DNA is converted to open circular DNA only when the concentration of the complex is up to 75 μM (Lane 21-22).

In the absence of an oxidative material in the medium, DNA cleavage is predicted to occur hydrolytically. In addition, in DNA cleavage mediated by certain copper complexes, the shearing activity has been found to be oxidative, even without the use of a reducing agent. The oxidative DNA cleavage in this scenario might be ligand-based, presumably due to the presence of a non-diffusible organic radical mechanism that induces oxidative DNA cleavage. An alternative approach is to produce dihydrogen peroxide when hydrogen is removed from the deoxyribose sugar in the presence of dioxygen. In a Fenton-type reaction, dihydrogen peroxide reacts with Cu(II) to form reactive oxygen species, making DNA cleavage oxidative or catalytic.

The reason why the $[Cu(L^1)_2]$ complex shows higher DNA cleavage activity than the $[Cu(L^2)_2]$ complex may be the inability of the radicals to take effect as a result of the steric effect of the long aliphatic chain of the ligand forming the $[Cu(L^2)_2]$ complex [18, 39- 40].

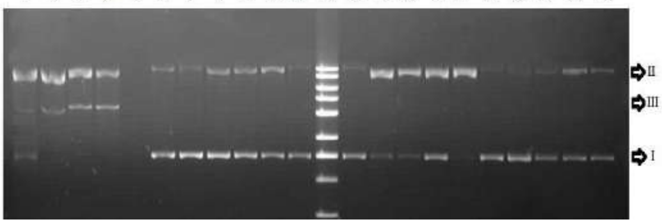

Figure 6 pBR322 plasmid DNA electrophoresis on an agarose gel with various amounts of copper(II) complexes. L1: $Cu(L^1)_2$ (10 μM) + DNA + H_2O_2, L2: $Cu(L^1)_2$ (25 μM) + DNA + H_2O_2, L3: $Cu(L^1)_2$ (50 μM) + DNA + H_2O_2, L4: $Cu(L^1)_2$ (75 μM) + DNA + H_2O_2, L5: $Cu(L^1)_2$ (100 μM) + DNA + H_2O_2, L6: $Cu(L^1)_2$ (10 μM) + DNA, L7: $Cu(L^1)_2$ (25 μM) + DNA, L8: $Cu(L^1)_2$ (50 μM) + DNA, L9: $Cu(L^1)_2$ (75 μM) + DNA, L10: $Cu(L^1)_2$ (100 μM) + DNA, L11: DNA control, L12: 1 kb marker, L13: $Cu(L^2)_2$ (10 μM) + DNA + H_2O_2, L14: $Cu(L^2)_2$ (25 μM) + DNA + H_2O_2, L15: $Cu(L^2)_2$ (50 μM) + DNA + H_2O_2, L16: $Cu(L^2)_2$ (75 μM) + DNA + H_2O_2, L17: $Cu(L^2)_2$ (100 μM) + DNA + H_2O_2, L18: $Cu(L^2)_2$ (10 μM) + DNA, L19: $Cu(L^2)_2$ (25 μM) + DNA, L20: $Cu(L^2)_2$ (50 μM) + DNA, L21: $Cu(L^2)_2$ (75 μM) + DNA, L22: $Cu(L^2)_2$ (100 μM) + DNA.$^{\text{*Lane:L}}$

3.8. Mechanistic pathway of DNA cleavage

Mechanistic pathway of pBR322 cleavage induced by the complex using different scavenging agents was investigated and revealed. To investigate the involvement of the metal center in cleavage, we utilized DMSO as a hydroxyl radical scavenger, NaN_3 as a singlet oxygen quencher, KI as a superoxide scavenger, catalase as a hydrogen peroxide scavenger, and EDTA as a chelating agent [39- 41]. (Figure 7). The potential molecular mechanism of the cleavage of pBR322 plasmid DNA produced by complexes $[Cu(L^1)_2]$ and $[Cu(L^2)_2]$ has also been identified.

There was no suppression of DNA cleavage for either complex when NaN_3 was added (lanes 3 and 7). This shows that the solitary oxygen radical is not the active oxidative species that causes the complexes to cleave DNA. In addition to presence of hydrogen peroxide scavenger and hydroxyl radical scavenger block the DNA strand breakage for the $[Cu(L^1)_2]$ complex (lanes 5 and 6), suggesting that these species are involved in the DNA cleavage reactions while DMSO and KI are ineffective in the cleavage reaction for the $[Cu(L^2)_2]$ complex (lanes 9 and 10). With the addition of EDTA, which has the ability to form stable complexes by showing a chelating effect with metals, a noticeable decrease was observed in the DNA cleavage activities of complex compounds. This reveals that Cu(II) ions in the structure of the complex contribute to the cleavage activity of the complex.

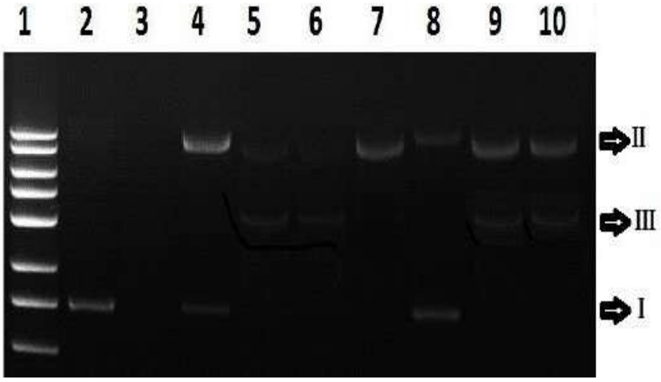

Figure 7 pBR322 plasmid DNA electrophoresis on an agarose gel after treatment with copper(II) complexes (100 µM) and possible inhibitors. L1: 1 kb marker, L2: DNA control, L3: $Cu(L^1)_2$ + DNA + H_2O_2 + NaN_3 , L4: $Cu(L^1)_2$ + DNA + H_2O_2 + EDTA, L5: $Cu(L^1)_2$ + DNA + H_2O_2+ KI, L6: $Cu(L^1)_2$ + DNA + H_2O_2 + DMSO, L7: $Cu(L^2)_2$ + DNA + H_2O_2 + NaN_3, L8: $Cu(L^2)_2$ + DNA + H_2O_2 + EDTA, L9: $Cu(L^2)_2$ + DNA + H_2O + KI, L10: $Cu(L^2)_2$ + DNA + H_2O_2 + DMSO. *Lane:L

4. CONCLUSION

Using distinct spectroscopic approaches, two novel copper(II) complexes containing arylhydrazones have been produced and studied. The arylhydrazones operate as monobasic bidentate ligands containing azomethine nitrogen and enolic oxygen, according to the elemental analyses, stoichiometric, and spectroscopic investigations detailed above. The copper(II) complexes' DNA cleavage capabilities in the presence of H_2O_2 indicated that the $[Cu(L^1)_2]$ complex cleaves circular supercoiled DNA into nicked DNA and linear DNA under aerobic conditions, whereas the $[Cu(L^2)_2]$ complex breaks circular supercoiled DNA into solely nicked DNA. In the absence of H_2O_2, however, they demonstrated decreased nuclease activity. In the absence of a reducing agent, both copper complexes have some nuclease activity. For both copper(II) complexes, increasing the concentration of the complexes resulted in more significant DNA scission. It was also shown that at concentrations of up to 100 µM, $[Cu(L^1)_2]$ fully destroys circular supercoiled DNA. Because it displays substantial DNA cleavage activity even in the absence of hydrogen peroxide, $[Cu(L^1)_2]$ has superior nuclease activity than $[Cu(L^2)_2]$. In the presence of reducing agents, both complexes are capable of performing effective oxidative cleavage of DNA, and copper(II) ion plays a crucial part in the cleavage process.

Funding
The author received no financial support for this study.

Conflict of interest
There is no conflict of interest to be declared.

The Declaration of Ethics Committee Approval
This study does not require ethics committee approval or any special permission.

The Declaration of Research and Publication Ethics
The author of the paper declares that he complies with the scientific, ethical and quotation rules of SAUJS in all processes of the article and that he does not make any falsification on the data collected. In addition, he declares that Sakarya University Journal of Science and its editorial board have no responsibility for any ethical violations that may be encountered, and that this study has not been evaluated in any academic publication environment other than Sakarya University Journal of Science

REFERENCES

[1] A.S. El-Tabl, F. A. El-Saied, W. Plass, A. N. Al- Hakimi, “Synthesis, spectroscopic characterization and biological activity of the metal complexes of the Schiff base derived from phenylaminoacetohydrazide and dibenzoylmethane,” Spectrochimica Acta Part A: Molecular and Biomolecular Spectroscopy, vol. 71, no. 1, pp. 90-99, 2008.

[2] Y. Li, Z. Y. Yang, M. F. Wang, “Synthesis, characterization, DNA binding properties, fluorescence studies and antioxidant activity of transition metal complexes with hesperetin-2-hydroxy benzoyl hydrazone,” Journal of Fluorescence, vol. 20, no. 4, pp. 891-905, 2010.

[3] M. A. El-Bindary, A. A. El-Bindary, “Synthesis, characterization, DNA binding, and biological action of dimedone arylhydrazone chelates,” Applied Organometallic Chemistry, vol. 36(4), pp. e6576, 2022.

[4] M. C. Rodrìguez-Arguelles, M. B. Ferrari, F. Bisceglie, C. Plizzi, G. Pelosi, S. Pinelli, M. Sassi, “Synthesis, characterization and biological activity of Ni, Cu and Zn complexes of isatin hydrazones,” Journal of Inorganic Biochemistry, vol. 98, no. 2, pp. 313-320, 2004.

[5] P. Yogeeswari, N. Menon, A. Semwal, M. Arjun, D. Sriram, “Discovery of molecules for the treatment of neuropathic pain: synthesis, antiallodynic and antihyperalgesic activities of 5-(4-nitrophenyl)furoic-2-acid hydrazones,” European Journal of Medicinal Chemistry., vol. 46, no. 7, pp. 2964-2971, 2011.

[6] M. S. S. Adam, O. M. El-Hady, M. M. Makhlouf, A. Bayazeed, N. M. El-Metwaly, A. D. M. Mohamad, “Effect of oxy-vanadium (IV) and oxy-zirconium (IV) ions in O, N-bidentate arylhydrazone complexes on their catalytic and biological potentials that supported via computerized usages,” Journal Of The Taiwan Institute Of Chemical Engineers., vol. 132, pp. 104168, 2022.

[7] M. C. Rodruguez-Arguelles, S. M. Vazques, P. T. Touceda, J. S. Matalobos, A. M .G. Deibe, M. B. Ferrari, G. Pelosi, C. Pelizzi, F. Zanil, “Complexes of 2-thio phene carbonyl and isonicotinoyl hydrazones of 3-(N-methyl)isatin. A study of their antimicrobial activity,” Journal of Inorganic Biochemistry, vol. 101, no. 1, pp. 138-147, 2007.

[8] C. Gokce, R. Gup, “Copper(II) complexes of acylhydrazones: synthesis, characterization and DNA interaction,” Applied Organometallic Chemistry, vol. 27, no. 5, pp. 263-268, 2013.

[9] C. Gokce, R. Gup, “Synthesis, characterization and DNA interaction of new copper(II) complexes of Schiff base-Arylhydrazones bearing naphthalene ring,” Journal of Photochemistry and Photobioloy B: Biology, vol. 122, pp. 15-23, 2013.

[10] J. R. Merchant, D. S. Clothia, “Antituberculous Schiff bases” Journal of Medicinal Chemistry, vol. 13, no. 2, pp. 335-336, 1970.

[11] J. O. Adeyemi, D. C. Onwudiwe, “The mechanisms of action involving dithiocarbamate complexes in biological systems,” Inorganica Chimica Acta, vol. 511, pp. 119809, 2020.

[12] K. Kiranmai, Y. Prashanthi, N .J. P. Subhashini, “Synthesis, characterization and biological activity of metal complexes of 3-amino-5-methyl isoxazole Schiff bases,” Journal of Chemical and Pharmaceutical Research, vol. 2, no.1, pp. 375-384, 2010.

[13] I. Kostova, L. Saso, “Advances in research of Schiff-base metal complexes as potent antioxidants,” Current Medicinal Chemistry, vol. 20(36), pp. 4609-4632, 2013.

[14] R. K. Crouch, T. W. Kensler, L. W. Oberley, J.R.J. Sorenson, “Possible medicinal uses of copper complexes. In: Biological and Inorganic Copper Chemistry,” Guilderland, New York, Adenine Press, 1986.

[15] J. R. Sorenson, “Bis(3,5-diisopropylsalicylato)copper(II), a potent radioprotectant with superoxide dismutase mimetic activity,” Journal of Medicinal Chemistry, vol. 27, no. 12, pp. 1747-1749,1984.

X. B. Yang, J. Feng, J. Zhang, Z. W. Zhang, manufactured products are ejected

[16] DNA binding and cleavage activities of the copper (II) complexes of estrogen-macrocyclic polyamine conjugates.," Bioorganic & Medicinal Chemistry, vol. 16, no.7, pp. 3871-3877,2008.

[17] S. Apelgot, J. Coppey, A. Fromentin, E. Guille, M.F. Poupon, A. Roussel , "Altered distribution of copper (^{64}Cu) in tumor-bearing mice and rats," Anticancer Research, vol. 6, no. 2, pp. 159-164,1986.

[18] P. P. Silva, W. Guerra, J. N. Silveira, A. M. C. Ferreira, T. Bortolotto, F. L. Fischer, H. Terenzi, A. Neves and E. C. Pereira-Maia, "Two new ternary complexes of copper(II) with tetracycline or doxycycline and 1,10-phenanthroline and their potential as antitumoral: cytotoxicity and DNA cleavage," Inorganic Chemistry., vol. 50, no.14, pp. 6414-6424, 2011.

[19] B. C. Bales, T. Kodama, Y. N. Weledji, M. Pitic, B. Mcunier, M. M. Greenberg, "Mechanistic studies on DNA damage by minor groove binding copper–phenanthroline conjugates," Nucleic Acids Research, vol. 33, no.16, pp. 5371-5379, 2005.

[20] N. Dilek, B. Güneş, R. Gup, "4-Butoxy-N'-[1-(4-methylphenyl)ethyl-idene]benzohydrazide," Acta Crystallographica Section E, vol. 68, no.9, pp.2763-2763, 2012.

[21] R. Gup, B. Kırkan, "Synthesis and spectroscopic studies of mixed-ligand and polymeric dinuclear transition metal complexes with bis-acylhydrazone tetradentate ligands and 1,10-phenanthroline," Spectrochimica Acta Part A: Molecular and Biomolecular Spectroscopy, vol, 64, no. 3, pp. 809-815, 2006.

[22] A. A. R. U. Despaigne, J. G. Da Silva, A. C. M. Do Carmo, O. E. Piro, E. E. Castellano, H. Beraldo, "Copper(II) and zinc(II) complexes with 2-benzoylpyridine–methyl hydrazone," Journal of Molecular Structure, vol. 920, no,1-3, pp. 97-102, 2009.

[23] A. P. Rebolledo, G. De Lima, L. N. Gambi, N. I. Speziali, D. F. Maia, C. B. Pinheiro, J. D. Ardisson, M. E. Cortes, H. Beraldo, "Tin(IV) complexes of 2-benzoylpyridine N(4)-phenylthiosemicarbazone: spectral characterization, structural studies and antifungal activity," Applied Organometallic Chemistry, vol. 17, no.12,pp. 945-951,2003.

[24] S. Kulaksızoglu, C. Gokce, R. Gup," Synthesis and characterization of bis(azine) ligands and metal complexes: DNA-interaction and extraction properties for metals and dichromate anions," Turkish Journal of Chemistry, vol. 36, no.5, pp. 717-733, 2012.

[25] S. Naskar, S. Biswas, D. Mishra, B. Adhikary, L. R. Falvello, T. Soler, C. H. Schwalbe, S. K. Chattopadhyay, "Studies on the relative stabilities of Mn(II) and Mn(III) in complexes with N_4O_2 donor environments: crystal structures of [Mn(pybzhz)$_2$] and [Mn(Ophsal)(imzH)$_2$]ClO_4 (pybzhz=N-(benzoyl)-N′-(picolinylidene) hydrazine, Ophsal= N, N′-o-phenylenebis(salicylideneimine), imzH= imidazole)," Inorganica Chimica Acta, vol. 357, no.14,pp. 4257-4264, 2004.

[26] R. Dinda, P. Sengupta, S. Ghash, T. C. M. Mak, "Valence delocalization in a mixed-oxidation divanadium(IV, V) complex electrogenerated from its structurally characterized divanadium(V) analogue with a tridentate (ONO) ligand," Inorganic Chemistry, vol. 41, no. 6, pp. 1684-1688, 2002.

[27] A. Sreekanth, C. R. Nayar, M. R. P. Kurup, “Cobalt(III) complexes of 2-hydroxyacetophenone N(4) phenyl semicarbazone containing heterocyclic coligands: syntheses, structure, and spectral studies,” *Polyhedron*, vol. 23, no.1, pp. 41-47, 2004.

[28] R. Dinda, P. Sengupta, S. Ghash, W. S. Sheldrick, “Synthesis, structure, and reactivity of a new mononuclear molybdenum (VI) complex resembling the active center of molybdenum oxotransferases,” European Journal of Inorganic Chemistry, vol. 2003, no. 2, pp. 363-369, 2003.

[29] R. Gup, “A new unsymmetrical vic-dioxime bearing salicylaldehyde 4-aminobenzoylhydrazone and its homo-and heterotrinuclear complexes with copper (II) and nickel (II) ions,” Russian Journal of Coordination Chemistry, vol. 32, no. 2, pp. 99-108, 2006.

[30] L .L. Koh, O. L. Kon, Y. C. Loh, R. C. Ranford, A. L. C. Tan, Y. Y. Tjan, “Complexes of salicylaldehyde acylhydrazones: cytotoxicity, QSAR and crystal structure of the sterically hindered t-butyl dimer,” Journal of Inorganic Biochemistry, vol. 72, no. 3-4, pp. 155-162,1998.

[31] R. Gup, E. Giziroğlu, “Metal complexes and solvent extraction properties of isonitrosoacetophenone 2-aminobenzoylhydrazone,” Spectrochimica Acta Part A: Molecular and Biomolecular Spectroscopy, vol. 65, no. (3-4), pp. 719-726, 2006.

[32] O. Usluer, R. Gup, “Synthesis and characterization of copper(ii) complexes containing isonitrosoacetophenone 4-aminobenzoylhydrazone,” Polish Journal of Chemistry, vol. 81, no. 7, pp. 1257-1265, 2007.

[33] F. Karipcin, B. Dede, S. Percin-Ozkorucuklu, E. Kabalcilar, “Mn(II), Co(II) and Ni(II) complexes of 4-(2-thiazolylazo)resorcinol: synthesis, characterization, catalase-like activity, thermal and electrochemical behavior,” Dyes and Pigments, vol. 84, no. 1, pp.14-18, 2010.

[34] S. Gama, F. Mendes, F. Marques, “Copper(II) complexes with tridentate pyrazole-based ligands: synthesis, characterization, DNA cleavage activity and cytotoxicity,” Journal of Inorganic Biochemistry, vol. 105, no. 5, pp. 637-644, 2011.

[35] D. Lahiri, S. Roy, S. Saha, R. Majumdar, R. R. Dighe, A. R. Chakravarty, “Anaerobic DNA cleavage activity in red light and photocytotoxicity of (pyridine-2-thiol) cobalt (III) complexes of phenanthroline bases,” Dalton Transactions, vol.39, no.7, pp.1807-1816, 2010.

[36] B. Dede, I. Özmen, F. Karipcin, M. Cengiz, “Homo- and heteropolynuclear copper(II) complexes containing a new diimine–dioxime ligand and 1,10-phenanthroline: synthesis, characterization, solvent-extraction studies, catalase-like functions and DNA cleavage abilities,” Applied Organometalic. Chemistry, vol. 23, no. 12, pp. 512-519, 2009.

[37] P. U. Maheswari, S. Barend, S. Özalp-Yaman, P. De Hoog, H. Casellas, A. J. Teat, C. Massera, M. Lutz, A. L. Spek, J. P. Van Wezel, P. Gamez, J. Reedijk, “Unique ligand based oxidative cleavage by zinc(II) complexes of hpyramol and hpyrimol” European Journal of Chemistry, vol. 13, no.18, pp. 5213-5222, 2007.

[38] X. Dong, X. Wan, M. Lin, H. Sun, X. Yang, Z. Guo, “Promotive effect of the platinum moiety on the DNA cleavage activity of copper-based artificial nucleases,” Inorganic Chemistry, vol. 49, no.5, pp. 2541-2549, 2010.

[39] L. Z. Li, C. Zhao, T. Xu, H. Wei Ji, Y. Hong Yu, G. Qiang Guo, H. Chao, “Synthesis, crystal structure and nuclease activity of a Schiff base copper(II) complex,” Journal of Inorganic Biochemistry, vol. 9 no.5, pp.1076-1082, 2005.

[40] E. Lamour, S. Routier, J. L. Bernier, J. P. Catteau, C. Bailly, H. Vezin, “Oxidation of Cu-II to Cu-III, free radical production, and DNA cleavage by hydroxy-salen-copper complexes. Isomeric effects studied by ESR and electrochemistry,” Journal of the American Chemical Society, 121(9), 1862-1869, 1999.

[41] C. Gökçe, R. Gup, “Synthesis, characterization and DNA interaction of the transition metal complexes with 2-formyl furan-derived aroylhydrazones,” Main Group Chemistry, vol. 12, no.1, pp. 25-38, 2013.

SAKARYA ÜNİVERSİTESİ
FEN BİLİMLERİ ENSTİTÜSÜ
DERGİSİ

Sakarya University Journal of Science
SAUJS

ISSN 1301-4048 | e-ISSN 2147-835X | Period Bimonthly | Founded: 1997 | Publisher Sakarya University |
http://www.saujs.sakarya.edu.tr/

Title: Determination of Resmethrin in Corn Silk Matrix by Gas Chromatography-Flame Ionization Detector (GC-FID)

Authors: Hakan SERBEST

Recieved: 2022-06-07 00:00:00

Accepted: 2022-09-02 00:00:00

Article Type: Research Article

Volume: 25
Issue: 5
Month: October
Year: 2022
Pages: 1022-1028

How to cite
Hakan SERBEST; (2022), Determination of Resmethrin in Corn Silk Matrix by Gas Chromatography-Flame Ionization Detector (GC-FID). Sakarya University Journal of Science, 25(5), 1022-1028, DOI: 10.16984/saufenbilder.1127368
Access link
http://www.saujs.sakarya.edu.tr/en/pub/issue/73051/1127368

Sakarya University Journal of Science 25(5), 1022-1028, 2022

Determination of Resmethrin in Corn Silk Matrix by Gas Chromatography-Flame Ionization Detector (GC-FID)

Hakan SERBEST*[1]

Abstract

The use of pesticides provides benefits such as growing food products necessary for life, sustainability of production efficiency and prevention of diseases caused by pests. However, these benefits can turn into negative effects for humans and other living organisms with the use of pesticides in inappropriate doses and application methods. In this study, it was aimed to determine resmethrin, which belongs to the insecticide class, by gas chromatography-flame ionization detector (GC-FID) method. Hence, a suitable temperature program was utilized to determine resmethrin at a certain retention time. Limit of detection (LOD) and limit of quantification (LOQ) values were recorded as 0.02 and 0.08 mg/L under the proposed conditions, respectively. After corn silk sample was extracted using acetonitrile, analytical measurements were carried out to investigate the presence of resmethrin. There was no analytical signal detected that belonged to resmethrin in the analyzed sample. Recovery experiments were performed using external calibration method with spiked samples at three different concentrations and good percent recovery results were obtained between 93 and 97%.

Keywords: Resmethrin, insecticide, pesticide, GC-FID, corn silk

1. INTRODUCTION

The use of pesticides is quite common in agriculture to preserve crop quality and yield, and in public health to prevent various diseases. Consumption of chemical pesticides helps to increase the yield at harvest time by protecting the crops, but it causes negative effects on species other than target organisms [1, 2]. The production rate of pesticides increased considerably in the 1940’s as dichlorodiphenyltrichloroethane (DDT) showed good results against insects that cause diseases such as typhus and malaria [3]. Over time, after understanding the toxic effects of DDT on living organisms, synthetic pyrethroids compounds were developed by British and Japanese chemists in the 1970s to meet the demand for a pesticide with better environmental properties and safer than DDT [1, 4]. Pesticides can be grouped into different classes based on the chemical type, target organisms, mechanism of action and type of application. According to their chemical types, they are categorized into four main groups

---

* Corresponding author: hakan.serbest@istun.edu.tr
[1] Istanbul Health and Technology University
ORCID: https://orcid.org/0000-0003-2303-0408

known as organochlorine pesticides, carbamate pesticides, pyrethroid pesticides and organophosphate pesticides [5-7]. Among the pesticides used for a variety of purposes, such as the protection of crops, fields, and trees, and the control of mosquitoes and other pests, pyrethroids insecticides are synthetic analogs of pyrethrin. The use of pyrethroids has gradually increased over the years with their prominent features such as low toxicity, resistance to environmental conditions and high insecticide activity [8]. Resmethrin, one of the first members of the synthetic pyrethroids, was synthesized as a mixture of four stereoisomers [9]. Resmethrin, which belongs to the Type 1 pyrethroid insecticide group for the control of insects, is generally used against mosquitoes and certain arthropods and whiteflies in agricultural activities [9, 10]. In addition, resmethrin plays an active role as a preventative against insects, especially in products such as flour, wheat, corn and cornmeal [11]. Like all pyrethroids, resmethrin causes changes in the electrical properties of insect neurosecretory neurons. When the insect is exposed to a pyrethroid member, neurons are rapidly and continuously stimulated and trembling begins, then this event ends in paralysis [12, 13]. According to USEPA, resmethrin is currently registered for use in vector control and public health studies to control pests such as mosquitoes, houseflies, and midges [14]. Considering the health effects of Resmethrin, it has been reported that it can cause toxic effects by inhalation, ingestion, and dermal contact [9]. In terms of aquatic organisms, resmethrin and its metabolites may pose an acute risk, as well as adversely affecting the reproductive and developmental activities of living things. Although terrestrial animals have low exposure rate to resmethrin, the risk is increased for non-target species such as honeybees [14]. Therefore, the qualitative/quantitative determination of resmethrin and other pesticide residues in food and environmental samples has a critical importance in preventing their effects on humans and other living organisms.

Chromatography is a frequently used technique for the separation and determination of pesticides and other pollutants and is classified into liquid chromatography (LC) [15] and gas chromatography (GC) [16] according to the physical properties of the mobile phase used [17]. GC which is used as an effective separation of volatile organic compounds, is combined with different detectors such as thermal conductivity detector (TCD) [18], mass spectrometry (MS) [19], electron capture detector (ECD) [20], flame photometric detector (PID) [21], nitrogen phosphorus detector (NPD) [22] and flame ionization detector (FID) [18] for the determination of compounds with high accuracy and precision. A hydrogen flow mixed with carrier gas is used in the FID system. After the mixture is ignited, ionization occurs by burning the analytes. The ions formed are converted into current by the voltage between the flame jet and collector electrodes, and the signal is amplified and detected [23].

In this study, it was aimed to determine resmethrin by GC-FID in cornsilk matrix with high accuracy and precision.

2. MATERIALS AND METHODS

2.1. Instrumentation

Separation and qualitative/quantitative determination of resmethrin was performed using an Agilent 6890N model gas chromatography (GC) system and a flame ionizer detector (FID). A Domnick Hunter model 40H hydrogen generator was employed to produce hydrogen gas, which was delivered to the system at a flow rate of 35 mL/min. Before detection of resmethrin, it was eluted through an HP-5MS column with a length of 30 m, a film thickness of 0.25 μm, and an inner diameter of 250 μm. The total run time was 5.7 min and it was achieved by employing the following oven temperature ramp program: 45 °C/min from 100 °C (initial temperature) to 200 °C and 55 °C/min to 280 °C (2.0 min hold time). The temperature of inlet port was set at 250 °C and 1.0 μL of solutions were injected in splitless mode. Nitrogen was used as carrier gas at a flow rate of 2.2 mL/min. The retention time of resmethrin was determined by injecting different concentrations of standards into the GC-FID system. An ultrasonic bath (Alex Machine) and a vortex (ISOLAB) were used to mix the corn silk sample with acetonitrile. A centrifuge (Hettich) was used for easy separation of the liquid phase.

2.2. Reagents

High purity standard of resmethrin (10453-86-8) was supplied from Dr. Erhrenstorfer (Augsburg – Germany) and dissolved in acetonitrile (Merck – Germany) to prepare a 1000 mg/L stock solution. Standard solutions of resmethrin at different concentrations were prepared by gravimetrically diluting the stock solution in a vial with acetonitrile. Before and after injection, analytical grade ethanol (Merck – Germany) was used to wash the 10 μL GC syringe.

2.3. Samples

Corn silk sample was purchased from an herbal market in İstanbul, Türkiye. Firstly, the corn silks were cut into very small pieces with a sterile cutter to increase surface area. Then, 0.50 g of the cut sample was weighed on a precision scale into a sample tube and acetonitrile was added so that the final weight was 5.0 g. Effective mixing was achieved by successively applying vortex mixing and sonication for 60 seconds. Then, the liquid phase was easily removed from the corn silk by centrifugation and filtration through a 0.45 μm syringe filter. Spiked samples were prepared from extracted corn silk matrix at 8.1, 16.2 and 40.2 mg/L concentrations.

3. RESULTS AND DISCUSSION

All standard solutions and samples were measured for triplicate to determine the precision and repeatability of the method. The average of peak areas of each measurement was used to get calibration plot. Percent recoveries of resmethrin were calculated from spiked samples to determine accuracy of the method.

3.1. Qualitative / quantitative determination of resmethrin

The operating conditions and temperature ramp program mentioned in Section 2.1 were used, and a total run time of 5.7 minutes was obtained for the elution of resmethrin. Measurements were performed for the calibration standard solutions prepared in the linear dynamic range of 0.10 – 163 mg/L. After the resulting peaks were integrated, the peak area values were used to develop a calibration plot that produced a coefficient of determination value equal to 1.000. The ChemStation software was used for data acquisition and evaluation of the signals and retention time of the analyte. The retention time for resmethrin was 4.8 min. The lowest concentration of the calibration plot of resmethrin (0.10 mg/L) was measured seven times to obtain the standard deviation values used to calculate the limit of detection (LOD), limit of quantification (LOQ) and percent relative standard deviation (%RSD) using the following formulas below:

$$\text{LOD} = 3 \times \text{Std Dev} / \text{Slope} \quad (1)$$

$$\text{LOQ} = 10 \times \text{Std Dev} / \text{Slope} \quad (2)$$

System analytical performance values calculated for resmethrin are presented in

Table 1. The calibration plot had linearity over a wide concentration range for the determination of resmethrin. The low %RSD values obtained in each measurement indicated that the repeatability was satisfactory. All chromatograms obtained for the measurements are shown in Figure 1.

Table 1 System analytical performances of GC-FID

Analyte	Resmethrin
LOD, mg/L	0.02
LOQ, mg/L	0.08
Linear Range, mg/L	0.10 - 163
Regression Coefficient	1.0000
Intra-day, %RSD	1.8
Inter-day, %RSD	7.7

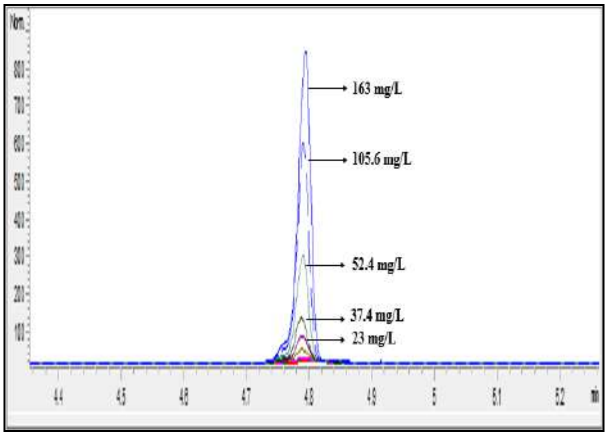

Figure 1 Overlay chromatograms of resmethrin calibration standards

3.2. Recovery experiments

The constant use of pesticides to control pests on farmlands and protect/increase the yield of farm products increases the risk of exposure to humans and other living organisms. After harvest, it is possible to encounter pesticide residues in products offered for human consumption. The aim of the recovery tests was to determine the amount of resmethrin that can be accurately and precisely quantified when present in corn silk samples. Since resmethrin showed high solubility in acetonitrile, the extraction process was performed as described in Section 2.3. Firstly, the blank extract of the sample was analyzed by the GC-FID system to determine the presence of resmethrin, but no analytical signal was observed at the retention time. Then, the corn silk sample was spiked at 0.31, 0.61, 8.1, 16.2 and 40.2 mg/L final concentrations. The percent recoveries calculated with the external calibration method under the proposed conditions are summarized in Table 2.

Table 2 Percent recoveries for corn silk sample spiked at different concentrations

Analyte	Spiked Concentration, mg/L	External Calibration Recovery ± Standard Deviation, %
Resmethrin	0.31	94.6 ± 3.3
	0.61	92.1 ± 2.3
	8.1	96.3 ± 2.5
	16.2	93.6 ± 1.8
	40.2	96.9 ± 2.0

4. CONCLUSION

In this study, a GC-FID analysis method was presented for the direct determination of resmethrin in corn silk samples. A suitable temperature program was used to elute the target analyte through the column within a short run time of 5.7 min. Percent recovery results calculated for the samples spiked at three different concentrations were in the range of 93.6 – 96.9%, and the relative standard deviation values recorded below 2.5% certified good repeatability for the method. Compared to the limit values of a study reported in the literature, the proposed method may be a good alternative for the determination of resmethrin with high accuracy [24].

Funding
The author did not receive any financial support for the research, authorship, or publication of this study.

Authors' Contribution
The author contributed solely to the study.

The Declaration of Conflict of Interest/ Common Interest
No conflict of interest or common interest has been declared by the author.

The Declaration of Ethics Committee Approval
This study does not require ethics committee permission or any special permission.

The Declaration of Research and Publication Ethics
The authors of the paper declare that they comply with the scientific, ethical and quotation rules of SAUJS in all processes of the paper and that they do not make any falsification on the data collected. In addition, they declare that Sakarya University Journal of Science and its editorial board have no responsibility for any ethical violations that may be encountered, and that this study has not been evaluated in any academic publication environment other than Sakarya University Journal of Science.

REFERENCES

[1] M. K. Ross, “Pyrethroids,” in Encyclopedia of Environmental Health, Elsevier, 2011, pp. 702–708.

[2] H. Seçilmiş Canbay, S. Öğüt, “Organik ve Organik Olmayan Elmalar ile Bu Elmaları Üreten Kişilerdeki Pestisit Kalıntıları ve Toplam Antioksidan Kapasiteleri,” Sakarya Üniversitesi Fen Bilimleri Enstitüsü Dergisi, pp. 1–1, Dec. 2017.

[3] D. S. Chormey, “Determination of Fenobucarb and Chlorbenside in Wastewater and Lake Water Samples by Gas Chromatography Mass Spectrometry” European Journal of Science and Technology, 2021.

[4] G. Rosini, V. Borzatta, C. Paolucci, P. Righi, “Comparative assessment of an alternative route to (5-benzylfuran-3-yl)methanol (Elliott’s alcohol), a key intermediate for the industrial production of resmethrins” Green Chemistry, vol. 10, no. 11, p. 1146, 2008.

[5] M. A. Hassaan, A. El Nemr, “Pesticides pollution: Classifications, human health impact, extraction and treatment techniques,” The Egyptian Journal of Aquatic Research, vol. 46, no. 3, pp. 207–220, 2020.

[6] R. Jayaraj, P. Megha, P. Sreedev, “Review Article. Organochlorine pesticides, their toxic effects on living organisms and their fate in the environment,” Interdisciplinary Toxicology, vol. 9, no. 3–4, pp. 90–100, 2016.

[7] N. Çördük, N. Akıncı, N. Kaya, G. Yücel, C. Akı, “Dodin Fungisitinin Vicia faba L. Bitkisinde Total Protein Miktarı ve Peroksidaz Aktivitesi Üzerine Etkisi,” Sakarya Üniversitesi Fen Bilimleri Enstitüsü Dergisi, vol. 20, no. 3, 2016.

[8] R. Le Grand, S. Dulaurent, J. M.

Gaulier, F. Saint-Marcoux, C. Moesch, G. Lachâtre, “Simultaneous determination of five synthetic pyrethroid metabolites in urine by liquid chromatography-tandem mass spectrometry: application to 39 persons without known exposure to pyrethroids,” Toxicology Letters, vol. 210, no. 2, pp. 248–53, 2012.

[9] M. Tao, G. Zhang, C. Xiong, J. Pan, “Characterization of the interaction between resmethrin and calf thymus DNA in vitro,” New Journal of Chemistry, vol. 39, no. 5, pp. 3665–3674, 2015.

[10] R. P. Pohanish, “R,” in Sittig’s Handbook of Pesticides and Agricultural Chemicals, Elsevier, pp. 730–737, 2015.

[11] R. A. Simonaitis, R. S. Cail, “Gas-liquid chromatographic determination of resmethrin in corn, cornmeal, flour, and wheat,” Journal - Association of Official Analytical Chemists, vol. 58, no. 5, pp. 1032–1036, 1975.

[12] T. Narahashi, “Mode of action of pyrethroids,” Bulletin of the World Health Organization, vol. 44, no. 1–3, pp. 337–45, 1971.

[13] D. M. Soderlund, J. R. Bloomquist, “Neurotoxic Actions of Pyrethroid Insecticides,” Annual Review of Entomology, vol. 34, no. 1, pp. 77–96, 1989.

[14] US EPA, “Reregistration Eligibility Decision for Ferbam,” Prevention, Pesticides and Toxin Substances, pp. 1–73, 2005.

[15] A. Masiá, C. Blasco, Y. Picó, “Last trends in pesticide residue determination by liquid chromatography–mass spectrometry,” Trends in Environmental Analytical Chemistry, vol. 2, pp. 11–24, 2014.

[16] J.-M. Lin, L.-B. Liu, Y. Liu, “Determination of Pesticide Residues in Fruits and Vegetables by Using GC–MS and LC–MS,” in Handbook of Pesticides, CRC Press, pp. 497–523, 2009.

[17] E. G. Bakırdere, “Simultaneous determination of selected alachlor, bifenox and nitrofen as herbicides in lake, municipal wastewater and soil samples by gas chromatography mass spectrometry,” European Journal of Science and Technology, pp. 108–111, 2018.

[18] H. Budiman, Nuryatini, O. Zuas, “Comparison between GC-TCD and GC-FID for the determination of propane in gas mixture,” Procedia Chemistry, vol. 16, pp. 465–472, 2015.

[19] M. P. Kavvalakis, M. N. Tzatzarakis, A. K. Alegakis, D. Vynias, A. K. Tsakalof, and A. M. Tsatsakis, “Development and application of GC-MS method for monitoring of long-term exposure to the pesticide cypermethrin,” Drug Testing and Analysis, vol. 6, no. S1, pp. 9–16, 2014.

[20] S. Tandon, S. Kumar, N. K. Sand, “Development and Validation of GC-ECD Method for the Determination of Metamitron in Soil,” International Journal of Analytical Chemistry, vol. 2015, pp. 1–5, 2015.

[21] M. Abbasghorbani, A. Attaran, M. Payehghadr, “Solvent-assisted dispersive micro-SPE by using aminopropyl-functionalized magnetite

nanoparticle followed by GC-PID for quantification of parabens in aqueous matrices,” Journal of Separation Science, vol. 36, no. 2, pp. 311–319, 2013.

[22] B. Bayrak, “Sudaki Pestisit Kalıntılarının Belirlenmesi için GC-NPD Kullanılarak Method Geliştirilmesi ve Validasyonu,” Journal of the Institute of Science and Technology, vol. 8, no. 1, pp. 133–141, 2018.

[23] E. Forgács, T. Cserháti, “Chromatography | Principles,” in Encyclopedia of Food Sciences and Nutrition, Elsevier, 2003, pp. 1259–1267.

[24] H. Nozawa, K. Minakata, K. Hasegawa, I. Yamagishi, M. Suzuki, T. Kitamoto, K. Watanabe, O. Suzuki, “A fatal case involved in pyrethroid insecticide ingestion: quantification of tetramethrin and resmethrin in body fluids of a deceased by LC–MS/MS,” Forensic Toxicology, vol. 40, no. 1, pp. 189–198, 2022.

SAKARYA ÜNİVERSİTESİ
FEN BİLİMLERİ ENSTİTÜSÜ
DERGİSİ

Sakarya University Journal of Science
SAUJS

ISSN 1301-4048 | e-ISSN 2147-835X | Period Bimonthly | Founded: 1997 | Publisher Sakarya University |
http://www.saujs.sakarya.edu.tr/

Title: An Innovative Application On Supermarket Selection Through Using Intuitionistic Fuzzy TOPSIS Method

Authors: Feride TUĞRUL

Recieved: 2022-07-22 00:00:00

Accepted: 2022-09-05 00:00:00

Article Type: Research Article

Volume: 25
Issue: 5
Month: October
Year: 2022
Pages: 1029-1039

How to cite
Feride TUĞRUL; (2022), An Innovative Application On Supermarket Selection Through Using Intuitionistic Fuzzy TOPSIS Method. Sakarya University Journal of Science, 25(5), 1029-1039, DOI: 10.16984/saufenbilder.1147123
Access link
http://www.saujs.sakarya.edu.tr/en/pub/issue/73051/1147123

Sakarya University Journal of Science 25(5), 1029-1039, 2022

An Innovative Application On Supermarket Selection Through Using Intuitionistic Fuzzy TOPSIS Method

Feride TUĞRUL*[1]

Abstract

Multi-criteria decision making methods have recently attracted the attention of researchers and have had a large share in multidisciplinary fields. In this study, using the intuitionistic fuzzy TOPSIS method, supermarket chains were evaluated in the consumer context and the most preferred supermarket was determined. Consumers' opinions were expressed using linguistic term. The reason why the intuitionistic fuzzy TOPSIS method is preferred; it is the ability of consumers to express their opinions easily, to take into account the undecided situations with the help of intuitionistic fuzzy sets, and thus to create an objective decision making mechanism.

Keywords: Intuitionistic fuzzy sets, TOPSIS, market selection.

1.INTRODUCTION

Many scientists have been doing research on fuzzy and intuitionistic fuzzy sets for a long time. Zadeh defined fuzzy sets [1]; After fuzzy logic was defined, many researchers have been used fuzzy logic in both theoretical and application areas. Fuzzy logic provides serious convenience in many areas. When concepts such as sensitivity, indecision and hesitation came into play, it became clear that researchers needed a new field. Atanassov firstly defined intuitionistic fuzzy (IF) sets in response to these needs [2]. Since it eliminates uncertainty in many application areas, its use gives favorable results.

Multi-criteria decision-making (MCDM) processes are a challenging processes for decision-makers. Because many factors come into play while making the decision. Decision-makers want to make decisions by considering all factors at the same time. Therefore, MCDM methods make it easier for decision-makers in many ways. Many methods were described and used by decision-makers so far; TOPSIS, PROMETHEE, ELECTRE, AHP, etc.

In this study, the evaluation of supermarket chains, which are an important part of people's lives, in the context of consumers has been made. Shopping has a wide range of products such as food and beverage, cleaning materials, care products. In today's conditions, it is very convenient for people

---

* Corresponding author: feridetugrul@gmail.com
[1] Kahramanmaraş Sütçü İmam University
ORCID: https://orcid.org/0000-0001-7690-8080

to act by choosing the market that suits their needs. To provide this convenience; in this study, a MCDM mechanism was established in order to evaluate the markets according to the perspective and needs of the consumers.

IF sets have been used to evaluate the situations in which consumers were undecided while reflecting their views. Consumers expressed their opinions about the markets with linguistic expressions, the values that these linguistic expressions correspond to as IF numbers are given in the tables.

The basic idea of this study is as follows: First of all, the 3 most preferred supermarkets in Turkey have been determined. Afterward, the criteria affecting the market preferences have been determined and classified. First of all, consumers' opinions about these criteria have been taken. Afterward, consumers have been asked to evaluate the markets according to the criteria. Linguistic expressions in the tables created according to the comments of the consumers are expressed by intuitionistic fuzzy numbers. These values have been evaluated within the decision-making mechanism with the IF TOPSIS method, which has a high rate of preference among MCDM methods.

According to the evaluation of the intuitionistic fuzzy TOPSIS method, a ranking has been made among the markets and the most preferred market has been determined in the context of consumers.

Market selection and evaluation has attracted the attention of many researchers. There are various researches in this field, some of them are as follows: Market segment evaluation, e-marketplace selection, competitiveness of supermarket chains, market selection in international expansion, consumer market for business, opinion of supermarket's executives, market segment evaluation with CODAS method, VIKOR method with research on fresh fruit-vegetable sector, market evaluation using by AHP and COPRAS-G method, etc. [3-10]

Today, most researchers have applications related to MCDM, especially in multidisciplinary fields. IF sets, TOPSIS, fuzzy TOPSIS and IF TOPSIS methods have been used by researchers both theoretically and in many application areas: Supplier selection, facility location selection, mobile phone selection, distance measure, developing new methods, renewable energy technologies, selecting school, furniture industry, departments' performances, selection of wind power plants, determination of physical conditions of schools, product concept selection, etc. [11-34].

In addition to these, innovative studies can be carried out in many fields by using IF sets and MCDM methods together; education, physics, geometry, algebraic structures, recycling, technology, and computers, etc.

The choices of alternatives and criteria, calculation methods, ordering method, distance measure used, equations used in the method, intuitionistic fuzzy expressions and all calculations are explained in detail.

1.1.Preliminaries

Definition 1: [2, 35] Let $X \neq \emptyset$. An intuitionistic fuzzy set A in X;

$$A = \{\langle x, \mu_A(x), \nu_A(x)\rangle \mid x \epsilon X\}, \qquad (1.1)$$

$$\mu_A(x), \nu_A(x), \pi_A(x): X \to [0,1] \qquad (1.2)$$

defined membership, nonmembership and hesitation degree of the element $x \in X$ respectively.

$$\mu_A(x) + \nu_A(x) + \pi_A(x) = 1 \qquad (1.3)$$

The IF TOPSIS algorithm which are m alternatives and n criteria is as follows [29]:

Step 1 Linguistic terms are used when determining the importance of each DM.

Table 1 Linguistic Terms for the Importance of DMs

Linguistic Terms	IFNs
Very Important	(0.8,0.1)
Important	(0.5,0.2)
Medium	(0.5,0.5)
Bad	(0.3,0.5)
Very Bad	(0.2,0.7)

$L = l_1, l_2, \dots, l_n$ is set of decision makers. $Dl = [\mu l, \nu l, \pi l]$ is calculated as follows [36]:

$$\lambda l = \frac{\left[\mu l + \pi l\left(\frac{\mu l}{\mu l + \nu l}\right)\right]}{\sum_{l=1}^{k}\left[\mu l + \pi l\left(\frac{\mu l}{\mu l + \nu l}\right)\right]} \qquad (1.4)$$

$\lambda 1 \in [0,1]$ and $\sum_{l=1}^{k} \lambda l = 1$.

Step 2 The importance of the criteria (W) is determined in linguistic terms depending on the views of the DMs:

Table 2 Linguistic Terms for Rating the Criterion

Linguistic Terms	IFNs
Very Important	(0.9,0.1)
Important	(0.75,0.2)
Medium	(0.5,0.45)
Unimportant	(0.35,0.6)
Very Unimportant	(0.1,0.9)

When calculating the weights of the criteria, The IFWA operator is used [37]. According to linguistic terms in Table 2, the weight of criteria is calculated as:

$$w_j = IFWAr_\lambda\left(w_j^{(1)}, w_j^{(2)}, \dots, w_j^{(l)}\right)$$
$$= \lambda_1 w_j^{(1)} \oplus \lambda_2 w_j^{(2)} \oplus, \dots, \oplus \lambda_k w_j^{(k)}$$
$$= \left[1 - \prod_{l=1}^{k}\left(1 - \mu_{ij}^{(l)}\right)^{\lambda l}, \left(\prod_{l=1}^{k}\left(\nu_{ij}^{(l)}\right)^{\lambda l}\right), \prod_{l=1}^{k}\left(1 - \mu_{ij}^{(l)}\right)^{\lambda l} - \prod_{l=1}^{k}\left(\nu_{ij}^{(l)}\right)^{\lambda l}\right] \qquad (1.5)$$

Step 3 Determine IF Decision Matrix (IFDM). In Table 3, the IF corresponding values of linguistic terms are given. These values are used when calculating the weights of the alternatives:

Table 3 Linguistic Terms for Rating the Alternatives

Linguistic Terms	IFNs
Very Good (VG)	(1.00,0.00)
Good (G)	(0.85,0.05)
MediumGood (MG)	(0.70,0.20)
Fair (F)	(0.50,0.50)
Medium Poor (MP)	(0.40,0.50)
Poor (P)	(0.25,0.60)
Very Poor (VP)	(0.00,0.90)

The Aggregated Intuitionistic Fuzzy Decision Matrix (AIFDM) is obtained [37].
$R^l = (r_{ij}^{(l)})_{m*n}$ is the IFDM of each DM.
$\lambda = \lambda_1, \lambda_2, \dots, \lambda_k$ is the weight of the DM.
$R = (r_{ij})_{m' \times n'}$

$$r_{ij} = IFWAr_\lambda\left(r_{ij}^{(1)}, r_{ij}^{(2)}, \dots, r_{ij}^{(l)}\right)$$
$$= \lambda_1 r_{ij}^{(1)} \oplus \lambda_2 r_{ij}^{(2)} \oplus, \dots, \oplus \lambda_k r_{ij}^{(k)}$$
$$= \left[1 - \prod_{l=1}^{k}\left(1 - \mu_{ij}^{(l)}\right)^{\lambda l}, \left(\prod_{l=1}^{k}\left(\nu_{ij}^{(l)}\right)^{\lambda l}\right), \prod_{l=1}^{k}\left(1 - \mu_{ij}^{(l)}\right)^{\lambda l} - \prod_{l=1}^{k}\left(\nu_{ij}^{(l)}\right)^{\lambda l}\right] \qquad (1.6)$$

Step 4 The S matrix is created. W with respect to IFDM (R) are defined as follows:

$$S = R \times W$$
$$R \otimes W = \left(\mu'_{ij}, \nu'_{ij}\right)$$
$$= \left\{\langle \mu_{ij} \times \mu_j, \nu_{ij} + \nu_j - \nu_{ij} \times \nu_j \rangle\right\}$$
(1.7)

Step 5 J_1 is the benefit criteria and J_2 is the cost criteria. A^+ is the IF positive ideal solution and A^- is the IF negative ideal solution. Then A^{+} and A^{-} are obtained as follows:

$$A^{+} = (r_1'^{*}, r_2'^{*}, \dots, r_n'^{*}), r_j'^{*} = (\mu_j'^{*}, \nu_j'^{*}, \pi_j'^{*}), \quad j = 1,2,\dots,n \tag{1.8}$$

$$A^{-} = (r_1'^{-}, r_2'^{-}, \dots, r_n'^{-}), r_j'^{-} = (\mu_j'^{-}, \nu_j'^{-}, \pi_j'^{-}) \quad j = 1,2,\dots,n \tag{1.9}$$

Where

$$\mu_j'^{*} = \left\{\left(\max_i\{\mu_{ij}'\} j \in J_1\right), \left(\min_i\{\mu_{ij}'\} j \in J_2\right)\right\}$$

$$\nu_j'^{*} = \left\{\left(\min_i\{\nu_{ij}'\} j \in J_1\right), \left(\max_i\{\nu_{ij}'\} j \in J_2\right)\right\}$$

$$\mu_j'^{-} = \left\{\left(\min_i\{\mu_{ij}'\} j \in J_1\right), \left(\max_i\{\mu_{ij}'\} j \in J_2\right)\right\}$$

$$\nu_j'^{-} = \left\{\left(\max_i\{\nu_{ij}'\} j \in J_1\right), \left(\min_i\{\nu_{ij}'\} j \in J_2\right)\right\}$$

Step 6 Many distance measures have been defined on IF sets [38, 39]. In this step of the study, unlike other methods, the normalized Hamming measure will be used. Studies have shown that the normalized Hamming measure is the most sensitive measure of distance compared to other distance measures. Therefore, in this study, the normalized Hamming distance measure was used. Through the positive and negative ideal solutions, S_i^{+} and S_i^{-} respectively, the separation measures of the alternatives are determined.

$$S_i^{+} = \frac{1}{2n}\sum_{i=1}^{n}\left[\left|\mu_{ij}' - \mu_{ij}'^{*}\right| + \left|\nu_{ij}' - \nu_{ij}'^{*}\right| + \left|\pi_{ij}' - \pi_{ij}'^{*}\right|\right] \tag{1.10}$$

$$S_i^{-} = \frac{1}{2n}\sum_{i=1}^{n}\left[\left|\mu_{ij}' - \mu_{ij}'^{-}\right| + \left|\nu_{ij}' - \nu_{ij}'^{-}\right| + \left|\pi_{ij}' - \pi_{ij}'^{-}\right|\right] \tag{1.11}$$

Step 7 The closeness coefficient between the positive ideal solution and the negative ideal solution is calculated by the formula:

$$C_i^{*} = \frac{S_i^{-}}{S_i^{+} + S_i^{-}}, \tag{1.12}$$

and $0 \le C_i^{*} \le 1$. The resulting value is ranked from largest to smallest. A larger C_i^{*} value indicates better alternative.

2. SUPERMARKET SELECTION USING THE IF TOPSIS METHOD

In this study, the 3 most preferred chain supermarkets in Turkey have been discussed. These supermarkets have been evaluated according to certain criteria by consumers. From many aspects, supermarkets have a very important role in people's lives. Chain supermarkets, on the other hand, are designed to serve the needs of people.

Supermarkets have been evaluated according to the opinions of consumers. IF sets have been used in order to consider all the ideas of the consumers while determining the opinions of the consumers. It is aimed to reflect the ideas of consumers in the most objective way, taking into account the undecided situations as well as positive and negative ideas. By using the IF TOPSIS method together with the IF sets, the distances to both the positive ideal solution and the negative ideal solution have been calculated, and a ranking has been made between the alternatives thanks to the closeness coefficient.

In this study; alternatives represent the markets and the criteria represent the issues that the markets pay attention to when choosing according to the consumers. Alternatives, criteria and explanations about them are as follows:
$M = \{M_1, M_2, M_3\}$ is the set of alternatives, namely, supermarkets. $C = \{C_1, C_2, C_3, C_4, C_5, C_6\}$ is the set of criteria.

C_1: Product quality
- Fresh produce
- Not selling defective products

- Paying attention to the expiry date of the products

C_2: Accessibility
- Excess number of branches
- Easy to reach the location
- No traffic, no parking problems

C_3: Product variety
- Easy access to every product
- Wide range of products
- Brand diversity

C_4: Economic

C_5: Access to products in the Market
- Number of employees
- Slabs, signboards for product promotion

C_6: The atmosphere of the market
- Hygiene
- Organized shelves
- Fresh environment

While determining the criteria for choosing supermarket chains, the concept of competition is remarkable for consumers. According to Levy and Weitz, they identified important factors affecting competition in the retail industry [40, 41] The steps of applying the IF TOPSIS method to the alternatives and criteria mentioned above and explained in detail are as follows:

Step 1: There are 2 DMs in this study. Decision maker 1 (DM_1): Consumer, Decision maker 2 (DM_2): Consumer. After determining the importance of DMs with linguistic variables according to Table 1; the importance of the DM_1 is "very important" and the importance of the DM_2 is "important". It has been converted into numerical data with the help of equation 1.4:

Numerical values of DM_1's importance weight: 0,55

Numerical values of DM_2's importance weight: 0,45

Step 2: Linguistic values have been assigned to each criterion by the decision makers and the importance values of the criteria were determined as linguistic expressions. Many different methods could be used when calculating weights of the criteria. One of the effective methods among these methods is controlled sets [42]. In this study, it has been preferred to use linguistic expressions. Table 4 represents the degree of importance of the criteria determined based on the opinions of the decision makers. Assigned numeric values to the linguistic expressions have been determined with the help of intuitionistic fuzzy numbers in Table 2. Using of Equation 1.5, weights of criteria are obtained values are shown in Table 5.

Table 4 Importance weights of criteria based on DMs opinion

	DM_1	DM_2
C_1	VI	VI
C_2	M	U
C_3	VI	I
C_4	I	VI
C_5	I	M
C_6	I	I

Table 5 Weights of criteria

C_1	(0.90, 0.10)
C_2	(0.44, 0.52)
C_3	(0.85, 0.14)
C_4	(0.83, 0.15)
C_5	(0.66, 0.29)
C_6	(0.75, 0.20)

The importance of the alternatives for each criterion has been determined by the DMs according to the linguistic expressions in Table 3 and has shown in Table 6.

Table 6 Importance of alternatives according to DMs

	C_1	C_2	C_3	C_4	C_5	C_6
DM_1						
M_1	G	F	VG	G	MP	P
M_2	MG	G	MG	G	G	MG
M_3	VG	F	VG	MP	MP	VG
DM_2						
M_1	G	MG	VG	G	MP	MP
M_2	G	VG	G	VG	VG	G
M_3	G	F	VG	MP	MP	G

Step 3: AIFDM has been calculated using by Equation 1.6. R matrix is obtained in Table 7.

Step 4: S matrix is obtained with the help of Equation 1.7. S matrix is obtained in Table 8.

Table 7 R Matrix

	C_1	C_2	C_3	C_4	C_5	C_6
M_1	(0.850, 0.050)	(0.602, 0.332)	(1.000, 0.000)	(0.850, 0.050)	(0.400,0.500)	(0.321, 0.553)
M_2	(0.780, 0.108)	(1.000, 0.000)	(0.780, 0.108)	(1.000, 0.000)	(1.000, 0.000)	(0.780, 0.108)
M_3	(1.000,0.000)	(0.500,0.500)	(1.000,0.000)	(0.400,0.500)	(0.400,0.500)	(1.000,0.000)

Table 8 S Matrix

	C_1	C_2	C_3	C_4	C_5	C_6
M_1	(0.765, 0.145)	(0.264, 0.674)	(0.850,0.136)	(0.709, 0.189)	(0.264, 0.644)	(0.241, 0.643)
M_2	(0.702, 0.197)	(0.438, 0.512)	(0.662, 0.229)	(0.834, 0.147)	(0.659, 0.287)	(0.585, 0.286)
M_3	(0.900,0.100)	(0.219, 0.756)	(0.849, 0.136)	(0.334, 0.573)	(0.264, 0.644)	(0.750, 0.200)

Step 5: The IF positive A^+ and negative ideal solution A^- are obtained using by Equation 1.8 and 1.9 in Table 9 and Table 10 respectively:

Table 9 The IF positive ideal solution A^+

A^+	
C_1	(0.900, 0.100)
C_2	(0.438, 0.512)
C_3	(0.849, 0.136)
C_4	(0.834, 0.147)
C_5	(0.659, 0.287)
C_6	(0.750, 0.200)

Table 10 The IF negative ideal solution A^-

A^-	
C_1	(0.702, 0.197)
C_2	(0.219, 0.756)
C_3	(0.663, 0.229)
C_4	(0.334, 0.574)
C_5	(0.264, 0.644)
C_6	(0.241, 0.643)

Step 6-7: Separation measures, namely, positive ideal solution S^+ and negative ideal solution S^- are obtained using by normalized Hamming distance measure (with by Equation 1.10 and 1.11). Also, The closeness coefficient C_i^* between the positive ideal solution and the negative

ideal solution is calculated using by Equation 1.12 in Table 11 and shown in Figure 1.

Table 11 Separation measures and closeness coefficient values

	S^+	S^-	C_i^*
M_1	0.22325	0.11937	0.34840
M_2	0.09177	0.24942	0.73102
M_3	0.19004	0.14911	0.43967

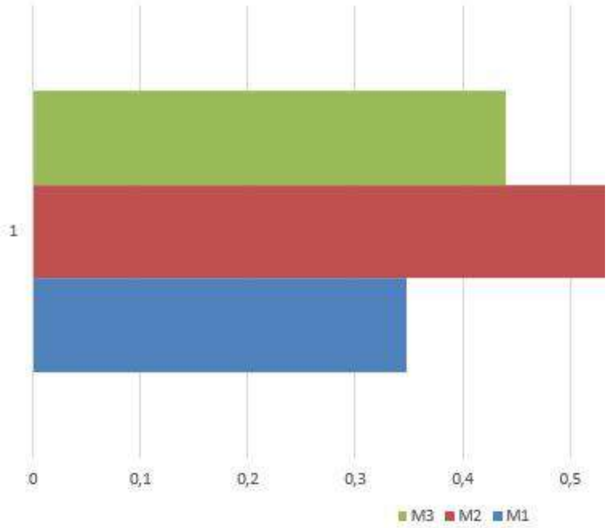

Figure 1 The Closeness Coefficient Values

When the values in Table 11 are examined, For the alternative to be good, the closeness coefficient is expected to be high. In other words, as the closeness coefficient value increases, the success of that alternative among all alternatives increases. Accordingly, the ranking among the alternatives is as follows: $M_2 - M_3 - M_1$.

According to this MCDM mechanism, which is prepared based on the opinions of consumers; the most preferred market is the M_2 market. In addition, according to consumers, the M_3 market is more preferred than the M_1 market.

3.CONCLUSION AND SUGGESTION

In this study, an application was made to the selection of supermarket chains in the context of consumers by using the intuitionistic fuzzy TOPSIS method. Purpose of the study; to evaluate the supermarket chains, which is a highly competitive market, according to the opinions of the consumers and to determine the most preferred market. For this purpose, consumers' ideas were evaluated as linguistic expressions and expressed with intuitionistic fuzzy numbers. According to this system, which is created by considering the needs, wishes and preferences of the consumers, the competition between the markets is reflected in the consumer. Supermarket chains should act in this direction by determining the factors that consumers pay special attention to in market selection.

By using the IF TOPSIS method, the distance to both the positive and negative ideal solution was calculated. While calculating the separation measures between the positive and negative ideal solutions, the normalized Hamming measure was used. According to the calculated closeness coefficient, a ranking was obtained among the markets from the best to the worst, and the most preferred market was determined.

If want to talk about another advantage of this method; it is very difficult for decision-makers to always express their views with numerical values. Therefore, decision-makers may both feel better and make more objective comments when expressing their ideas in linguistic terms. For these reasons, advantageous results were emerged by making use of the IF TOPSIS method, which gives decision-makers the chance to express their ideas in linguistic terms.

This study is an exemplary study in the multidisciplinary field. The method used in the study; it may be used in all application areas. This method will guide researchers who want to use an algorithm based on the ideas of decision makers while selecting, evaluating and ranking by using a MCDM mechanism. In the continuation of this study; a more comprehensive study may be obtained with different market chains. The IF TOPSIS method may be compared with other MCDM methods such as PROMETHEE, ELECTRE, AHP, etc. The criteria may be expanded by making a study on the factors of preference of supermarket chains.

Acknowledgment
The author would like to thank the reviewers and editors.

Funding
The author declared that has no received any financial support for the research, authorship or publication of this study.

The Declaration of Conflict of Interest/ Common Interest

The author declared that no conflict of interest or common interest.

Authors' Contribution

The authors contributed equally to the study.

The Declaration of Ethics Committee Approval

This study does not be necessary ethical committee permission or any special permission.

The Declaration of Research and Publication Ethics

The author(s) declared that they comply with the scientific, ethical, and citation rules of Sakarya University Journal of Science in all processes of the study and that they do not make any falsification on the data collected. Besides, the author(s) declared that Sakarya University Journal of Science and its editorial board have no responsibility for any ethical violations that may be encountered and this study has not been evaluated in any academic publication environment other than Sakarya University Journal of Science.

REFERENCES

[1] L. A. Zadeh, “Information and Control,” Fuzzy sets, vol.8, no.3, pp.338-353, 1965.

[2] K. T. Atanassov, “Intuitionistic Fuzzy Sets,” VII ITKR's Session, Sofia, June 1983 (Deposed in Central Sci. - Techn. Library of Bulg. Acad. of Sci., 1697/84) (in Bulg.). Reprinted: Int. J. Bioautomation, 20(S1), pp.1-6, 2016.

[3] M. H. Aghdaie, S. Hashemkhani Zolfani, E. K. Zavadskas, “Market Segment Evaluation And Selection Based on Application of Fuzzy AHP and Copras-G Methods,” Journal of Business Economics and Management, vol.14, no.1, pp.213–233, 2013.

[4] G. Büyüközkan, “Multi-Criteria Decision Making For E-Marketplace Selection,” Internet Research, vol.14, no.2, pp. 139-154, 2004.

[5] M. K. Ghorabaee, M. Amiri, E. K. Zavadskas, R. Hooshmand, J. Antuchevičienė, “Fuzzy Extension of the CODAS Method for Multi-Criteria Market Segment Evaluation,” Journal of Business Economics and Management, vol.18, no.1, pp.1-19, 2017.

[6] D. Górecka, M. Szałucka, "Country Market Selection in International Expansion Using Multicriteria Decision Aiding Methods," Multiple Criteria Decision Making, vol.8, pp.32-55, 2013.

[7] M. Keshavarz Ghorabaee, M. Amiri, E. K. Zavadskas, R. Hooshmand, J. Antuchevıčıenė, “Fuzzy Extension Of The Codas Method For Multi-Criteria Market Segment Evaluation,” Journal of Business Economics and

Management, vol.18, no.1, pp.1-19, 2017.

[8] L. A. A. Teixeira, Á. M. F. Pires, M. A. Alvarenga, J. T. M. Silva, “Supermarket’s Executives and the Decision Process about Format Location and Price,” Aust. J. Basic & Appl. Sci., vol.9, no.7, pp.503-511, 2015.

[9] N. Tosun, “Target Market Selection in Fresh Fruit-Vegetable Sector Using Fuzzy VIKOR Method,” Journal of Management Marketing and Logistics, vol.4, no.4, pp.465-471, 2017.

[10] K. Valaskova, K. Kramarova, V. Bartosova, Multi Criteria Models Used in Slovak Consumer Market For Business Decision Making. Procedia Economics and Finance, vol.26, pp.174-182, 2015.

[11] K. T. Atanassov, “Intuitionistic Fuzzy Sets,” Springer, Berlin, Heidelberg, 1999.

[12] M. B. Ayhan, “An Integrated Hesitant Fuzzy AHP And TOPSIS Approach For Selecting Summer Sport School,” Sakarya Unıversity Journal of Science, vol.22, no.2, pp.269-284, 2018.

[13] F. E. Boran, S. Genç, M. Kurt, D. Akay,“A Multi-Criteria Intuitionistic Fuzzy Group Decision Making For Supplier Selection With TOPSIS Method,” Expert Systems with Applications, vol.36, no.8, pp.11363-11368, 2009.

[14] F. E. Boran, “An Integrated Intuitionistic Fuzzy Multi Criteria Decision Making Method For Facility Location Selection,” Mathematical and Computational Applications, vol.16, no.2, pp.487-496, 2011.

[15] F. E. Boran, K. Boran, T. Menlik, “The Evaluation of Renewable Energy Technologies For Electricity Generation in Turkey Using Intuitionistic Fuzzy TOPSIS,” Energy Sources, Part B: Economics, Planning, and Policy, vol.7, no.1, pp.81-90, 2012.

[16] G. Büyüközkan, S. Güleryüz, “An Application of Intuitionistic Fuzzy Topsis on Mobile Phone Selection,” In 2015 IEEE International Conference on Fuzzy Systems (FUZZ-IEEE), pp. 1-8, August, 2015.

[17] T. Y. Chen, C. Y. Tsao, “The Interval-Valued Fuzzy TOPSIS Method and Experimental Analysis,” Fuzzy Sets and Systems, vol.159, no.11, pp.1410-1428, 2008.

[18] M. Çitil, F. Tuğrul, “Some New Equalities On The Intuitionistic Fuzzy Modal Operators,” Sakarya University Journal of Science, vol.22, no.6, pp.1524-1531, 2018.

[19] G. Çuvalcıoğlu, S. Tarsuslu, A. Bal, G. Artun, “Intuitionistic Fuzzy Modal Operators in Intelligent System for Pesticide and Fertilization" Annals of Fuzzy Mathematics and Informatics, vol.16, no.1, pp.117-132, 2018.

[20] G. Çuvalcıoğlu, S. Yılmaz, K. T. Atanassov, “Matrix Representation Of The Second Type Of Intuitionistic Fuzzy Modal Operators,” Notes on Intuitionistic Fuzzy Sets, vol.20, no.5, pp.9-16, 2014.

[21] E. Damgacı, K. Boran, F. Boran, “Evaluation of Turkey's Renewable Energy Using Intuitionistic Fuzzy TOPSIS Method,” Journal of

Polytechnic, vol.20, no.3, pp.629-637, 2017.

[22] L. Dymova, K. Kaczmarek, P. Sevastjanov, Ł. Sułkowski, K. Przybyszewski, “An Approach to Generalization of the Intuitionistic Fuzzy TOPSIS Method in The Framework of Evidence Theory,” Journal of Artificial Intelligence and Soft Computing Research, 11, 2021.

[23] B. Efe, F. E. Boran, M. Kurt, “Ergonomic Product Concept Selection Using Intuitionistic Fuzzy TOPSIS,” Suleyman Demirel University Journal of Engineering Sciences and Design, vol.3, no.3, pp.433-440, 2015.

[24] M. Erdoğan, “A New Fuzzy Approach for Analyzing the Smartness of Cities: Case Study for Turkey,” Sakarya University Journal of Science, vol.25, no.2, pp.308-325, 2021.

[25] İ. Güven, F. Şimşir, “Machine-Part Formation for Cellular Manufacturing in Group Technology: An Application for Furniture Company,” Sakarya University Journal of Science, vol.25, no.2, pp.466-483, 2021.

[26] D. Joshi, S. Kumar, “Intuitionistic Fuzzy Entropy and Distance Measure Based TOPSIS Method For Multi-Criteria Decision Making,” Egyptian Informatics Journal, vol.15, no.2, pp.97-104, 2014.

[27] B. D. Rouyendegh, “The DEA And Intuitionistic Fuzzy TOPSIS Approach To Departments' Performances: A Pilot Study,” Journal of Applied Mathematics, 2011.

[28] B .D. Rouyendegh, T. E. Saputro, “Supplier Selection Using Integrated Fuzzy TOPSIS And MCGP: A Case Study,” Procedia-Social and Behavioral Sciences, vol.116, pp.3957-3970, 2014.

[29] B. D. Rouyendegh, “Developing an Integrated ANP and Intuitionistic Fuzzy TOPSIS Model For Supplier Selection,” Journal of Testing and Evaluation, vol. 43, no. 3, pp. 664–672, 2015.

[30] B. D. Rouyendegh, A. Yıldızbaşı, Ü. Z. Arıkan, “Using Intuitionistic Fuzzy TOPSIS in Site Selection Of Wind Power Plants in Turkey,” Advances in Fuzzy Systems, 2018.

[31] B. D. Rouyendegh, A. Yıldızbaşı, P. Üstünyer, “Intuitionistic Fuzzy TOPSIS Method For Green Supplier Selection Problem,” Soft Computing, vol.24, no.3, pp.2215-2228, 2020.

[32] E. K. Tekez, N. Bark, “Supplier Selection For Furniture Industry with Fuzzy TOPSIS Method,” Sakarya Unıversity Journal of Science, vol.20, no.1, pp.55-63, 2016.

[33] F. Tuğrul, M. Çitil, S. Balcı, “On The Determination Students’ Aptitude Using Intuitionistic Fuzzy Logic,” Journal of Universal Mathematics, vol.2, no.1, pp.36-41, 2019.

[34] F. Tuğrul, M. Çitil, B. Karasolak, M. Dağlı, “Interpretation of Physical Conditions of Schools with Fuzzy Multi Criteria Decision Making,” Journal of Universal Mathematics, vol.3, no.1, pp.46-52, 2020.

[35] K. T. Atanassov, “Intuitionistic fuzzy sets, Fuzzy Sets and Systems,” vol.20, no.1, pp.87-96, 1986.

[36] Y. Wu, J. Zhang, J. Yuan, S. Geng, H. Zhang, "Study Of Decision Framework Of Offshore Wind Power Station Site Selection Based On ELECTRE-III Under Intuitionistic Fuzzy Environment: A Case Of China," Energy Convers Manag, vol.113, pp.66-81, 2016.

[37] Z. S. Xu, "Intuitionistic Fuzzy Aggregation Operators," IEEE Transactions on Fuzzy Systems, vol.15, pp.1179-1187, 2007.

[38] M. Çitil, "Application of the Intuitionistic Fuzzy Logic in Education," Communications in Mathematics and Applications, vol.10, no.1, pp.131-143, 2019.

[39] E. Szmidt, J. Kacprzyk, "Distances Between Intuitionistic Fuzzy Sets," Fuzzy Sets Syst., vol. 114, pp.505-518, 2000.

[40] M. Levy, B. Weitz, "Retailing Management" McGraw-Hill/Irwin Publisher, 2008.

[41] A.Yang, B. Do, G.L. Wang, L. Y. Chang, F. C. Hung, "Assessing Competitiveness of Foreign And Local Supermarket Chains in Vietnamese Market by Using Fuzzy TOPSIS Method," E3 Journal of Business Management and Economics, vol.2, no.5, pp.209-216, 2011.

[42] G. Çuvalcıoğlu, "Some Properties of Controlled Set Theory," Notes on Intuitionistic Fuzzy Sets, vol.20, no.2, pp.37-42, 2014.

Sakarya University Journal of Science
SAUJS

ISSN 1301-4048 | e-ISSN 2147-835X | Period Bimonthly | Founded: 1997 | Publisher Sakarya University |
http://www.saujs.sakarya.edu.tr/

Title: Keyframe Extraction Using Linear Rotation Invariant Coordinates

Authors: Hasan MUTLU, Ufuk ÇELİKCAN

Recieved: 2022-07-25 00:00:00

Accepted: 2022-09-05 00:00:00

Article Type: Research Article

Volume: 25
Issue: 5
Month: October
Year: 2022
Pages: 1040-1051

How to cite
Hasan MUTLU, Ufuk ÇELİKCAN; (2022), Keyframe Extraction Using Linear Rotation Invariant Coordinates. Sakarya University Journal of Science, 25(5), 1040-1051,
DOI: 10.16984/saufenbilder.1148511
Access link
http://www.saujs.sakarya.edu.tr/en/pub/issue/73051/1148511

Sakarya University Journal of Science 25(5), 1040-1051, 2022

Keyframe Extraction Using Linear Rotation Invariant Coordinates

Hasan MUTLU*[1], Ufuk ÇELİKCAN[1]

Abstract

Keyframe extraction is a widely applied remedy for issues faced with 3D motion capture -based computer animation. In this paper, we propose a novel keyframe extraction method, where the motion is represented in linear rotation invariant coordinates and the dimensions covering 95% of the data are automatically selected using principal component analysis. Then, by K-means classification, the summarized data is clustered and a keyframe is extracted from each cluster based on cosine similarity. To validate the method, an online user study was conducted. The results of the user study show that 45% of the participants preferred the keyframes extracted using the proposed method, outperforming the alternative by 6%.

Keywords: Keyframe extraction, linear rotation invariant coordinates, motion data summarization

1. INTRODUCTION

In today's world, motion capture technology is used in many areas, especially in movies and video games. At the same time, editing and transmission of motion capture data are still difficult due to large data sizes. Hence, representing motion capture data compactly continues to be a vital consideration of research.

Skeletal animation is the most effective and commonly used technique of exploiting motion capture data. Skeletal animation consists of two parts, a mesh and a hierarchical set of bones. The mesh part contains surface (skin) information of the character to be rendered, while animation is realized with the spatio-temporal information by the latter. As skeletal animation is performed, the technique fills the gap between two keyframes with interpolation on the timeline. Although skeletal animation provides a solution to represent motions compactly, frame counts remain problematically large for processing, storing and editing. As a remedy, keyframe extraction has been a widely applied solution for issues faced in motion capture -based skeletal animation.

A keyframe extraction method must be capable of sorting out significant keyframes from the others. Also, to improve the success rate of the solution, deriving the characteristics of vertices

---

* Corresponding author: hasanmutlu9@gmail.com
[1] Hacettepe University
ORCID: https://orcid.org/0000-0001-8686-6988, https://orcid.org/0000-0001-6421-185X
E-mail: ufuk.celikcan@gmail.com

concerning both the vertex itself and its neighbor vertices is important. For these reasons, we argue that representing vertices of joints in alternative coordinate systems and processing the motion data accordingly can provide a better solution.

In this article, we propose a novel keyframe extraction approach. In our approach, we represent the joints in the frames with linear rotation invariant (LRI) coordinates [1], apply principal component analysis (PCA) [2] to reduce the data dimension and extract summary data of each keyframe. Then, we divide them into clusters with the K-means algorithm [3] and select keyframes according to cosine similarity concerning adjacent keyframes. Also, we examine the performance effect of LRI transformation on our method against using regular Cartesian coordinates without LRI.

The structure of this paper is as follows: Section 2 gives a review of prior work on the subject matter. After that, we detail our solution and provide experimental results collected with our online user study in Sections 3 and 4, respectively. Finally, Section 5 concludes the paper.

2. RELATED WORK

There have been a number of different approaches for keyframe extraction. These previous methods either convert the motion data into various spaces, use motion/frame data as trajectory/motion curves, apply clustering algorithms, handle a matrix factorization problem, or solve a kind of machine learning problem with a genetic algorithm.

Representing skeletal animations in different spaces can provide the facility to determine the difference between frames. The method by Kapadia et al. [4] indexes the motion data in a trie-based structure according to structural, geometrically, and dynamic features. This trie-based structure contains most salience keyframes of the animation. Jin et al.'s method [5] focuses on determining the saliency of the frames. The method computes the saliency of each frame and selects groups from these frames. After this step, the solution uses a non-linear dimension reduction algorithm and extracts keyframes. The method proposed by Voulodimos et al. [6] creates physics-based temporal summaries and determines different keyframes, while Sapinski et al.'s method [7] defines a new representation using the spatial location and orientation of the keyframe joints and selects keyframes from this representation. Xia et al. [8] defines a joint kernel sparse representation, and the algorithm determines the sparseness of the frames and then decides keyframes according to the calculated sparseness value. Choensawat et al. [9] introduced an algorithm named GENLABAN by which they calculate a score for each frame by analyzing body motion, body postures, and weight of the body parts. With these scores, the algorithm extracts keyframes.

Solutions based on trajectory or motion curves convert skeletal animation to a curve and then apply their algorithms to this curve. Miura et al. [10] combines curve-simplification and Bayesian information criterion to extract keyframes from given motion capture data. After the algorithm generates the motion curve, the method divides the curve into two segments at the point most distant from the straight line connecting the endpoints. For the calculated error between the curve and simplified line, the method uses the Bayesian information criterion to select keyframes. Bulut and Capin [11] defined a metric named curve saliency. The solution detects salient parts of the curve and uses Gaussian weighted average value distribution to select keyframes. In the method by Togawa and Okuda [12], after the joints in the animation are converted into curves, the algorithm calculates the cost value for all frames and conducts elimination of frames accordingly. These steps repeat until the most important keyframes remain. The algorithm by Yang et al. [13] applies Butterworth filtering and PCA to the input data and then selects keyframes with zero-crossing points of velocity. Zhang et al.'s method [14] creates motion curves from the amplitudes of motion of joints, applies PCA, defines a distance characteristic curve, and eventually uses this curve to extract keyframes. The method proposed by Halit and Capin [15] defined a metric named 'motion saliency'. With this metric, their method analyzes the motion curve of the animation and extracts keyframes.

In contrast, clustering-based approaches convert skeletal animation into a different dimension and handle the task as a type of shortest-path problem. One such method by Roberts et al. [16] simplifies the motion frames by around 10% while retaining most of its detail. The method considers each frame as a node in a weighted graph and calculates the weights of the graph with the perpendicular distance between joint positions in each node (frame). After these calculations, the algorithm selects the nearest N keyframes according to weights. Sun et al.'s method [17] defines the inter-frame similarity metric based on a group of motion joints and uses affine propagation clustering to extract keyframes. Qiang Zhang et al.'s method [18] uses an unsupervised clustering algorithm to divide frames into two classes by similarity distances and, in the last step, uses dynamic clustering ISODATA to centralize similar frames and eliminate them.

Matrix factorization solutions represent given skeletal animation data as matrices. The algorithm by Huang et al. [19] provides a solution handled as a constrained matrix factorization problem with a least-squares optimization technique. This method represents the animation as matrices that contain key weights and non-keyframe weights. The algorithm uses these two matrices to extract keyframes according to user-specified error tolerance iteratively.

Machine learning solutions often use genetic algorithms to determine keyframes from the animation data. For instance, the method by Zhang et al. [20] uses a multiple-population-based genetic algorithm and defines a fitness method to meet minimizing the reconstruction error to select keyframes. Liu et al.'s method [21] uses genetic optimization algorithms and calculates the sparseness of the frames for determining keyframes.

3. METHOD

Although our method uses a clustering approach, unlike other solutions, it applies LRI and PCA methods before the clustering process. Applying LRI and PCA algorithms summarizes the characteristic information of each keyframe. Also, our solution makes use of the cosine similarity measure to estimate similarity between summarized keyframes.

Our proposed method consists of two main steps. The first step comprises representing skeletal motion frames in LRI local frames and dimension reduction by applying PCA. At the end of the first step, we get summarized data for each frame in the motion data. For the second step, we divide obtained data from the first step into clusters with the K-means algorithm. Then we use cosine similarity to determine the selected keyframe for each cluster.

In the following,$A = \left(F_{1,}F_{2,}, F_{3,}, \dots, F_k\right)$ defines a skeletal motion where *k* is the keyframe count of the motion and *F* defines a keyframe of a skeletal motion such that $F_i = (j_1, j_2, j_3 \dots, j_n)$, $j_n \in R^3$ where *n* is the number of joints *j* in the skeleton model so that F_i defines the set of joint positions for the i^{th} keyframe of the given motion.

As mentioned above, our solution *O(A)* outputs $(C_1^1, C_2^1, C_3^1, C_n^1, C_1^2, C_2^2, C_3^2, \dots, C_{n2}^2, \dots, C_{nm}^m)$ where *O* applies LRI, PCA, and K-means algorithms, respectively over *A*. *C* defines a cluster in the result that contains summarized data for each keyframe in the same order after applied LRI conversion and PCA algorithm. *m* is the total number of clusters. n_i is the element count of the i^{th} cluster. Accordingly, n_m is the element count of the related extracted cluster.

After obtaining clusters from the first step, we use cosine similarity *S* as a measure of detecting similarity between two summarized keyframes for the clusters of summarized keyframes as follows.

$$S(X, Y) = \frac{\sum_{n=1}^{3} X_n \times Y_n}{\sqrt{\sum_{n=1}^{3} X_n^2} \times \sqrt{\sum_{n=1}^{3} Y_n^2}} \qquad (1)$$

Our algorithm selects a keyframe from the obtained cluster iteratively. To accomplish that, we define two vectors for each iteration. The first vector is the difference between the candidate summarized frame data and the previous one. The second vector is the difference between the next one and the candidate summarized frame data. With these two vectors, our algorithm gathers information about the motion changes. If these vectors are similar, that means these frames are also similar. For this reason, initially, the algorithm determines the second summarized keyframe C_m^2 as the first candidate keyframe where m is the iterating cluster in the algorithm and calculates two vectors using that. The first one of these is $v_1 = C_m^i - C_m^{i-1}$ where i is the iterating (candidate) summarized keyframe. The equation gives the difference between the candidate summarized keyframe and the previous one. The second one $v_2 = C_m^{i+1} - C_m^i$ is the difference between next one and candidate summarized keyframe. With these two vectors, the first similarity value σ initialized by using the Equation 1 above as

$$\sigma = S(v_1, v_2) \qquad (2)$$

and the selected pose *sp* is initialized as 2.

After this initialization, σ will be updated when the new similarity in the processed iteration is less than the current value. The algorithm tries to find the keyframe that has the least similarity with the rest iteratively, as follows.

$$(sp, \sigma) = \left\{ \begin{array}{ll} sp = i, \sigma = S(V_{i-1}^c, V_{i+1}^c), & if\ S(V_{i-1}^c, V_{i+1}^c) \leq \sigma \\ resume & , otherwise \end{array} \right\} \qquad (3)$$

In this equation, V_{i-1}^c defines the vector difference between the current summarized keyframe in the iteration and the previous one in the cluster *c*. Similarly, V_{i+1}^c defines the vector difference between the current summarized keyframe in the iteration and the next one in the related cluster *c*.

3.1. Representing Motion as LRI Local Frames

As a representation, LRI defines a separate local frame for each vertex, where the discrete forms encode the relationship and change between adjacent local frames. A local frame contains all characteristic properties of the vertex it belongs to and encodes properties relative to the neighboring vertices.

LRI defines two discrete forms. The first discrete form is for the projections of the neighboring vertices into the tangent plane of the vertex. It also denotes lengths of the projected edges on the tangent plane and signed angles between every two adjacent projected edges. The first discrete form provides invariability for positions of vertices, but it lacks information in the normal direction of neighboring vertices. For this reason, LRI also provides a second discrete form. The second discrete form can be considered as a function that defines height distances from vertex to tangent plane. LRI calculates unit vectors as the differences of these discrete forms of neighbor vertices. In the last step, LRI uses only the coefficients of this calculation to represent meshes.

The critical feature of the LRI representation is that the vertices of a given mesh are represented in relative coordinates using these specified local frames. Because this relative definition contains no global information about the mesh's location or orientation, it also ensures invariance under rigid transformations.

For the discrete equations, vertices are denoted by x^i, their corresponding positions in R^3 are denoted by $\hat{x}^i$. The edge towards the k^{th} neighbor of i is x_k^i. Mesh edges in R^3 are denoted by $\hat{x}_k^i$, and their projection onto the tangent plane by $\tilde{x}_k^i$. Each vertex and their neighboring vertices are parameterized as U_i and triangles are denoted by $\triangle_k^i$ for defined set U_i consisting of vertices x^i, x_k^i and x_{k+1}^i. The first discrete form uses the standard inner product of triangles corresponding in the tangent plane T_iM. Let $\mu = \mu_1 x_k^i + \mu_2 x_{k+1}^i$ be a vector in $\triangle_k^i$. Here, μ_1 and μ_2 are the vector components of the defined triangle. According to this equation, μ becomes the diagonal vector of the triangle.

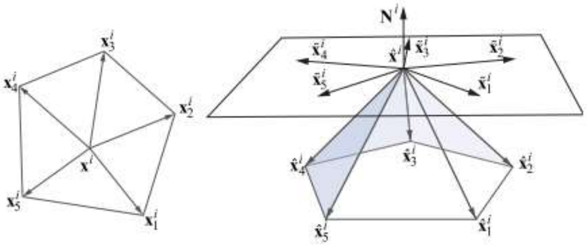

Figure 1 Representing 1-ring neighborhood mesh and tangent plane

The first discrete form equation is given as

$$\tilde{I}(.): \bigcup_{k1}^{d_i-1} \triangle_k^i \to R. \tag{4}$$

where

$$\tilde{I}(\mu) = \langle \mu, \mu \rangle_{R^3} = \left\langle \mu_1 \widetilde{x_k^i} + \mu_2 \widetilde{x_{k+1}^i}, \mu_1 \widetilde{x_k^i} + \mu_2 \widetilde{x_{k+1}^i} \right\rangle_{R^3} = \mu_1^2 \widetilde{g_{k,k}^i} + 2\mu_1\mu_2 \widetilde{g_{k,k+1}^i} + \mu_2^2 \widetilde{g_{k+1,k+1}^i} \tag{5}$$

and the second discrete form equation is given as

$$\widetilde{II}(.): \bigcup_{k1}^{d_i-1} \triangle_k^i \to R. \tag{6}$$

where

$$\widetilde{II^i}(\mu) := \mu_1 \left\langle \widehat{x_k^i}, N^i \right\rangle_{R^3} + \mu_2 \left\langle \widetilde{x_{k+1}^i}, N^i \right\rangle_{R^3} = \mu_1 \widetilde{L_k^i} + \mu_2 \widetilde{L_{k+1}^i} \tag{7}$$

in which the coefficients $\tilde{L} = \left\langle \widetilde{x_k^i}, N^i \right\rangle_{R^3}$ and N^i is the normal of the vertex i in the tangent plane. LRI defines the local frame with a triplet b_1^i, b_2^i, N^i using these two discrete forms, where $b_1^i \in T_iM$ is a unit vector parallel to $\widetilde{x_1^i}$, b_2^i is a unit vector orthogonal to $\widetilde{x_1^i}$ and δ is the difference operator on the discrete frame vectors:

$$\delta_j(b_1^i) = b_1^j - b_1^i \tag{8}$$
$$\delta_j(b_2^i) = b_2^j - b_2^i \tag{9}$$
$$\delta_j(N^i) = N^j - N^i \tag{10}$$

Finally, the discrete local frame equations

$$\delta_j(b_1^i) = \Gamma_{j,1}^{i,1} b_1^i + \Gamma_{j,1}^{i,2} b_2^i + A_{j,1}^1 N^i \tag{11}$$
$$\delta_j(b_2^i) = \Gamma_{j,2}^{i,1} b_1^i + \Gamma_{j,2}^{i,2} b_2^i + A_{j,2}^1 N^i \tag{12}$$
$$\delta_j(N^i) = \Gamma_{j,3}^{i,1} b_1^i + \Gamma_{j,3}^{i,2} b_2^i + A_{j,3}^1 N^i \tag{13}$$

As previously stated, LRI representation defines local frames that filter out global positions and rotations from the mesh. We use these local frames in our solution. Since the LRI method is defined for meshes, in the first step of our solution, we transform skeleton data for each frame into a 1-ring neighborhood mesh. We assume that each joint position of the skeleton data is a vertex of a 1-ring neighborhood mesh (see Figure 1). After that, we apply LRI to this assumed mesh to extract LRI local frames for each vertex. LRI local frames are a matrix that consists of 9 values and encode characteristic properties of the related vertex and relation between neighborhood vertices. We construct a matrix whose dimension is 9 times the total number of employed joints for each keyframe. Although the extracted local frames are enough to detect similarity between adjacent vertices, we apply dimension reduction by PCA to all keyframe matrices. This way, PCA provides to eliminate the sparse density of the matrices, improving the performance of selecting keyframes computing and obtaining more meaningful data (Figure 2)

In the dimension reduction step, instead of representing LRI data in fixed number of dimensions, our algorithm uses representations of dynamically changing dimensions. This implies that the dimensionality adapts to the given motion. This is carried out according to principles of the PCA method with the condition that the sum of them explains the given LRI data with at least 95% accuracy. Our tests show that between 4 and 12 dimensions are sufficient to explain LRI data with at least 95% accuracy, in general. After these steps, the processed data can be used for extraction and reduction operations.

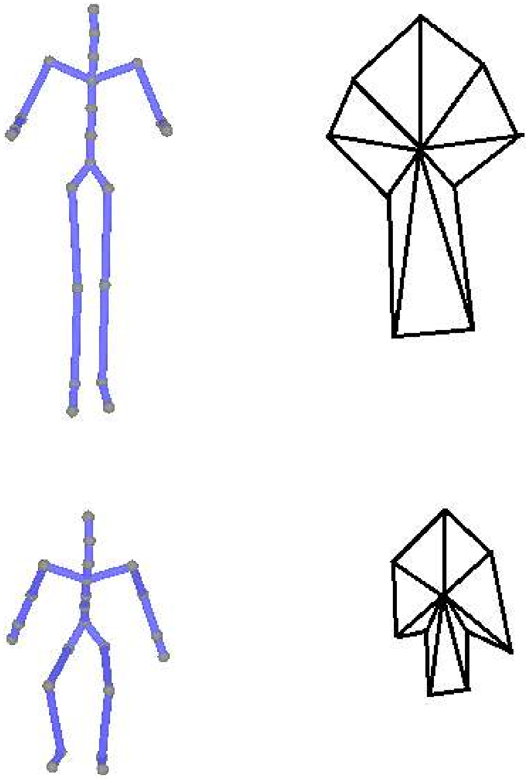

Figure 2 Skeleton data representation as a 1-ring neighborhood mesh

3.2. Clustering and Reducing Keyframes

Our approach uses the K-means classification algorithm for clustering and cosine similarity to measure similarity between keyframes. Firstly, we apply the K-means clustering algorithm to the dimensionally reduced the data (Figures 3 and 4). Our method dynamically clusters up to the desired number of keyframes and calculates the cosine similarity between sequential candidate keyframe changes. Thus, our method selects a keyframe that has the minimum similarity value relative to the rest of the cluster values for each cluster. As a result, the most different keyframes are selected.

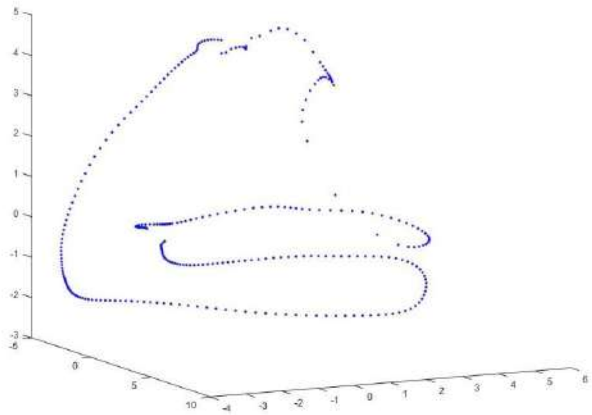

Figure 3 Motion data representation after LRI and PCA steps are applied. The graph shows the distribution of the frames in the motion in 3D space

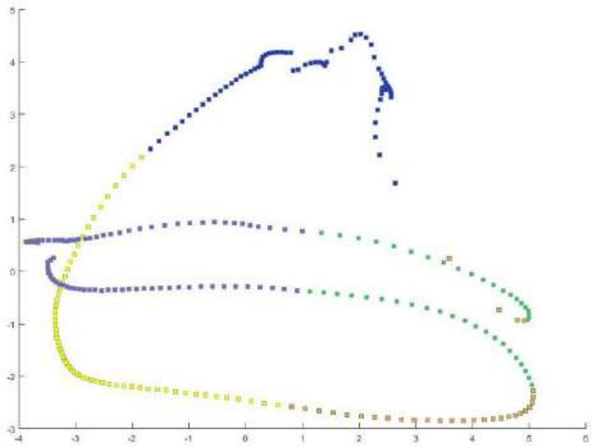

Figure 4 Clustering result of the motion after K-Means applied. This graph contains the distribution of the motion as divided into 5 clusters. Each color (yellow, blue, gold, green, and purple) in the graph represents a distinct cluster. Accordingly, one keyframe for each cluster will be extracted

4. RESULTS

In this study, we used the HDM05 dataset for testing and evaluation of our proposed method. HDM05 is a royalty-free motion capture dataset created by Müller et al. [22]. It features more than 70 motion classes in ten to fifty realizations performed by a variety of performers. The sampling rate of performances in the dataset is 120 Hz. For evaluation, we selected 10 relatively short motions (Table 1) from the dataset and used our method to extract five keyframes from each motion. Figure 5 demonstrates sample sets of keyframes extracted from three of these motions using our proposed method.

Furthermore, as our study results can be subjective, we prepared a website to survey subjective performance evaluations of the participants comparing the results obtained by our method using LRI representations to the ones without. The survey included the ten pre-selected motions under consideration with two sets of five extracted keyframes for each motion, one set including the results of our method and the other including the results obtained using the standard Cartesian coordinate representation. Figures 6 and 7 demonstrate sample results for cartwheel and punch motions in both representations.

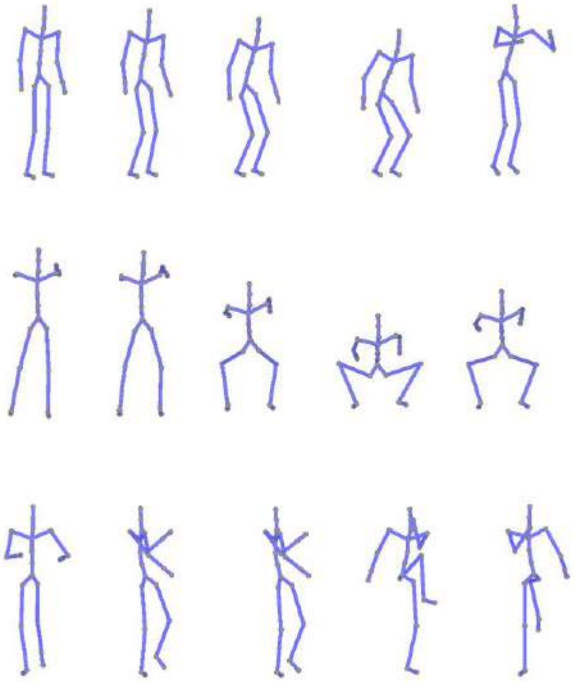

Figure 5 Sample sets of keyframes extracted using our method. Each row illustrates a set of 5 keyframes extracted from jumping, squat and knee to elbows motions, respectively

With the survey, only the gender and age information were collected from the participants, remaining otherwise anonymous. All participants volunteered to take the online survey and none of them have been compensated in any way.

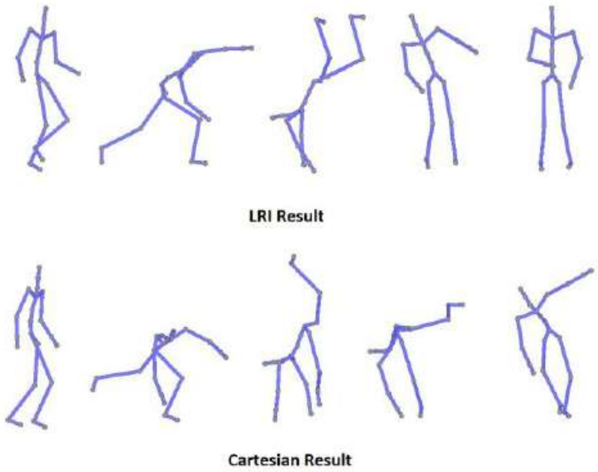

Figure 6 Extracted keyframes from cartwheel motion

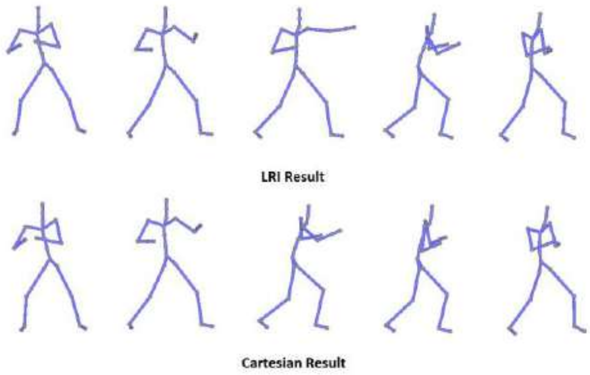

Figure 7 Extracted keyframes from punch motion

Table 1 The motions used in the experiment and their corresponding frame counts

#	Motion	Frame Count
1	Cartwheel	401
2	Elbow to Knee	319
3	Jump Down	272
4	Jumping Jack	142
5	Kick	295
6	Lie Down	621
7	Punch	115
8	Squat	191
9	Throw Basketball	452
10	Throw Ball	427

The survey procedure took place as follows. When a participant visited our online survey website, they were first briefly informed about the study and their gender and age information were collected at this step (Figure 8). Then, the participant started the evaluation of the results. For each motion queried, the participant initially watched the motion in a skeletal animation twice as given in Figure 9. Next, each set of extracted keyframes from the original motion were shown to the participant where the order of the two sets were randomized (Figure 11). Afterwards, the participant watched the original motion with the sets of extracted keyframes shown flanking the original motion on each side as in Figure 12 so that the participant could further assess the differences between the two sets of results. On this page, the participant responded by choosing either of the sets as the best representation of the original motion or 'none' if no significant difference was observed. This is repeated until the participant registered their responses for all 10 motions.

About the Thesis project

This Thesis study aims to detect the most important keyframes and reduction of the keyframe count of the given skeleton animation.
In the next step. We will ask you 10 questions and you answer the result that you think is the closest to the animation above in each question.
Thank you for your contribution, please answer the following questions.

Figure 8 Test step where a participant is informed about the study and reports their gender and age

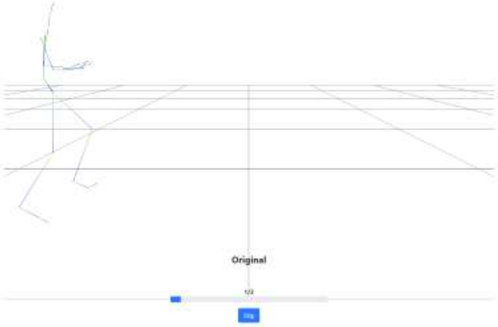

Figure 9 Sample preview of an original motion as shown to the participants with the online survey interface

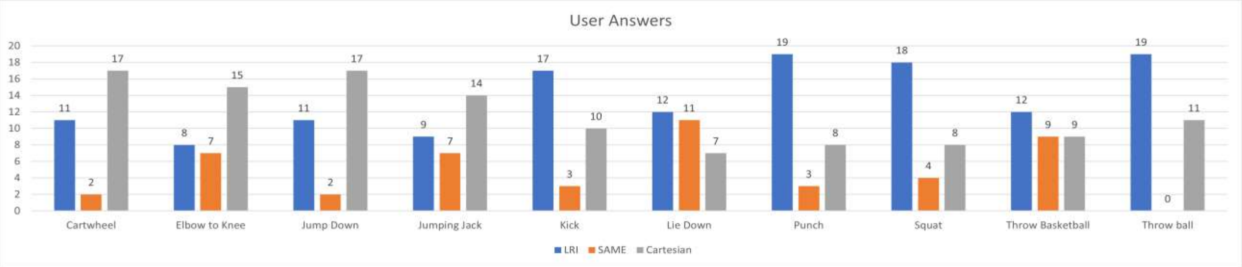

Figure 10 Distribution of participants' preferences per each motion queried. The order of the motions in the figure is the same as in Table 1

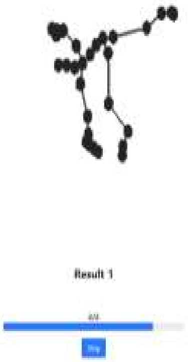

Figure 11 Sample instance where the participant is shown one of the extracted keyframes with the online survey interface

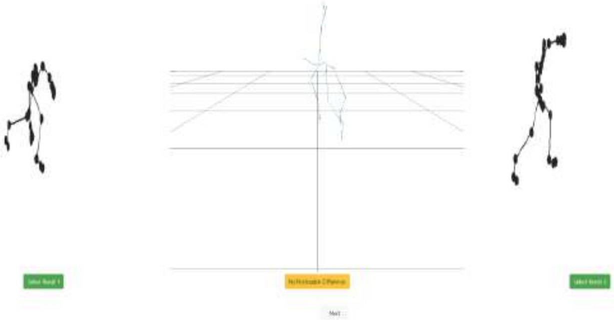

Figure 12 Sample preview of the online survey instance where an original motion is shown to the participant with extracted keyframes of the two alternatives shown consecutively on each side of it

A total of 30 people, 12 female (40%) and 18 male (60%), participated in this study. The average age of the participants was 28 ± 3.14. Evaluation results are provided in Figures 10 and 13. Figure 10 gives participants' preferences for each motion, while Figure 13 gives the overall distribution of all participants' preferences.

The survey outcomes per motion as shown in Figure 10 demonstrate that the participants preferred mostly the sets of keyframes extracted using the Cartesian coordinate system representation for the first four motions under consideration. However, the keyframes obtained using the LRI representation were preferred by more participants for the remaining six motions. Over the whole set of 10 motion queries, the average preference ratio of the LRI results was 13.6% (±4%) while the average for the alternative was 11.6% (±3.64%).

The aggregated preference results given in Figure 13 show that the participants preferred the keyframes extracted by our proposed approach more than the standard alternative by 6% in general while 16% of the votes indicated no preference.

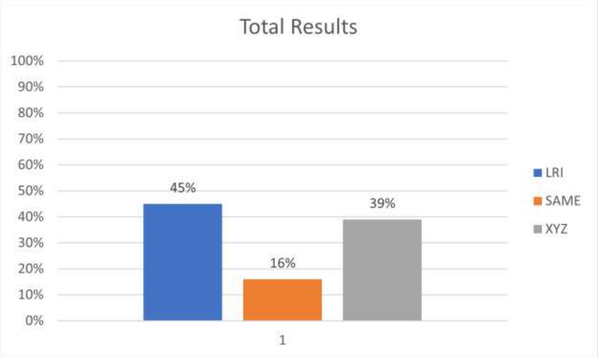

Figure 8 Overall distribution of all participants' preferences collected with the online survey

5. CONCLUSION

We have presented a keyframe extraction method based on LRI coordinates representation and evaluated the method's performance against the ones based on Cartesian coordinates. Our study results underline the potential of LRI for keyframe extraction such that using our solution based on it outperforms the standard representation with a slightly better performance (6%).

This work shows that representing animation keyframes using alternative representations, such as LRI, can provide better extraction performance for skeletal animations. For future work, it is possible to combine our LRI based approach with deep learning methods such as using transformer networks. Our method can use different similarity measures rather than the cosine similarity or it can be combined with other keyframe extraction methods such as curve simplification or matrix factorization approaches towards achieving better performance. Our proposed method can be used for keyframe reduction and compression purposes, as well.

Acknowledgments

The authors would like to thank all volunteers who participated in the online survey anonymously.

Funding

The authors have not received any financial support for the research, authorship, or publication of this study.

Authors' Contribution

The authors contributed equally to the study.

The Declaration of Conflict of Interest/ Common Interest

The authors declare no conflict of interest or common interest.

The Declaration of Ethics Committee Approval

This study does not require ethics committee permission or any special permission.

The Declaration of Research and Publication Ethics

The authors of the paper declare that they comply with the scientific, ethical and quotation rules of SAUJS in all processes of the paper and that they do not make any falsification on the data collected. In addition, they declare that Sakarya University Journal of Science and its editorial board have no responsibility for any ethical violations that may be encountered, and that this study has not been evaluated in any academic publication environment other than Sakarya University Journal of Science.

REFERENCES

[1] Y. Lipman, O. Sorkine, D. Levin, D. Cohen-Or, “Linear rotation-invariant coordinates for meshes” ACM Transactions on Graphics, vol. 24, no. 3, p. 479–487, jul 2005.

[2] A. Mackiewicz, W. Ratajczak, “Principal components analysis (pca)” Computers & Geosciences, vol. 19, no. 3, pp. 303–342, 1993.

[3] S. Lloyd, “Least squares quantization in pcm,” IEEE Transactions on Information Theory, vol. 28, no. 2, pp. 129–137, 1982.

[4] M. Kapadia, I.-k. Chiang, T. Thomas, N. I. Badler, J. T. Kider, “Efficient motion retrieval in large motion databases,” in Proceedings of the ACM SIGGRAPH Symposium on Interactive 3D Graphics and Games, ser. I3D ’13. New York, NY, USA: Association for Computing Machinery, 2013, p. 19–28.

[5] C. Jin, T. Fevens, S. Mudur, “Optimized keyframe extraction for 3d character animations,” Computer Animation and Virtual Worlds, vol. 23, no. 6, pp. 559–568, 2012.

[6] A. Voulodimos, I. Rallis, N. Doulamis, “Physics-based keyframe selection for human motion summarization,” Multimedia Tools and Applications, vol. 79, no. 5, pp. 3243–3259, 2020.

[7] T. Sapinski, D. Kaminska, A. Pelikant, G. Anbarjafari, “Emotion recognition from skeletal movements,” Entropy, vol. 21, no. 7, 2019.

[8] G. Xia, H. Sun, X. Niu, G. Zhang, L. Feng, “Keyframe extraction for human motion capture data based on joint kernel sparse representation,” IEEE Transactions on Industrial Electronics, vol. 64, no. 2, pp. 1589–1599, 2017.

[9] W. Choensawat, M. Nakamura, K. Hachimura, “Genlaban: A tool for generating labanotation from motion capture data,” Multimedia Tools and Applications, vol. 74, no. 23, pp. 10823-10846, 2015.

[10] T. Miura, T. Kaiga, N. Matsumoto, H. Katsura, K. Tajima, H. Tamamoto, “Application of the bayesian information criterion to keyframe extraction from motion capture data,” in SIGGRAPH Asia 2011 Posters, ser. SA ’11. New York, NY, USA: Association for Computing Machinery, 2011.

[11] E. Bulut, T. Capin, “Key frame extraction from motion capture data by curve saliency,” CASA, 2007.

[12] H. Togawa, M. Okuda, “Position-based keyframe selection for human motion animation,” in 11th International Conference on Parallel and Distributed Systems (ICPADS’05), vol. 2, 2005, pp. 182–185

[13] Y. Yang, L. Zeng, H. Leung, “Keyframe extraction from motion capture data for visualization,” in 2016 International Conference on Virtual Reality and

Visualization (ICVRV), 2016, pp. 154–157.

[14] Q. Zhang, X. Xue, D. Zhou, X. Wei, "Motion key-frames extraction based on amplitude of distance characteristic curve," International Journal of Computational Intelligence Systems, vol. 7, no. 3, pp. 506–514, 2014.

[15] C. Halit, T. Capin, "Multiscale motion saliency for keyframe extraction from motion capture sequences," Computer Animation and Virtual Worlds, vol. 22, no. 1, pp. 3–14, 2011.

[16] R. Roberts, J. P. Lewis, K. Anjyo, J. Seo, Y. Seol, "Optimal and interactive keyframe selection for motion capture," in SIGGRAPH Asia 2018 Technical Briefs, ser. SA '18. New York, NY, USA: Association for Computing Machinery, 2018.

[17] B. Sun, D. Kong, S. Wang, J. Li, "Keyframe extraction for human motion capture data based on affinity propagation," in 2018 IEEE 9th Annual Information Technology, Electronics and Mobile Communication Conference (IEMCON), 2018, pp. 107–112.

[18] Q. Zhang, S.-P. Yu, D.-S. Zhou, X.-P. Wei, "An efficient method of key-frame extraction based on a cluster algorithm," Journal of Human Kinetics, vol. 39, no. 1, pp. 5–14, 2013.

[19] K.-S. Huang, C.-F. Chang, Y.-Y. Hsu, S.-N. Yang, "Key probe: A technique for animation keyframe extraction," The Visual Computer, vol. 21, pp. 532–541, 2005.

[20] Q. Zhang, S. Zhang, D. Zhou, "Keyframe extraction from human motion capture data based on a multiple population genetic algorithm," Symmetry, vol. 6, pp. 926–937, 2014.

[21] X.-m. Liu, A.-m. Hao, D. Zhao, "Optimization-based key frame extraction for motion capture animation," The Visual Computer, vol. 29, 2012.

[22] M. Müller, T. Röder, M. Clausen, B. Eberhardt, B. Krüger, A. Weber, "Documentation mocap database hdm05," Universität Bonn, Tech. Rep. CG-2007-2, 2007.

SAKARYA ÜNİVERSİTESİ

FEN BİLİMLERİ ENSTİTÜSÜ
DERGİSİ

Sakarya University Journal of Science
SAUJS

ISSN 1301-4048 | e-ISSN 2147-835X | Period Bimonthly | Founded: 1997 | Publisher Sakarya University |
http://www.saujs.sakarya.edu.tr/

Title: A Remarkable Record of Little-Known Parasitoid Wasp Helorus striolatus (Hymenoptera: Heloridae) from Türkiye with A Global Checklist of the this Family

Authors: İlyas CAN

Recieved: 2022-01-07 00:00:00

Accepted: 2022-09-09 00:00:00

Article Type: Research Article

Volume: 25
Issue: 5
Month: October
Year: 2022
Pages: 1052-1058

How to cite
İlyas CAN; (2022), A Remarkable Record of Little-Known Parasitoid Wasp Helorus striolatus (Hymenoptera: Heloridae) from Türkiye with A Global Checklist of the this Family . Sakarya University Journal of Science, 25(5), 1052-1058, DOI: 10.16984/saufenbilder.1054074
Access link
http://www.saujs.sakarya.edu.tr/en/pub/issue/73051/1054074

Sakarya University Journal of Science 25(5), 1052-1058, 2022

A Remarkable Record of Little-Known Parasitoid Wasp *Helorus striolatus* (Hymenoptera: Heloridae) from Türkiye with A Global Checklist of the this Family

İlyas CAN*[1]

Abstract

The Heloridae (Hymenoptera: Proctorupoidea) is a family of parasitoid wasps composed of a single genus, *Helorus* with eighteen extant species. For Türkiye, only two species have been reported: *Helorus anomalipes* (from Ankara, Central Anatolia) and *H. striolatus* (from Bingöl, Eastern Anatolia). In this study, a new distribution record is given for *H. striolatus* from Kocaeli province (Marmara region), which is the second record of this relatively little-known species in this country. In addition, an updated checklist of the family Heloridae is presented.

Keywords: Hymenoptera, heloridae, parasitoid, *Helorus striolatus,* second record, Türkiye

1. INTRODUCTION

The Heloridae Foerster, 1856 is a small family belonging to superfamily Proctotrupoidea of order Hymenoptera. Members of this family are solitary endoparasites of green lacewings larvae (Neuroptera: Chrysopidae). Their larvae feed on the nutrition contents of the host and emerge as adults from the cocoon [1].

This family contains only one genus: *Helorus* Latreille, 1802, and 18 valid species described nearly worldwide. So far, four species of the genus have been recorded in the western Palearctic and two of them are known from Türkiye: *H. anomalipes* (Panzer, 1798) and *H. striolatus* Cameron, 1906. These species were recorded from the country based on only one specimen of each species collected in 1977 and 1985 [2, 3]. As in the rest of the world, information about this group is also very rare in Türkiye. On the other hand, the species list of Heloridae has been given in a few articles [2-4], so the updated data of the family in the world have not been compiled.

In this study, it was aimed to provide the second record of *H. striolatus* from Türkiye over 35 years. In addition, data on the distribution and biology of all species of the family are provided.

2. MATERIALS AND METHODS

The adult wasp specimen was collected using an insect net in the Kocaeli province of Türkiye. Identification and nomenclature of *Helorus striolatus,* follows van Achterberg [3], and Izadizadeh et al. [4]. The collected material is deposited in the Entomological Research Laboratory, in

---

* Corresponding author: ilyas.can@gop.edu.tr
[1] Tokat Gaziosmanpaşa University
ORCID: https://orcid.org/0000-0003-3013-6614

Gaziosmanpaşa University, Tokat, Türkiye. Based on the literature review, the species list and information about Heloridae are given in Table 1. The photographs of the specimen were taken using a Leica M205C stereomicroscope controlled by the Leica Application Suite 3 software.

3. RESULTS

Order: Hymenoptera

Superfamily: Proctotrupoidea

Family: Heloridae Förster, 1856

Genus: *Helorus* Latreille, 1802

Members of the Heloridae have a general morphology, with the robust, usually black body (6-8 mm); long, sickle-shaped, and crossing over scissor-like mandibles; long and narrow labrum; ring-like article between pedicel and first flagellomere; pectinated tarsal claws; distinctly elongated first metasomal segment; fore wing with five closed cells; metasomal terga 2-4 fused into syntergite [1].

***Helorus anomalipes* (Panzer, 1798)**

Global distribution: Austria, Belgium, Bulgaria, Canada, China, England, Estonia, France, Germany, Hungary, Ireland, Korea, Lebanon, Mongolia, Netherlands, Spain, Sweden, Türkiye, United States of America (Figure 1a).

The previous record in Türkiye: Ankara (no specific locality) [2] (Figure 1b).

***Helorus striolatus* Cameron, 1906** (Figure 2)

Global Distribution: Austria, Bulgaria, Czechia, Estonia, Finland, France, Germany, Greece, Hungary, Italy, Lithuania, Netherlands, Poland, Russia (south), Spain, Sweden, Switzerland, Türkiye, Ukraine (Figure 1a).

The previous record in Türkiye (Figure 1b)**:** Bingöl, 15 km S Genç, 1400 m, 13.viii.1985 [3].

Material examined: Kocaeli, Gölcük, İhsaniye, 40°41'00" N; 29°48'56" E, 111 m, 06.vi.2019, ♀.

Figure 1 Distribution maps of Heloridae species found in Türkiye; a) Western Palearctic distribution of *Helorus anomalipes* (stars) and *Helorus striolatus* (circles); b) previous locality record of *H. anomalipes* (red) and *H. striolatus* (black), and new locality record of *H. striolatus* (blue) in Türkiye

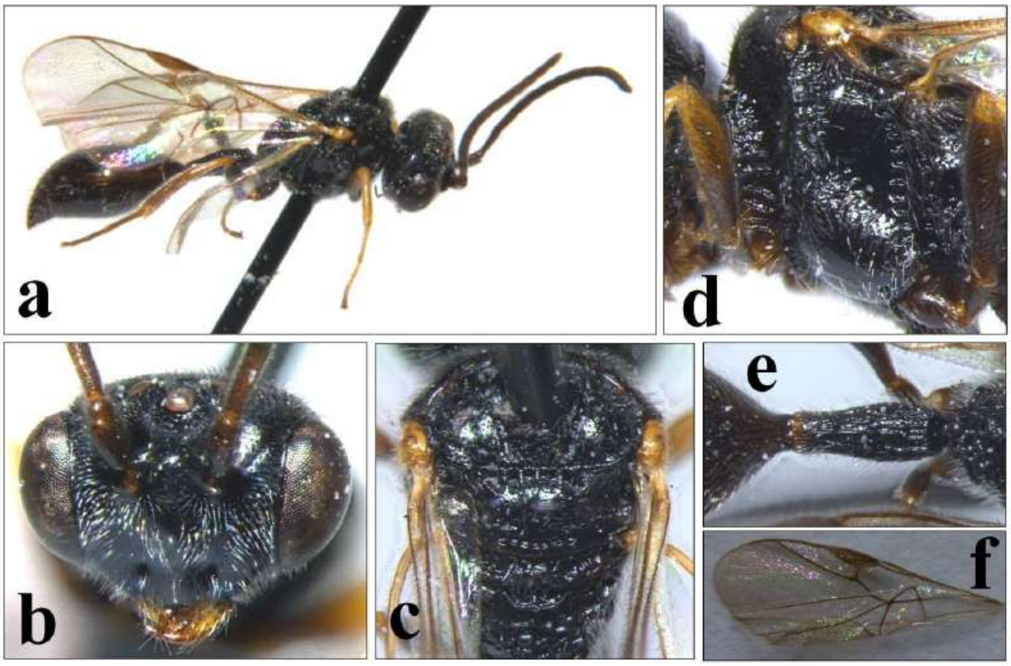

Figure 2 Some taxonomic characters of *Helorus striolatus* Cameron, 1906, ♀; a) general habitus; b) frontal view of the head; c) dorsal view of mesosoma; d) mesopleuron; e) dorsal view of first metasomal tergite; f) forewing

4. DISCUSSION

The first specimen of *H. striolatus* was collected from the Bingöl province in the eastern Anatolian region of Türkiye in 1985 by R. Hensen and deposited in the National Museum of Natural History, Leiden, Netherlands. Then this specimen was identified and recorded for the first time from Türkiye by van Achterbeg [3]. Almost thirty-five years after the first detection date, this species was recorded for the second time from the Marmara region of Türkiye, and its presence in the country was verified by this study (Figure 1b). While the individual belonging to this species had been caught almost in the middle of August in the Eastern Anatolia region in the previous study, it was caught in the Marmara region at the beginning of June in this study. The material in this study based on a randomly collected specimen during field studies. Thus, more rigorous work is necessary for revealing Heloridae taxa currently found in Türkiye. If the habitats of their prey, Chrysopidae (Neuroptera), are followed in subsequent studies, more specimens will be able to be caught with Malaise traps.

The updated checklist of family Heloridae

Townes [2] carried out the most important research on the first revision of Heloridae and gave detailed information about all species. Subsequently, van Achterberg [3] provided the relevant details on European species of genus *Helorus* as well as describing additional new species based on Sulawesi specimens.

Table 1 Information about species of Heloridae family in the world

Number	Name of Species	Synonym	Described sexes	Host	Recorded Country	References
1	*Helorus alborzicus* Izadizadeh, van Achterberg and Talebi, 2015	*H. xinjiangensis* He and Xu, 2015	♀, ♂	Unknown specific host	Iran	[4, 5]
2	*Helorus anomalipes* (Panzer, 1798)	*Sphex anomalipes* Panzer, 1798 *Helorus ater* Latreille, 1802 *Copelus paradoxus* Provancher, 1881	♀, ♂	*Chrysopa majuscula* *Dichochrysa prasina* *Chrysoperla carnea* *Chrysopa rufilabris?*	Austria, Belgium, Bulgaria, Canada, China, England, Estonia, France, Germany, Hungary, Ireland, Korea, Lebanon, Mongolia, Netherlands, Spain, Sweden, Türkiye, USA	[3, 4, 6]
3	*Helorus antefurcalis* He and Xu,2015	–	♀, ♂	Unknown specific host	China	[4]
4	*Helorus australiensis* New, 1975	–	♀, ♂	*Chrysopa ramburi* *Chrysopa near* *Chrysopa near dispar* *Chrysopa near signata*	Australia	[2]
5	*Helorus brethesi* Ogloblin,1928	–	♀, ♂	Unknown specific host	Argentina, Brazil, Colombia, Costa Rica, Mexico, Panama	[7]
6	*Helorus caii* He and Xu, 2015	–	♂	Unknown specific host	China	[4]
7	*Helorus celebensis* van Achterberg, 2006	–	♀, ♂	Unknown specific host	Indonesia	[3]
8	*Helorus chinensis* He, 1992	–	♀, ♂	*Chrysopa septempunctata*	China	[8, 9]
9	*Helorus elgoni* Risbec, 1950	–	♀, ♂	*Chrysoperla spp*	Kenya	[2]
10	*Helorus heilongjiangensis* He & Xu, 2015	–	♀	Unknown specific host	China	[9]
11	*Helorus jilinensis* He and Xu, 2015	–	♀	Unknown specific host	China	[9]
12	*Helorus nigripes* Foerster, 1856	*H. rugosus* Thomson, 1858	♀, ♂	*Chrysopa nigricostata* *Chrysopa septempunctata* *Chrysopa spp.*	Austria, Belgium, Bulgaria, Czechia, Denmark, England, Estonia, France, Germany, Hungary, Moldova, Netherlands, Sweden, Switzerland, Ukraine	[2, 3, 6, 10]

Table 1 Information about species of Heloridae family in the world (continue)

Number	Name of Species	Synonym	Described sexes	Host	Recorded Country	References
13	*Helorus niuginiae* Naumann, 1983	–	♂	Unknown specific host	New Guinea	[11]
14	*Helorus reni* He and Xu, 2015	–	♂	Unknown specific host	China	[9]
15	*Helorus ruficornis* Foerster, 1956	*H. coruscus* Haliday, 1857 *H. flavipes* Kieffer, 1907	♀, ♂	*Chrysopa prasina* *Chrysopa ventralis* *Chrysopa shansiensis* *Dichochrysa ventralis* *Pseudomallada prasinus*	Andorra, Austria, Bulgaria, Burundi, Czechia, England, Estonia, Finland, France, French Polynesia (Tahiti), Germany, Hawaiian Islands, Italy, Japan, Kenya, Korea, Nepal, Pakistan, Saouth Africa, Spain, Sweden, Switzerland, U. S. A	[2-4, 6, 9, 12-14]
16	*Helorus striolatus* Cameron, 1906	*H. meridionalis* Pschorn-Walcher, 1955	♀, ♂	*Chrysopa flavifrons* *Chrysopa septempunctata*	Austria, Bulgaria, Czechia, Estonia, Finland, France, Germany, Greece, Hungary, Italy, Lithuania, Netherlands, Poland, Russia (south), Spain, Sweden, Switzerland, Türkiye, Ukraine	[2, 3, 6]
17	*Helorus suwai* Kusigemati, 1987	–	♀	Unknown specific host	Japan	[15]
18	*Helorus yezoensis* Kusigemati, 1987	–	♂	Unknown specific host	Japan	[15]

More information on Heloridae was provided by Izadizadeh [5] that a new species was described from Iran and new species records were given in that study. Zhang et al. [4], with the studies carried out on the Chinese fauna, created the identification key for all species except the Australian region and described unknown female of Helorus caii. In the same study, they reported that the Helorus xinjiangensis He and Xu, 2015 is a junior synonym of H. alborzicus Izadizadeh, van Achterberg and Talebi, 2015. In this study, some important data belonging to the family so far have been compiled and brought together in Table 1

Acknowledgments
The author wants to thank the reviewers for all useful and instructive comments on the manuscript.

Funding
The author received no financial support for the research, authorship, and/or publication of this paper.

The Declaration of Conflict of Interest/ Common Interest

No conflict of interest or common interest has been declared by the author.

The Declaration of Ethics Committee Approval

The author declares that this document does not require an ethics committee approval or any special permission.

The Declaration of Research and Publication Ethics

The author of the paper declares that he complies with the scientific, ethical, and quotation rules of SAUJS in all processes of the paper and that he does not make any falsification on the data collected. In addition, he declares that Sakarya University Journal of Science and its editorial board have no responsibility for any ethical violations that may be encountered and that this study has not been evaluated in any academic publication environment other than Sakarya University Journal of Science.

REFERENCES

[1] H. Goulet, J. T. Huber, “Hymenoptera of the world: An identification guide to families.” Centre for Land and Biological Resources Research, Ottawa, Ontario, 1993.

[2] H. K. Townes, “A revision of the Heloridae (Hymenoptera).” Contributions of the American entomological Institute, vol. 15, no 2, pp. 1–12, 1977.

[3] C. van Achterberg, “European species of the genus *Helorus* Latreille (Hymenoptera: Heloridae), with description of a new species from Sulawesi (Indonesia).” Zoologische Mededelingen, vol. 80, no 1, pp. 1–12, 2006.

[4] R. Zhang, C. van Achterberg, X. Tian, C. He, J. Tan, “Sexual variation in two species of *Helorus* Latreille (Hymenoptera, Heloridae) from NW China, with description of female of *Helorus caii* He & Xu.” Zootaxa, vol. 4821, no 3, pp. 570–584, 2020.

[5] M. Izadizadeh, A. A. Talebi, C. van Achterberg, E. Rakhshani, “First record of the family Heloridae (Hymenoptera: Proctotrupoidea) from Iran, with description of a new species.” Zootaxa, vol. 3946, no 4, pp. 577–582, 2015.

[6] V. Soon, P. Tarlap, “First records of the family Heloridae (Hymenoptera) from Estonia.” Sahlbergia, vol. 24, no 2, pp. 12-13, 2018.

[7] C, Dorfey, A. Köhler, K. Schoeninger, “First register of *Helorus brethesi* Oglobin, 1928 (Insecta, Hymenoptera, Heloridae) in Palmeira, PR, Brazil.” Biotemas, vol. 24, no 4, pp. 183-185, 2011.

[8] J. H. He, Heloridae. *In:* J. W. Peng, Y. Q. Liu, (Eds.), “Iconography of forest insects in Hunan, China.” Science Press, Changsha, pp. 1293–1296, 1992.

[9] J. H. He, Z. F. Xu, “Hymenoptera Proctotrupoidea (I), *Fauna Sinica, Insecta Vol. 56, Hymenoptera Proctotrupoidea (I)*.” Science Press, Beijing, 2015.

[10] M. V. L. Barclay, “An interesting insect assemblage reared from the bracket fungus Inonotus hispidus (Bull. Ex Fr.) karst from Hyde Park, Middlesex.” British Journal of Entomology and Natural History, vol. 18, pp. 41-44, 2005.

[11] I. D. Naumann, “A new species of *Helorus* Latreille (Hymenoptera: Proctotrupoidea) from New Guinea.” Journal of Australian Entomological Society, vol. 22, pp. 253-255, 1983.

[12] G. W. Choi, C. J. Kim, J. W Lee, “First record of the family Heloridae (Hymenoptera: Proctotrupoidea) from Korea.” Entomological Research, vol. 42, pp. 122-126, 2011.

[13] M. Buffington, R. S. Copeland, “Redescription of *Helorus ruficornis* Förster (Hymenoptera: Heloridae), with a new synonymy and new Afrotropical specimen records.” Proceedings of the entomological Society of Washington, vol. 118, no 3, pp. 330–344, 2016.

[14] T. Ramage, “First record of the superfamily Proctotrupoidea from French Polynesia (Hymenoptera).” Bulletin de la Societe Entomologique de France, vol. 125, no 4, pp. 404-406, 2020.

[15] K. Kusigemati, “The Heloridae (Hymenoptera: Proctotrupoidea) of Japan.” Kontyu, Tokyo, vol. 55, no 3, pp. 477–485, 1987.

SAKARYA ÜNİVERSİTESİ
FEN BİLİMLERİ ENSTİTÜSÜ
DERGİSİ

Sakarya University Journal of Science
SAUJS

ISSN 1301-4048 | e-ISSN 2147-835X | Period Bimonthly | Founded: 1997 | Publisher Sakarya University |
http://www.saujs.sakarya.edu.tr/

Title: Characterization of Cobalt Oxalate Dihydrate Obtained from Spent Co-Mo/Al2O3 Hydrodesulfurization Catalyst

Authors: Ahmet Orkun KALPAKLI

Recieved: 2022-05-31 00:00:00

Accepted: 2022-09-18 00:00:00

Article Type: Research Article

Volume: 25
Issue: 5
Month: October
Year: 2022
Pages: 1059-1070

How to cite
Ahmet Orkun KALPAKLI; (2022), Characterization of Cobalt Oxalate Dihydrate Obtained from Spent Co-Mo/Al2O3 Hydrodesulfurization Catalyst. Sakarya University Journal of Science, 25(5), 1059-1070, DOI: 10.16984/saufenbilder.1124183
Access link
http://www.saujs.sakarya.edu.tr/en/pub/issue/73051/1124183

Sakarya University Journal of Science 25(5), 1059-1070, 2022

Characterization of Cobalt Oxalate Dihydrate Obtained from Spent Co-Mo/Al_2O_3 Hydrodesulfurization Catalyst

Ahmet Orkun KALPAKLI*[1]

Abstract

In this study, roasted spent Co-Mo/Al_2O_3 hydrodesulfurization (HDS) catalyst was dissolved in oxalic acid ($H_2C_2O_4$) solution and optimum conditions were determined for obtaining cobalt oxalate dihydrate ($CoC_2O_4 \cdot 2H_2O$). The thermal decomposition behavior of the obtained $CoC_2O_4 \cdot 2H_2O$ was investigated by TG/DTG-DTA analysis. The characterization of $CoC_2O_4 \cdot 2H_2O$ was carried out by XRD, FT-IR and SEM-EDS analytical techniques. Optimum conditions for the production of $CoC_2O_4 \cdot 2H_2O$ were determined as 25 ^oC temperature, 0.25 M $H_2C_2O_4$ concentration, 1/20 g mL^{-1} solid/liquid ratio and 300 rpm stirring speed. $CoC_2O_4 \cdot 2H_2O$ was obtained with a reaction yield of 90.9 %. TG/DTG-DTA analysis carried out in dry air atmosphere showed that $CoC_2O_4 \cdot 2H_2O$ decomposed in two steps. In the first step that occurs between 118-196 ^oC temperatures, $CoC_2O_4 \cdot 2H_2O$ is dehydrated. In the second step, which occurs between 248-279 ^oC temperatures, it was determined that metallic cobalt was formed first, and then metallic cobalt was oxidized and converted into Co_3O_4 compound because it was performed in the air atmosphere.

Keywords: Hydrodesulfurization catalyst, cobalt oxalate dihydrate, cobalt oxide, characterization.

1. INTRODUCTION

Hydrodesulfurization (HDS) is a catalytic chemical process applied to remove sulfur from natural gas and refined petroleum products (petroleum, jet fuel, fuel oil, gasoline). The purpose of removing sulfur is to reduce the SO_2 emissions that are released during the use of natural gas and petroleum products. In the HDS process, catalysts containing Mo, Co, Ni and V are used on γ-Al_2O_3 substrate. The catalysts used in the process can be regenerated and reused, but after a certain number of regenerations, they become waste [1, 2]. The disposal or storage of spent catalysts requires compliance with strict environmental regulations. Spent HDS catalysts are classified as hazardous waste by the US Environmental Protection Agency (EPA) [3].

HDS catalysts account for one-third of the world's catalyst consumption. The generation of spent HDS catalyst is estimated to be 1-1.2x10^5 tons per year around the world [4, 5]. Recovery of metals from spent catalysts has become more important in recent years. Metal recycling is crucial not only for metal recovery, but also for making waste catalysts

---

* Correspondingauthor: aok13@iuc.edu.tr
[1] İstanbul Cerrahpaşa University
ORCID: https://orcid.org/0000-0002-8382-4085

harmless to the environment [3]. Spent HDS catalysts are an important secondary source in the production of molybdenum, nickel and cobalt [6, 7]. Alkali or acidic leaching is generally used for metal recovery from spent catalysts [8- 10]. Precious metals dissolved by leaching are recovered by solvent extraction or precipitation processes [11- 14]. Before the leaching process, oxidative roasting is applied to remove the volatile components and sulfur in the spent catalyst in order to increase the leaching efficiency and prevent possible secondary reactions [15- 17].

Spent Co-Mo/Al_2O_3 HDS catalysts contain 10-15 % Mo, 2-4 % Co, 25-30 % Al and very low amounts of P, Si, Fe and Ca. The remaining part consists of volatile components and sulfur [18, 19].

In the literature, there are many studies on the leaching of spent Co-Mo/Al_2O_3 HDS catalysts with acidic and basic solutions. By using H_2SO_4 [18, 20, 21], HNO_3 [19], HCl [12], H_2SO_4-HNO_3 mixture [6], first Na_2CO_3, then H_2SO_4 solutions (two stage alkali-acid leaching) [22, 23] and NaOH [21], Co and Mo in Co-Mo/Al_2O_3 HDS catalyst can be dissolved with high efficiency. However, these leaching agents are more expensive and require more safety precautions compared to organic acids. Therefore, the use of organic acids as a leaching agent provides advantages. Oxalic acid is a strong organic acid and oxidizer, cheaper and has good chelating properties [24].

Cobalt oxalate has two hydrated crystal forms, $CoC_2O_4{\cdot}4H_2O$ and $CoC_2O_4{\cdot}2H_2O$. $CoC_2O_4{\cdot}4H_2O$ dehydrates to $CoC_2O_4{\cdot}2H_2O$ at low temperatures such as 7-8 ^oC. $CoC_2O_4{\cdot}2H_2O$ crystallizes in β-form orthorhombic crystal structure and then recrystallizes into α-form monoclinic crystal structure which thermodynamically stable [25].

No study has been found in the literature on the production of $CoC_2O_4{\cdot}2H_2O$ from Co-Mo/Al_2O_3 HDS catalyst. Therefore, this study was the first study in which $CoC_2O_4{\cdot}2H_2O$ was obtained from Co-Mo/Al_2O_3 HDS catalyst. Ilhan obtained nickel oxalate dihydrate ($NiC_2O_4{\cdot}2H_2O$) from the spent Ni-Mo HDS catalyst and carried out its characterization [26].

In this study, roasted spent Co-Mo/Al_2O_3 HDS catalyst was dissolved in 0.25 M $H_2C_2O_4$ solution at 4 different temperatures (25, 40, 55 and 70 ^oC) and optimum conditions were determined for obtaining $CoC_2O_4{\cdot}2H_2O$. The characterization of the obtained $CoC_2O_4{\cdot}2H_2O$ was carried out using XRD, FT-IR, SEM-EDS and TG/DTG-DTA analysis techniques and its thermal decomposition behavior was investigated.

2. EXPERIMENTAL

Spent Co-Mo/Al_2O_3 HDS catalyst was obtained from a refinery. Co-Mo/Al_2O_3 HDS catalyst is cylindrical in shape, 1.2 mm in diameter and 1.3 mm in length. The CHNS analysis (Thermo Finnigan Flash EA 1112) of the catalyst was carried out to determine the amount of volatile compounds. Catalyst was heated to 500 °C with a heating rate of 5 °C min^{-1} and roasted for 4 h in a dynamic air atmosphere in a tube furnace (Lenton) in order to convert sulfur compounds into oxidized compounds and to remove volatile compounds. Air was passed through the system during the roasting process. XRF analysis (PANalytical Axios Minerals) was carried out to quantitatively determine the chemical composition of the roasted catalyst. XRD analysis (Rigaku D/Max-2200, Cu-Kα monochromatic X-Ray) was performed to determine the phases in the samples. Experiments for the production of $CoC_2O_4{\cdot}2H_2O$ from spent Co-Mo/Al_2O_3 HDS catalyst were carried out in a water–heated, jacketed borosilicate glass reactor system (HWS) having a volume of 500 mL. 25 g of spent Co-Mo/Al_2O_3 HDS catalyst (solid/liquid ratio: 1/20 g mL^{-1}) sample were dissolved using 300 rpm stirring speed in 0.25 M, 500 mL of oxalic acid ($H_2C_2O_4$) solution at 25, 40, 55 and 70°C temperatures. $H_2C_2O_4$ solutions used in the experiments were prepared using anhydrous $H_2C_2O_4$ (Fluka). The acid solution in the reactor was heated to the experimental temperature and the sample was added to the reactor when isothermal conditions were obtained. Solutions were taken from the reactor at certain time intervals and dissolved elements were analyzed quantitatively by inductively coupled plasma–optic emission spectroscope (ICP-OES) (Spectro Ciros Vision). After the experiments were completed, the reactor contents were taken into a beaker. Solid/liquid separation was carried out by filtering the contents of the beaker through a G-4 Gooch crucible. It was observed that the solid material contained a different material in light pink color with a very fine particle size in addition to the granular leach residue. This solid material was collected from the bottom of the Gooch crucible with a spatula, dried in an oven at 105 ^{o}C for 3 h. The characterization of the obtained solid was carried out using XRD, TG/DTG-DTA (TA SDT Q600), FT-IR (Perkin Elmer Spectrum 100), SEM (Jeol JSM 5600), EDS (iXRF 500) and ICP-OES analytical techniques.

3. RESULTS AND DISCUSSION

a.Spent Co-Mo/Al_2O_3 HDS Catalyst

CHNS analysis of the spent Co-Mo/Al_2O_3 HDS catalyst sample is shown in Table 1. Quantitative analysis results show that the catalyst contains high sulfur content. It is seen that the total amount of volatile material in the catalyst is 19.43 %.

The results of XRF analysis of Co-Mo/Al_2O_3 HDS catalyst applied oxidative roasting at 500 ^{o}C for 4 h are given in Table 2. The catalyst contains 35.13 % Al, 16.66 % Mo and 3.71 % Co. The fact that the amount of S was determined as 0.004 % indicates that the roasting process was carried out successfully. The XRD diagram of the spent Co-Mo/Al_2O_3 HDS catalyst (Figure 1) applied to the oxidative roasting process includes the peaks of the Al_2O_3 (ICDD No: 050-0741), MoO_3 (ICDD No: 005-0508), Co_3O_4 (ICDD No: 009-0418) and $AlPO_4$ (ICDD No: 003-0447) phases.

Table 1 CHNS analysis of spent Co-Mo/Al_2O_3 HDS catalyst

Element	C	H	N	S
Wt. (%)	5.92	1.12	0.59	11.80

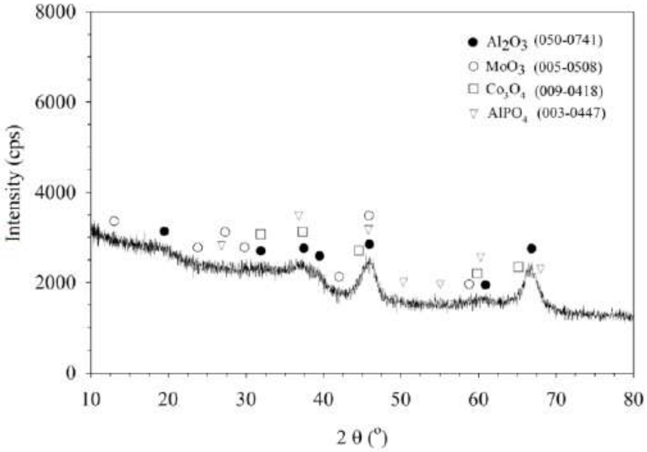

Figure 1 XRD diagram of Co-Mo/Al_2O_3 HDS catalyst oxidative roasted

Table 2 Elemental analysis of oxidative roasted Co-Mo/Al_2O_3 HDS catalyst

Element	Al	Mo	Co	P	Si	Fe	Ca	S
Wt. (%)	35.131	16.656	3.706	1.170	0.312	0.104	0.041	0.004

b.Characterization of Cobalt Oxalate Dihydrate Produced from Spent Co-Mo/Al_2O_3 HDS Catalyst

In order to determine optimum conditions for the production of cobalt oxalate dihydrate from spent Co-Mo/Al_2O_3 HDS catalyst, dissolution experiments were carried out in 0.25 M $H_2C_2O_4$ solution at 300 rpm stirring speed at different temperatures. In these experiments, the results obtained from the % Co extraction - time diagrams drawn by using the ICP-OES analysis results of the solutions taken from the reactor at different times (Figure 2), showed that the optimum conditions for the production of cobalt oxalate dihydrate ($CoC_2O_4{\cdot}2H_2O$) were 25 ^oC temperature, 0.25 M $H_2C_2O_4$ concentration, 1/20 g mL^{-1} solid/liquid ratio and 300 rpm stirring speed. Therefore, solid material obtained from the experiment performed under these conditions was used in the characterization analyses.

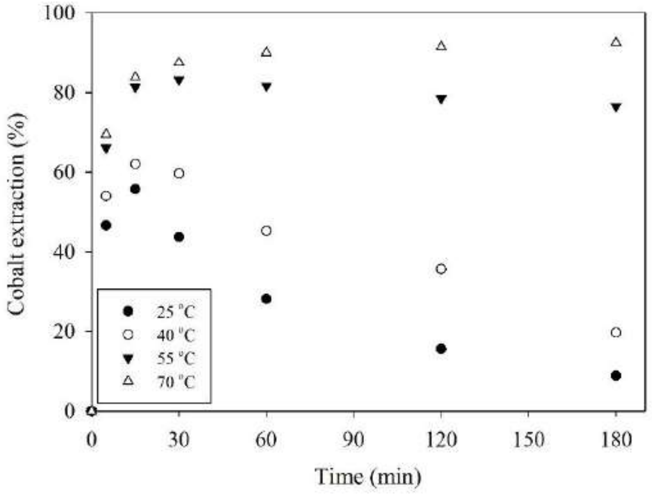

Figure 2 Cobalt extraction (%) – time diagram obtained by dissolving oxidative roasted Co-Mo/Al_2O_3 HDS catalyst in oxalic acid (Sample: 25 g, $H_2C_2O_4$ solution: 0.25 M, 500 mL, stirring speed: 300 rpm)

When the cobalt extraction (%) - time diagrams are examined, it is seen that the amount of cobalt in the solution increases rapidly at the beginning of the experiment for all experimental temperatures (Figure 2). The results obtained from the experiment carried out at 70 ^oC show that the dissolves at a rate of 70 % in the first 5 minutes of the experiment. It is seen that the amount of cobalt in the solution reached 90 % at the 60th minute of the experiment, and then remained constant and took the value of 92.5 % at the end of the 180 minutes experiment period. In the experiment carried out at 55 ^oC, the value of the cobalt amount in the solution, which took its highest value with 83 % at the 30th minute, decreased slowly in the following experiment periods and decreased to 76 % at the end of the 180 minutes experiment period. The results of the experiments carried out at 25 and 40 ^oC differ greatly from the results of the experiments carried out at 55 and 70 ^oC. The amount of cobalt in the solution, which reaches its maximum value at the end of 30 minutes in both experiments (25 ^oC: 56 %, 40 ^oC: 62 %), decreases rapidly in the following reaction times and takes its lowest value at the end of the 180 minutes experiment period. While the amount of cobalt in the solution was 19.7 % at the end of 180 minutes in the experiment carried out at 40 ^oC, this amount was 8.86 % in the same test period in the experiment carried out at 25 ^oC. Cobalt is present as Co_3O_4 in the spent Co-Mo/Al_2O_3 HDS catalyst after oxidizing roasting (Figure 1). $CoC_2O_4{\cdot}2H_2O$ is formed as a result of the reaction of Co_3O_4 with $H_2C_2O_4$ (Reaction 1).

$$Co_3O_{4\,(s)} + 3\,H_2C_2O_{4\,(aq)} + 3\,H_2O_{(aq)} \rightarrow 3\,CoC_2O_4{\cdot}2H_2O_{(s)} + 1/2\,O_{2\,(g)} \qquad (1)$$

$CoC_2O_4{\cdot}2H_2O$, which is formed according to Reaction 1, has a high solubility in acidic medium at high temperatures. $CoC_2O_4{\cdot}2H_2O$ precipitates at low temperatures and increasing pH values. The ICP-OES quantitative analysis showed that 8.86 % cobalt was present in the solution after 3 h of reaction time in the experiment using 0.25 M $H_2C_2O_4$ solution (Figure 2). Since other components (MoO_3, Al_2O_3, $AlPO_4$) in the spent Co-Mo/Al_2O_3 HDS catalyst also react with $H_2C_2O_4$ during the experiment, $H_2C_2O_4$ is consumed and the pH value of the solution is constantly increasing. According to these findings, the optimum concentration of $H_2C_2O_4$ for precipitation of $CoC_2O_4·2H_2O$ was determined as 0.25 M.

The ICP-OES quantitative analysis results showed that MoO_3, Al_2O_3 and $AlPO_4$ compounds in the spent Co-Mo/Al_2O_3 HDS catalyst were also dissolved under experimental conditions. As a result of the dissolution of these compounds, Mo, Al and P also pass into solution. The % extraction values calculated using the ICP-OES analysis results of the solutions taken from the reactor at the end of the 3 hours experiment period are given in Table 3. When Table 3 is examined, it is seen that the % extraction values of Mo, Al and P increase with increasing temperature. While the temperature dependence of the Mo and P amounts in the solution is relatively low, the temperature dependence of Al is quite high. 97.9 % of Mo, 56.2 % of Al and 63 % of P in spent Co-Mo/Al_2O_3 HDS catalyst can be taken into solution at 70 ^oC (Table 3).

Table 3 Extraction (%) values of Mo, Al and P obtained by dissolving oxidative roasted Co-Mo/Al_2O_3 HDS catalyst in oxalic acid (Sample: 25 g, $H_2C_2O_4$ solution: 0.25 M, 500 mL, stirring speed: 300 rpm, reaction time: 3 h)

Temperature	25 ^oC	40 ^oC	55 ^oC	70 ^oC
Mo extraction (%)	84.8	89.7	95.7	97.9
Al extraction (%)	8.2	13.9	32.7	56.2
P extraction (%)	32.1	40.5	56.3	63.0

Cobalt can be found as a result of the dissolution of $CoC_2O_4·2H_2O$ in the $H_2C_2O_4$ solution during the dissolution experiment, as well as in the form of cobalt oxalato ($Co(C_2O_4)_2^{2-}$), cobalt biokzalato $(Co(HC_2O_4)^+$ components and $Co(HC_2O_4)_2$) [27, 28].

The XRD diagram of the light pink solid material obtained after dissolution experiment performed at 25 ^oC temperature, 0.25 M $H_2C_2O_4$ concentration and 300 rpm stirring speed is given in Figure 3. In the XRD diagram, the peaks of $CoC_2O_4·2H_2O$ (ICDD No: 025-0250) are seen. SEM-EDS analysis of solid material is given in Figure 4. From the SEM micrograph, acicular (needle-like) crystals of $CoC_2O_4·2H_2O$ are seen. The acicular morphological structure of $CoC_2O_4·2H_2O$ is compatible with the morphological structure in Romero et al.'s study [29]. The EDS analysis of the solid material includes the peaks of cobalt and oxygen. SEM-EDS analysis also shows that the solid is $CoC_2O_4·2H_2O$.

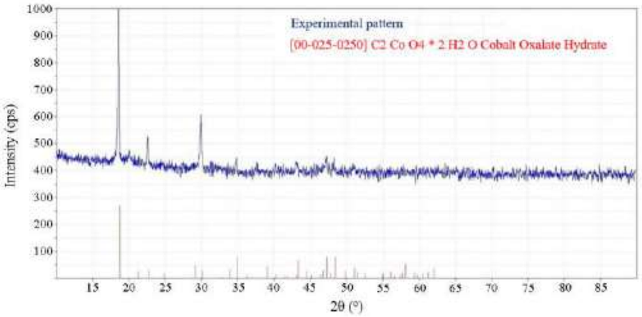

Figure 3 XRD analysis of light pink solid obtained by dissolving spent Co-Mo/Al_2O_3 HDS catalyst in oxalic acid

In order to determine the thermal decomposition behavior and decomposition reactions of the light pink solid material obtained as result of the dissolution experiment performed at 25 ^oC temperature, 0.25 M $H_2C_2O_4$ concentration and 300 rpm stirring speed, TG-DTA analysis was carried out in dry air atmosphere with a linear heating rate of 5 C min^{-1} and gas flow rate of 100 mL min^{-1} (Figure 5-a). In order to clearly determine the number of decomposition steps, DTG diagram is also given in Figure 5-b. Decomposition start and finish temperatures and DTG_{max} values are indicated on the DTG diagram.

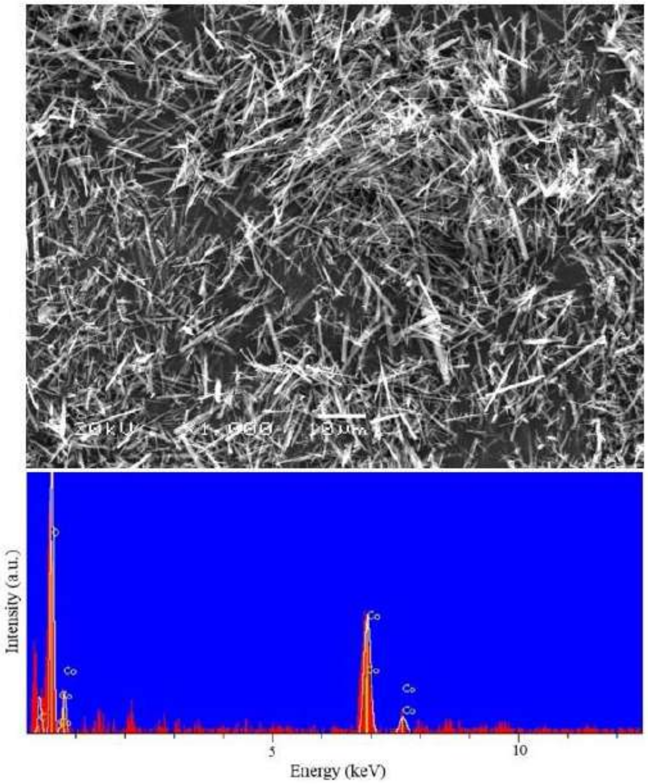

Figure 4 SEM-EDS analysis of solid obtained by dissolving spent Co-Mo/Al_2O_3 HDS catalyst in oxalic acid

When the TG and DTG diagrams is examined, no significant weight loss is observed up to 118 °C. Weight loss occurs from 118 °C and the material loses H_2O rapidly up to 196 °C. The substance loses 17.42 % weight up to 196 °C and continues to lose water slowly from this temperature up to 248 °C. At 248 °C, the weight loss is 18.40 %. According to Reaction 2, when the material is completely dehydrated and converted to CoC_2O_4, the theoretically calculated weight loss is 19.68 %. This decomposition step causes the endothermic peak to be observed in the DTA diagram.

In the second decomposition step occurring between 248-279 °C temperatures, the weight loss was determined as 42.73 %. In this step, two successive reactions occur. First, CoC_2O_4 converted to Co (Reaction 3), and then the Co formed is oxidized to Co_3O_4 (Reaction 4) due to performing in air atmosphere. The theoretically calculated weight loss during the conversion of CoC_2O_4 to Co_3O_4 is 45.38 %. Reaction 3 is an endothermic reaction. However, a sharp exothermic peak occurs because the highly exothermic reaction heat formed during the oxidation of Co to Co_3O_4 dominates the endothermic heat of Reaction 3.

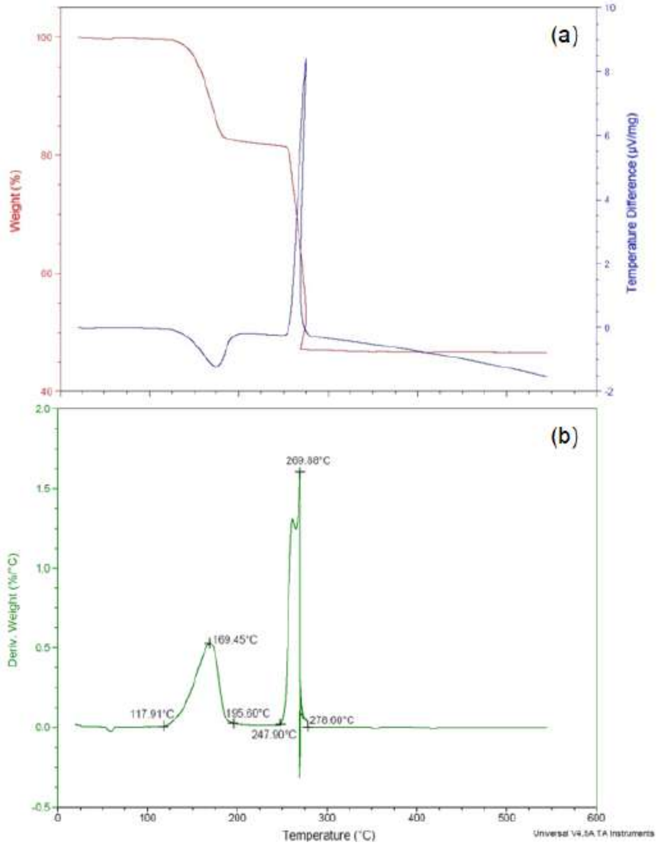

Figure 5 TG-DTA (a) and DTG (b) diagrams of the solid obtained by dissolving the spent Co-Mo/Al_2O_3 HDS catalyst in oxalic acid in dry air atmosphere (heating rate: 5 °C min^{-1}, air flow rate: 100 mL min^{-1})

$$CoC_2O_4 \cdot 2H_2O \rightarrow CoC_2O_4 + 2\ H_2O \qquad (2)$$

$$CoC_2O_4 \rightarrow Co + 2\ CO_2 \qquad (3)$$

$$3\ Co + 2\ O_2 \rightarrow Co_3O_4 \qquad (4)$$

Decomposition start-finish temperatures, derivative thermogravimetric curve (DTG_{max}) temperatures, % weight loss and % total weight loss values were determined using the data obtained from TG-DTA and DTG diagrams and are given in Table 4.

Table 4 Details of decomposition steps of solid obtained by dissolving the spent Co-Mo/Al_2O_3 HDS catalyst in oxalic acid in dry air atmosphere

	Start temperature (°C)	Finish temperature (°C)	DTG_{max} (°C)	% Weight loss	% Total weight loss
First step (Reaction 2)	118	196	169.5	17.42*	17.42
Second step (Reaction 3 and 4)	248	279	269.9	42.73	53.27

Molecular weight of $CoC_2O_4 \cdot 2H_2O$ = 182.98 g mol^{-1}

(*) After 196 °C, the substance continues to lose water slowly up to 248 °C. At 248 °C, the weight loss is 18.40 %.

Majumdar et al. [30] studied the thermal decomposition behavior of $CoC_2O_4 \cdot 2H_2O$ in an inert gas atmosphere. In Majumdar et al.'s study [30], Reaction 4 does not occur because it is performed in an inert gas atmosphere. The results obtained in this study are in agreement with the findings of Majumdar et al. [30]. Maciejewski et al. [31] determined that metallic Co formed as a result of the decomposition of CoC_2O_4 is highly active and converts to Co_3O_4 by oxidizing with O_2 when performing in air atmosphere.

Co_3O_4, obtained by thermal decomposition of $CoC_2O_4 \cdot 2H_2O$ in the air atmosphere, is in the form of nanorods or nanoparticles [32]. Co_3O_4 nanoparticles can be produced by thermal decomposition of $CoC_2O_4 \cdot 2H_2O$ in air atmosphere, as well as by methods such as microwave-assisted method, hydrothermal method, sol-gel technique, vapor deposition method, solution combustion method and chemical spray pyrolysis [32- 40].

Co_3O_4 in nanorod or nanoparticle form has many applications due to its optical, magnetic and electronic properties as well as its biological properties (antibacterial, antiviral, antifungal, antileishmanial, therapeutic agents, anticancer, and drug delivery). These nanostructures are used as anode material in lithium-ion rechargeable batteries as well as catalyst, phosphate ion sensors, electrochromic sensors, supercapacitor. Co_3O_4 nanoparticles are also used in electronics and electrooptic fields due to its p-type semiconductor properties [34- 42].

FT-IR diagram of the light pink solid material obtained after leaching experiment performed at 25 °C temperature, 0.25 M $H_2C_2O_4$ concentration and 300 rpm stirring speed is given in Figure 6-a. FT-IR spectrum includes vibration bands of ν(Co-O) at 486 cm^{-1}, ν(CC) + δ(CO_2) at 740 and 821 cm^{-1}, ν_{sym}(CO) at 1315 cm^{-1}, ν_{asym}(CO) at 1361 cm^{-1}, ν(CO) at 1612 cm^{-1} and ν(OH)(H_2O) at 3350 cm^{-1} (Figure 6-a). These results are in good agreement with the FT-IR spectral analysis findings of Prananto et al. [32] and support that the light pink solid material obtained is $CoC_2O_4 \cdot 2H_2O$.

FT-IR diagram of the final product obtained by decomposition of light pink solid material in air atmosphere is given in Fig 6-b. FT-IR spectrum includes broad absorption band of ν(Co-O) at 488 cm^{-1} and narrow sharp absorption band of O-Co-O at 655 cm^{-1}. Patel et al. [43] stated that the strong absorption band determined at 662 cm^{-1} belongs to the stretching vibrations of the octahedrally coordinated Co^{3+} metal ions in the metal oxide. Prabaharan et al. [33] stated that the absorption band determined at 661 cm^{-1} is the stretching vibration of the O-Co-O bond. The findings obtained in this study are in good agreement with the findings of Patel et al. [43] and Prabaharan et al. [33] and it shows that the final product obtained by the decomposition of the light pink solid material in the air atmosphere is Co_3O_4.

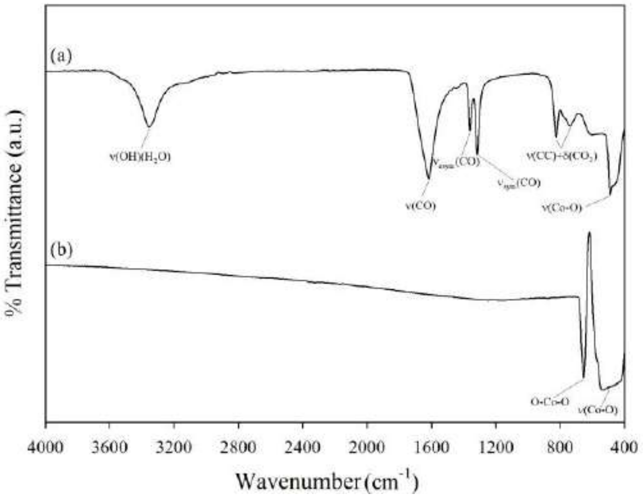

Figure 6 FT-IR diagrams of solid obtained by dissolving spent Co-Mo/Al_2O_3 HDS catalyst in oxalic acid (a) and the final product obtained by decomposition of this solid in air atmosphere (b)

In addition to XRD, SEM-EDS and TG/DTG-DTA analyses, FT-IR analysis also shows that the light pink colored material obtained is $CoC_2O_4{\cdot}2H_2O$. The decomposition steps and the decomposition start and finish temperatures in the TG-DTA and DTG diagrams given in Figure 5 are in good agreement with the literature [30]. On the other hand, it is seen that the weight loss values obtained from the TG diagram are slightly lower than the theoretically calculated weight loss values.

In order to determine the Co content of the light pink solid material ($CoC_2O_4{\cdot}2H_2O$) obtained, 100 mg of solid was completely dissolved in 1 M NH_3 (ammonia) solution. As a result of the ICP-OES quantitative analysis of the obtained solution, the Co content of $CoC_2O_4{\cdot}2H_2O$ solid was determined as 31.45 %.

By using the ICP-OES quantitative analysis results of the solution obtained at the end of the experiment carried out at 25 ^{o}C temperature, 0.25 M $H_2C_2O_4$ concentration, 300 rpm stirring speed and by weighing the light pink solid obtained from dissolving the spent Co-Mo/Al_2O_3 HDS catalyst in oxalic acid solution, the reaction yield of obtaining $CoC_2O_4{\cdot}2H_2O$ solid was calculated as 90.9 %.

4. CONCLUSION

In this study, roasted spent Co-Mo/Al_2O_3 HDS catalyst was dissolved in $H_2C_2O_4$ solution and optimum conditions were determined for obtaining $CoC_2O_4{\cdot}2H_2O$. The characterization of the obtained $CoC_2O_4{\cdot}2H_2O$ was carried out and its thermal decomposition behavior was investigated. The conclusions can be summarized as follows;

- It is determined that $CoC_2O_4{\cdot}2H_2O$ can be obtained by dissolving the spent Co-Mo/Al_2O_3 HDS catalyst in $H_2C_2O_4$ solution. Optimum conditions for $CoC_2O_4{\cdot}2H_2O$ production were determined as 25 ^{o}C temperature, 0.25 M $H_2C_2O_4$ concentration, 1/20 g mL^{-1} solid/liquid ratio and 300 rpm stirring speed. $CoC_2O_4{\cdot}2H_2O$ was obtained with a reaction yield of 90.9 %.

- $CoC_2O_4{\cdot}2H_2O$ is formed in accordance with the following reaction of Co_3O_4, in Co-Mo/Al_2O_3 HDS catalyst after oxidizing roasting, with $H_2C_2O_4$.

$$Co_3O_4\,_{(s)} + 3\ H_2C_2O_4\,_{(aq)} + 3\ H_2O\,_{(aq)} \rightarrow$$
$$3\ CoC_2O_4{\cdot}2H_2O\,_{(s)} + 1/2\ O_2\,_{(g)}$$

- The light pink solid material obtained from dissolving of spent Co-Mo/Al_2O_3 HDS catalyst in solution containing $H_2C_2O_4$ was characterized by XRD, SEM-EDS, TG/DTG-DTA and FT-IR analyzes and it was determined as $CoC_2O_4{\cdot}2H_2O$.

- Co_3O_4 is obtained by decomposition of $CoC_2O_4{\cdot}2H_2O$ in air at temperatures above 280 ^{o}C.

- Co_3O_4 is a multifunctional material and has many applications such as biomedical applications, catalysts, phosphate ion sensors, electrochromic sensors, supercapacitor, as anode material in lithium ion rechargeable batteries. The fact that Co_3O_4 is produced by thermal decomposition of $CoC_2O_4{\cdot}2H_2O$ obtained from spent Co-Mo/Al_2O_3 HDS catalyst, which is a waste, in the air atmosphere is important for the studies to be carried out on this subject.

Funding

The author has no received any financial support for the research, authorship or publication of this study.

The Declaration of Conflict of Interest/Common Interest

No conflict of interest or common interest has been declared by the author.

The Declaration of Ethics Committee Approval

This study does not require ethics committee permission or any special permission.

The Declaration of Research and Publication Ethics

The author of the paper declare that he comply with the scientific, ethical and quotation rules of SAUJS in all processes of the paper and that he do not make any falsification on the data collected. In addition, he declare that Sakarya University Journal of Science and its editorial board have no responsibility for any ethical violations that may be encountered, and that this study has not been evaluated in any academic publication environment other than Sakarya University Journal of Science.

REFERENCES

[1] M. Marafi, A. Stanislaus, E. Furimsky, Handbook of Spent Hydroprocessing Catalysts: Second Edition. Elsevier Inc., 2017.

[2] P. Dufresne, “Hydroprocessing catalysts regeneration and recycling,” Applied Catalysis A: General, vol. 322, pp. 67–75, 2007.

[3] “Federal Register : Hazardous Waste Management System: Petroleum Refining Process Wastes; Identification of Characteristically Hazardous Self-Heating Solids; Land Disposal Restrictions: Treatment Standards for Spent Hydrorefining Catalyst (K172) Hazardous Waste.” https://www.federalregister.gov/documents/2003/10/20/03-26411/hazardous-waste-management-system-petroleum-refining-process-wastes-identification-of (accessed April 25, 2022).

[4] C. Yang, J. Zhanga, Y. Chen, C. Wang, “Efficient removal of oil from spent hydrodesulphurization catalysts using microwave pyrolysis method,” Journal of Analytical and Applied Pyrolysis, vol. 135, pp. 169–175, 2018.

[5] J. Z. Wang, H. Du, A. Olayiwola, B. Liu, F. Gao, M. L. Jia, M. H. Wang, M. L. Gao, X. D. Wang, S. N. Wang, “Recent advances in the recovery of transition metals from spent hydrodesulfurization catalysts,” Tungsten, vol. 3, pp. 305–328, 2021.

[6] S. P. Barik, K. H. Park, P. K. Parhi, J. T. Park, C. W. Nam, “Extraction of metal values from waste spent petroleum catalyst using acidic solutions,” Separation and Purification Technology, vol. 101, pp. 85–90, 2012.

[7] E. Furimsky, “Spent refinery catalysts: Environment, safety and utilization,” Catalysis Today, vol. 30, no. 4, pp. 223–286, 1996.

[8] L. Zeng, C. Y. Cheng, “A literature review of the recovery of molybdenum and vanadium from spent hydrodesulphurisation catalysts: Part I: Metallurgical processes,” Hydrometallurgy, vol. 98, no. 1–2, pp. 1–9, 2009.

[9] M. S. Villarreal, B. I. Kharisov, L. M. Torres-Martinez, V. N. Elizondo, “Recovery of vanadium and molybdenum from spent petroleum catalyst of PEMEX,” Industrial and Engineering Chemistry Research, vol. 38, no. 12, pp. 4624–4628, 1999.

[10] M. Marafi, A. Stanislaus, “Waste catalyst utilization: Extraction of valuable metals from spent hydroprocessing catalysts by ultrasonic-assisted leaching with acids,” Industrial and Engineering Chemistry Research, vol. 50, no. 16, pp. 9495–9501, 2011.

[11] A. Akcil, F. Vegliò, F. Ferella, M. D. Okudan, A. Tuncuk, “A review of metal recovery from spent petroleum catalysts and ash,” Waste Management, vol. 45, pp. 420–433, 2015.

[12] R. Banda, T. H. Nguyen, S. H. Sohn, M. S. Lee, “Recovery of valuable metals and regeneration of acid from the leaching solution of spent HDS catalysts by solvent extraction,” Hydrometallurgy, vol. 133, pp. 161–167, 2013.

[13] A. K. Nayak, N. Devi, K. Sarangi, “Use of Cyanex 572 as an effective extractant for the recovery of Mo(VI) and V(V) from HDS spent catalyst leach liquor,” Separation and Purification Technology, vol. 275, p. 118960, 2021.

[14] P. C. Rout, G. K. Mishra, B. Padh, K. R. Suresh, B. Ramachandra Reddy, “Solvent extraction separation of molybdenum as thio-molybdate complex from alkaline tungsten leach liquor of spent HDS catalyst – A pilot study,” Hydrometallurgy, vol. 174, pp. 140–146, 2017.

[15] K. H. Park, D. Mohapatra, C. W. Nam, “Two stage leaching of activated spent HDS catalyst and solvent extraction of aluminium using organo-phosphinic extractant, Cyanex 272,” Journal of Hazardous Materials, vol. 148, no. 1–2, pp. 287–295, 2007.

[16] D. D. Sun, J. H. Tay, H. K. Cheong, D. L. K. Leung, G. R. Qian, “Recovery of heavy metals and stabilization of spent hydrotreating catalyst using a glass–ceramic matrix,” Journal of Hazardous Materials, vol. 87, no. 1–3, pp. 213–223, 2001.

[17] I. M. Valverde, J. F. Paulino, J. C. Afonso, “Hydrometallurgical route to recover molybdenum, nickel, cobalt and aluminum from spent hydrotreating catalysts in sulphuric acid medium,” Journal of Hazardous Materials, vol. 160, no. 2–3, pp. 310–317, 2008.

[18] S. P. Barik, K. H. Park, P. K. Parhi, J. T. Park, “Direct leaching of molybdenum and cobalt from spent hydrodesulphurization catalyst with sulphuric acid,” Hydrometallurgy, vol. 111–112, no. 1, pp. 46–51, 2012.

[19] I. Susoglu, “Dissolution of used cobalt-molybdenum hydrodesulfurization (HDS) catalyst in nitric acid solutions”, MSc thesis, Department of Metallurgical and Materials Engineering, Istanbul University-Cerrahpasa, Istanbul, 2019.

[20] H. I. Kim, K. H. Park, D. Mishra, “Sulfuric acid baking and leaching of spent Co-Mo/Al_2O_3 catalyst,” Journal of Hazardous Materials, vol. 166, no. 2–3, pp. 1540–1544, 2009.

[21] M. D. Okudan, “Acidic and alkaline leaching application to spent hydrodesulfurization (HDS) catalysts including cobalt and molybdenum”, Msc thesis, Department of Mining Engineering, Suleyman Demirel University, Isparta, 2009.

[22] D. Mohapatra, K. H. Park, “Selective recovery of Mo, Co and Al from spent Co/Mo/γ-Al_2O_3 catalyst: Effect of calcination temperature,” Journal of Environmental Science and Health, Part A, vol. 42, no. 4, pp. 507–515, 2007.

[23] W. T. Mohammed, N. S. Ahmedzeki, M. F. AbdulNabi, “Extraction of valuable metals from spent hydrodesulfurization catalyst by

two stage leaching method," Iraqi Journal of Chemical and Petroleum Engineering, vol. 12, no. 4, pp. 21–35, 2011.

[24] S. Ilhan, "Extraction of molybdenum, nickel and aluminium from spent Ni–Mo hydrodesulphurization (HDS) catalyst in oxalic acid solutions," Canadian Metallurgical Quarterly, vol. 59, no. 1, pp. 26–35, 2020.

[25] A. Taskinen, P. Taskinen, M. H. Tikkanen, "Thermal decomposition of cobalt oxalate," Reactivity of Solids, pp. 617–624, 1977.

[26] S. Ilhan, "Kullanılmış Ni–Mo hidrodesülfürizasyon katalizöründen nikel okzalat dihidrat üretimi," Politeknik Dergisi, vol. 23, no. 1, pp. 105–110, 2020.

[27] E. Tóth-Szeles, G. Schuszter, Á. Tóth, Z. Kónya, D. Horváth, "Flow-driven morphology control in the cobalt–oxalate system," CrystEngComm, vol. 18, no. 12, pp. 2057–2064, 2016.

[28] G. M. Armitage, H. S. Dunsmore, "Stability of the hydrogen–oxalate complexes of calcium and strontium," Journal of Inorganic and Nuclear Chemistry, vol. 35, no. 3, pp. 817–822, 1973.

[29] E. Romero, M. E. Mendoza, R. Escudero, "Weak ferromagnetism in cobalt oxalate crystals," Physica Status Solidi (B), vol. 248, no. 6, pp. 1519–1525, 2011.

[30] S. Majumdar, I. G. Sharma, A. C. Bidaye, A. K. Suri, "A study on isothermal kinetics of thermal decomposition of cobalt oxalate to cobalt," Thermochimica Acta, vol. 473, no. 1–2, pp. 45–49, 2008.

[31] M. Maciejewski, E. Ingier-Stocka, W. D. Emmerich, A. Baiker, "Monitoring of the gas phase composition: A prerequisite for unravelling the mechanism of decomposition of solids. Thermal decomposition of cobalt oxalate dihydrate," Journal of Thermal Analysis and Calorimetry, vol. 60, no. 3, pp. 735–758, 2000.

[32] Y. P. Prananto, M. M. Khunur, D. T. Wahyuni, R. A. Shobirin, Y. R. Nata, E. Riskah, "Study of gel growth cobalt (II) oxalate crystals as precursor of Co_3O_4 nano particles," Bulletin of Chemical Reaction Engineering and Catalysis, vol. 7, no. 3, pp 198–204, 2013.

[33] D. D. M. Prabaharan, K. Sadaiyandi, M. Mahendran, S. Sagadevan, "Precipitation method and characterization of cobalt oxide nanoparticles," Applied Physics A, vol. 123, pp. 264, 2017.

[34] G. Asha, V. Rajeshwari, G. Stephen, S. Gurusamy, D. C. J. Rachel, "Eco–friendly synthesis and characterization of cobalt oxide nanoparticles by sativum species and its photo-catalytic activity," Materials Today: Proceedings, vol. 48, no. 2, pp. 486–493, 2022.

[35] M. Salavati-Niasari, N. Mir, F. Davar, "Synthesis and characterization of Co_3O_4 nanorods by thermal decomposition of cobalt oxalate," Journal of Physics and Chemistry of Solids, vol. 70, no. 5, pp. 847–852, 2009.

[36] M. T. Makhlouf, B. M. Abu-Zied, T. H. Mansoure, "Effect of calcination temperature on the H_2O_2 decomposition activity of nano-crystalline Co_3O_4 prepared by combustion method," Applied Surface Science, vol. 274, pp. 45–52, 2013.

[37] S. Farhadi, K. Pourzare, S. Sadeghinejad, "Simple preparation of ferromagnetic Co_3O_4 nanoparticles by thermal dissociation of the $[Co^{II}(NH_3)_6](NO_3)_2$ complex at low temperature," Journal of Nanostructure in Chemistry, vol.3, no. 1, pp. 16, 2013.

[38] P. Zhang, G. X. Hu, S. J. Bao, J. Guo, C. Lei, C. J. Cai, D. Z. Jia, R. Y. Wang, “One step microwave synthesis and magnetic properties of Co_3O_4 octahedrons,” Materials Letters, vol. 83, 195–197, 2012.

[39] S. Thota, A. Kumar, J. Kumar, “Optical, electrical and magnetic properties of Co_3O_4 nanocrystallites obtained by thermal decomposition of sol–gel derived oxalates,” Materials Science and Engineering: B, vol. 164, no. 1, pp. 30–37, 2009.

[40] C. Dong, X. Xiao, G. Chen, H. Guan, Y. Wang, “Hydrothermal synthesis of Co_3O_4 nanorods on nickel foil,” Materials Letters, vol. 123, pp. 187–190, 2014.

[41] A. T. Khalil, M. Ovais, I. Ullah, M. Ali, Z. K. Shinwari, M. Maaza, “Physical properties, biological applications and biocompatibility studies on biosynthesized single phase cobalt oxide (Co_3O_4) nanoparticles via Sageretia thea (Osbeck.),” Arabian Journal of Chemistry, vol. 13, no. 1, pp. 606–619, 2020.

[42] A. Waris, M. Din, A. Ali, S. Afridi, A. Baset, A. U. Khan, M. Ali, “Green fabrication of Co and Co_3O_4 nanoparticles and their biomedical applications: A review,” Open Life Sciences, vol. 16, pp. 14–30, 2021.

[43] V. K. Patel, J. R. Saurav, K. Gangopadhyay, S. Gangopadhyay, S. Bhattacharya, “Combustion characterization and modeling of novel nanoenergetic composites of Co_3O_4/nAl,” RSC Advances, vol. 5, pp. 21471–21479, 2015.